



# Approche multi-échelle de l'interaction des biocarburants avec les surfaces métalliques des circuits carburants des transports terrestres et aéronautiques

Claudia Cantarelli

## ► To cite this version:

Claudia Cantarelli. Approche multi-échelle de l'interaction des biocarburants avec les surfaces métalliques des circuits carburants des transports terrestres et aéronautiques. Chimie analytique. Université Paris sciences et lettres, 2021. Français. NNT : 2021UPSLC017 . tel-03956254

**HAL Id: tel-03956254**

**<https://pastel.hal.science/tel-03956254>**

Submitted on 25 Jan 2023

**HAL** is a multi-disciplinary open access archive for the deposit and dissemination of scientific research documents, whether they are published or not. The documents may come from teaching and research institutions in France or abroad, or from public or private research centers.

L'archive ouverte pluridisciplinaire **HAL**, est destinée au dépôt et à la diffusion de documents scientifiques de niveau recherche, publiés ou non, émanant des établissements d'enseignement et de recherche français ou étrangers, des laboratoires publics ou privés.



**THÈSE DE DOCTORAT**  
**DE L'UNIVERSITÉ PSL**

Préparée à École Nationale Supérieure de Chimie de Paris

**Approche multi-échelle de l'interaction des biocarburants avec  
les surfaces métalliques des circuits carburants des transports  
terrestres et aéronautiques**

Soutenue par

**Claudia CANTARELLI**

Le 17 novembre 2021

Ecole doctorale n° 388

**Chimie Physique et Chimie  
Analytique de Paris centre**

Spécialité

**Chimie physique**

Composition du jury :

M. André NICOLLE Ingénieur de recherche HDR, Aramco Fuel	<i>Président de jury</i>
Mme. Anne HEMERYCK Chargé de Recherche, CNRS-LAAS	<i>Rapporteuse</i>
Mme. Corinne DUFAURE Professeure, ENSIACET	<i>Rapporteuse</i>
M. Anton KOKALJ Professeur, Institut "Jožef Stefan"	<i>Examineur</i>
Mme. Dominique COSTA Directrice de recherche, ENSCP	<i>Directrice de thèse</i>

*This page is intentionally left blank*

## Abstract

The use of biofuels is one of the main levers for the transport industry to meet the ambitious environmental targets. However, one of their major drawbacks is their thermal and chemical stability towards oxidation. Indeed oxidation causes hydrocarbon degradation, which results in the formation of insoluble aggregates and deposits in the fuel system of automobiles and aircraft that consequently leads to mechanical engine failures, such as injector blockage or filter plugging.

The objective of this thesis is to better understand the phenomenology related to the formation of deposits produced by the autoxidation process that occurs for fossil and renewable fuels and the impact of the metal surface in contact with the fuel. To achieve this goal, the methodology adopted for this thesis is based on the combination of two different numerical approaches: *ab initio* Density Functional Theory (DFT) and an empirical atomistic reactive force field simulations.

Using DFT we calculated the reaction energies of a set of representative reactions describing the toluene autoxidation. Furthermore, we studied the interaction between small representative organic molecules (i.e. models of deposit precursors) and representative models for both aluminum, i.e.  $\alpha$ -Al<sub>2</sub>O<sub>3</sub> and stainless-steel surfaces ( $\alpha$ -Cr<sub>2</sub>O<sub>3</sub>). Both anhydrous and hydrated surface states were considered. For the anhydrous surfaces, the alumina surface was found to be more reactive than the chromia surface, but the same ordering in adsorption energies was calculated: oxygenated molecules > aromatics > linear alkanes. Generally, the adsorption energies attenuated for the hydroxylated surfaces and hydroxylated alumina and chromia showed practically equal reactivity. Hence, the DFT calculations evidence the influence of the surface state on the adhesion properties.

The DFT results were subsequently used as reference data to train the force field parameters of the ReaxFF force field. Two different force fields were considered: one describing alumina-based systems (FFA) and the other of chromia-based systems (FFB). The quality of the optimized force field parameters was evaluated against the reproduction of the data of the training set and a validation set that includes cell parameters of the bulk oxides, adsorption energies and energy curves of organic molecules, representative reactions of the autoxidation of toluene, and the

dynamic structuration of pure organic liquids (mass/volume density, radial distribution functions). Only FFA (for alumina-based systems) could be validated and was retained to a model fuel blend in contact with alumina.

The model blend, consisting of 95 mol% toluene and 5 mol% benzyl hydroperoxide, was firstly modeled in absence of a solid phase. From NPT simulations it resulted that the liquid density corresponds reasonably well the experimental value. Moreover, the benzyl hydroperoxide was chemically stabled, although these molecules tend to aggregate to form di- and trimers.

Next, the interaction between model blend and anhydrous alumina was studied, by putting a small “drop” of the model mixture on the surface. A dense toluene monolayer is formed that is stable at  $T=400$  K, a result confirmed by DFT BOMD calculations, issue of a strong adsorption energy. However, if alumina is completely hydroxylated, a 0.2 ML is formed. This is in accordance with the DFT calculated, smaller interaction energies between hydroxylated alumina and toluene.

Finally, the blend was put in contact with both anhydrous and hydroxylated alumina. We observed a toluene structuration as a monolayer on the hydroxylated  $\text{Al}_2\text{O}_3$  surface and a bilayer for the dry  $\text{Al}_2\text{O}_3$  surface. Yet, a tendency to aggregation of benzyl hydroperoxides was observed on both surface types. Importantly, only on the anhydrous alumina surface the benzyl hydroperoxides undergo O-O bond cleavage after adsorption on a terminal surface Al atom, thereby showing that the degree of hydroxylation of the aluminium surface plays a key role in the molecule-surface reactivity. As expected, at larger distances from the surface, the influence of the alumina surface quickly diminishes and the blend behaves as a “homogeneous” liquid phase as described above where benzyl hydroperoxides aggregate but no bond dissociation has been registered.

## Résumé

L'utilisation des biocarburants est l'un des principaux leviers permettant à l'industrie des transports de faire face aux objectifs environnementaux ambitieux qui lui sont assignés en général. Dans les dernières études statistiques européennes concernant l'énergie, les transports et l'environnement, il a été signalé que les transports représentent actuellement un quart des émissions de gaz à effet de serre (GES) de l'UE. Au cours des dernières années, la Commission européenne a annoncé de nombreux objectifs ambitieux concernant la question des GES, tels que leur réduction de 60 % par rapport à 1990 d'ici 2050 et l'adoption du "Green Deal" européen, qui définit un cadre stratégique pour une économie européenne climatiquement neutre d'ici 2050. Pour atteindre tous ces objectifs ambitieux, il sera nécessaire, selon ces rapports, de parvenir à une réduction de 90 % des émissions du secteur des transports d'ici à 2050.

Les biocarburants ont une composition chimique et des propriétés physiques qui, tout en respectant les normes internationales de qualité des carburants, peuvent présenter des différences chimiques et physiques par rapport aux carburants fossiles classiques.

Cependant, cette plus grande variété de composition chimique conduit à l'un de leur principal inconvénient, à savoir leur stabilité thermique et d'oxydation. Leur susceptibilité à l'oxydation conduit à l'activation de la dégradation des hydrocarbures, qui aboutit finalement à la formation d'agrégats insolubles et de dépôts dans le système de carburant des automobiles et des avions. Ce phénomène est très problématique car il peut provoquer des défaillances mécaniques du moteur, telles que le blocage des injecteurs ou le colmatage des filtres.

L'objectif de cette thèse est de mieux comprendre la phénoménologie liée à la formation de dépôts produits par le processus d'autoxydation qui se produit pour les combustibles fossiles et renouvelables stockés dans les systèmes d'injection des moteurs diesel. Il est également primordial pour cette étude de déterminer quels sont les paramètres et les conditions de fonctionnement qui peuvent avoir le plus d'impact sur le processus d'adhésion/précipitation de ces dépôts, en particulier dans le cas des surfaces métalliques du système d'injection puisqu'elles sont constamment en contact avec le carburant stocké.

Cette thèse consiste en une étude computationnelle multi-échelle de l'interaction biocarburant/métal. L'idée derrière une approche multi-échelle est de décomposer le système entier et les phénomènes pertinents en plusieurs domaines (par exemple, la phase solide métallique, la couche d'oxyde, l'interface liquide-solide et la masse liquide). Dans chacun de ces domaines, la décomposition en facteurs opérant à différentes échelles peut être envisagée et décrite par divers modèles. Le modèle intégré multi-échelles prend en compte des processus tels que l'autoxydation des molécules en solution, la migration des agrégats vers la surface du métal, le rôle de la surface dans l'oxydation des produits et la formation des agrégats. A notre connaissance, une telle approche intégrée appliquée à l'interaction combustible-surface n'a pas encore été réalisée.

Dans une approche multi-échelle, les méthodes atomistiques devraient apporter des informations importantes qui ne sont pas accessibles par l'expérience.

Ainsi, les méthodes atomistiques DFT et ReaxFF sont utiles pour les études suivantes: les calculs quantiques peuvent être effectués pour estimer les énergies de déprotonation et de solvation des molécules dans le carburant et les calculs ReaxFF peuvent aider à estimer la tendance des molécules à former des agrégats. Les calculs MD ReaxFF peuvent apporter un éclairage sur les tensions de surface et d'interface, les données de diffusivité de diverses espèces dans les phases liquides. Les calculs de premiers principes associés à la thermodynamique atomistique (qui permet de calculer les énergies de réaction d'autoxydation) sont utiles pour construire des diagrammes de phase de surface et pour prédire, dans des conditions thermodynamiques données, la terminaison de surface et la composition du film d'oxyde. Les calculs DFT sont l'outil principal pour modéliser les réactions entre les molécules dans un liquide et sur une surface donnée.

Cependant, les simulations de mécanique quantique DFT peuvent présenter une limitation significative en termes de temps de calcul, en particulier lorsque la taille des systèmes chimiques est supérieure à 100-200 atomes. Un autre facteur pertinent qui peut sûrement avoir un impact sur cet aspect est la complexité des systèmes où différentes espèces chimiques sont impliquées, puisque les prédictions de leurs propriétés en plus de leurs interactions peuvent ralentir considérablement les simulations DFT.

L'un des concepts fondamentaux de la chimie et de la science des matériaux est sans aucun doute la "rupture et la formation de liaisons". La modélisation précise des processus de rupture de

liaison continue d'être un défi informatique, en particulier dans la description de grandes molécules. Les progrès récents dans l'implémentation de la DFT de Kohn-Sham non restreinte (spin polarisée) ont permis de prendre en compte la rupture homolytique des liaisons, rendant possible la description des réactions se produisant entre des molécules avec des électrons non appariés (c'est-à-dire des radicaux libres). Puisque dans cette étude, nous voulions simuler les processus associés à l'autoxydation des molécules, où des espèces très réactives comme les radicaux sont formées, des calculs DFT polarisés en spin étaient nécessaires.

Des champs de force réactifs paramétrés empiriquement, basés sur des concepts d'ordre des liaisons (comme ReaxFF) et permettant de modéliser la rupture des liaisons, ont été développés ces dernières années. Les champs de force réactifs incluent des résultats de DFT dans des ensembles d'entraînement, ce qui permet de les paramétrer afin de mieux modéliser la rupture de liaison des molécules qui se produit au cours d'un processus chimique.

C'est la méthodologie adoptée pour cette thèse, qui est basée sur la combinaison de ces deux approches numériques différentes: une étude *ab initio* menée via la Théorie de la Fonctionnelle de la Densité (DFT) et une approche successive de Dynamique Moléculaire (MD) réalisée via l'implémentation d'un Champ de Force Réactif (ReaxFF). L'étude théorique préliminaire DFT a été réalisée pour acquérir des données thermodynamiques utiles (c'est-à-dire les énergies d'adsorption, les énergies de réaction de l'autoxydation, etc.) à partir de l'optimisation de la géométrie des systèmes gazeux/solides d'intérêt dans l'intention de les utiliser comme données d'entrée pour entraîner le champ de force empirique afin d'obtenir un champ de force capable de prédire correctement le comportement des espèces chimiques impliquées, à la fois dans les phases homogènes et hétérogènes. Une fois le champ de force validé, l'objectif principal est d'obtenir des informations utiles sur les processus d'adsorption et de dépôt tout en considérant les phénomènes de dégradation/oxydation qui se produisent dans la phase liquide du combustible.

Avec ces prémisses, nous commençons notre discussion sur la méthodologie choisie en présentant d'abord la méthode de mécanique quantique DFT, suivie par la description des principes de dynamique moléculaire définissant la méthode ReaxFF (**Chapitre 2**).

Dans le cadre de cette thèse, nous avons choisi d'utiliser les résultats DFT obtenus lors de l'étude théorique préliminaire comme données d'entrée pour paramétrer ReaxFF en les ajoutant à l'ensemble d'entraînement. Pour obtenir un champ de force capable de décrire correctement les

propriétés et les caractéristiques des systèmes moléculaires d'intérêt, le *training set* doit inclure l'ensemble des configurations DFT optimisées qui représentent le mieux le système chimique analysé. Dans notre cas, puisque nous étions intéressés par la description du phénomène lié à la formation de dépôts de carburant, nous avons choisi d'ajouter à notre ensemble d'entraînement principalement les configurations d'adsorption optimisées par DFT des molécules modèles représentant les précurseurs de dépôts sur le dessus des substituts d'aluminium et d'acier inoxydable dans des conditions anhydres et hydroxylées.

Notre *training set* était composé principalement des configurations d'adsorption d'une grande variété de molécules modèles afin d'assurer une plus grande possibilité pour le champ de force réactif d'être bien ajusté pour prédire correctement les systèmes moléculaires analysés. Cette méthodologie mise en œuvre pour l'amélioration du ReaxFF dans la description des propriétés chimiques et des réactivités de nos systèmes a envisagé un cycle itératif, dont les deux parties principales peuvent être définies comme la "paramétrisation du ReaxFF" et la "validation du ReaxFF". Pour la première partie, l'objectif était de définir un ensemble d'entraînement approprié qui nous aiderait à améliorer les champs de force implémentés, tandis que la deuxième partie de ce cycle a été conçue pour les valider.

L'intérêt majeur de cette thèse est l'étude des interactions se produisant entre une phase liquide organique, substitut des précurseurs de dépôts, et une phase solide d'oxyde métallique, représentative des matériaux métalliques recouvrant couramment les systèmes d'injection des moteurs.

Comme surfaces métalliques, nous avons opté pour l'aluminium et l'acier inoxydable car ces deux matériaux sont très utilisés comme revêtements dans le secteur des transports. Ils présentent tous deux une résistance à la corrosion grâce à la présence d'un film d'oxyde passif protecteur (**Chapitre 3**).

En ce qui concerne les substituts des précurseurs de dépôts, les principaux produits issus de l'autoxydation des carburants sont des composés oxygénés comme les alcools, les aldéhydes, les cétones, les époxydes et les acides carboxyliques. Pour ces raisons, dans la présente étude, de petites molécules oxygénées ont été préférées comme molécules modèles sur la base de leur groupe fonctionnel chimique, c'est-à-dire l'éthanol pour la famille des alcools, l'acétaldéhyde et l'acétone pour représenter respectivement les aldéhydes et les cétones, le 2-éthyle-3-

méthyloxirane pour les époxydes et l'acide acétique pour les acides carboxyliques. En outre, trois autres types de familles chimiques ont été considérés:

(1) les espèces aromatiques puisqu'elles constituent l'un des composants du diesel raffiné à partir du pétrole brut et qu'elles sont donc présentes dans les mélanges diesel/biodiesel sur le marché, nous considérons ici le benzène et le toluène comme des composés aromatiques modèles.

(2) les esters: propionate de méthyle, esters méthyliques insaturés (par exemple, acrylate de méthyle et 3-trans-hexénoate de méthyle), en tant que représentants des dépôts dérivés des mélanges biodiesel.

(3) alcanes puisqu'ils sont le principal composant des carburants en général, nous considérons ici le n-propane comme substitut des dépôts de chaînes alkyles produits par la dégradation des n-alcanes.

Pour améliorer notre compréhension des formations de dépôts indésirables observées pour les biodiesels dans les circuits de carburant des moteurs, nous avons effectué des calculs DFT sur des molécules modèles de différents produits d'autoxydation. Une analyse thermodynamique nous a permis de calculer les facteurs entropiques en phase gaz de ces molécules. Nous avons aussi étudié plusieurs réactions d'autoxydation du toluène par DFT. Ces travaux font l'objet du **Chapitre 4**. Les résultats serviront de première base à l'élaboration des champs de force.

L'adsorption des petites molécules organiques représentatives susmentionnées sur des surfaces représentatives d'aluminium et d'acier inoxydable a ensuite été étudiée par DFT (**Chapitre 4**). Le circuit de carburant en acier inoxydable a été représenté par  $\alpha\text{-Cr}_2\text{O}_3$  et les circuits à base d'aluminium par  $\alpha\text{-Al}_2\text{O}_3$ , dans lesquels chaque orientation de surface étudiée était soit anhydre, soit totalement hydroxylée (**Chapitre 3**).

A partir de cette étude DFT, nous avons constaté que les circuits en acier inoxydable, qui est la surface la plus problématique puisqu'elle est le matériau des injecteurs, ne joueraient pas un rôle plus important dans les réactions d'autoxydation par rapport aux circuits à base d'aluminium. Ce résultat est important car il corrobore le fait que les agrégats de produits d'oxydation du carburant semblent être principalement formés dans la phase liquide et se déposer ensuite sur une surface par différents mécanismes. De plus, les interactions relativement faibles (-30 à -70 kJ/mol) entre la surface et la molécule semblent être insuffisantes pour provoquer des distorsions significatives

dans la molécule organique elle-même, ce qui pourrait conduire à une plus grande réactivité et rendre la molécule plus encline aux réactions d'autoxydation en phase liquide.

Pour obtenir un champ de force capable de décrire correctement les propriétés et les caractéristiques des systèmes moléculaires d'intérêt, nous avons choisi d'utiliser nos résultats DFT comme données d'entrée pour paramétrer ReaxFF en les ajoutant au *training set*. Ainsi, nous avons ajouté à notre *training set* principalement les configurations d'adsorption optimisées par la DFT des molécules modèles représentant les précurseurs de dépôt sur le dessus des substituts d'aluminium et d'acier inoxydable dans des conditions anhydres et hydroxylées.

Dans cette étude, nous avons mis en œuvre deux champs de force réactifs différents à optimiser, à savoir FFA et FFB pour la description de surfaces  $\alpha$ -Al<sub>2</sub>O<sub>3</sub> et  $\alpha$ -Cr<sub>2</sub>O<sub>3</sub>, respectivement. C'est l'objet du **Chapitre 5**. Ce chapitre représente le cœur du travail de cette thèse.

Pour vérifier le résultat des simulations d'optimisation ReaxFF, nous avons choisi de rapporter les comparaisons entre les résultats DFT et les prédictions ReaxFF obtenues à partir de ces simulations. À partir de ces comparaisons, nous avons constaté que FFA et FFB reproduisaient discrètement les valeurs DFT correspondantes.

Notons de plus que le training set contenant à la fois des réactions en phase homogène (solide ou gaz) et d'interface, nous avons ainsi calibré le champ de force pour l'ensemble des parties du système, solide, gaz et interface solide-gaz. Toutefois, pour mieux confirmer ce résultat, une étape de validation de deux champs de force a été aussi considérée. Dans cette partie, nous avons décidé de diviser cette étape de validation dans deux sous-études différentes, notamment une étude « statique » et une étude « dynamique ». Pour la première étude « statique », trois aspects ont été considérés et comparés entre les deux approches DFT et ReaxFF, respectivement: l'étude des deux phases de bulk pour  $\alpha$ -Al<sub>2</sub>O<sub>3</sub> et  $\alpha$ -Cr<sub>2</sub>O<sub>3</sub>, les énergies de réactions d'autoxydation (décrites dans le **Chapitre 4**) et les énergies d'adsorption de nouvelles molécules modèles du dépôts adsorbés au-dessus des deux surface d'alumine et oxyde de chrome (anhydre et hydroxylée). Dans cette étude « statique » de validation de ReaxFF nous avons obtenu une bonne description des résultats issus de la DFT de la part de deux champs de force FFA et FFB, et nous avons pu les valider en tant que corrects pour ces systèmes. La deuxième étude « dynamique » de validation a été faite par comparaison des phases homogènes liquides. Nous avons obtenu des densités de liquide pur proches des valeurs expérimentales (écart < 9%) pour  $\alpha$ -Al<sub>2</sub>O<sub>3</sub>. La

comparaison par exemple de la fonction de distribution radiale de l'eau est très proche de la fonction expérimentale.

Ces valeurs sont malheureusement très erronées pour  $\alpha\text{-Cr}_2\text{O}_3$ , ce qui nous a conduit à abandonner les calculs sur ce système pour la suite de la thèse.

Après avoir finalement validé le champ de force réactifFFA, nous procédons dans le **Chapitre 6** à l'analyse MD d'un système en phase liquide représenté par un mélange de substitution "combustible-oxygène", où le combustible (c'est-à-dire le solvant) est modélisé par des molécules de toluène, tandis que l'oxygène (c'est-à-dire le soluté) est plutôt modélisé par des molécules d'hydroperoxyde de benzyle.

Le choix de ces molécules définissant notre mélange de substitution "carburant-oxygène" est donné par le fait que d'une part nous voulions simuler un mélange organique qui serait une bonne représentation d'un carburant en phase liquide subissant déjà une dégradation oxydative et d'autre part nous voulions lier ce phénomène au processus d'autoxydation du toluène. Pour cette raison, nous avons choisi le toluène comme solvant et l'hydroperoxyde de benzyle, un intermédiaire bien connu dans le processus d'autoxydation du toluène, comme soluté.

Le mélange "carburant-oxygène" simulé dans cette étude est composé de 95% molaire de toluène et 5% molaire d'hydroperoxyde de benzyle. Le choix de cette composition est dû à notre objectif d'observer le comportement du carburant lorsque le processus d'autoxydation est déjà vu à son état de propagation (c'est-à-dire que les intermédiaires pertinents sont déjà formés, par exemple l'hydroperoxyde de benzyle).

Notre étude MD visait à décrire le comportement d'un substitut de mélange "carburant-oxygène" d'abord comme un système homogène et ensuite dans des conditions hétérogènes lorsqu'il est adsorbé au-dessus de la surface d'alumine. Pour tous les systèmes hétérogènes, nous avons considéré les surfaces d'alumine à l'état anhydre et entièrement hydroxylées, respectivement.

Nous avons analysé le comportement du mélange "carburant-oxygène" en phase liquide dans des conditions ambiantes ( $T = 25^\circ\text{C}$  et  $P = 1\text{ atm}$ ). Nous avons choisi comme modèle pour ce mélange organique un rapport molaire 95:5 de toluène (comme solvant) et d'hydroperoxyde de benzyle (comme soluté oxygéné) puisque les composés aromatiques représentent un composant majeur des carburants liquides de transport.

Dans un premier temps, une « goutte » du mélange a été déposée sur les surfaces  $\alpha$ -Al<sub>2</sub>O<sub>3</sub> et  $\alpha$ -Al<sub>2</sub>O<sub>3</sub>-HY (c'est-à-dire l'alumine complètement hydroxylée), de façon à estimer le « mouillage » de la surface par cette gouttelette. Nous observons un comportement radicalement différent en surface anhydre et hydroxylée: la goutte s'étale sur la surface anhydre, et forme une couche dense auto assemblée de densité 3.7 molécule/nm<sup>2</sup>, stable jusqu'à 450K. Une étude parallèle de dynamique en DFT (Born Oppenheimer Molecular Dynamics) confirme la stabilité de cette monocouche dense de toluène en surface. Il y a très peu de mobilité en surface (adsorption/désorption ou diffusion).

La situation est très différente sur surface  $\alpha$ -Al<sub>2</sub>O<sub>3</sub> hydroxylée: il y a peu de mouillage de la surface, les molécules commençant à diffuser et à désorber/réadsorber sans former de couche dense. La proportion de molécules adsorbées sur surface hydroxylée est seulement de 20% de celle formée sur la surface anhydre.

Cette première étude par champ de force permet de mettre en évidence l'effet majeur de l'état de la surface (hydroxylée ou anhydre) sur les processus d'adsorption, diffusion de surface et auto-organisation de toluène.

L'étape suivante consiste à considérer la phase liquide dans son ensemble, cette fois ci en phase homogène, en interaction avec  $\alpha$ -Al<sub>2</sub>O<sub>3</sub> anhydre et hydroxylée.

Ici aussi, on observe une grande différence de réactivité entre l'alumine anhydre et hydroxylée: il y a agrégation des molécules oxygénées sur la surface anhydre et aussi des phénomènes de dissociation des liaisons O-O des hydroperoxydes de benzyle qui ne se manifestent pas à l'interface avec la surface hydroxylée. Toutefois, dans les deux cas, nous avons observé des phénomènes de « clusterisation » des hydroperoxydes de benzyle dans le milieu organique liquide. Il est probable que cette clusterisation de molécules réactives mène à une augmentation des phénomènes d'autoxydation.

## Acknowledgements

The redaction of this thesis represents for me not only the end of my PhD, but rather what I would describe as the end of a journey. A journey of learning, but more specifically of growth. For most of the cases, the concepts of learning and growth are intertwined between them, a real growth comes from experience, experience comes from learning one or multiple lessons.

In these three years, I was able to achieve a higher level of knowledge and experience mostly thanks to the incredible support of my IFPEN supervisors Mrs. Maira Alves Fortunato and Mr. Theodorus de Bruin and my thesis director Mrs. Dominique Costa. The growth that I'm able to perceive now is certainly thanks to their help and teaching, of which I will be always grateful. On the same length, I cannot thank enough the R104 and R10 department chiefs Mr. Julian Kashdan, Mr. Christian Angelberger and Mr. Richard Tilagone for having accepted me as a good candidate for this thesis together with my IFPEN supervisors three years ago. Of course, I cannot forget how grateful I am to the honorable jury members: Mrs. Anne Hemeryck, Mrs. Corinne Dufaure, Mr. Anton Kokalj and Mr. André Nicolle, for having accepted to evaluate this work and to participate as jury members for my thesis defense.

These three years have not been easy: between emerging work difficulties and the pandemic, there have been many moments where I've sincerely (and sadly) thought that I could not be able to finish my thesis. Luckily, I was able to face and, more importantly, to overcome these negative thoughts thanks to not only my supervisors' aid, but also thanks to the crucial support that all my dears have shared with me, never renouncing to always remind me to trust more myself and my own capabilities. I will be always grateful to them for being so patient and present with my struggles, but even more for having been with me in the moments of joy and satisfaction that I did not hesitate to share with them.

I will never thank enough my parents Agostino and Franca, who have always believed in me without any hesitation even when for me everything seemed to fall apart and of course my boyfriend Vittorio, for simply being present with his support and wise guidance, as it has always been since the start of everything. I cannot forget the enjoyable moments passed together with my dear PhD colleagues, in particular with Ivano, Erwan, Mouad and Daniel, which I will always

treasure as fond memories. A special thanks is for Lucia, a dear friend before being a valuable colleague, who never ceased to encourage and guide me as a real supervisor, which I am sure she will become very soon.

From the bottom of my heart, thank you very much to everyone. Just one last reminder:

***“Per aspera, ad astra”.***

# Table of contents

Abstract .....	2
Résumé.....	4
Acknowledgements .....	12
Chapter 1. State of the art.....	19
1.1. Context of the study.....	19
1.1.1 Fuel stability and deposits .....	22
1.2. Motivation of the study.....	24
1.3. Liquid Phase Autoxidation process .....	26
1.3.1. Chemical kinetics of autoxidation.....	26
1.3.2. Key parameters in liquid phase autoxidation .....	29
1.3.3. Deposits formation from fuel autoxidation .....	34
1.3.4. Deposits typologies and chemical composition .....	34
1.3.5. Deposits interaction with the metallic surface .....	35
1.4. Adsorption of organic molecules on metallic surfaces .....	37
1.4.1. Experimental studies .....	37
1.4.2. Theoretical DFT studies.....	38
1.4.3. ReaxFF studies of the homogeneous phase .....	41
1.4.4. ReaxFF studies of the liquid-surface interactions .....	45
1.5. Conclusion .....	55
References .....	57
Chapter 2. Methodology.....	63
2.1 Introduction.....	63
2.2 Quantum mechanics basics .....	65
2.2.1 Born-Oppenheimer approximation.....	66
2.2.2 Hartree-Fock approximation .....	67
2.2.3 LCAO approximation.....	67
2.2.4 Correlated models .....	68
2.3 Density Functional Theory (DFT) .....	69
2.3.1 Kohn-Sham formalism .....	69
2.3.2 Generalized Gradient Approximation (GGA) .....	71
2.4 DFT calculations for periodic systems.....	72
2.4.1 Bloch's Theorem.....	73
2.4.2 Pseudopotentials.....	73
2.4.3 DFT+ $U$ method.....	74
2.4.4 DFT-D dispersion corrections .....	75

2.4.5	DFT calculation of the total electron energy .....	78
2.4.6	Geometry optimization of molecular structures .....	79
2.4.7	Nudged Elastic Band method .....	81
2.5	Relative energy calculations .....	82
2.6	Thermodynamic calculations .....	83
2.7	Implemented QM based softwares .....	86
2.8	Bader charge calculation .....	87
2.9	From ab-initio to empirical molecular dynamics .....	87
2.10	Force field (FF) methods.....	88
2.11	ReaxFF (Reactive Force Field) methods.....	89
2.11.1	ReaxFF parametrization .....	91
2.11.2	ReaxFF optimization algorithms .....	95
2.11.3	ReaxFF optimization via CMA-ES optimizer .....	96
2.11.4	Required files for ReaxFF training-set .....	98
2.11.5	ReaxFF validation-set .....	99
2.11.6	ReaxFF validation .....	99
2.12	Molecular Dynamics .....	101
2.12.1	Radial distribution function (RDF) .....	103
	References.....	105
	Chapter 3. Studied surfaces .....	109
3.1	Choice of corundum $\alpha$ -Al <sub>2</sub> O <sub>3</sub> and $\alpha$ -Cr <sub>2</sub> O <sub>3</sub> surfaces.....	109
3.2	Introduction to $\alpha$ -(0001) Al <sub>2</sub> O <sub>3</sub> and $\alpha$ -Cr <sub>2</sub> O <sub>3</sub> surfaces .....	110
3.2.1	Bulk structures of $\alpha$ -Al <sub>2</sub> O <sub>3</sub> and $\alpha$ -Cr <sub>2</sub> O <sub>3</sub> .....	110
3.2.2	Surface terminations of $\alpha$ -(0001) Al <sub>2</sub> O <sub>3</sub> and Cr <sub>2</sub> O <sub>3</sub> .....	112
3.2.3	Experimental studies of $\alpha$ -(0001) Al <sub>2</sub> O <sub>3</sub> and Cr <sub>2</sub> O <sub>3</sub> surfaces.....	114
3.2.4	DFT modeling of $\alpha$ -(0001) Cr <sub>2</sub> O <sub>3</sub> and Al <sub>2</sub> O <sub>3</sub> surfaces.....	115
3.2.5	Hydration condition.....	118
	References .....	129
	Chapter 4. DFT study: analysis of gas-phase reactions and gas-solid interface interactions .....	132
4.1	Introduction.....	132
4.2	Model of deposit surrogate .....	133
4.3	Gas phase autoxidation reactions .....	135
4.3.1	Computational details.....	136
4.3.2	Results and discussion.....	138
4.4	Adsorption on $\alpha$ -(0001) Al <sub>2</sub> O <sub>3</sub> and $\alpha$ -(0001) Cr <sub>2</sub> O <sub>3</sub> surfaces .....	139
4.4.1	Computational details.....	139
4.4.2	Results and discussion.....	141
4.5	Surface impact on intramolecular distortion .....	149
4.6	Water/OH substitution on corundum surfaces .....	150

4.6.1	Implemented scheme .....	150
4.6.2	Results and discussion.....	153
4.7	Conclusion .....	155
	References .....	157
	Chapter 5. ReaxFF development and validation .....	159
5.1	Introduction.....	159
5.2	FFA and FFB reparametrizations .....	160
5.2.1	Computational details.....	161
5.2.2	Results and discussion.....	163
5.3	FFA and FFB validation: “Static” study .....	167
5.3.1	Comparison of the lattice parameters .....	169
5.3.1.1	Computational details.....	169
5.3.1.2	Results and discussion.....	169
5.3.2	Comparison of the energies .....	172
5.3.2.1	Computational details.....	172
5.3.2.2	Results and discussion.....	173
5.3.3	Conclusion of the “static” study .....	180
5.4	FFA and FFB validation: “Dynamic” study.....	182
5.4.1	Liquid-phase solvents at ambient conditions.....	183
5.4.1.1	Computational details.....	183
5.4.1.2	Results and discussion.....	184
5.5	Final conclusion .....	187
	References .....	190
	Chapter 6. ReaxFF study of biofuel-alumina interactions.....	193
6.1	Liquid-phase “fuel-oxygen” mixture .....	193
6.1.1	Computational details.....	194
6.1.2	Results and discussion: physico-chemical analysis.....	194
6.1.3	Results and discussion: reactivity analysis .....	196
6.2	Heating of hydroxylated alumina up to 500 K .....	198
6.2.1	Computational details.....	198
6.2.2	Results and Discussion.....	199
6.3	Droplets of liquid “fuel-oxygen” mixture adsorbed on alumina .....	203
6.3.1	Computational details.....	203
6.3.2	Results and Discussion.....	204
6.4	Liquid-phase “fuel-oxygen” mixture adsorbed on alumina .....	214
6.4.1	Computational details.....	215
6.4.2	Results and discussion: toluene-surface interaction .....	217
6.4.3	Results and Discussion: benzyl hydroperoxides-surface interaction.....	221
6.4.4	Results and discussion: chemical reactivity .....	224

6.4.5	Conclusion of ReaxFF study of liquid-phase “fuel-oxygen” mixture- $\text{Al}_2\text{O}_3$ system .....	228
6.5	Conclusions.....	229
	References.....	232
	General conclusions and Perspectives.....	233
	Annexes.....	237
	Chapter 4.....	237
	Bulk oxides .....	237
	Comparison between Gaussian and VASP results for the reaction energies.....	239
	Water/OH substitution on corundum surfaces .....	239
	Thermodynamic data.....	240
	Desorption temperature calculations .....	241
	Computational details .....	241
	Results and discussion .....	243
	Chapter 5.....	245
	CMA-ES algorithm .....	245
	Binding energy calculations: dissociation curves .....	246
	Preliminary ReaxFF study.....	247
5.1	First “static” test: adsorption energies.....	247
5.1.1	Computational details.....	247
5.1.2	Results and discussion of the 1 <sup>st</sup> static test .....	248
5.2	First “dynamic” test: acetic acid desorption from $\alpha\text{-Cr}_2\text{O}_3$ .....	249
5.2.1	Computational details.....	249
5.2.2	Results and discussion of dynamic test for acetic acid desorption from $\alpha\text{-Cr}_2\text{O}_3$ .....	249
5.3	DFT study of the lactone intermediate .....	252
5.3.1	Computational details.....	252
5.3.2	Results and discussion for lactone formation .....	252
5.4	First ReaxFF parametrization test .....	253
5.4.1	Computational details.....	253
5.4.2	Results and discussion.....	255
5.5	First ReaxFF MD test of a surrogate “fuel-oxygen” blend: Production set .....	256
5.5.1	Computational details.....	257
5.5.2	Results and discussion of ReaxFF MD test: “fuel-oxygen” blend .....	258
5.6	Second “static” test: adsorption energies .....	260
5.6.1	Computational details.....	260
5.6.2	Results and discussion of 2 <sup>nd</sup> static test .....	262
5.7	Conclusion of the preliminary ReaxFF study .....	264
5.8	Heterogeneous systems: Desorption temperature analysis.....	265
5.8.1	Computational details.....	265
5.8.2	Results and discussion.....	266

Chapter 6 .....	272
Liquid-phase “fuel-oxygen” mixture .....	272
Droplets of liquid “fuel-oxygen” mixture adsorbed on alumina .....	273
Liquid-phase “fuel-oxygen” mixture adsorbed on alumina .....	274

# Chapter 1. State of the art

## 1.1. Context of the study

The use of biofuels is one of the main levers for the transportation industry to face the ambitious environmental targets for the transportation industry in general [1, 2]. In the last European statistical studies concerning energy, transport and environment, it has been reported that transportation currently accounts for a quarter of the EU's greenhouse gas (GHG) emissions[3]. In the last years, the European Commission has announced many ambitious targets concerning the GHG issue, such as their reduction by 60% compared to 1990 by 2050 and the adoption of the European Green Deal, which sets a strategic framework for a climate-neutral EU economy by 2050. To reach all these challenging objectives, according to these reports it will be necessary to reach a 90% reduction in transport emission by 2050 [3]. The aviation sector is also concerned by the GHG issue, since the International Civil Aviation Organization (ICAO) has agreed a carbon-neutral growth from 2020[4]. The International Air Transport Association (IATA) has also proposed a roadmap for carbon-neutral growth from 2020, and a reduction in net aviation CO<sub>2</sub> emissions of 50% by 2050 from 2005 levels[3].

Several biofuels and sustainable fuels (SF), for road and aviation transport, are already available in the market such as fuel ethers like ethyl-tert-butyl ether (ETBE), ethanol (e.g. E10, E15 and E85 blends), hydrotreated vegetable oils (HVO), alcohol-to-jet (ATJ) synthetic fuel, fatty acid methyl esters (FAMEs), hydroprocessed esters and fatty acids (HEFA) fuels among others.

The introduction of this large variety of fuels in the market leads to a larger range of fuels suppliers, quality, logistics and chemical composition than the industries were used to handle; indeed, the market has now very broad range of fuels properties and possible fuels-systems interaction. Biofuels have a chemical composition and physical properties that, while complying with international fuel quality standards, may have chemical and physical differences from conventional fossil fuels.

This is the case of diesel and biodiesel fuels. We define as “biodiesel” a fuel constituted of mono-alkyl esters of long-chain fatty acids derived from vegetable oils or animal fats [2] and it is

designated “B100” as formulated in the biodiesel standard ASTM D6751 [5], with the European standard EN 14214 [6] referring to fatty acid methyl esters (FAME) as fuel.

Diesel fuel is obtained through the fractional distillation of crude oil. It contains hydrocarbon molecules that range in size from 8 to 21 carbon atoms. Instead, FAME fuels contain long chain of hydrocarbons, but with an additional ester functional group (-COOR).

Depending on the feedstock, the produced biodiesel presents a different fatty acid composition, as reported in **Table 1**.

**Table 1: Fatty acid composition of biodiesel from various feedstock. Table taken from ref.[7].**

Biodiesel	Lauric C12:0	Myristic C14:0	Palmitic C16:0	Palmitoleic C16:1	Steric C18:0	Oleic C18:1	Linoleic C18:2	Linolenic C18:3	Arachidic C20:0	Eicosenic C20:1	Behnic C22:0
Jatropha	-	1.0	3.5	-	0.9	64.1	22.5	8.0	-	-	-
Karanja	-	-	10.056	-	6.6153	55.517	17.513	3.0426	1.5047	1.3632	4.38
Soybean	-	0.9635	24.808	0.6486	3.1883	19.665	50.213	0.1782	0.3353	-	-
Sunflower	-	0.221	15.590	0.164	2.281	38.224	38.554	1.522	0.704	0.418	0.27
Cottonseed	-	0.9755	24.079	0.6681	3.1575	18.681	51.919	0.1781	0.3442	-	-
Coconut	19.47	8.538	26.44	-	3.507	27.09	9.161	0.18	0.263	-	-
Test Technique / Method		EN 14103 (Using Gas Chromatograph)									

The difference in chemical composition can be also observed between diesel and HVO fuels as reported in the work of Bhardwaj et al. [8] (**Figure 1**), where in case of HVO fuels of C14-C16 carbon chain the iso-paraffinic content can be in the range of 20-25% of the total mass fraction, while for diesel fuels with the same hydrocarbon chain content the maximum value is up to 0,5-1%. On the contrary for the n-paraffinic content, the HVO fuels show very low values (less than 1%), while for diesel values can arrive up to 9% of the mass fraction.

A comparison in terms of chemical composition can be also found for the jet-fuels and the sustainable aviation fuels (SAF), as shown in **Figure 2**. We have an almost 100% iso-paraffinic composition for the ATJ fuel and a slightly above 80% similar chemical composition for the HEFA fuels compared to the classic jet-fuel Jet-A1, while the CHCJ fuel show an almost double naphthene content compared to the Jet-A1 reference.

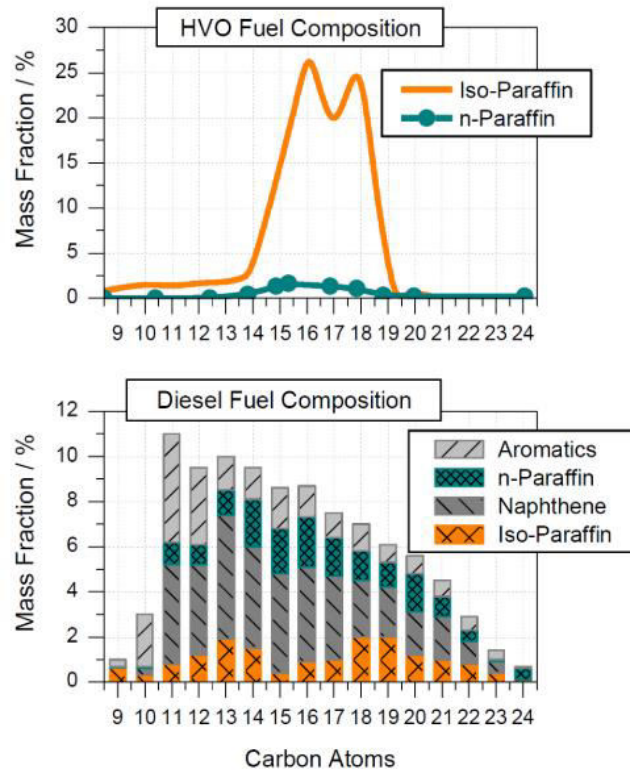


Figure 1: Carbon atom distribution of petroleum diesel and HVO as reported in ref. [8].

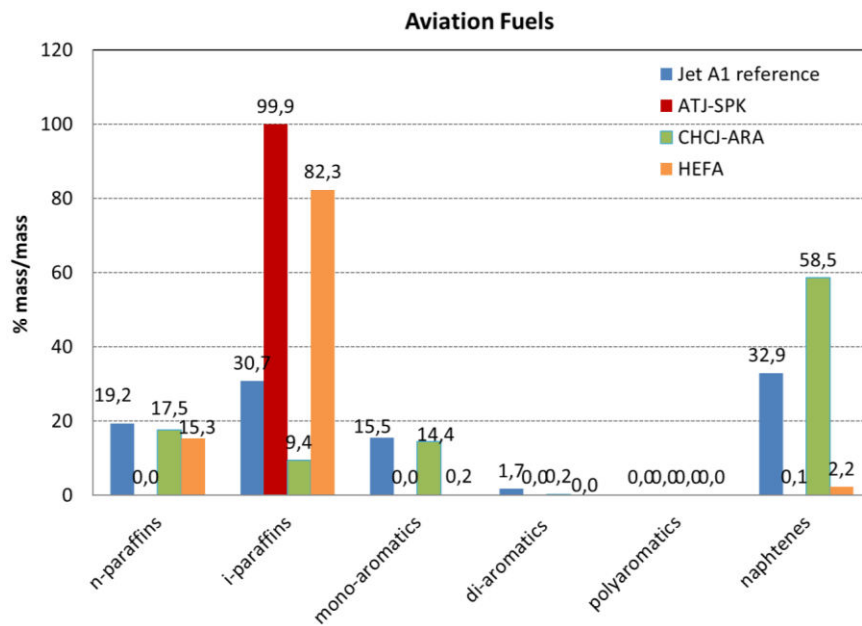


Figure 2: Comparison in terms of chemical composition of different jet-fuels and SAFs [9].

Therefore, the gradual introduction of biofuels has had a significant impact on the intrinsic chemistry of fuels, and therefore on fuel quality and stability.

### **1.1.1 Fuel stability and deposits**

Fuel stability refers to the ability of the fuel to resist degradation [10]. It is possible to distinguish between different mechanisms of fuel degradation: autoxidation, from room temperature to 300°C; cracking or pyrolysis, for temperatures above 400°C; hydrolysis from water condensation in tanks and transport systems; and microbiological contamination from bacteria and fungi in water or dust [11].

This thesis is interested mainly by the autoxidation process since it is one of the main concerns for the transportation industry. Autoxidation stability refers to the tendency of a fuel to degrade from the oxidation of its compounds. The autoxidation process in fuel compounds results in the formation of insolubles and deposits (also commonly named “lacquer” deposits) [12] in fuel system of automobiles and aircrafts.

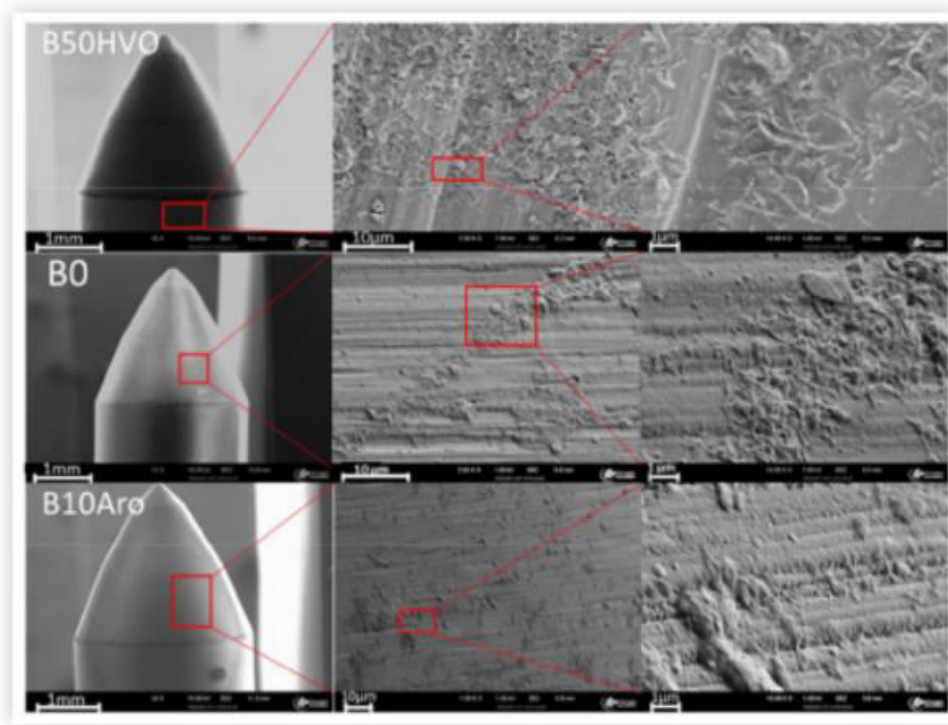
This phenomenon is very problematic since it can provoke engine mechanical failure, such as injector blockage or filter plugging [13, 14].

To solve these old and well-known degradation process [15, 16], antioxidants are added to the fuel in order to prevent this issue. However according to Zabarnick et al. [15] antioxidants seem to effectively present a bivalent behavior depending on their low or high concentration, thus they can either inhibit or promote these autoxidation processes. The use of different anti-oxidation or anti-adherence coatings has been also investigated [16, 17]; nevertheless, it has been shown that material coating can delay the deposits appearance but not completely avoid it.

The formation of deposits was observed for all type fuels, starting from the common fossil diesel (standardized as EN 590 [18]) to the renewable biofuels like biodiesel and HVO and also for fuels where additives were added to prevent fuel oxidation. The main objectives of their work were to identify the inclination of different types of fuels or additives to deposit formation and to find a method that would help them to distinguish the different deposits on the basis of the fuel formulation.

Fortunato et al. [19] showed that fuels can be distinguished in terms of their tendency to form deposits at the same operating conditions; they reported that high aromatic fuels (B10Aro) presents the same propensity to deposit formation as 100% RME (Rapeseed-oil Methyl Esters), with the only difference being the fact that the B10Aro forms only a very thin deposit film, whereas the RME (B100, rapeseed methyl ester) showed a high deposits thickness around 1  $\mu\text{m}$  (**Figure 3**). Plus, in their test conditions the highly paraffinic 100% HVO (hydrotreated vegetable oils) fuel presented higher propensity to block the injector than the RME fuel; however, when mixed with 50% diesel (becoming so B50HVO fuel), it was showed that the HVO deposits formation was drastically reduced and that its deposits present similarities with B0 deposits.

According to several studies in the literature, the fuel chemical composition represents a keen factor for the deposit formation. Another parameter that is not negligible in this subject is the role of the surfaces in fuel systems. The study conducted by Bacha [16] discussed the role of different substrates in the formation and adhesion of fuel deposits. From this study, it seems that the nature of the substrate could influence the deposit thickness and chemical composition.



**Figure 3: Injector needle deposits morphology at 1mm as well as the enlargement of the red zones at 10  $\mu\text{m}$  and 1  $\mu\text{m}$  [19].**

It is noteworthy that fuel deposits above different coatings, such as the high temperature resistant thermoplasticPolyEtherEtherKetone (PEEK), aluminium, aluminium coated in gold, stainless steel and stainless steel treated with silcoklean1000 (i.e. high temperature precision anti-coking coating process) were compared and it was found out that the quantity of deposits formed on the PEEK substrate was lower than the one observed on the metallic surfaces (aluminium, stainless steel and gold-coated aluminium), while the deposits revealed above the silcoklean coating was observed to be thinner and distributed on the whole surface. This feature demonstrate that the surface in contact with the fuel can play a role in the deposits formation process.

In the same study, it was hypothesized that the deposit precursors are composed by polar oxidation products that are closer to an amphiphilic structures resembling an inverted micelles; these new-formed micellar structures start forming nanoparticles in the liquid phase through their agglomeration, leading to the constitution of deposit agglomerates above the surfaces. However this hypothesis was not further studied.

Thus, there is a gap in the understanding of the interaction fuel-material leading to the deposits formation and the chemical mechanisms involved as well as the role of the surfaces in this process.

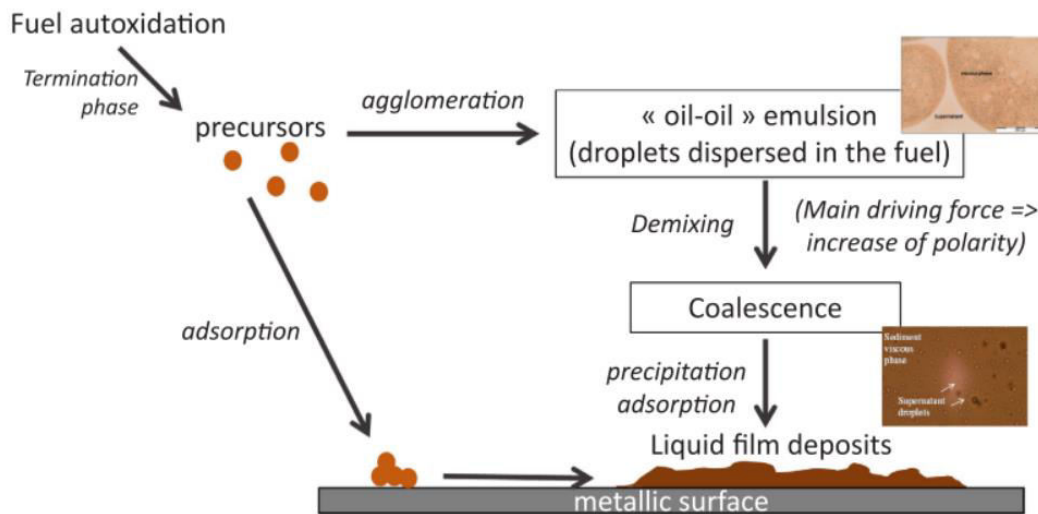
## **1.2. Motivation of the study**

Given the lack of understanding of the interface interactions occurring between the fuel liquid phase and the metallic solid phase, the objective of this thesis is to better comprehend the phenomenology linked to this fuel degradation process — focused in the autoxidation mechanism [20]— where the so-formed liquid deposits start aggregating in liquid phase forming small polymers that are considered to be the precursors of the “lacquer” deposits on the metallic surfaces of the real systems. For this study in fact, what is paramount to find out is how the interactions between the deposits precursors and the metallic walls actually play a role in this precipitation/adsorption process.

In their recent works Fortunato et al. [21, 22] have investigated on the fuel oxidation process where the characterization of oxidation products was conducted to identify the main factors that

could prevent deposit formation in engines. They found that during the oxidation process of biofuel surrogate (methyl oleate/n-dodecane) small aggregates are formed and, as consequence, fuel color changes and a phase separation occurs. Plus, they pointed out that the deposit observed in injector systems would be formed when polarity of the autoxidation products in suspension is high enough to induce precipitation of polymeric deposit. This polarity factor was also reported in the already mentioned study [16], where it was pointed out that the chemical composition of aged biofuels is mainly composed of oxygenated products (i.e. polarity) and that the molecular weights of these products were observed to be higher than the fuel initial products.

From their FTIR results, Fortunato et al. [21] showed that deposit formation seems to be mainly related to the polarity (i.e. oxygenated products) content differences of both sediment and supernatant phases leading a phase separation process. This characteristic may imply the formation of deposits already in the fuel liquid phase, in this way alluding that it might not be initiated by the surface being in contact with the fuel. In connection with their results, they proposed a mechanism for deposit formation where the two main pathways were highlighted according to which deposit precursors could later become liquid deposits precipitated above the engine metallic surface.



**Figure 4: Scheme of the deposits formation mechanism proposed in ref. [21].**

As showed above in **Figure 4**, deposit formation could follow two possible pathways, one implying that the liquid film deposits comes from a previous adsorption process of the precursors

and the other instead implying an agglomeration step of deposit precursors directed towards a consequent precipitation and formation of liquid deposits above the metallic substrate. Both proposed mechanism pathways may be valid and further investigation is required to understanding the mechanisms involved.

To better understand how the phenomenology of the oxidative fuel degradation is linked to the investigation of the biofuel-surface interactions, in the next paragraphs we will first introduce the “Liquid Phase Autoxidation” (LPA) process and its key factors, successively we will describe the state of the art of the experimental and theoretical studies aimed to the investigation of interface interactions occurring between the organic compounds produced from biofuel autoxidation and the metallic surfaces coating the fuel injection systems of diesel engines.

### **1.3. Liquid Phase Autoxidation process**

Phenomena related to fuel autoxidation have been studied in several industrial contexts in the last decades, starting from studies on crude oil for exploring refinery fouling [20] to fuel aging [23] arising in engines injection systems. The first part of this state of the art review will be dedicated to the chemical kinetics and chain mechanisms describing the Liquid Phase Autoxidation (LPA); then major researches conducted on this topic will be mentioned to identify the key parameters and species involved in this process.

#### **1.3.1. Chemical kinetics of autoxidation**

As it has consistently been assessed in many several studies concerning fuel autoxidation, oxygen presence is a prerequisite for low temperature deposit formation in the liquid phase [20].

In these previous studies it has been assumed that autoxidation processes proceed through a chain mechanism [10, 20]. In literature, many global chemical mechanisms [24, 25] for fuel autoxidation have been proposed and in **Figure 5** below we report the one proposed by Watkinson and Wilson [20].

The choice of specifically reporting this mechanism is because of its clarity for showing the formation of hydroperoxides as intermediates and the final production obtained from hydroperoxides decomposition (e.g. alcohols, carbonyl compounds, epoxides, etc.). The autoxidation mechanism is commonly divided in three main phases: initiation, propagation and termination as indicated in the **Figure 5** and which are described below.

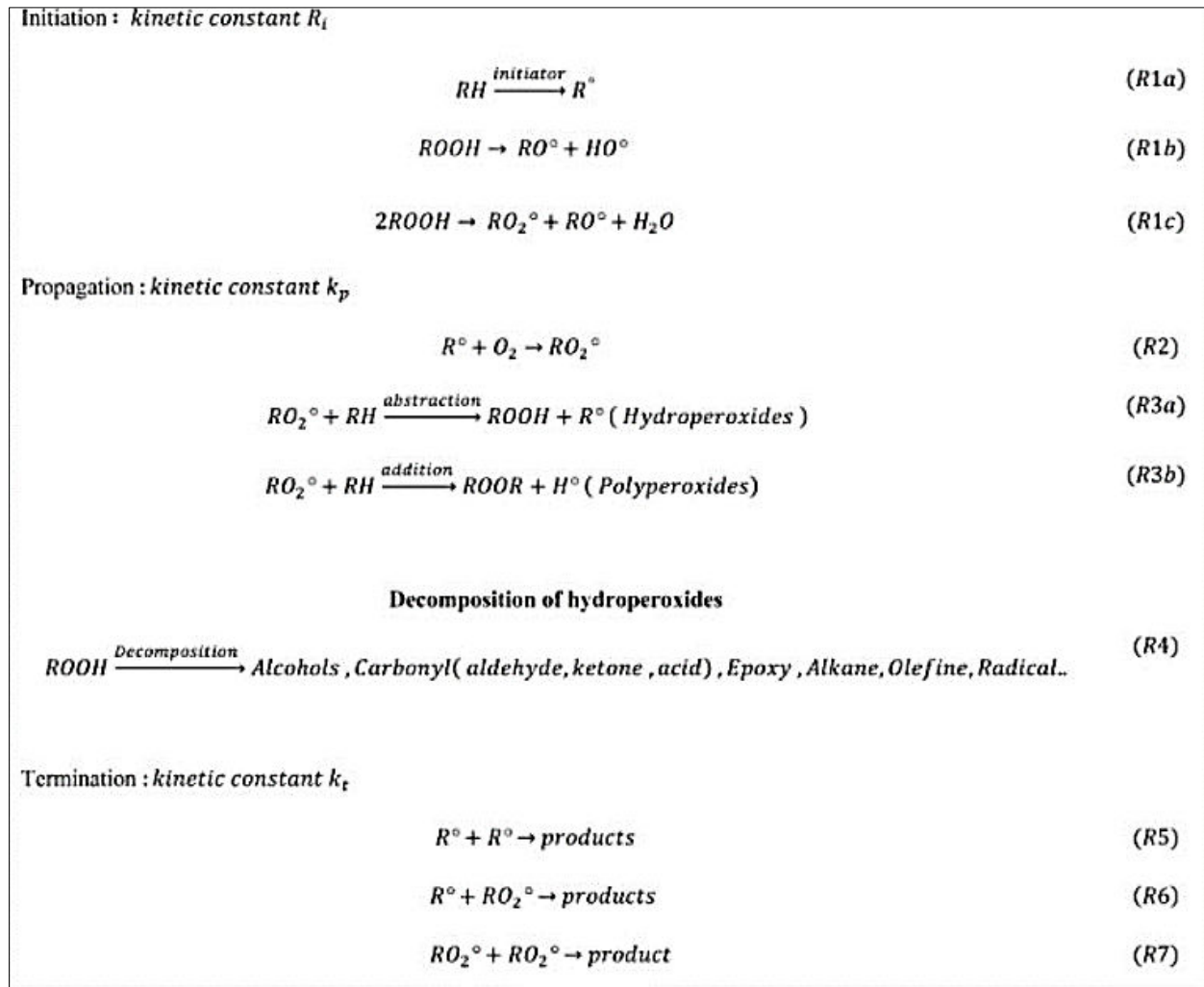
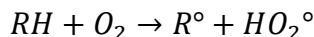


Figure 5: Global mechanism for liquid phase autoxidation proposed by ref. [20].

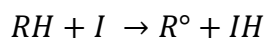
In LTO (i.e. Low Temperature Oxidation) regime, the thermal energy registered in the fuel liquid phase appear to be modest and the initiation step has several different pathways (**Equation 1-Equation 2-Equation 3**).

One route considers the initiation step coming from traces of hydroperoxides decomposition via H abstraction with O<sub>2</sub>[15, 20], but it can also be interpreted as a photochemical initiation (which however cannot be considered in case of tanks being opaque to UV-visible light).

Another route considers instead the first step as being any compound able to carry out an H-abstraction from the alkyl molecule and tries to describe it as an activated initiator that becomes the first alkyl radical.



**Equation 1**

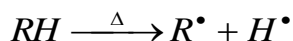


**Equation 2**

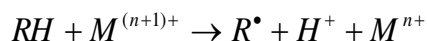


**Equation 3**

In addition, initiation step may be catalytically enhanced by dissolved metals, surface effects, acid catalyzed, ionic reactions [12, 20, 24] (**Equation 4-Equation 5**).

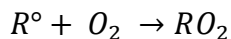


**Equation 4**

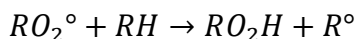


**Equation 5**

The first propagation step (**Equation 6**) where alkyl radicals react with molecular oxygen represents the main propagation path due to its low energy barrier (close to 0 kJ/mol) [26]. Then this chain mechanism proceeds through the second propagation step (**Equation 7**) where the peroxy-radical species reacts with the initial hydrocarbon, resulting into new hydroperoxide and alkyl radical.



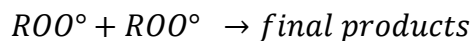
**Equation 6**



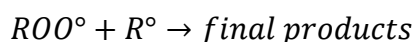
**Equation 7**

This chain mechanism is now well established in literature [24–26] from the 1930’s with Semenov’s theory [27].

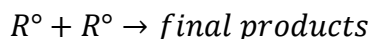
The conclusive termination step (**Equation 8-Equation 9-Equation 10**) can be simplified as a sum of all the intermediates reaction paths and can go towards dimerization [28]; particularly in case of biofuel blends, oxygenated products such as epoxides, aldehydes, carboxylic acids and alcohols have been found [12, 22].



**Equation 8**



**Equation 9**



**Equation 10**

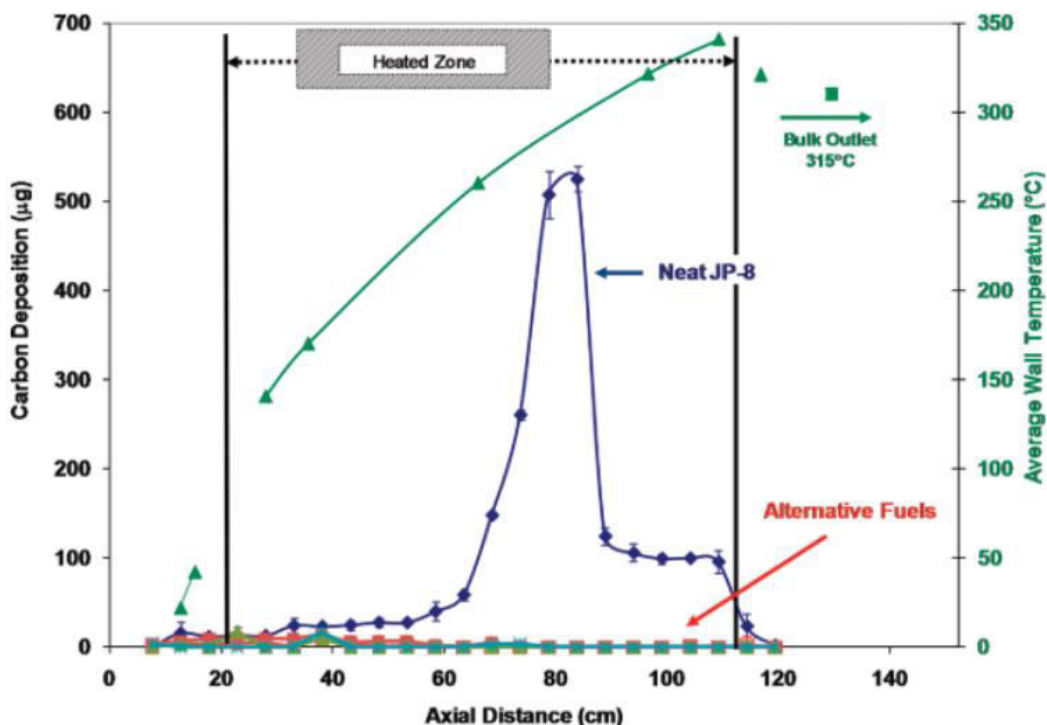
### 1.3.2. Key parameters in liquid phase autoxidation

The first key parameter truly impacting in liquid phase autoxidation issues is the reactant itself or, to be more precise, the fuel chemical composition; in fact, the system reactivity is highly correlated with the fuel chemical formulation. Its impact on the reactivity is well-defined by the C-H bond breaking energy, which can be certainly different depending on the given chemical species involved in the process [29].

This behavior is well-illustrated in **Figure 6** taken from the work of Corporan et al. [30], where they studied the chemical and thermal stability of six alternative jet-fuels, among which three of the fuels were produced via Fischer-Tropsch (FT) synthesis (e.g. Shell FT, Sasol FT and Rentech FT) while the other three were “hydroprocessed renewable jet” (HRJ) fuels produced via the hydroprocessing of animal fat/vegetable oils (e.g. R-8 HRJ, tallow RHJ, cameline HRJ). In their work, Corporan et al. [30] reported a comparison of the surface deposition profiles between these

six alternative fuels and the standard JP-8 (“Jet Propellant 8”) fuel. **Figure 6** shows that all alternative fuels depicted excellent oxidative stability characteristics during the tests resulting in minimal surface deposition and, according to them, the improved stability features of the alternative fuels relative to the specification JP-8 were most likely due to the absence of heteroatomic-containing species in these fuels, which have previously been implicated as promoters of undesirable deposit formation in the oxidative regime.

This composition effect is also showed in **Figure 7** taken from ref. [31], where the oxidation stability of four different blends of methyl oleate (MO) and n-dodecane ( $n\text{-C}_{12}\text{H}_{16}$ ) was considered. The parameter representing the oxidation stability of the MO/ $n\text{-C}_{12}\text{H}_{16}$  blends is the induction period (IP), which defines the time corresponding to the onset of the oxidation regime. We can imagine that the more oxygenated the system is in terms of chemical composition, the lower the IP value can be at the same thermal conditions.



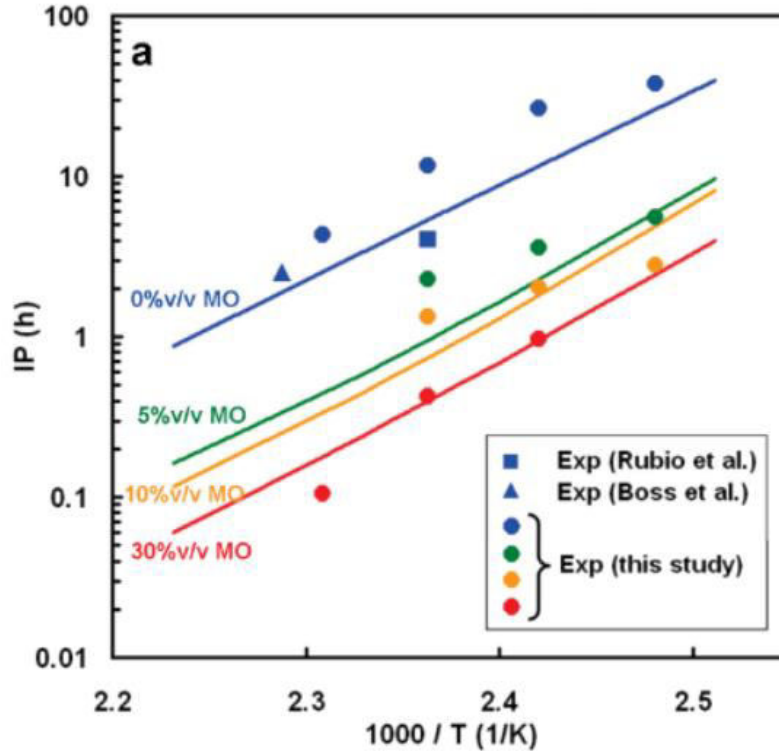
**Figure 6:** Comparison of carbon deposition and wall temperature profiles for oxidative stability of the alternative fuels and a specification of JP-8 fuel of ref. [30].

This is confirmed in **Figure 7**, where we can see the lowest IP is indicated for the 30% v/v MO/ $n\text{-C}_{12}\text{H}_{16}$  blend when considering a fixed temperature. On the other hand we can also notice

that, when considering a specific MO/n-C<sub>12</sub>H<sub>16</sub> blend (i.e. fixed molecular oxygen content) the increase in temperature implies a reduction in IP, which is to be expected.

The second key parameter which affects autoxidation and especially the deposition process is the oxygen availability in the liquid phase [12, 32] From the deposition rate presented in **Figure 8**, it is possible to identify two different reaction regimes: a pyrolytic regime (common to both oxygenated and de-oxygenated fuels) and an oxidative regime (which is driven by the oxygen concentration in the system).

The **Figure 8** illustrates a) that there are two possible chain mechanisms leading to deposits (one is the oxidative route, the other the pyrolytic route) and b) that some diffusion limitation may be encountered under specific operating conditions. As the temperature range considered for this thesis lies under 750 K, it confirms that the oxygen concentration present in the system is indeed not all negligible, rather it represents an important parameter to be considered.



**Figure 7:** Induction period measurements from Ben Amara et al. [31] for different n-dodecane/methyl oleate mixture as function of temperature.

Heteroatomic species (like nitrogen, sulfur or oxygen containing molecules) present in the fuel can also promote deposits formation [24, 33]. Without any distinction of chemical groups in the fuel, polar species have shown to promote deposit formation [34]. In particular, the most impacting heteroatomic species have been identified with the hydroperoxides, which were found to be key species in LPA [10, 20].

The last promoting effect underlined in literature is identified with the homogeneous catalytic effect of dissolved metals [35] and the heterogeneous catalytic effect of the walls [20]. To reduce heterogeneous catalytic effects, passivation processes have been investigated in literature and demonstrated a reactivity decrease [36]. Being dissolved metals already present in fuels liquid phases [24], initiation steps involving dissolved metals should be considered as preferential when studying real fuel autoxidation.

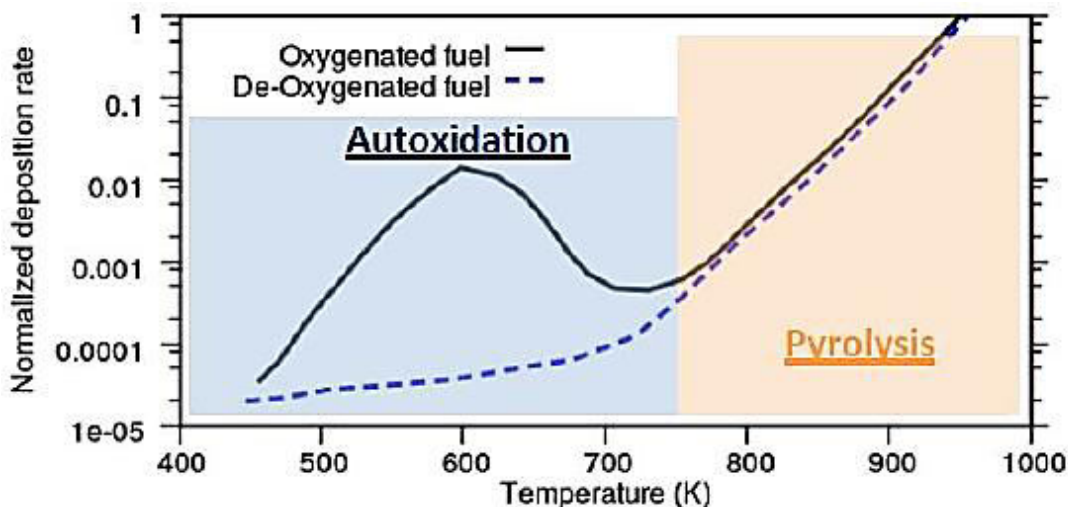
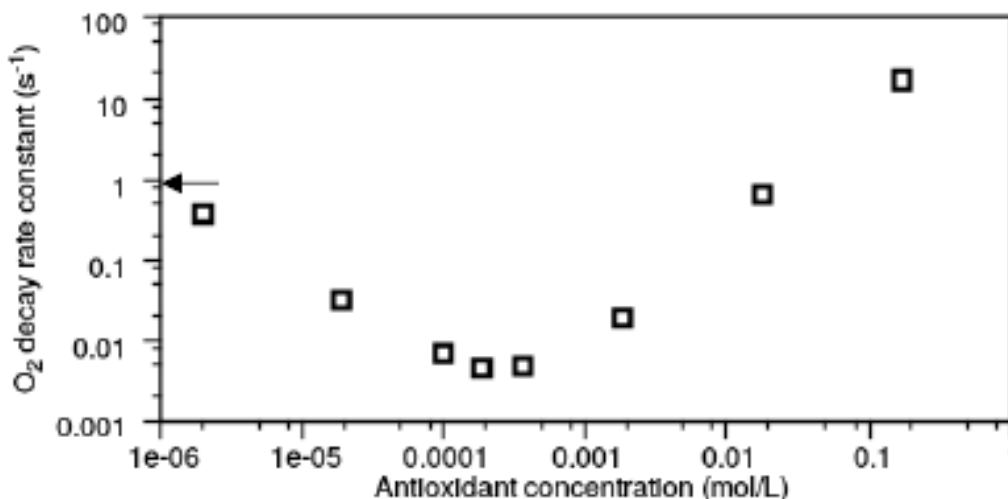


Figure 8: Deposition rate as function of temperature for oxygenated and de-oxygenated fuel from ref. [37].

In conclusion, reactivity can be highly enhanced by trace level species. To reduce all those impacts, stabilizing species called “antioxidants” (AH) are added into (bio)fuels to limit their low temperature reactivity [38, 39] and their deposit formation tendency. Several families of antioxidants are commonly added to fuels, generally identified with peroxy inhibitors species, hydrogen donors and complexing agents. However Zabarnick [15] pointed out a somewhat ambivalent behavior of antioxidants in oxidative fuel stability, as it is also shown in **Figure 9**.

In his work Zabarnick [15] was able to find out that the introduction of antioxidants at low concentrations ( $< 0.0001$  mol/L) resulted in the increase of fuel stability and a maximum stability was reached at 60 ppm; however, at higher concentrations ( $> 0.0001$  mol/L) the introduction of antioxidant contributes to accelerate the oxidation process as shown in **Figure 9**.



**Figure 9:** Autoxidation effect on O<sub>2</sub> decay rate constant. Data were obtained with n-dodecane at 200°C from ref. [15]. The arrow illustrates the O<sub>2</sub> decay without antioxidant.

### 1.3.3. Deposits formation from fuel autoxidation

In order to study how (bio)fuels undergo the deposition process caused by their autoxidation, it is paramount to identify the nature of the deposits precursors. This analysis will start from the consideration of the major factors contributing to deposits formation, namely the deposits chemical composition and how they interact with the surfaces with whom they enter in contact inside the engines injection circuits.

Also, in this analysis the given fuel nature (oxygenated or de-oxygenated) has to be necessarily considered, since for this thesis the interest is focused on the deployment of both fossil and renewable fuels being injected inside vehicles and aircrafts engines.

### **1.3.4. Deposits typologies and chemical composition**

As it has already been mentioned before, these formed liquid deposits can provoke some failures on many spots of the injection circuit, so investigating the interactions between the injected fuel blend and the surfaces of the injection systems components represents indeed a fundamental task. What happens in fact is that some liquid deposits are likely to be found especially at the injector level (needle) and pump inside the injection circuit.

However, it should be mentioned beforehand that actually there are two kinds of deposits that can be found inside injection systems: the soap-type and wax-type deposits respectively. In this thesis, we chose to focus on lacquer type deposits since they are the main type of deposits formed from hydrocarbons autoxidation mechanism. The lacquer type deposits are polymeric (usually brown dark-colored) and they present tendency to adhere on surfaces. They are generally insoluble in the usual used solvents and they can be divided in two different categories: a) the deposits with an amide function coming from the presence of the PIBSI additive and b) the deposits coming from the biofuels oxidation and from the formation of the derived polymers [22, 40].

According to Singer et al. [41] the heavy polar products coming from (bio)fuels autoxidation have the tendency to form deposits that resemble polymers of heavy molecular weight; these polymers also can generate intertwined systems and, when a so-called critic temperature is reached, they transform into an insoluble reticular network.

About the petroleum-derived fuels (like diesel and jet-fuels), the reference [42, 43] shows that the deposits produced from diesel and jet-fuel oxidation are mainly composed of polar polycyclic aromatic species, although polar aliphatic species were also detected as oxidation products.

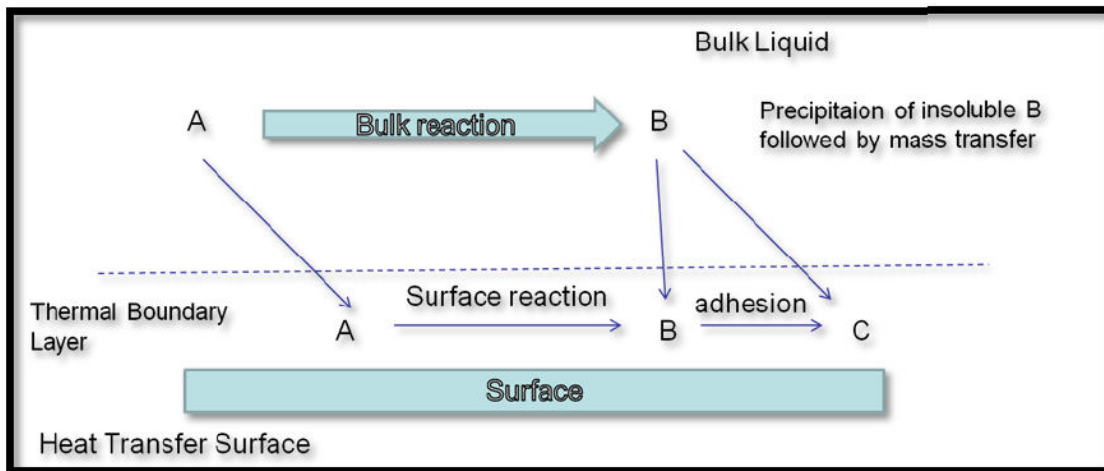
### **1.3.5. Deposits interaction with the metallic surface**

The second aspect to analyze about the nature of deposits precursors is identified with the surface effect of the used material in regards of the formation of deposits.

This aspect can be considered under two different perspectives: the first related to the material catalytic effect on the fuel oxidation and the second instead related to the material effect on the morphology and adhesion tendency of the deposits on the given surfaces.

As shown in **Figure 10**, deposits formation can happen on the basis of three different mechanisms:

1. Precipitation of insoluble particles produced from the fuel oxidation over hot surface, followed by the generation of agglomerates.
2. Formation of insoluble particles directly at the surface level via a catalytic effect of the same surface.
3. A combination of the two aforementioned mechanisms.



**Figure 10: Mechanisms of deposits formation as illustrated in Ref. [2].**

The comprehension of these deposits adhesion mechanisms occurring on the surface may allow to better identify the typologies of bonds and energies involved in their adsorption processes, which can be distinguished into the following mechanisms: physisorption, chemisorption and formation of organometallic complexes.

These information could provide useful insights to solve deposits issues, like for example the possibility to re-solubilize completely or partially the deposits in the fuel or in a suitable solvent; in fact according to the reference [44], the injected fuel presented a solvent power over the formed autoxidation deposits.

A good solution could be represented for example by the implementation of special coatings on the surfaces in order to reduce the number of active sites on their substrates, like the DLC coating (Diamond Like Carbon), which has been found to minimize the adhesion of deposits at the injector level [44].

Interesting results about the depiction of the interactions between the precursors deposits and metallic surfaces have been achieved in the two references [45, 46]; in these works it had been found that, when FAME fuel undergoes oxidation on aluminum, copper and stainless steel surfaces, covalent bonds [COO-Metal] between the deposits and the metallic substrates are formed.

This result proves to be very meaningful for this thesis, since it gives a very useful picture of the bonds that can be established between ester molecules coming from biofuels blends and stainless steel surfaces, which is the reference model for the walls of the injection circuit.

## **1.4. Adsorption of organic molecules on metallic surfaces**

### **1.4.1. Experimental studies**

Biodiesel oxidation products are mainly composed of molecules containing methyl esters, carboxylic acids, ketones, aldehydes, alcohols or epoxides as the main chemical functions [12, 22, 47]. Some of these oxygenated species seem to be the precursors of deposits observed in aluminum and stainless steel surfaces [19, 48].

Interaction of oxygenated species on aluminium surfaces have been widely studied in the literature. Alexander et al. identified via Fourier-transform infrared spectroscopy (FTIR) the formation of bonds between carboxylic acids and hydroxylated AlOOH surfaces [49].

Soo Lim et al. studied the adsorption and desorption of stearic acid self-assembled monolayers on aluminium oxide via XPS and IR spectroscopy analyses [50]. They found that stearic acid makes both monodentate and bidentate bonds with the alumina surface.

Hafidi et al. studied the interactions between vegetable oils (containing methyl esters) and alumina membranes by FTIR [51]. They found that all selected lipids in their study adsorbed on alumina. The adsorption proceeds by the surface hydroxyl groups and the polar groups of the

lipids, in particular tri- and di-acylglycerols species adsorb physically via H bonds through the carbonyl ester group ( $\text{C=O}$ ). Oleic acid is chemically adsorbed by ionic interaction between the carboxylate anion ( $\text{RCOO}^-$ ) and the metal oxide.

Esters are known to adsorb to stainless steel surfaces and are used as lubricants. Yan et al. [52] have studied the interactions between metals and oil-in-water (o/w) emulsions, where the metallic surfaces were modeled by the stainless steel and a CoCrMo alloy, while the selected lubricant was a commercial rapeseed oil (RME). From the XPS analyses they were able to observe that, under boundary lubrication conditions, the active additive components of the lubricant adsorb on the metal surface after the oil droplet of the emulsion is broken, forming a protective layer on the surfaces.

#### 1.4.2. Theoretical DFT studies

Understanding the role of molecular interactions between biodiesel molecules with the metallic surfaces is of ubiquitous importance to predict and enhance fuel system performances. The metal/alloy surfaces of our concern are stainless steel and aluminum as they are largely used in the injection systems.

The DFT method can be a valid tool for the detailed investigation of the interface interactions occurring on metal/alloy surfaces. At the same time, we have to select suitable surface models that can better represent the specific properties of these types of materials. In our case, we wanted to be as close as possible to the real conditions at which deposit formation may occur inside the injection systems, thus we chose to model and study via DFT the aluminium and stainless steel with the (0001)  $\alpha\text{Al}_2\text{O}_3$  and  $\alpha\text{Cr}_2\text{O}_3$  surfaces respectively, with a particular focus on their hydration states. We sustained this choice because the temperature of the injector in fuel systems can achieve 150 °C with a water residual content of 1000 ppm under engine working conditions and, in this conditions, aluminum is covered with an oxide and a hydrated film [53]. The same is observed for the stainless steel, as shown by experimental [54–57] and theoretical studies [58–62]. The oxides covering the aluminum surfaces are generally simulated by model oxides like  $\alpha$ -[63–65] or  $\gamma$ -[66] alumina ( $\text{Al}_2\text{O}_3$ ).

Seminal works on water adsorption on  $\alpha$ -Al<sub>2</sub>O<sub>3</sub> and  $\gamma$ -Al<sub>2</sub>O<sub>3</sub> provided useful models, which will be used here. The (100) and (110) gamma alumina models, developed by Digne et al. [67] have become one of the reference models as shown by the fact that several works have reused them [68–71]. Digne et al. [67], followed by Arrouvel et al. [72–74] have tried to understand water adsorption and predict the water coverage as a function of the thermodynamical conditions (temperature and partial water pressure). They highlighted that the (100) facet dehydrated at lower temperatures as compared to the (110) for a given partial water pressure.

The adsorption of molecules on alumina surfaces has been widely studied with DFT [59, 67–69, 72–90].

Many theoretical works have been published regarding adsorption on Al<sub>2</sub>O<sub>3</sub> surfaces. Wang et al. [87] have investigated the adsorption of methyl nitrate on dry (0001)  $\alpha$ -Al<sub>2</sub>O<sub>3</sub> and (110)  $\gamma$ -Al<sub>2</sub>O<sub>3</sub>. They found that the adsorption on (110) surface is more stable than on  $\alpha$ -Al<sub>2</sub>O<sub>3</sub>.

A DFT study by Kistamurthy et al. [89] showed the dissociative adsorption of acetic acid on the (100) and (110)  $\gamma$ -Al<sub>2</sub>O<sub>3</sub> anhydrous surfaces, where both oxygen atoms of the acetate coordinate to the surface.

Heiden et al. [91] calculated with PBE-D3 a value of -157.3 kJ/mol for the dissociative and -124.5 kJ/mol for molecular water adsorption on  $\alpha$ -Al<sub>2</sub>O<sub>3</sub> (0001) (1/4 ML coverage on a (2x2) surface). Borck et al. [84] studied the methanol adsorption at the (0001) surface of  $\alpha$ -Al<sub>2</sub>O<sub>3</sub>. They found that the adsorption mechanism is a donor–acceptor interaction, where the methanol’s oxygen lone pair orbital donates electron density into Al conduction band.

Arrouvel et al. [59] have studied the glycine adsorption on anhydrous and hydroxylated (0001) surfaces of  $\alpha$ -Al<sub>2</sub>O<sub>3</sub> showing that on the dry surface, the glycinate anion forms an ionic-covalent Al–OC bond and it is stabilized in a unidentate perpendicular configuration with an adsorption energy of -214 kJ/mol. In the case of the hydroxylated surface, it is observed that the substitution of a surface OH group by glycine is thermodynamically favored ( $\Delta E_{\text{ads}} = -213$  kJ/mol). The adsorption of CO<sub>2</sub> on  $\gamma$ -alumina using DFT has been studied by Pan et al. [85] they also found that the adsorption energy decreased when the water coverage increased in agreement the previously mentioned studies.

Recently, Blanck et al [92] studied the solvation and adsorption properties of various species of lubricant additives to investigate the most suitable among them that favors the wetting of  $\gamma$ -

alumina surface. From the results, they concluded that the adsorption of protic molecules (e.g. water, amines, alcohols and carboxylic acids) on the (100)  $\gamma$ -alumina surface leads in most cases to a dissociative adsorption for acidic molecules, where their adsorption energies decrease with increasing pKa values of the functional groups.

Xu et al. [90] studied the adsorption of oleate methyl ester on diaspore and kaolinite crystals with the generic UFF force field combined with an experimental study. They found that the oleate chemisorbs on the surface of diaspore and kaolinite rendering the mineral surface hydrophobic.

Concerning stainless steel surfaces, less literature data is available and studied by DFT/ab-initio principles approaches. The adsorption of CO<sub>2</sub> on different Cr<sub>2</sub>O<sub>3</sub> surfaces terminations (0001), (01 $\bar{1}$ 2) and (10 $\bar{1}$ 2) was studied by Kumar et al. [93]. They found that CO<sub>2</sub> can either physisorb or chemisorb on Cr<sub>2</sub>O<sub>3</sub> surfaces, in the first case conserving its linear structure while in the second case a “bent-like” structure was observed. Also, CO<sub>2</sub> chemisorption on the Cr<sub>2</sub>O<sub>3</sub> (1012) surfaces exhibits an  $E_{\text{ads}} = -103.2$  kJ/mol that is very close to the experimental values (-104.2 kJ/mol).

Costa et al. [60] studied water adsorption on the (0001)-Cr<sub>2</sub>O<sub>3</sub>-Cr terminated facet, and found that molecular and dissociative adsorption were isoenergetics with values of -82.2 (dissociative) and -82.6 (molecular) kJ/mol. For three water molecules adsorbed per Cr, the average adsorption energy was calculated as -93.2 kJ/mol.

Souvi et al. [58] calculated an adsorption energy of -80.3 kJ/mol for dissociative water adsorption (more stable than the molecular one). At saturation (3 water molecules per Cr), the average adsorption energy was calculated as -87.9 kJ/mol. Matthew et al. studied water adsorption on Cr<sub>2</sub>O<sub>3</sub> with DFT + U and found that the adsorption energy of the first water is 96.5 kJ/mol, for 80.1 kJ/mol average adsorption energy at saturation [94].

Gouron et al. [61] studied by DFT the adsorption of monoethanolamine on the hydroxylated Cr<sub>2</sub>O<sub>3</sub> (0001) orientation where it follows that MEA adsorbs in a bidentate fashion, preferentially on top of the water molecules forming the hydroxylated surface, while the water substitution is thermodynamically not favorable at room temperature.

Ethanol adsorption on  $\text{Cr}_2\text{O}_3(0001)$  was studied by Zhang et al. and found to be exothermic by 90.7 kJ/mol [95]. However, the authors performed DFT calculations without explicit dispersion corrections.

Huš et al. [96] studied the adsorption of propane on dry (0001)  $\text{Cr}_2\text{O}_3$  with DFT+U including van der Waals forces described by Grimme D3 method [97]. According to their results, the adsorption energy for propane on dry (0001)  $\text{Cr}_2\text{O}_3$  is -34.7 kJ/mol. Benzene was adsorbed on corundum-type surfaces [98]. The adsorption energy was calculated as -50.2 kJ/mol and -53.1 kJ/mol for dry  $\text{Cr}_2\text{O}_3$  and  $\text{Al}_2\text{O}_3$ , respectively.

According to Garrain's work on the glycine adsorption on hydroxylated  $\alpha\text{-Cr}_2\text{O}_3$ , the major contribution to the adsorbate/surface interaction comes from the H-bonds between the COOH function and the surface OH groups. Two scenarios have been envisaged: the adsorption of the amino-acid on the surface OH groups labeled as "outer sphere adsorption" and the substitution of a surface OH group with the glycine molecule in its anionic form labeled as "inner sphere adsorption". They found that outer-sphere adsorption of amino-acids like glycine is poorly surface site-specific, where they molecularly adsorb above the surface hydroxyls, while the inner-sphere adsorption of these biomolecules is site specific.

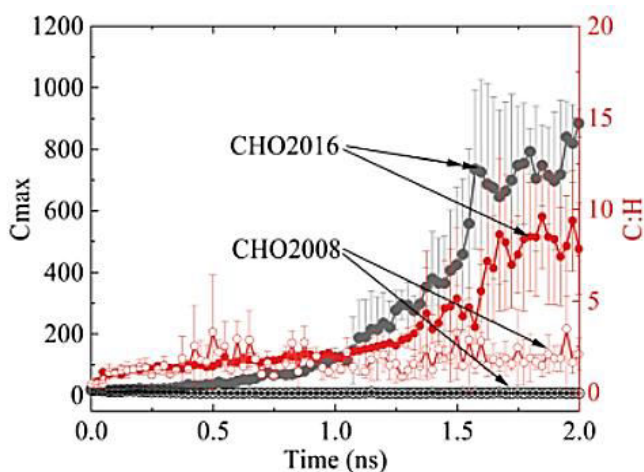
### 1.4.3. ReaxFF studies of the homogeneous phase

Most of the ReaxFF studies about fuels are related to gas phase reactions, combustion and soot formation. There is a lack of studies in fuel liquid phase at the best of our knowledge. Nevertheless, among the ReaxFF studies related to a fluid homogeneous phase, an interesting work is the one conducted by Chen et al. [99] which was centered on the investigation of the soot formation process of diesel combustion using ReaxFF by examining the effects of oxygenated additives on diesel soot reduction. The ReaxFF employed in their study allowed them to model the kinetics of large hydrocarbons fuels and to describe the chemistry of carbon condensed phase. In their study, they employed a diesel surrogate proposed by Qian et al. [100] that could accurately reproduce the gaseous emission of the target diesel fuel under actual engine combustion conditions. Their reactive system consisted in 149 pure diesel surrogate molecules with 150 oxygen molecules to model fuel-rich combustion. Also, to study the effect of fuel

additives, oxygenated fuel molecules were doped into their simulation boxes containing their diesel model.

In their work, Chen et al. [99] chose to implement two different sets of widely used reactive force field parameters for combustion reactions, CHO2016 and CHO2008 force field parameters respectively. Between these two sets of parameters, the first retained the capability of the second for predicting complex hydrocarbon pyrolysis and oxidation reactions but was capable to reproduce more accurate chemical pathways important for soot formation. Despite their work was centered exclusively on the hydrocarbons homogeneous phase, in gas phase, is worth mentioning since it is linked to the description of decomposition phenomena occurring to hydrocarbons species with oxygenated additives, which could be interesting to this thesis.

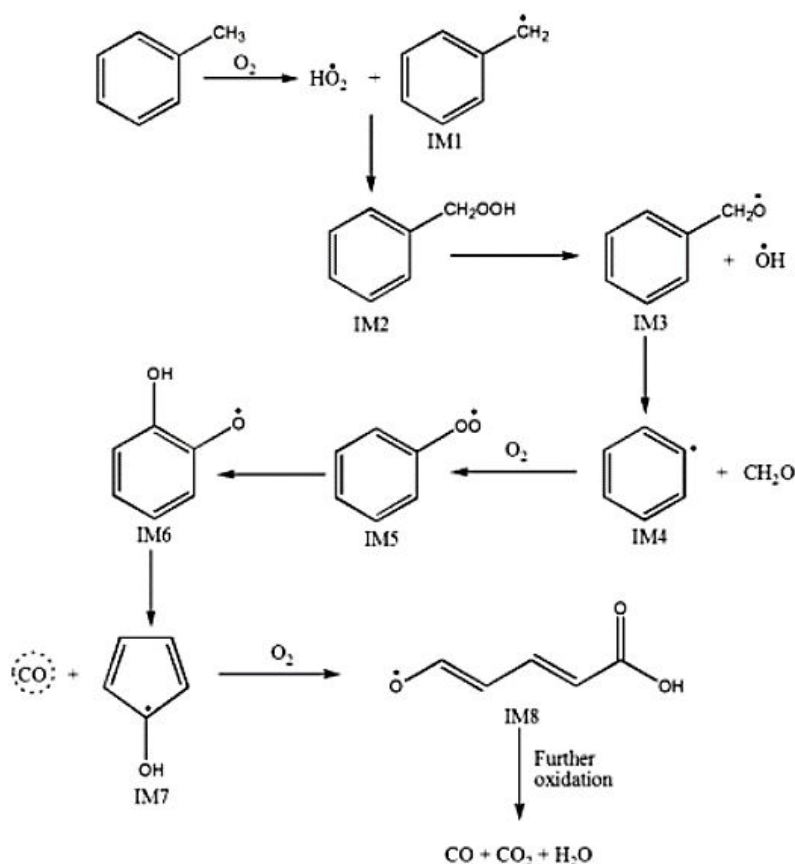
The feasibility of these two sets of ReaxFF parameters in predicting particle growth during soot inception process was evaluated and shown in **Figure 11** below. The carbon number of the largest particle in CHO2016 can be as large as 1000 after the initial fuel decomposition, whereas CHO2008 fails to predict the particle growth with the carbon number remaining at an extremely low level. Chen et al. [99] observed that, after 1.6 ns, the C:H ratio of the largest molecule in CHO2016 started to increase and became much higher than that of CHO2008, indicating that CHO2016 was able to describe the continuous dehydrogenation reasonably during soot inception. As a consequence, CHO2016 parameters were employed in their following study.



**Figure 11: Evaluation of CHO2008 and CHO2016 force field parameters in predicting diesel incipient soot formation in terms of the number of carbon atoms in the largest molecule and the C:H ratio of the largest molecule, where the solid cycle represents CHO2016 while the hollow cycle represents CHO2008. Image taken from ref.[99].**

From their ReaxFF simulations, they found that large hydrocarbons clusters undergo coalescence through aliphatic chain connection and that this process results in rapid mass growth eventually leading to the condensed nascent root particle. Plus, they observed that the effects of the oxygenated molecular structures on soot formation are quantified and reflected in two aspects, i.e. removing C-atoms from the soot precursor pool through combination with O-atoms and contributing to soot precursor formation due to the existence of C-C bonds simultaneously.

On a similar page, Cheng, Wang et al. [101] studied the high-temperature oxidation mechanisms of toluene at different temperatures and densities by employing the ReaxFF reactive force field. To validate their reactive force field and its transferability, they performed QM calculations on the key intermediates and reactions observed during the ReaxFF MD simulations. Geometry optimization of the heats of formation for key reactions at 298 K were calculated by using the Gaussian 03 program[102].



**Figure 12:** Simplified scheme of toluene partial oxidation pathway observed in the ReaxFF NVT-MD simulation at  $T = 2700$  K performed by Cheng et al. [101].

To investigate the initial reaction mechanisms of toluene oxidation, Cheng et al. [101] performed a series of NVT-MD simulations on unimolecular combustion models (which contained 100 oxygen molecules and 1 toluene molecule) and multimolecular combustion models (which instead contained 90 oxygen molecules and 10 toluene molecules). These simulations were performed at  $0.35 \text{ g/cm}^3$  with temperature ranging from 2500 to 3000 K in 100 K intervals. These two independent sets of simulations showed that benzyl radical ( $\text{C}_7\text{H}_7^\circ$ ) was a dominant intermediate at different temperatures and this was found as reasonable since the methyl C-H bond is the weakest (89.2 kcal/mol). Cheng et al. [101] reported a simplified scheme of toluene oxidation shown in **Figure 12** below, where dash cycles indicate the final carbon dioxide.

They also found that the extended simulation time of 1 ns for high temperature simulation (3000 K) did not result in further oxidation of carbon monoxide to carbon dioxide and they attributed this possibility to a longer simulation time required for the further oxidation of carbon monoxide to occur.

From their MD simulations, they found that the consumption of toluene mainly happens in three ways: (1) the hydrogen abstraction reactions by oxygen molecules or other small radicals to form benzyl radical, (2) the cleavage of the C-H bond to form benzyl and hydrogen radicals and (3) the cleavage of the C-C bond to form phenyl and methyl radicals. All these basic reaction mechanisms were observed to be in good agreement with available chemical kinetic models.

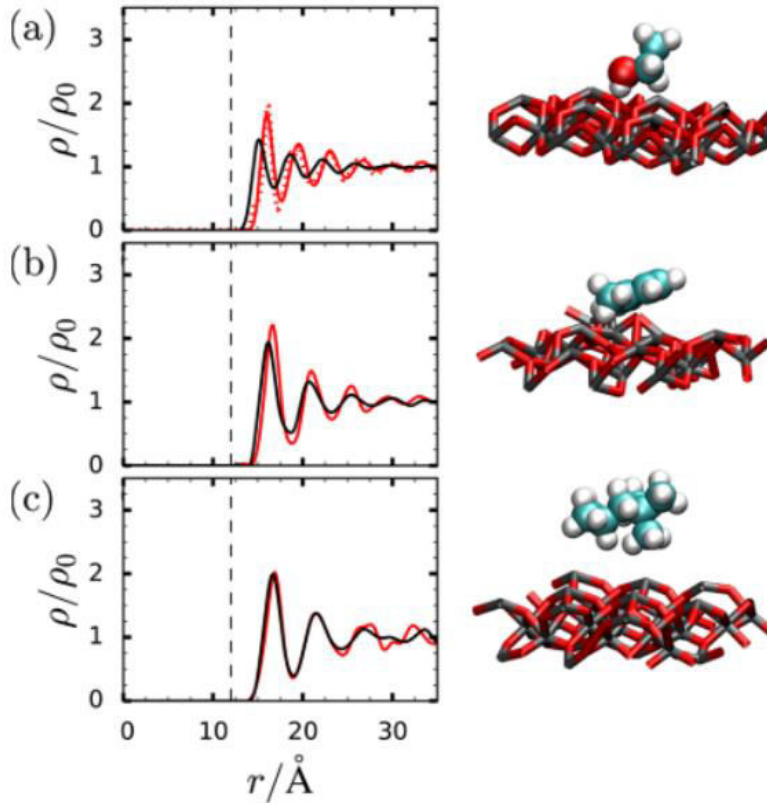
#### 1.4.4. ReaxFF studies of the liquid-surface interactions

In the work of Chia et al. [103] the liquid adsorption of organic compounds on hematite  $\alpha\text{-Fe}_2\text{O}_3$  using ReaxFF was discussed. The adsorbed species were small molecules like ethanol ( $\text{C}_2\text{H}_6\text{O}$ ), toluene ( $\text{C}_7\text{H}_8$ ) and iso-octane ( $\text{C}_8\text{H}_{18}$ ) and hematite ( $\alpha\text{-Fe}_2\text{O}_3$ ) as surface since it is often formed on the surface of iron-containing alloys [104, 105].

The objective of this research was to study the effect that organic molecules of different polarity can have on the structure of a crystal surface; their aim was to assess the impact that the surface distortions can have on the properties of this adsorbed liquid phase, as well as the ability of this solvent to affect both the structure and properties of the solid surface. To validate their force

field, they calculated the structure of bulk hematite by using a MD-NVT simulations with the ReaxFF parameters at 298 K and 1 atm and then compared the obtained results with experimental crystallographic data. From this comparison, they found their ReaxFF results to be in agreement with the reference experimental data.

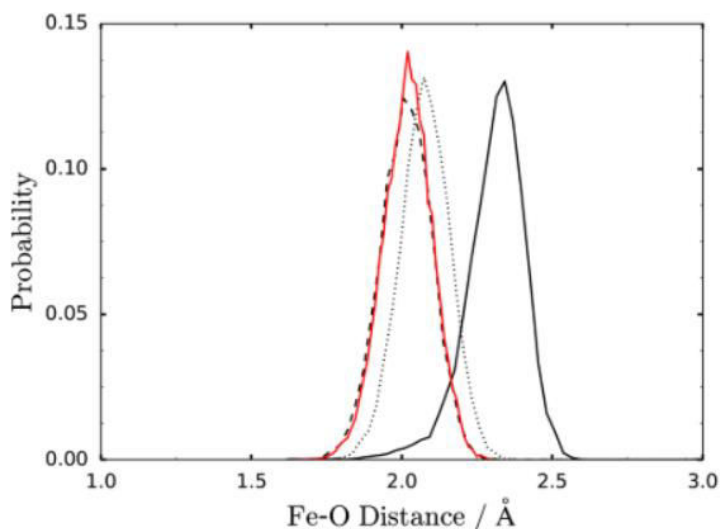
Their ReaxFF study showed that, when ethanol and toluene were adsorbed on the surface in the flexible slab case, they were shift to slightly larger distances than the rigid slab case as consequence of an expansion occurred at the outermost surface atoms of the hematite surface (**Figure 13**). Plus, from their calculations resulted that the first layer of adsorbed ethanol have shown a parallel configuration to the surface, while the toluene molecule adsorbed tilted on the surface, with an average tilt angle of approximately  $35^\circ$  with respect to the normal direction of the slab; for the iso-octane case, results have confirmed that the polarity of the molecules indeed has an effect on the structure of hematite near the surface [103].



**Figure 13: Density profiles along the z axis normalized by the bulk liquid density  $\rho_0$  and visualization of a typical molecule's orientation for (a) ethanol, (b) toluene and (c) iso-octane. Results obtained for the flexible slab are shown in red and the results for the rigid slab are in black. Image taken from ref.[103].**

To validate the influence of the adsorbate polarity on the outermost layers of the hematite surface, Chia et al. showed from their results that significant differences in the bond lengths of the surface atoms were found by comparing the rigid and the flexible solid models. The **Figure 14** below shows the bond lengths of the outermost layer of the flexible hematite slab in contact with different fluids. It was observed that the Fe-O bond length distributions in the presence of ethanol is nonsymmetrical and slightly wider than for the other fluids. According to Chia et al, the stronger attraction of liquid molecules to the surface is a result of the increase in nonbonded electrostatic interactions.

As conclusion of their work, they showed that the polarity of the liquid has indeed a strong influence on the structure of the iron oxide surface model since it modified the positions of the outermost surface atoms together with their partial charges; this result is not to be underestimated since the change in position and charge can actually lead towards larger electrostatic interactions and a stronger liquid adsorption, even in the absence of chemical reactions.



**Figure 14: Probability distribution function of the Fe-O bond length in the outermost layer of flexible solid in contact with ethanol (solid line), toluene (dotted line), iso-octane (dashed line) and vacuum (red).Image taken from ref.[103].**

It is worthy to highlight their research contribution since in this thesis it has similarly been considered a liquid phase in which they are present fuel oxidation precursors, most likely in the form of alcohols, esters and epoxides which can add polarity to the system; plus, being the hematite  $\alpha\text{-Fe}_2\text{O}_3$  analyzed in this work a corundum-type oxide exactly as the chromia  $\alpha\text{-Cr}_2\text{O}_3$ ,

similar structural and electronic properties are expected. For these reasons, seen the similarities between the two systems, their results could be eventually considered as future reference for the ReaxFF parameterization of this study.

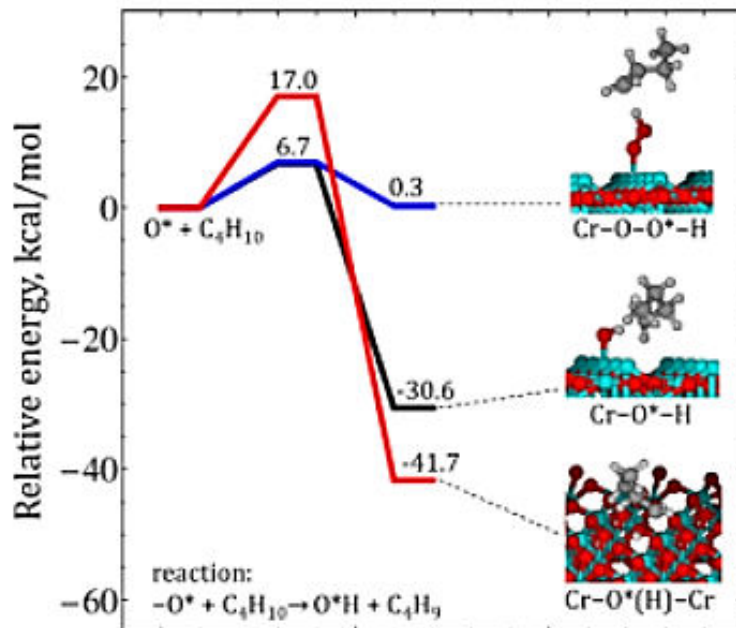
Another interesting work related to ReaxFF is the research conducted by Shin, Kwak et al. [106], where they were able to develop a ReaxFF force field for the Fe/Cr/O/S system by ReaxFF parameterization via QM calculation data. For ReaxFF parameterization, they opted to compare the QM values for the lattice parameters and cohesive energy of Cr for three different crystal structures (bcc, fcc and a15) since the energy-volume relationship of metals and alloys was considered of great importance for predicting phase stability of the crystal structures and structural phase transitions under pressure and temperature.

The objective of this study was to investigate about the Cr-oxide catalytic activity regarding the butane oxidation reaction carried out at 1600 K. To validate their ReaxFF force field for describing the catalytic oxidation reactions, Shin et al. performed NVT-MD oxidation simulations of butane on  $\text{Cr}_2\text{O}_3$  and  $\text{Cr}_2\text{O}_3$ /pyrite surfaces and then compared the obtained reactions with these catalysts to the oxidation of with  $\text{O}_2$  oxidant. They investigated the reaction mechanisms in small model systems and then analyzed the product distribution in large-scale simulations.

From **Figure 15** below reports the energy barriers required for the first dehydrogenation of the terminal carbon investigated at different oxygen sites. The potential energy curve calculated by Shin et al. along the dehydrogenation reaction reveals that the energy barriers are 6.7 kcal/mol at the terminal oxygen sites, 6.9 kcal/mol at the peroxo oxygen site and 17 kcal/mol at the bridging oxygen site. All these energy barriers agree that binding the H atom to the terminal oxygen is easier kinetically and thermodynamically than that to the bridging and peroxo oxygens and in their simulations, Shin et al. observed that the abstraction of hydrogen from butane is carried out by all three oxygen types (e.g. the terminal oxygen, the bridging oxygen and the peroxo oxygen).

In fact, thanks to their simulations results, they were able to demonstrate that the active oxygen species present on the oxide surface actually play an important role regarding this oxidation reaction, since they appeared to be very reactive by readily interacting with the butane molecules.

Indeed, Cr-oxide is able to catalyze several chemical reactions, e.g. dehydrogenation, oxidation and polymerization [107–110]. Plus, the Cr-oxide is a highly efficient catalyst for full combustion [111].



**Figure 15: Energy barrier and reaction energy for the dehydrogenation of a butane terminal carbon at active oxygen sites on  $Cr_2O_3$  (1000) surface. Image taken from ref.[106].**

It is certainly well-known that in oxidation processes the active oxygen species present on these metal oxides surfaces play an important role in their catalytic activity [112]. Indeed, this aspect should not be overlooked in this thesis, since in the future molecular simulations a catalytic behavior from chromia  $\alpha$ - $Cr_2O_3$  could happen to be detected.

Another interesting work is the one conducted by Soleymanibrojeni M. et al. [113], where MD ReaxFF simulations have been computed for the study of epoxy/water/alumina systems; these system, similarly as the one considered for this thesis, can be divided into three parts: (i) organic phase, (ii) substrate, (iii) interface between the organic phase and the substrate. In particular, in this work the interaction energies of different configuration of epoxy and water over an alumina substrate was studied.

In their work, Soleymanibrojeni M. et al. [113] compared ReaxFF results against the density functional tight binding (DFTB) calculations. The simulations were implemented for three different systems: the organic system (C/H/N/O), the organic phase on hydroxylated  $\gamma$ -alumina substrate (C/H/O/Al) and the reaction of aluminum with water (Al/H/O).

The force fields used in their study were labeled as ReaxFF-13, ReaxFF-15 and ReaxFF-18; to compare and validate them, density and structural analysis of four crystalline organic compounds were used. The selected compounds are Trimethylamine, (20R,24S)-20,24-Epoxy dammarane-3 $\beta$ ,12 $\beta$ ,25-triol (EDT), Diglycidyl Ether of Bisphenol-A (DGEBA), (S)-3-Hydroxymethyl-1,2,3,4-tetrahydroisoquinoline (HMTQ). The density of each compound was measured with Nosé-Hoover method at constant particle number, pressure and temperature (NPT) at 298.2 K for 200 ps. The density is the average of the final 50 ps values and the simulation boxes were made by 4x4x4 replication of the crystalline unit cells.

From their results on the description of the organic molecules, the ReaxFF-18 gave the most accurate reproduction of the experimental values of densities, with errors between the 0.1%-7%, while the least accurate prediction was given by ReaxFF-13, which gave errors between 18.5%-45.1% [113]. To complete their structural analyses on these selected compounds, Soleymanibrojeni et al. also calculated the radial distribution functions  $g(r)$  and its integral, which gave the mean number of atoms around a specific type of atom at distance  $r$ . The  $g(r)$  and its integral for C-N pairs of Trimethylamine, and C-C pairs of EDT, DGEBA and HMTQ were calculated.

Plus, they also calculated the self-diffusion, density and structure of 864 water molecules by using 100 ps Nosé-Hoover NPT simulations at 298.2 K with each force field and the results from the final 50 ps were used for calculation of density. In particular, the RDF of O-O, O-H and H-H pairs of water molecules were obtained and compared with experimental data.

About their study on the interface interactions of the epoxy/water/surface system, they calculated the interaction energies of DGEAB molecules with a hydroxylated (001)  $\gamma$ -alumina substrate with and without adsorbed water molecules with each force-field.

For these calculations, they created the following systems: six DGEBA molecules (Epoxy) were placed on a 27.9 Å x 24.9 Å hydroxylated (001)  $\gamma$ -alumina interface ( $\text{Al}_2\text{O}_3$ ) with 70, 140 or 210

surface adsorbed water molecules ( $\text{H}_2\text{O}$ ). The  $\text{Al}_2\text{O}_3$  and surface  $\text{H}_2\text{O}$  together is considered as the Substrate, defining in this way the Epoxy/Substrate-(70  $\text{H}_2\text{O}$ ), the Epoxy/Substrate-(140  $\text{H}_2\text{O}$ ) and the Epoxy/Substrate-(210  $\text{H}_2\text{O}$ ). Direct interaction energies of Epoxy with  $\text{Al}_2\text{O}_3$  for different systems (70  $\text{H}_2\text{O}$ , 140  $\text{H}_2\text{O}$  and 210  $\text{H}_2\text{O}$ ) were also measured (i.e. Epoxy/ $\text{Al}_2\text{O}_3$ -70  $\text{H}_2\text{O}$ , Epoxy/ $\text{Al}_2\text{O}_3$ -140  $\text{H}_2\text{O}$  and Epoxy/ $\text{Al}_2\text{O}_3$ -210  $\text{H}_2\text{O}$ ). Finally, direct interaction energies between Epoxy and different number of water molecules were additionally calculated: Epoxy/Water-(70  $\text{H}_2\text{O}$ ), Epoxy/Water-(140  $\text{H}_2\text{O}$ ) and Epoxy/Water-(210  $\text{H}_2\text{O}$ ).

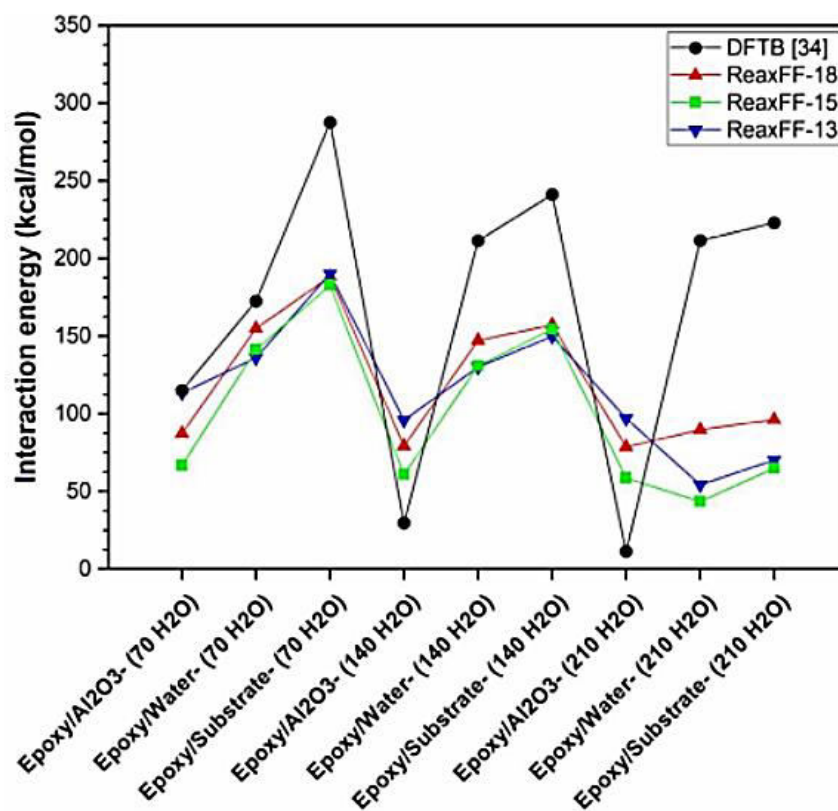


Figure 16: Interactions energies of DGEBA and hydroxylated alumina with DFTB and ReaxFF methods. Image taken from ref.[113].

The ReaxFF results were compared with DFTB calculations and reported below in **Figure 16**. **Figure 16** shows that the interaction energies generally decrease as the number of water molecules increase. From their results, they came to the following conclusions: i) interaction energies of the Epoxy with water are greater than those of Epoxy with  $\text{Al}_2\text{O}_3$ ; ii) interaction energies of Epoxy with Substrate decrease by increasing the number of water molecules; iii)

DFTB interaction energies of Epoxy with  $\text{Al}_2\text{O}_3$  decreased by increasing the number of water molecules, but ReaxFF interaction energies showed less sensitivity to this parameter [113].

The behavior of the epoxy with the water and alumina substrate found from their work could be helpful for this thesis, since it gives insights of how this molecule seems to interact when in contact with a hydroxylated metal oxide substrate with additional water molecules.

In the work of Sengul et al. [114] the reaction dynamics of liquid-solid interface with the example of an acetic acid/ water solution interacting with a  $\text{ZnO}(1010)$  surface was investigated using ReaxFF reactive force field-based molecular dynamics. Even though the  $\text{ZnO}(1010)$  surface is not treated in our study, the study of the interface interactions of organic molecule/water/metal-oxide systems is a topic of major interest in this thesis framework.

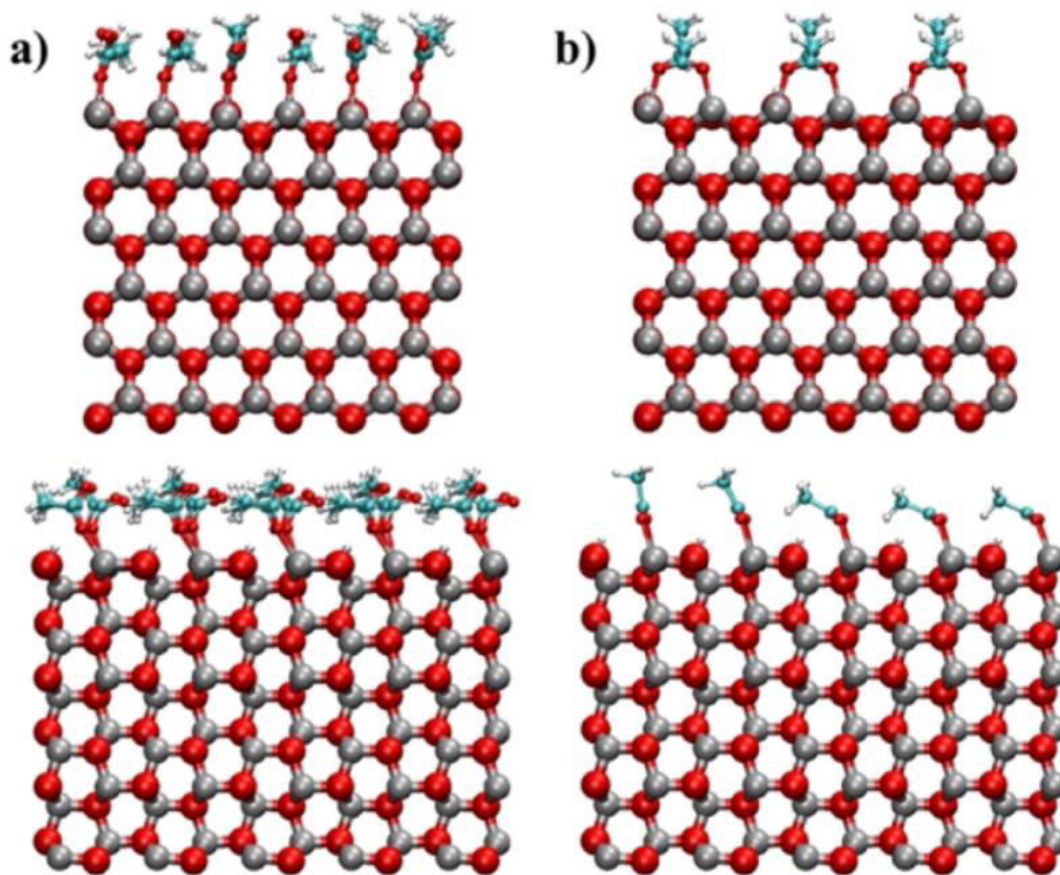
To conduct their dynamic study, Sengul et al. [115] opted to use a new ReaxFF potential to model the acetic acid/water/ $\text{ZnO}$  interfacial reactions by combining two previously developed potentials, the potential for H/O/Zn interaction [116] and the potential for C/H/O interaction [117], respectively. They investigated the interaction between solvent molecules and surfaces through the adsorption energies, thus they conducted energy minimization simulations in order to obtain data on the adsorption. In their minimization calculations, they used 12 layers of  $\text{ZnO}$  slabs, each of them composed of 360 zinc (Zn) and oxygen (O) atoms. The amount of coverage on the surface by the acetic acid molecules was indicated as  $\theta$ , where the number of the acetic molecules for  $\theta = 1.0$  was 30 (one molecule per surface Zn) and  $\theta = 0.5$  (half monolayer) was 15. In their work, Sengul et al. [115] reported the minimum energy configurations that are shown in **Figure 17**. They observed that a dissociative adsorption is favored for acetic acid molecules on  $\text{ZnO}(1010)$  surface and that, in the case of full coverage ( $\theta = 1.0$ ), the hydrogen bonds with oxygens of other acetates affected the orientation of acetates with respect to the surface normal.

Sengul et al. [115] calculated the adsorption energies values using ReaxFF and these results were compared with DFT calculations results provided by ref. [118] and were found to be in a very good agreement with this reference.

To investigate the reaction dynamics between acetic acid molecules and  $\text{ZnO}(1010)$  surface in the presence of water, ReaxFF MD simulations were performed at effective temperatures ranging

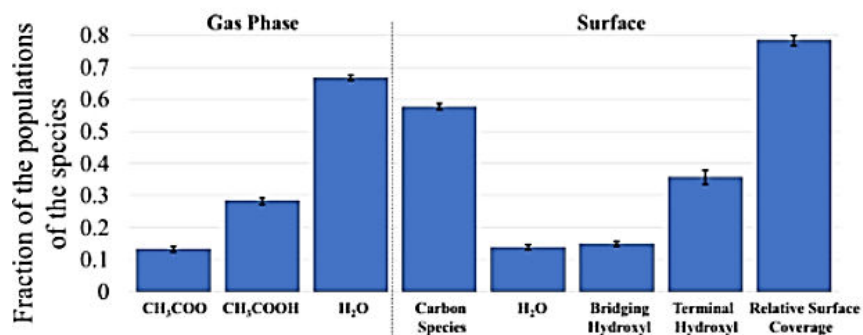
between 300 K and 1200 K to drive the reactions within the computational time. The population of the molecular species were calculated in the bulk phase and on the surface separately.

The molecules with a distance of 3.0 Å or less from surface cations were counted as surface species and the rest were counted as bulk species. The fractions were calculated by dividing by the total number of corresponding species: the fraction of acetate, acetic acid and carbon species were calculated with respect to the total number of acetic acids in the system; the relative surface coverage was calculated with respect to the total number of available sites for adsorption on surface. The results obtained for the case run at  $T = 300$  K are reported in the **Figure 18** below. [115]



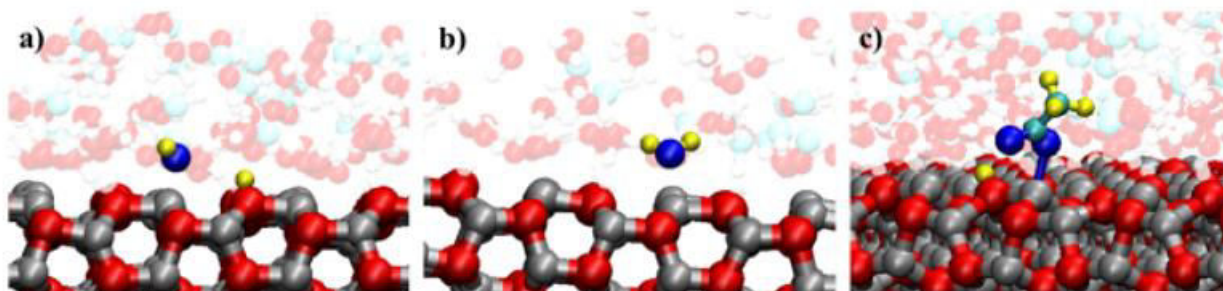
**Figure 17:** Minimum energy configurations of ZnO(1010) covered by acetic acid molecules reported in ref. [115]. Top: [0001] view, bottom: [1210] view. Oxygen, hydrogen, carbon and zinc atoms are visualized as red, white, cyan and silver spheres, respectively. (a) 100% coverage ( $\theta = 1,0$ ) configuration, (b) 50% coverage ( $\theta = 0,5$ ) configuration.

According to their results at  $T = 300$  K, Sengul et al. [115] found that 33% of water molecules were adsorbed on the surface either molecularly or dissociatively and the remaining 66.7% were in the bulk phase. Similar dissociation ratios have been reported by DFT and previous ReaxFF studies.



**Figure 18:** Fractions of populations of the species in the gas phase and on the surface at room temperature according to ref. [115].

For the acetic acid molecules, approximately 58% of the molecules in the system were adsorbed on the surface and a dissociation of Brønsted acids (i.e. acetic acid) mechanism on this metal oxide surface was also observed in their simulations, as reported in **Figure 19** below.



**Figure 19:** Snapshots of ReaxFF MD simulations from ref. [115] showing the different adsorption states of water and acetic acid on ZnO surface. (a) Bridging and surface hydroxyls, (b) molecularly adsorbed water, (c) adsorbed acetate and surface hydroxyl. Oxygen, hydrogen, carbon and zinc atoms are visualized as red, white, cyan and silver spheres, respectively. Oxygen and hydrogen atoms that are of interest are visualized as blue and yellow, respectively.

In their work, Sengul et al. found that the acetic acid dissociation mechanisms are observed in the simulations: (1) deprotonation to surface cation, which produces a terminal hydroxyl and (2)

deprotonation to a bridging hydroxyl, which results in water production. According to them, an increase in temperature promotes the dissociation of acetic acids and its adsorption surface at first, but as temperature increase continues, the surface coverage by acetates decreases due to evaporation from the surface or decomposition.

## **1.5. Conclusion**

Fuel degradation is a major concern to the transportation industry since it can lead to liquid and insoluble deposits in several parts of the engine in contact with the fuel, and in particular they are one of the major causes for the malfunctioning and failures of engine injectors. This bibliographic study shows that these deposits are directly linked to the hydrocarbons autoxidation occurring in the liquid phase and to their interaction with the metallic surfaces in contact with the fuel. Experimental data have shown that the small oxygenated molecules obtained from the autoxidation process such as alcohols, aldehydes, ketones, epoxides and carboxylic acids are considered as deposits precursors. The oxygenated polar “head” of these molecules seems to form chemical bonds with different metal-oxide surfaces, but also with polymers and coatings. Two mechanisms were proposed for understanding the deposits formation observed in engines parts: (1) the adsorption of these precursors directly to the surfaces forming a first liquid film layer; or (2) the aggregation and coalescence process in the liquid phase and depending on the polarity, weight and operation conditions, these aggregates would precipitate adsorbing on the different surfaces. Both mechanisms are not completely understood.

Several numerical works focused on the investigation of organic condensed phase or organic/metal-oxides surfaces by using DFT and/or ReaxFF method. However, the theoretical studies with focus on fuels are mostly dedicated to homogeneous gas phase and combustion. There is a lack of data available for fuels in liquid phase in low temperature range (<300°C), which would be more pertinent for studying fuels autoxidation process. Some theoretical studies dedicated to heterogeneous phases, i.e. organic molecules in liquid phase/metal-oxides surfaces interfaces are quite interesting. They have shown that the hydration state of the surface may play an important role for the adsorption of oxygenated molecules such as epoxides and carboxylic acids on the oxide surface. However, despite the literature available, there is still a lack of understanding about the interactions of organic molecules over metallic surfaces like aluminum

and stainless steel in conditions that are closer to real engine systems, (e.g. surface hydration variation), as well as to evaluate molecules that are better representing fuels oxidation products and not yet studied in the literature, such as acetaldehyde, ketones, epoxides and acetic acid, at the best of our knowledge.

Therefore, the objective of this thesis is to obtain a reactive force field able to handle the reactions of organic molecules representative of the fuel in the liquid phase and their interaction with two metallic surfaces representative of engine materials. The developed reactive force field will be used to study deposits formation process. To achieve this goal this thesis is structured as follows:

- **Chapter 2** describes in detail the methodology used during this thesis which is based in a multiscale approach combining two different numerical approaches: a preliminary ab initio study conducted via DFT (Density Functional Theory) and a successive MD (Molecular Dynamics) approach carried out via the implementation of a reactive force field (ReaxFF). The theoretical notions behind both numerical approaches are also discussed.
- The choice of model surfaces representing aluminum and stainless steel as well as the different hydration conditions (partial pressure of water in the system) is presented in **Chapter 3**.
- **Chapter 4** is dedicated to the quantum mechanical (QM) study using DFT calculations to study the toluene autoxidation reactions in the gas phase and the adsorption of small organic molecules (models of deposit precursors) on representative aluminum and stainless-steel surfaces. All DFT parameters about the system energy of reaction, adsorption, charge transfers, and the reactivity of the molecules over surfaces in which each studied surface orientation was either anhydrous or fully hydroxylated was studied. All these data are necessary to calibrate the reactive force field.
- Once the DFT data are available, a ReaxFF study was carried out and presented in **Chapter 5** with the objective to build a solid ReaxFF methodology suitable for our research. In this chapter, we thoroughly describe the ReaxFF reparametrization and validation steps of two different force fields, one exclusively for the description of

alumina configurations and the other for the description of chromia configurations, respectively.

- **Chapter 6** focus is then to present the application of the obtained reactive force field to the autoxidation reaction of toluene in both homogeneous (i.e. liquid phase) and heterogeneous (i.e. liquid/solid interface) conditions.
- Finally, the conclusion and perspectives are discussed in **Chapter 7**.

## References

- 1 Office P. Directive 2009/28/EC of the European Parliament and of the Council of 23 April 2009 on the promotion of the use of energy from renewable sources and amending and subsequently repealing Directives 2001/77/EC and 2003/30/EC.
- 2 Knothe G., Krahl J., van Gerpen J. *The Biodiesel Handbook*, Elsevier (2015). ISBN: 9780983507260.
- 3 *Energy, transport and environment statistics*, Imprimeries Bietlot Frères, Belgium, Luxembourg (2020). ISBN: 978-92-76-20736-8.
- 4 Resolution A40-18 Climate change: <https://www.icao.int/environmental-protection/pages/climate-change.aspx>.
- 5 American Society for Testing and Materials (ASTM) standard D6751. Standard specification for biodiesel fuel blend stock (B100) for middle distillate fuels., *ASTM*.
- 6 European Committee for Standardization. Standard EN 14214. Automotive fuels – fatty acid methyl esters (FAME) for diesel engines – requirements and test methods.
- 7 Anand P. Dahiya, A. K. Berwal, B. K. Khan Combustion analysis in a compression ignition engine powered by biodiesel, *Int. J. Eng. Technol. Manag. Appl. Sci.* **3**, 9 (2015), 40–53.
- 8 Bhardwaj O.P., Lüers B., Holderbaum B., Koerfer T., Pischinger S., Honkanen M. Utilization of HVO Fuel Properties in a High Efficiency Combustion System: Part 2: Relationship of Soot Characteristics with its Oxidation Behavior in DPF, *SAE Int. J. Fuels Lubr.* **7**, 3 (2014), 979–994. DOI: 10.4271/2014-01-2846.
- 9 The EU Framework Programme for Research and Innovation Horizon 2020: H2020 Programme AGA - Annotated Model Grant Agreement. Available at: [https://ec.europa.eu/research/participants/data/ref/h2020/grants\\_manual/amga](https://ec.europa.eu/research/participants/data/ref/h2020/grants_manual/amga) (2019).
- 10 Pullen J., Saeed K. An overview of biodiesel oxidation stability, *Renewable and Sustainable Energy Reviews* **16**, 8 (2012), 5924–5950. DOI: 10.1016/j.rser.2012.06.024.
- 11 Dunn R.O. Antioxidants for improving storage stability of biodiesel, *Biofuels, Bioprod. Bioref.* **2**, 4 (2008), 304–318. DOI: 10.1002/bbb.83.
- 12 Bacha K., Ben-Amara A., Vannier A., Alves-Fortunato M., Nardin M. Oxidation Stability of Diesel/Biodiesel Fuels Measured by a PetroOxy Device and Characterization of Oxidation Products, *Energy Fuels* **29**, 7 (2015), 4345–4355. DOI: 10.1021/acs.energyfuels.5b00450.
- 13 Ullmann J., Geduldig M., Stutzenberger H., Caprotti R., Balfour G. Investigation into the Formation and Prevention of Internal Diesel Injector Deposits, *SAE Int. J. Fuels Lubr.*, 2008-01-0926 (2008). DOI: 10.4271/2008-01-0926.
- 14 J Barker, P Richards, C Snape, W Meredith Diesel injection deposits - An issue that has evolved with engine technology, *SAE Int. J. Fuels Lubr.* (2011).
- 15 Zabarnick S. Chemical kinetic modeling of jet fuel autoxidation and antioxidant chemistry, *Ind. Eng. Chem. Res.* **32** (1993), 1012–1017.
- 16 Bacha K. These de Doctorat "Etude de l'interaction entre le carburant diesel et les composants du système d'injection diesel", *Physique des matériaux*, Université de Haute Alsace (2016).
- 17 Jones E.G., Balster L.M. Interaction of a Synthetic Hindered-Phenol with Natural Fuel Antioxidants in the Autoxidation of Paraffins, *Energy Fuels* **14**, 3 (2000), 640–645. DOI: 10.1021/ef990216q.
- 18 EN 590: Automotive fuels-Diesel-Requirements and test methods. 2009.
- 19 Alves Fortunato M., Lenglet F., Ben Amara A., Starck L. Are Internal Diesel Injector Deposits (IDID) Mainly Linked to Biofuel Chemical Composition or/and Engine Operation Condition?, *SAE Int. J. Fuels Lubr.*, 2019-01-0061 (2019). DOI: 10.4271/2019-01-0061.
- 20 Watkinson A.P., Wilson D.I. Chemical reaction fouling: A review, *Experimental Thermal and Fluid Science* **14**, 4 (1997), 361–374. DOI: 10.1016/S0894-1777(96)00138-0.
- 21 Alves-Fortunato M., Ayoub E., Bacha K., Mouret A., Dalmazzone C. Fatty Acids Methyl Esters (FAME) autoxidation: New insights on insoluble deposit formation process in biofuels, *Fuel* **268** (2020), 117074. DOI: 10.1016/j.fuel.2020.117074.

- 22 Alves-Fortunato M., Labaume J., Cologon P., Barré L. Biofuel Surrogate Oxidation: Insoluble Deposits Formation Studied by Small-Angle X-ray Scattering and Small Angle Neutron Scattering, *Energy Fuels***32**, 9 (2018), 9559–9567. DOI: 10.1021/acs.energyfuels.8b02055.
- 23 Thomas R. Sem Investigation of injector tip deposits on transport refrigeration units running on biodiesel fuel, *SAE Int. J. Fuels Lubr.***1801** (2004).
- 24 Kuprowicz N.J., Zabarnick S., West Z.J., Ervin J.S. Use of Measured Species Class Concentrations with Chemical Kinetic Modeling for the Prediction of Autoxidation and Deposition of Jet Fuels, *Energy Fuels***21**, 2 (2007), 530–544. DOI: 10.1021/ef060391o.
- 25 W. Mathieu Zongo Etude de l'oxydation des huiles de poisson microencapsulées par DSC sous pression, *Chimie Analytique* (2009).
- 26 Pfaendtner J., Broadbelt L.J. Mechanistic Modeling of Lubricant Degradation. 1. Structure–Reactivity Relationships for Free-Radical Oxidation, *Ind. Eng. Chem. Res.***47**, 9 (2008), 2886–2896. DOI: 10.1021/ie0714807.
- 27 Nikolai N. Semenov: Nobel Lecture (1956).
- 28 K. T. Reddy, Nicholas P. Cernansky, and R. S. Cohen Modified reaction mechanism of aerated n-dodecane liquid flowing over heated metal tubes (1987).
- 29 Evgeny T. Denisov Igor B. Afanas'ev (ed.) *Oxidation and Antioxidants in Organic Chemistry and Biology*. ISBN: ISBN 0-8247-5356-9 (alk. paper).
- 30 Corporan E., Edwards T., Shafer L., DeWitt M.J., Klingshirn C., Zabarnick S., West Z., Striebich R., Graham J., Klein J. Chemical, Thermal Stability, Seal Swell, and Emissions Studies of Alternative Jet Fuels, *Energy Fuels***25**, 3 (2011), 955–966. DOI: 10.1021/ef101520v.
- 31 Ben Amara A., Nicolle A., Alves-Fortunato M., Jeuland N. Toward Predictive Modeling of Petroleum and Biobased Fuel Stability: Kinetics of Methyl Oleate/ n -Dodecane Autoxidation, *Energy Fuels***27**, 10 (2013), 6125–6133. DOI: 10.1021/ef401360k.
- 32 Balamurali Navaneetha Sundaram The effects of oxygen on synthetic crude oil fouling, *Master of Applied Science*, Annamalai University (1998).
- 33 Balster L.M., Zabarnick S., Striebich R.C., Shafer L.M., West Z.J. Analysis of Polar Species in Jet Fuel and Determination of Their Role in Autoxidative Deposit Formation †, *Energy Fuels***20**, 6 (2006), 2564–2571. DOI: 10.1021/ef060275l.
- 34 Balster L.M., Corporan E., DeWitt M.J., Edwards J.T., Ervin J.S., Graham J.L., Lee S.-Y., Pal S., Phelps D.K., Rudnick L.R., Santoro R.J., Schobert H.H., Shafer L.M., Striebich R.C., West Z.J., Wilson G.R., Woodward R., Zabarnick S. Development of an advanced, thermally stable, coal-based jet fuel, *Fuel Processing Technology***89**, 4 (2008), 364–378. DOI: 10.1016/j.fuproc.2007.11.018.
- 35 B. D. Batts and A. Zuhdan Fathoni A literature review on fuel stability studies with particular emphasis on diesel oil, *Energy Fuels***5** (1991), 2–21.
- 36 Ervin J.S., Ward T.A., Williams T.F., Bento J. Surface Deposition within Treated and Untreated Stainless Steel Tubes Resulting from Thermal-Oxidative and Pyrolytic Degradation of Jet Fuel, *Energy Fuels***17**, 3 (2003), 577–586. DOI: 10.1021/ef020180t.
- 37 L.J. Spadaccini, R.A. Meinzer, He Huang Membrane based fuel deoxygenator, US 6,315,815 B1.
- 38 Karavalakis G., Hilari D., Givalou L., Karonis D., Stournas S. Storage stability and ageing effect of biodiesel blends treated with different antioxidants, *Energy***36**, 1 (2011), 369–374. DOI: 10.1016/j.energy.2010.10.029.
- 39 Grinstead B., Zabarnick S. Studies of Jet Fuel Thermal Stability, Oxidation, and Additives Using an Isothermal Oxidation Apparatus Equipped with an Oxygen Sensor, *Energy Fuels***13** (1999), 756–760. DOI: 10.1021/ef980252+.
- 40 Arondel M., Rodeschini H., Lopes M., Dequenne B. Fuel Additives for Reduction of Internal Diesel Injectors Deposits (IDID, “lacquering”): A Critical and Priority Route, *SAE Int. J. Fuels Lubr.* (2012). DOI: 10.4271/2012-01-1687.
- 41 Singer P., Rühe J. On the mechanism of deposit formation during thermal oxidation of mineral diesel and diesel/biodiesel blends under accelerated conditions, *Fuel***133** (2014), 245–252. DOI: 10.1016/j.fuel.2014.04.041.
- 42 Jones C.C., Chughtai A.R., Murugaverl B., Smith D.M. Effects of air/fuel combustion ratio on the polycyclic aromatic hydrocarbon content of carbonaceous soots from selected fuels, *Carbon***42**, 12-13 (2004), 2471–2484. DOI: 10.1016/j.carbon.2004.04.042.

- 43 Wong O. Design and Development of an Apparatus to Study Aviation Jet Fuel Thermal Stability, *Master of Applied Science and Engineering* (2010).
- 44 Bouilly J., Mohammadi A., Iida Y., Hashimoto H., Geivanidis S., Samaras Z. Biodiesel Stability and its Effects on Diesel Fuel Injection Equipment, *SAE Int. J. Fuels Lubr.* (2012). DOI: 10.4271/2012-01-0860.
- 45 Hu E., Xu Y., Hu X., Pan L., Jiang S. Corrosion behaviors of metals in biodiesel from rapeseed oil and methanol, *Renewable Energy* **37**, 1 (2012), 371–378. DOI: 10.1016/j.renene.2011.07.010.
- 46 Norouzi S., Eslami F., Wyszynski M.L., Tsolakis A. Corrosion effects of RME in blends with ULSD on aluminium and copper, *Fuel Processing Technology* **104** (2012), 204–210. DOI: 10.1016/j.fuproc.2012.05.016.
- 47 Chatelain K., Nicolle A., Ben Amara A., Catoire L., Starck L. Wide Range Experimental and Kinetic Modeling Study of Chain Length Impact on n -Alkanes Autoxidation, *Energy Fuels* **30** (2016), 1294–1303. DOI: 10.1021/acs.energyfuels.5b02470.
- 48 Richter B., Crusius S., Schümann U., Handorf H. Characterisation of Internal Deposits in Common-Rail Injectors, *MTZ worldwide* **74** (2013), 50–56.
- 49 Alexander M. R., Beamson G., Blomfield C. J., Leggett G., Duc T. M. Interaction of carboxylic acids with the oxyhydroxide surface of aluminium : poly(acrylic acid), acetic acid and propionic acid on pseudoboehmite, *J Electron Spectros Relat Phenomena* **121** (2001), 19–32. DOI: 10.1016/S0368-2048(01)00324-3.
- 50 Lim M.S., Feng K., Chen X., Wu N., Raman A., Nightingale J., Gawalt E.S., Korakakis D., Hornak L.A., Timperman A.T. Adsorption and desorption of stearic acid self-assembled monolayers on aluminum oxide, *Langmuir* (2007), 2444–2452. DOI: 10.1021/la061914n.
- 51 Hafidi A., Anglaret E., Pioch D., Ajana H. Characterization of vegetable oils-alumina membranes interactions by diffuse reflectance Fourier transform infrared spectroscopy, *Eur. J. Lipid Sci. Technol.* **106**, 1 (2004), 11–21. DOI: 10.1002/ejlt.200300851.
- 52 Yan J., Zeng X., Ren T., van der Heide E. Boundary lubrication of stainless steel and CoCrMo alloy based on phosphorous and boron compounds in oil-in-water emulsion, *Appl. Surf. Sci.* **315** (2014), 415–424. DOI: 10.1016/j.apsusc.2014.07.160.
- 53 Łodziana Z., Nørskov J.K., Stoltze P. The stability of the hydroxylated (0001) surface of  $\alpha$ -Al<sub>2</sub>O<sub>3</sub>, *The Journal of Chemical Physics* **118**, 24 (2003), 11179–11188. DOI: 10.1063/1.1574798.
- 54 Massoud T., Maurice V., Klein L. H., Seyeux A., Marcus P. Nanostructure and local properties of oxide layers grown on stainless steel in simulated pressurized water reactor environment, *Corros. Sci.* **84** (2014), 198–203. DOI: 10.1016/j.corsci.2014.03.030.
- 55 Bikondoa O., Moritz W., Torrelles X., Kim H.J., Thornton G., Lindsay R. Impact of ambient oxygen on the surface structure of  $\alpha$ -Cr<sub>2</sub>O<sub>3</sub>(0001), *Phys. Rev.* **B81**, 205439 (2010). DOI: 10.1103/PhysRevB.81.205439.
- 56 Lübke M., Moritz W. A LEED analysis of the clean surfaces of  $\alpha$ -Fe<sub>2</sub>O<sub>3</sub>(0001) and  $\alpha$ -Cr<sub>2</sub>O<sub>3</sub>(0001) bulk single crystals, *J. Phys.: Condens. Matter* **21**, 134010 (2009). DOI: 10.1088/0953-8984/21/13/134010.
- 57 M. Bender et al. Structural rearrangement and surface magnetism on oxide surfaces : a temperature-dependent low-energy electron diffraction-electron energy loss spectroscopy study of Cr<sub>2</sub>O<sub>3</sub>(111)/Cr(110), *J. Phys.: Condens. Matter* **7**, 27 (1995), 5289–5302. DOI: 10.1088/0953-8984/7/27/014.
- 58 Souvi S.M., Badawi M., Virot F., Cristol S., Cantrel L., Paul J.-F. Influence of water, dihydrogen and dioxygen on the stability of the Cr<sub>2</sub>O<sub>3</sub> surface: A first-principles investigation, *Surf. Sci.* **666** (2017), 44–52. DOI: 10.1016/j.susc.2017.08.005.
- 59 Arrouvel C., Diawara B., Costa D., Marcus P. DFT Periodic Study of the Adsorption of Glycine on the Anhydrous and Hydroxylated (0001) Surfaces of  $\alpha$ -Alumina, *J. Phys. Chem. C* **111**, 49 (2007), 18164–18173. DOI: 10.1021/jp0741408.
- 60 Costa D., Sharkas K., Islam M.M., Marcus P. Ab initio study of the chemical states of water on Cr<sub>2</sub>O<sub>3</sub>(0001): From the isolated molecule to saturation coverage, *Surf. Sci.* **603**, 16 (2009), 2484–2493. DOI: 10.1016/j.susc.2009.05.037.
- 61 Gouron A., Kittel J., Bruin T. de, Diawara B. Density Functional Theory Study of Monoethanolamine Adsorption on Hydroxylated Cr<sub>2</sub>O<sub>3</sub> Surfaces, *J. Phys. Chem. C* **119**, 40 (2015), 22889–22898. DOI: 10.1021/acs.jpcc.5b05375.
- 62 Nigussa K.N., Nielsen K.L., Borck Ø., Støvneng J.A. Adsorption of hydrogen, chlorine, and sulfur atoms on  $\alpha$ -Cr<sub>2</sub>O<sub>3</sub>(0001) surfaces: A density functional theory investigation, *Corros. Sci.* **53**, 11 (2011), 3612–3622. DOI: 10.1016/j.corsci.2011.07.005.

- 63 Baran J.D., Grönbeck H., Hellman A. Mechanism for limiting thickness of thin oxide films on aluminum, *Phys. Rev. Lett.* **112** (2014), 146103-1 -146103-5. DOI: 10.1103/PhysRevLett.112.146103.
- 64 Siegel D.J., Hector L.G., Adams J.B. Adhesion, atomic structure, and bonding at the Al(111)/ $\alpha$ -Al<sub>2</sub>O<sub>3</sub>(0001) interface: A first principles study, *Phys. Rev. B* **65**, 8 (2002). DOI: 10.1103/PhysRevB.65.085415.
- 65 Renaud G. Oxide surface and metal/oxide interfaces studied by grazing incidence X-ray scattering, *Surf. Sci. Rep.* **32** (1998), 1–90.
- 66 Costa D., Ribeiro T., Mercuri F., Pacchioni G., Marcus P. Atomistic Modeling of Corrosion Resistance: A First Principles Study of O<sub>2</sub> Reduction on the Al(111) Surface Covered with a Thin Hydroxylated Alumina Film, *Adv. Mater. Interfaces* **1**, 3 (2014), 1300072. DOI: 10.1002/admi.201300072.
- 67 Digne M., Sautet P., Raybaud P., Euzen P., Toulhoat H. Hydroxyl Groups on  $\gamma$ -Alumina Surfaces: A DFT Study, *J. Catal.* **211**, 1 (2002), 1–5. DOI: 10.1006/jcat.2002.3741.
- 68 Jenness G.R., Christiansen M.A., Caratzoulas S., Vlachos D.G., Gorte R.J. Site-Dependent Lewis Acidity of  $\gamma$ -Al<sub>2</sub>O<sub>3</sub> and Its Impact on Ethanol Dehydration and Etherification, *J. Phys. Chem. C* **118**, 24 (2014), 12899–12907. DOI: 10.1021/jp5028349.
- 69 Wischert R., Laurent P., Copéret C., Delbecq F., Sautet P.  $\gamma$ -Alumina: the essential and unexpected role of water for the structure, stability, and reactivity of "defect" sites, *J. Am. Chem. Soc.* (2012), 14430–14449. DOI: 10.1021/ja3042383.
- 70 Valero M.C., Raybaud P., Sautet P. Influence of the hydroxylation of gamma-Al<sub>2</sub>O<sub>3</sub> surfaces on the stability and diffusion of single Pd atoms: a DFT study, *J. Phys. Chem. B* **110**, 4 (2006), 1759–1767. DOI: 10.1021/jp0554240.
- 71 Ngouana-Wakou B.F., Cornette P., Corral Valero M., Costa D., Raybaud P. An Atomistic Description of the  $\gamma$ -Alumina/Water Interface Revealed by Ab Initio Molecular Dynamics, *J. Phys. Chem. C* **121**, 19 (2017), 10351–10363. DOI: 10.1021/acs.jpcc.7b00101.
- 72 Arrouvel C., Digne M., Breyse M., Toulhoat H., Raybaud P. Effects of morphology on surface hydroxyl concentration: a DFT comparison of anatase–TiO<sub>2</sub> and  $\gamma$ -alumina catalytic supports, *J. Catal.* **222**, 1 (2004), 152–166. DOI: 10.1016/j.jcat.2003.10.016.
- 73 Arrouvel C., Breyse M., Toulhoat H., Raybaud P. A density functional theory comparison of anatase (TiO<sub>2</sub>)- and  $\gamma$ -Al<sub>2</sub>O<sub>3</sub>-supported MoS<sub>2</sub> catalysts, *J. Catal.* **232**, 1 (2005), 161–178. DOI: 10.1016/j.jcat.2005.02.018.
- 74 Arrouvel C., Toulhoat H., Breyse M., Raybaud P. Effects of PH<sub>2</sub>O, PH<sub>2</sub>S, PH<sub>2</sub> on the surface properties of anatase -TiO<sub>2</sub> and  $\gamma$ -Al<sub>2</sub>O<sub>3</sub>: a DFT study, *J. Catal.* **226**, 2 (2004), 260–272. DOI: 10.1016/j.jcat.2004.05.019.
- 75 J. M. Wittbrodt, W. L. Hase, and H. B. Schlegel Ab initio study of the interaction of water cluster models of the aluminum terminated (0001)  $\alpha$ -aluminum oxide surface, *J. Phys. Chem. B* **102** (1998), 6539–6548. DOI: 10.1021/jp981516w.
- 76 X-G. Wang, A. Chaka, M. Scheffler Effect of the Environment on alpha-Al<sub>2</sub>O<sub>3</sub> (0001) Surface Structures, *Phys. Rev. Lett.* **84**, 16 (2000), 3650–3653. DOI: 10.1103/PhysRevLett.84.3650.
- 77 Di Felice R., Northrup J. E Theory of the clean and hydrogenated Al<sub>2</sub>O<sub>3</sub> (0001) - (1x1) surfaces, *Phys. Rev. B* **60**, Iss. 24 - 15 (1999). DOI: 10.1103/PhysRevB.60.R16287.
- 78 Tepesch P. D., Quong A. A First-Principles Calculations of  $\alpha$ -Alumina (0001) Surfaces Energies with and without Hydrogen, *Phys. Stat. Sol (b)* **217** (2000), 377–387. DOI: 10.1002/(SICI)1521-3951(200001)217:1%3C377:AID-PSSB377%3E3.0.CO;2-B.
- 79 Hass, Schneider, Curioni, Andreoni The chemistry of water on alumina surfaces: reaction dynamics from first principles, *Science* **282**, 5387 (1998), 265–268. DOI: 10.1126/science.282.5387.265.
- 80 Hass K.C., Schneider W.F., Curioni A., Andreoni W. First-Principles Molecular Dynamics Simulations of H<sub>2</sub>O on  $\alpha$ -Al<sub>2</sub>O<sub>3</sub> (0001), *J. Phys. Chem. B* **104**, 23 (2000), 5527–5540. DOI: 10.1021/jp000040p.
- 81 Borck Ø., Hyldgaard P., Schröder E. Adsorption of methylamine on  $\alpha$ -Al<sub>2</sub>O<sub>3</sub>(0001) and  $\alpha$ -Cr<sub>2</sub>O<sub>3</sub>(0001) : Density functional theory, *Phys. Rev. B* **75**, 3 (2007). DOI: 10.1103/PhysRevB.75.035403.
- 82 Borck Ø., Schroder E. Adsorption of Methanol on Aluminum Oxide : A Density Functional Study, *Phys. Rep.* (2003), 1–11.
- 83 Chakarova-Käck S.D., Borck Ø., Schröder E., Lundqvist B.I. Adsorption of phenol on graphite(0001) and  $\alpha$ -Al<sub>2</sub>O<sub>3</sub>(0001) : Nature of van der Waals bonds from first-principles calculations, *Phys. Rev. B* **74**, 15 (2006). DOI: 10.1103/PhysRevB.74.155402.

- 84 Borck Ø., Schröder E. First-principles study of the adsorption of methanol at the  $\alpha$ -Al<sub>2</sub>O<sub>3</sub> (0001) surface, *J. Phys.: Condens. Matter***18**, 1 (2006), 1–12. DOI: 10.1088/0953-8984/18/1/001.
- 85 Pan Y., Liu C., Ge Q. Adsorption and protonation of CO<sub>2</sub> on partially hydroxylated gamma-Al<sub>2</sub>O<sub>3</sub> surfaces: a density functional theory study, *Langmuir* (2008), 12410–12419. DOI: 10.1021/la802295x.
- 86 Pan Y., Liu C., Ge Q. Effect of surface hydroxyls on selective CO<sub>2</sub> hydrogenation over Ni $\gamma$ -Al<sub>2</sub>O<sub>3</sub>: A density functional theory study, *J. Catal.***272**, 2 (2010), 227–234. DOI: 10.1016/j.jcat.2010.04.003.
- 87 Wang Y., Yan X., Xiao W., Shao Y. DFT Analysis of the Adsorption of Methyl Nitrate on Al<sub>2</sub>O<sub>3</sub> Surfaces, *Bull. Korean Chem. Soc.***38**, 6 (2017), 625–631. DOI: 10.1002/bkcs.11136.
- 88 Shukla M.K., Hill F. Computational Investigation of Adsorption of 2,4,6-Trinitrotoluene on (0001) Surface of (4  $\times$  4)  $\alpha$ -Alumina, *J. Phys. Chem. C***117**, 25 (2013), 13136–13142. DOI: 10.1021/jp403499p.
- 89 Kistamurthy D., Saib A.M., Moodley D.J., Preston H., Ciobîcă I.M., van Rensburg W.J., Niemantsverdriet J.W., Weststrate C.J. The role of carboxylic acid in cobalt Fischer-Tropsch synthesis catalyst deactivation, *Catal. Today***275** (2016), 127–134. DOI: 10.1016/j.cattod.2015.11.012.
- 90 Xu L., Hu Y., Dong F., Gao Z., Wu H., Wang Z. Anisotropic adsorption of oleate on diasporite and kaolinite crystals: Implications for their flotation separation, *Appl. Surf. Sci.***321** (2014), 331–338. DOI: 10.1016/j.apsusc.2014.10.042.
- 91 Heiden S., Usvyat D., Saalfeld P. Theoretical Surface Science Beyond Gradient-Corrected Density Functional Theory: Water at  $\alpha$ -Al<sub>2</sub>O<sub>3</sub> (0001) as a Case Study, *J. Phys. Chem. C***123**, 11 (2019), 6675–6684. DOI: 10.1021/acs.jpcc.9b00407.
- 92 Blanck S., Loehlé S., Steinmann S.N., Michel C. Adhesion of lubricant on aluminium through adsorption of additive head-groups on  $\gamma$ -alumina: A DFT study, *Tribol. Int.***145** (2020), 106140. DOI: 10.1016/j.triboint.2019.106140.
- 93 Kumar A., Ropital F., Bruin T. de, Diawara B. Effects of surface orientations of Cr<sub>2</sub>O<sub>3</sub> on CO<sub>2</sub> adsorption: A DFT approach, *Appl. Surf. Sci.***529** (2020), 147127. DOI: 10.1016/j.apsusc.2020.147127.
- 94 J. Matthew D Lane, K. Leung, A. P. Thompson, M. E. Cuneo Water Desorption from Rapidly-Heated Metal Oxide Surfaces - First Principles Molecular Dynamics and the Temkin Isotherm, *J. Phys.: Condens. Matter***30**, 46 (2018), 1–32. DOI: 10.1088/1361-648X/aae4af.
- 95 Zhang M., Huang Y., Li R., Li G., Yu Y. A DFT Study of Ethanol Adsorption and Dehydrogenation on Cu/Cr<sub>2</sub>O<sub>3</sub> Catalyst, *Catal Lett***144**, 11 (2014), 1978–1986. DOI: 10.1007/s10562-014-1356-8.
- 96 Huš M., Kopáč D., Likožar B. Kinetics of non-oxidative propane dehydrogenation on Cr<sub>2</sub>O<sub>3</sub> and the nature of catalyst deactivation from first-principles simulations, *J. Catal.***386** (2020), 126–138. DOI: 10.1016/j.jcat.2020.03.037.
- 97 Grimme S., Antony J., Ehrlich S., Krieg H. A consistent and accurate ab initio parametrization of density functional dispersion correction (DFT-D) for the 94 elements H-Pu, *J. Chem. Phys.***132**, 15 (2010), 154104. DOI: 10.1063/1.3382344.
- 98 Dabaghmanesh S., Neyts E.C., Partoens B. van der Waals density functionals applied to corundum-type sesquioxides: Bulk properties and adsorption of CH<sub>3</sub> and C<sub>6</sub>H<sub>6</sub> on (0001) surfaces, *Phys. Chem. Chem. Phys.***18**, 33 (2016), 23139–23146. DOI: 10.1039/c6cp00346j.
- 99 Chen C., Jiang X. Molecular dynamics simulation of soot formation during diesel combustion with oxygenated fuel addition, *Phys. Chem. Chem. Phys.***61** (2020), 113. DOI: 10.1039/D0CP01917H.
- 100 Qian Y., Yu L., Li Z., Zhang Y., Xu L., Zhou Q., Han D., Lu X. A new methodology for diesel surrogate fuel formulation: Bridging fuel fundamental properties and real engine combustion characteristics.
- 101 Cheng X.-M., Wang Q.-D., Li J.-Q., Wang J.-B., Li X.-Y. ReaxFF molecular dynamics simulations of oxidation of toluene at high temperatures, *J. Phys. Chem. A***116**, 40 (2012), 9811–9818. DOI: 10.1021/jp304040q.
- 102 Frisch M.J., Trucks G.W., Schlegel H.B., Scuseria G.E., Robb M.A., Cheeseman J.R., Montgomery, J. A., Jr., Vreven T., Kudin K.N., Burant J.C., Millam J.M., Iyengar S.S., Tomasi J., Barone V., Mennucci B., Cossi M., Scalmani G., Rega N., Petersson G.A., Nakatsuji H., Hada M., Ehara M., Toyota K., Fukuda R., Hasegawa J., Ishida M., Nakajima T., Honda Y., Kitao O., Nakai H., Klene M., Li X., Knox J.E., Hratchian H.P., Cross J.B., Bakken V., Adamo C., Jaramillo J., Gomperts R., Stratmann R.E., Yazyev O., Austin A.J., Cammi R., Pomelli C., Ochterski J.W., Ayala P.Y., Morokuma K., Voth G.A., Salvador P., Dannenberg J.J., Zakrzewski V.G., Dapprich S., Daniels A.D., Strain M.C., Farkas O., Malick D.K., Rabuck A.D., Raghavachari K., Foresman J.B., Ortiz J.V., Cui Q., Baboul A.G., Clifford S., Cioslowski J., Stefanov B.B., Liu G., Liashenko A., Piskorz P., Komaromi I., Martin R.L., Fox D.J., Keith T., Al-Laham M.A., Peng C.Y., Nanayakkara A., Challacombe

- M., Gill P.M.W., Johnson B., Chen W., Wong M.W., Gonzalez C., Pople J.A. *Gaussian 03, Revision C. 02*. Wallingford, CT: Gaussian (2004).
- 103 Chia C.-L., Avendaño C., Siperstein F.R., Filip S. Liquid Adsorption of Organic Compounds on Hematite  $\alpha$ -Fe<sub>2</sub>O<sub>3</sub> Using ReaxFF, *Langmuir* **33**, 42 (2017), 11257–11263. DOI: 10.1021/acs.langmuir.7b02374.
  - 104 Olsson C.-O., Landolt D. Passive films on stainless steels—chemistry, structure and growth, *Electrochimica Acta* **48**, 9 (2003), 1093–1104. DOI: 10.1016/S0013-4686(02)00841-1.
  - 105 Dwivedi D., Lepková K., Becker T. Carbon steel corrosion: A review of key surface properties and characterization methods, *RSC Adv.* **7**, 8 (2017), 4580–4610. DOI: 10.1039/C6RA25094G.
  - 106 Shin Y.K., Kwak H., Vasenkov A.V., Sengupta D., van Duin A.C. Development of a ReaxFF Reactive Force Field for Fe/Cr/O/S and Application to Oxidation of Butane over a Pyrite-Covered Cr<sub>2</sub>O<sub>3</sub> Catalyst, *ACS Catal.* **5**, 12 (2015), 7226–7236. DOI: 10.1021/acscatal.5b01766.
  - 107 Kim D S Tatibouet J-M Wachs I E Surface Structure and Reactivity of CrO<sub>3</sub>/SiO<sub>2</sub> Catalysts, *Journal of Catalysis* **136** (1992), 209–221.
  - 108 De Rossi S, Ferraris G, Fremiotti S, Cimino A, Indovina V Propane dehydrogenation on chromia/zirconia catalysts, *Applied Catalysis A: General* **81** (1992), 113–132.
  - 109 Chatterjee S, Greene H L, Park J Y Comparison of Modified Transition Metal-Exchanged Zeolite Catalysts for Oxidation of Chlorinated Hydrocarbons, *Journal of Catalysis* **138**, 179–194 (1992).
  - 110 Chen J D, Dakka J, Sheldon R A Selective decomposition of cyclohexyl hydroperoxide to cyclohexanone catalyzed by chromium aluminophosphate-5, *Applied Catalysis A: General* **108** (1994), L1–L6.
  - 111 Pradier C M, Rodrigues F, Marcus P, Landau M V, Kaliya M L, Gutman A, Herskowitz Supported chromia catalysts for oxidation of organic compounds: The state of chromia phase and catalytic performance, *Applied Catalysis B: Environmental* **27** (2000), 73–85.
  - 112 Tokarz-Sobieraj R., Witko M., Gryboś R. Reduction and re-oxidation of molybdena and vanadia: DFT cluster model studies, *Catalysis Today* **99**, 1–2 (2005), 241–253. DOI: 10.1016/j.cattod.2004.09.046.
  - 113 Soleymanibrojani M., Shi H., Liu F., Han E.-H. Atomistic simulations of Epoxy/Water/Aluminum systems using the ReaxFF method, *Comput. Mater. Sci.* **173** (2020), 109424. DOI: 10.1016/j.commatsci.2019.109424.
  - 114 Sengul M.Y., Randall C.A., van Duin A.C.T. ReaxFF molecular dynamics simulation of intermolecular structure formation in acetic acid-water mixtures at elevated temperatures and pressures, *J. Chem. Phys.* DOI: 10.1063/1.5025932.
  - 115 Sengul M.Y., Randall C.A., van Duin A.C.T. ReaxFF Molecular Dynamics Study on the Influence of Temperature on Adsorption, Desorption, and Decomposition at the Acetic Acid/Water/ZnO(10 $\bar{1}$ 0) Interface Enabling Cold Sintering, *ACS Appl. Mater. Interfaces* **10**, 43 (2018), 37717–37724. DOI: 10.1021/acsami.8b13630.
  - 116 Raymand D., van Duin A.C., Baudin M., Hermansson K. A reactive force field (ReaxFF) for zinc oxide, *Surface Science* **602**, 5 (2008), 1020–1031. DOI: 10.1016/j.susc.2007.12.023.
  - 117 Monti S., Corozzi A., Frstrup P., Joshi K.L., Shin Y.K., Oelschlaeger P., van Duin A.C.T., Barone V. Exploring the conformational and reactive dynamics of biomolecules in solution using an extended version of the glycine reactive force field, *Phys. Chem. Chem. Phys.* **15**, 36 (2013), 15062–15077. DOI: 10.1039/c3cp51931g.
  - 118 Moreira N.H., Dominguez A., Frauenheim T., Da Rosa A.L. On the stabilization mechanisms of organic functional groups on ZnO surfaces, *Physical chemistry chemical physics : PCCP* **14**, 44 (2012), 15445–15451. DOI: 10.1039/c2cp42435e.

## Chapter 2. Methodology

### 2.1 Introduction

To better understand the phenomenology related to the formation of deposits produced from the autoxidation process, it is paramount to identify which parameters and operating conditions can mostly impact on these deposits adhesion/precipitation process, especially concerning the case of metallic surfaces of the injection system since they are constantly in contact with the stored fuel.

This thesis consists in a multi-scale computational study of the biofuel/metal interaction. The idea behind a multi-scale approach is to decompose the whole system and relevant phenomena in multiple domains (e.g. metallic solid phase, oxide film layer, liquid-solid interface and the liquid bulk). In each of these domains, decomposition into factors operating at different length scales can be considered and described by various models. The integrated multi-scale model considers processes, such as autoxidation of molecules in solution, migration of the aggregates to the metal surface, the role of the surface in products oxidation and aggregates formation. To our knowledge, such an integrated approach applied to fuel-surface interaction is still to be done.

In a multi-scale approach, atomistic methods are expected to bring important insight and information that is not reachable by experiment.

Thus, atomistic DFT and FF methods are useful for the following studies: quantum calculations can be done to estimate deprotonation and solvation energies of molecules in fuel, and FF calculations can help estimate the tendency of molecules to form aggregates. FF MD calculations can bring insight into surface and interface tensions, diffusivity data of various species in liquid phases. First principles calculations associated with atomistic thermodynamics (that allows calculating Gibbs free energies) are useful to construct surface phase diagrams and to predict under given thermodynamic conditions surface termination and composition of the oxide film. DFT calculations are the major tool to model the reactions between molecules in liquid and on a given surface. From adsorption energies, completed with evaluation of vibrational and rotational energies, the Gibbs free energy of the molecule adsorption can be calculated.

However, DFT quantum-mechanical simulations may present a significant limitation in terms of computational time, in particular when the size of the chemical systems consists of more than 100-200 atoms. Another relevant factor that can surely impact on this aspect is the complexity of the systems where different chemical species are involved, since the predictions of their properties in addition to their interactions may slow down significantly DFT simulations.

One of the fundamental concepts of chemistry and materials science is undoubtedly the “bond breaking and forming”. The accurate modeling of bond-breaking processes continues to be a computational challenge, especially in the description of large molecules. Recent progresses on the implementation of unrestricted (spin-polarized) Kohn-Sham DFT allowed to account for homolytic bond breaking, making it possible the description of reactions occurring between molecules with unpaired electrons (i.e. free radicals). Since in this study we wanted to simulate the processes associated with the autoxidation of molecules, where very reactive species like radicals are formed, DFT spin-polarized calculations were required. However, DFT recent studies have been focused on heterolytic bond cleavage, as mentioned in the work of Kim et al. [69], where they overviewed the DFT major applications in the merits of iron-containing molecules of bioorganic interest.

Empirically parameterized reactive force fields based on bond-order concepts (like ReaxFF) that include the ability to model bond breaking have been developed in the last years. The reactive force fields include DFT results in training sets, which allow them to be parameterized in order to better model the molecules bond breaking occurring during a chemical process.

Therefore the methodology adopted for this thesis is based on the combination of these two different numerical approaches: an *ab initio* study conducted via Density Functional Theory (DFT) and a successive Molecular Dynamics (MD) approach carried out via the implementation of a reactive force field (ReaxFF). The preliminary theoretical DFT study will be carried out to acquire useful energetic data (i.e. reaction and adsorption energies) from the geometry optimization of gas-phase and gas/solid systems of interest with the intention to use them as input data to train the empirical force field to obtain a force field able to correctly predict the behavior of the chemical species involved, in both homogeneous and heterogeneous phases. Once validated the force field, the main objective is to obtain useful insights into the adsorption and

deposition processes while considering the degradation/oxidation phenomena occurring in the fuel liquid phase.

With this premise, this chapter first introduces the DFT quantum mechanical method, followed by the description of the molecular dynamics principles defining the ReaxFF method that was used for this thesis.

## 2.2 Quantum mechanics basics

As reported in the “*Schrödinger Equation*” paragraph of ref. [1], quantum mechanics describes the behavior of molecules in terms of interactions among nuclei and electrons and molecular geometry in terms of minimum energy of particles nuclei. All the quantum mechanical methods known so far are based on the resolution of the *Schrödinger equation*, of which below we report the particular case of the hydrogen atom as a single electron in three dimensions:

$$\left[ -\frac{1}{2} \nabla^2 - \frac{Z}{r} \right] \psi(\mathbf{r}) = E \psi(\mathbf{r})$$

Equation 11

Where the quantity in square brackets represents the kinetic and potential energy of an electron at a distance  $r$  from a nucleus of charge  $Z$  (1 for hydrogen). The terms  $E$  and  $\psi(\mathbf{r})$  respectively represent the electronic energy of the system and the wave function (in function of the electron coordinates  $\mathbf{r}$ ) describing the motion of the electrons.

The generalization of the Schrödinger equation for a multinuclear, thus multielectron system may be described with the following equation below:

$$\hat{H} \Psi = E \Psi$$

Equation 12

Where the  $\Psi$  is a many-electron wavefunction and  $\hat{H}$  is the so-called Hamiltonian operator (or more simply the Hamiltonian), which in the atomic units is given by the following expression:

$$\hat{H} = -\frac{1}{2} \sum_i^{electrons} \nabla_i^2 - \frac{1}{2} \sum_A^{nuclei} \frac{1}{M_A} \nabla_A^2 - \sum_i^{electrons} \sum_A^{nuclei} \frac{Z_A}{r_{iA}} + \sum_{i<j}^{electrons} \sum \frac{1}{r_{ij}} + \sum_{A<B}^{nuclei} \sum \frac{Z_A Z_B}{R_{AB}}$$

**Equation 13**

Where we define  $Z_A$  as the nuclear charge,  $M_A$  as the ratio of the mass of nucleus  $A$  to the mass of an electron,  $R_{AB}$  as the distance between nuclei  $A$  and  $B$ ,  $r_{ij}$  as the distance between electrons  $i$  and  $j$  and  $r_{iA}$  as the distance between electron  $i$  and nucleus  $A$ .

The many-electron Schrödinger equation cannot be solved exactly, not even in for a simple two-electron system such as the hydrogen molecule. Thus, numerical approximations need to be introduced to provide possible resolutions to this equation.

### 2.2.1 Born-Oppenheimer approximation

As reported in the homonymous paragraph of ref. [1], one way to simplify the Schrödinger equation for molecular systems is to assume that the electronic motion and the nuclear motion in molecules can be separated. This leads to a molecular wave function in terms of electron positions and nuclear positions and, as consequence, the Hamiltonian can be split into an electronic part and nuclei part. This statement is known as the *Born-Oppenheimer approximation* that defines an “electronic” Schrödinger equation:

$$\hat{H}^{el} \psi^{el} = E^{el} \psi^{el}$$

**Equation 14**

$$\hat{H}^{el} = -\frac{1}{2} \sum_i^{electrons} \nabla_i^2 - \sum_i^{electrons} \sum_A^{nuclei} \frac{Z_A}{r_{iA}} + \sum_{i<j}^{electrons} \sum \frac{1}{r_{ij}}$$

**Equation 15**

The term defining the nuclear kinetic energy in **Equation 13** is absent in the **Equation 15** above since it is zero, while the nuclear-nuclear Coulomb term present in **Equation 13** is a constant and needs to be added to the electronic energy  $E^{el}$  to define the total energy,  $E$ , for the system:

$$E = E^{el} + \sum_{A < B}^{nuclei} \sum \frac{Z_A Z_B}{Z_{AB}}$$

**Equation 16**

It should be noticed that the nuclear mass does not appear in the electronic Schrödinger equation; so that the Born-Oppenheimer approximation may be valid, the mass effects on molecular properties and chemical reactivities should be seen of different origins.

### 2.2.2 Hartree-Fock approximation

As mentioned in the homonymous paragraph of ref. [1], the electronic Schrödinger equation is still intractable and further approximations are required. According to the variational Hartree-Fock (HF) method, the wave functions of a many-body system are assumed to be in the form of a Slater determinant. The variational parameters of the method are the single-particle wave functions composing the many-body wave function. The simplest approximation is a single Slater determinant. The ground state energy might be poorly approximated if an arbitrary single-particle basis were chosen. The Hartree-Fock (HF) approximation enables one to determine the best—in the meaning of giving the lowest energy—set of single particle states that is optimized for each Hamiltonian and for a given number of particles. Since a single Slater determinant corresponds to non-interacting particles, the method is also called the “independent-particle model”. In practice, individual electrons are confined to functions known as molecular orbitals, each of which is determined by assuming that the electron is moving within an average field of all the other electrons. The set of molecular orbitals leading to the lowest energy are obtained by a process referred as a *self-consistent-field* or SCF procedure.

### 2.2.3 LCAO approximation

As stated in the homonymous paragraph of ref. [1], the Hartree-Fock approximation leads to a set of coupled differential equations (the Hartree-Fock equations), each involving the coordinates of

a single electron. While they may be solved numerically, it is advantageous to introduce an additional approximation to transform the Hartree-Fock equations into a set of algebraic equations.

Practically, the molecular orbitals are expressed as linear combinations of a finite set (a basis set) of prescribed functions known as basis functions  $\phi$ :

$$\Psi_i = \sum_{\mu}^{\text{basis functions}} c_{\mu i} \phi_{\mu}$$

**Equation 17**

Here we introduce  $c$  as the (unknown) molecular orbital coefficients, often referred to simply (and incorrectly) as the molecular orbitals. Because the localized basis functions are usually centered at the nuclear positions, they are referred to as atomic orbitals and the equation above is known as the *Linear Combination of Atomic Orbitals* (or *LCAO approximation*).

## 2.2.4 Correlated models

As described in homonymous paragraph of ref. [1], Hartree-Fock models treat the motions of individual electrons as independent of one another. To do this, they replace “instantaneous interactions” between single electrons by interactions between a particular electron and the average field created by all the other electrons. Because of this, electrons “get in each other way” to greater extent than they should, causing an overestimation of the electron-electron repulsion energy and to a too high total energy. Electron correlation, as it is defined, accounts for coupling or “correlation” of electron motions and leads to a lessening of the electron-electron repulsion energy (thus to a lowering of the total energy). The correlation energy is defined as the difference between the Hartree-Fock energy and the exact energy.

Among known correlated models, the density functional models introduce an “approximate” correlation term in an explicit manner. Although they offer the advantage to be less costly than Hartree-Fock models, the “quality” of density functional models strongly depends on the choice of the specific correlation term.

A detailed overview of the density functional model implemented in this thesis, known as *Density Functional Theory* (DFT), is proposed in the next following paragraph.

## 2.3 Density Functional Theory (DFT)

*Density Functional Theory* (DFT) is a computational quantum-mechanical modeling method widely used in both physics and chemistry to investigate the electronic (and magnetic) properties of the so-called “many-body systems”. Depending on the case, these quantum-mechanical systems can be identified either as atoms, molecules or ultimately as condensed phases. Particularly about the latter, DFT currently represents the most popular approach for the description of the electronic structure of solid materials since its ratio precision/CPU cost is relatively favorable with respect to other QM methods. Hence, it is largely used in scientific disciplines like condensed-matter physics, computational physics and computational chemistry.

### 2.3.1 Kohn-Sham formalism

As mentioned in the “*Kohn-Sham Equations and Density Functional Models*” paragraph of ref. [1], one approach to the treatment of electron correlation is referred to as *Density Functional Theory* (DFT). Density functional models are identified by the electron density,  $\rho(\mathbf{r})$ , as opposed to the many-electron wave function,  $\Psi(r_1, r_2, \dots)$ . There are both distinct similarities and distinct differences between traditional wave function-based approaches and electron-density-based approaches. First, the essential building blocks of a many-electron wavefunction are single-electron (molecular) orbitals, which are directly analogous to the orbitals used in density functional methodologies. Second, both the electron density and the many-electron wave function are constructed from an SCF approach which requires nearly identical matrix elements.

The density functional theory of Hohenberg, Kohn and Sham is based on the fact that the sum of the exchange and correlation energies of a uniform electron gas can be calculated exactly knowing only its density. In the Kohn-Sham formalism, the ground-state electronic energy,  $E$ , is

written as a sum of the kinetic energy,  $E_T$ , the electron-nuclear interaction energy,  $E_V$ , the Coulomb energy,  $E_J$ , and the exchange/correlation energy,  $E_{xc}$ .

$$E = E_T + E_V + E_J + E_{xc}$$

**Equation 18**

Except for  $E_T$ , all components depend on the total electron density,  $\rho(\mathbf{r})$ , defined as follows:

$$\rho(\mathbf{r}) = 2 \sum_i^{\text{orbitals}} |\Psi_i(\mathbf{r})|^2$$

**Equation 19**

Here,  $\Psi_i$  are the so-called Kohn-Sham orbitals and the summation is carried out over pairs of electrons. If we adopt an unrestricted format, the  $\alpha$  and  $\beta$  total electron densities can be written as:

$$\rho_\alpha(\mathbf{r}) = \sum_{i=1}^{n_\alpha} |\Psi_i^\alpha|^2$$

**Equation 20**

$$\rho_\beta(\mathbf{r}) = \sum_{i=1}^{n_\beta} |\Psi_i^\beta|^2$$

**Equation 21**

Where the  $n_\alpha$  and  $n_\beta$  are the number of  $\alpha$  and  $\beta$  electrons respectively and  $\Psi_i$  are the Kohn-Sham orbitals. Thus, the total electron density is:

$$\rho(\mathbf{r}) = \rho_\alpha(\mathbf{r}) + \rho_\beta(\mathbf{r})$$

**Equation 22**

The various energy components in **Equation 18** can now be written:

$$E_T = \sum_{i=1}^{n_\alpha} \langle \Psi_i^\alpha | -\frac{1}{2} \nabla^2 | \Psi_i^\alpha \rangle + \sum_{i=1}^{n_\beta} \langle \Psi_i^\beta | -\frac{1}{2} \nabla^2 | \Psi_i^\beta \rangle$$

Equation 23

$$E_V = \sum_{A=1}^M Z_A \int \frac{\rho(\mathbf{r})}{|\mathbf{r} - \mathbf{R}_A|} d(\mathbf{r})$$

Equation 24

$$E_J = \frac{1}{2} \langle \rho(\mathbf{r}_1) | \frac{1}{|\mathbf{r}_1 - \mathbf{r}_2|} | \rho(\mathbf{r}_2) \rangle$$

Equation 25

$$E_{xc} = \int f[\rho(\mathbf{r}), \nabla \rho(\mathbf{r}), \dots] \rho(\mathbf{r}) d\mathbf{r}$$

Equation 26

From the equations above we define  $Z$  as the nuclear charge,  $\mathbf{r} - \mathbf{R}_A$  as the distance between the nucleus and the electron,  $\mathbf{r}_1 - \mathbf{r}_2$  as the distance between two electrons defined by their corresponding electron densities  $\rho(\mathbf{r}_1)$  and  $\rho(\mathbf{r}_2)$ .

There are two types of exchange/correlation functionals that can be employed in the DFT:

- i. Functionals based on the *local density approximation* (LDA).
- ii. Functionals based on the *generalized gradient approximation* (GGA).

The first functional typology is referred as local density models, while the second category is referred to as semi non-local models or alternatively as gradient-corrected models.

### 2.3.2 Generalized Gradient Approximation (GGA)

An improvement to LDA *local density approximation* (or LDA) proposed by Parr and Yang [2] functionals can be made by considering the gradient of the electron density, the so-called

*generalized gradient approximation* (GGA). This exchange/correlation functional can be written as follows:

$$E_{xc}^{GGA} = E_{xc}[\rho(\mathbf{r}), \nabla\rho(\mathbf{r})]$$

**Equation 27**

There are several different parameterizations of the GGA functionals. Some of these are semi-empirical, where experimental data (e.g. atomization energies) are used in their derivation; however, other GGA parameterizations may be found entirely from first principles. Very commonly used GGA functionals nowadays are the PW91 (by Perdew and Wang) [3] and the PBE functionals (by Perdew, Burke and Ernzerhof) [4], the latter being used for the DFT calculations implemented in this thesis.

The GGA corrects the overbinding tendency inherent in the LDA, albeit with a certain tendency to overcorrect: lattice constants are on average underestimated in the LSDA by about 1%, PBE overestimates them by nearly the same amount [5]. However, it must also be pointed out that the GGA produces the correct ground state for magnetic transition metals where the LSDA fails quite badly: in the LSDA, Fe is predicted to be hexagonal close-packed and nonmagnetic instead of body-centered cubic and ferromagnetic [6], and body-centered cubic Cr is predicted to be nonmagnetic instead of antiferromagnetic. [7] For the adsorption energies of small molecules on solid surfaces, the values predicted by GGA are definitely superior to the LSDA results.

However, even if these GGA functionals work better than LDA, they still present an inaccuracy in terms of overestimation of bond lengths and on the evaluation of the intermolecular interactions like van der Waals forces and hydrogen bonds.

## 2.4 DFT calculations for periodic systems

In condensed matter physics, realistic systems are composed by  $\approx 10^{20}$  atoms in a cubic millimeter, thus we can easily imagine that this task could be impossible to treat by any numerical known method. However, at this scale systems are often made of repeating units (crystals), making systems be seen as periodic. For this reason, we can decide to numerically

describe these kinds of systems in two distinct ways: either through periodic boundary conditions or as isolated (saturated) cluster.

### 2.4.1 Bloch's Theorem

*Bloch's theorem* states that solutions to the Schrödinger equation in a periodic potential take the form of a plane wave modulated by a periodic function, which can be described as below:

$$\Psi(\mathbf{r}) = e^{i\mathbf{k}\cdot\mathbf{r}}u(\mathbf{r})$$

Equation 28

Where  $\mathbf{r}$  is position,  $\Psi$  is the wave function,  $u$  is the periodic function with the same periodicity as the crystal, the wave vector  $\mathbf{k}$  is the crystal momentum vector,  $e$  is the Euler's number,  $i$  is the imaginary unit. Functions of this form are known as *Bloch functions* or *Bloch states* and serve as a suitable basis for the wave functions or states of electrons in crystalline solids.

The description of electrons in terms of Bloch functions, termed *Bloch electrons* underlies the concept of the electronic band structures.

### 2.4.2 Pseudopotentials

As described in the homonymous paragraph of ref. [8], core electrons present inside atoms or molecules are not especially important in defining chemical bonding and other physical characteristics of materials; these properties are dominated by less tightly bound valence electrons. From the beginning of the development of plane-wave methods, it was clear that there could be great advantages in calculations that approximated the properties of core electrons in a way that could reduce the number of plane waves necessary in a calculation.

The most important approach to minimizing this limitation due to the core electrons is identified by the use of *pseudopotentials*. Theoretically, a pseudopotential replaces the electron density from a chosen set of core electrons with a smoothed density chosen to match various important physical properties of the true ion core. The properties of the core electrons are then fixed in this

approximate fashion in all subsequent calculations. This approach is known as the *frozen core approximation*.

A pseudopotential is developed by considering an isolated atom of one element, but the resulting pseudopotential can then be used reliably for calculations that place this atom in any chemical environment without further adjustment of the pseudopotential. This desirable property is referred to as the transferability of the pseudopotential.

Even though the pseudopotentials offer an important reduction of the number of plane waves for a certain calculation, it is also true that the more plane waves are included in a basis set for describing the wavefunction, the more accurate would be the wave function representation. In these calculations, the functions are discretized on numerical grids, meaning that plane waves with higher frequency (e.g. higher energy) require increasingly finer grid points to be described. However, with finer grid points comes a higher computational cost. For this reason, it is necessary to establish an energetic threshold value beyond which plane waves with higher energy would not be considered in these calculations. This threshold is defined as the cutoff energy.

The details of a particular pseudopotential define a minimum energy cutoff that should be used in calculations including atoms associated with that pseudopotential. The most widely used method of defining pseudopotentials is based on the work by Vanderbilt [9] and these are known as *ultrasoft pseudopotentials* (USPPs). As it is suggested by their name, these pseudopotentials require substantially lower cutoff energies than alternative approaches. However, another well-known frozen core approach which overcomes some of the USPPs is given by the *projector augmented-wave* (PAW) method, which was originally introduced by Blöchl [10] and later adapted for plane-wave calculations by Kresse and Joubert [11]. A major advantage of the PAW method (which is implemented in VASP) is that it is more suitable than USPPs for the description of materials with very strong magnetic moments (like for Fe and Cr atoms) or with atoms that have a large difference in electronegativity.

### 2.4.3 DFT+*U* method

In the last decades, DFT method has achieved a substantial progress for the investigation of the physical properties of various compounds. In fact, for the description of the properties related to

metals, semiconductors and insulators, density functionals like LSDA proved to provide a reliable variational description of the ground state of the electronic structure of the solid. However, difficulties have arisen when a conventional DFT-LSDA approach is applied to the treatment of the electronic structure of the material where some of the ions contain partly filled valence  $d$  or  $f$  shells. This issue especially surges in regards of the transitional metal oxides (like chromia), since DFT-LSDA approach predicts metallic ground states instead of experimentally observed insulating ones.

The origin of this failure is because DFT-LSDA is not able to adequately describe the strong Coulomb repulsion between  $3d$  electrons localized on metal ions. In addition to making incorrect predictions on the nature of the ground state of transition metals, the DFT-LSDA systematically underestimates their equilibrium lattice constants and overestimates binding energy. To overcome this issue, Dudarev et al. [12] coupled the DFT-LSDA with the unrestricted Hartree-Fock (UHF) approximation, which is known as the LSDA+ $U$  method and representing one of the mostly implemented in the DFT+ $U$  realm.

According to DFT+ $U$  theory, the interactions between electrons in states localized on the same atomic center (i.e. on-site interactions) are treated in an Hartree-Fock-like manner (where HF calculations contain exact exchange), while the remaining interactions are treated with DFT. In this way, the errors incurred by DFT largely due to the intra-atomic self-interaction error would be corrected by an HF description. In practice, the on-site interaction energy is evaluated with a parametrized Hamiltonian, whose parameters correspond to the average Coulomb and exchange interactions between electrons of the same angular momentum localized on the same atom. These parameters are designated as  $U_{I\ell}$  and  $J_{I\ell}$ , respectively, where  $I$  indicate the atomic center on which the electrons are localized and  $\ell$  denotes their angular momentum. The key to performing an accurate DFT+ $U$  calculation lies in selecting suitable values for these parameters.

#### 2.4.4 DFT-D dispersion corrections

Despite DFT currently represents the most widely used approach to describe the electronic structure and properties of materials, it is well-known that the correct description of systems in which dispersion forces are prominent still results in a major challenge. In fact, the contribution

of vdW forces is absent in commonly-used density functionals like both LDA and GGA, thus imposing a limitation on their study. For this reason, in the last decades many adjustments have been attempted in order to attain more insights and better descriptions on the major role of vdW and dispersion forces, one of them being represented by the DFT dispersion correction method created by Grimme et al. [13], known as the DFT-D method. This method can be expressed through the equation below:

$$E_{DFT-disp} = E_{KS-DFT} + E_{disp}$$

**Equation 29**

From Eq.28 we can see that the DFT-D dispersion method consists into the addition of a correction to the conventional Kohn-Sham DFT energy  $E_{KS-DFT}$  through the  $E_{disp}$  term which can be identified by the implemented vdW correction.

DFT-D method accounts for the missing dispersion energy in DFT that includes the proper description of non-covalent interactions that require the inclusion of long-term electron correlation effects, like for example the treatment of the weak London forces.

In the DFT-D2 method of Grimme [14], the correction term  $E_{disp}$  takes the form:

$$E_{disp} = -\frac{1}{2} \sum_{i=1}^{N_{at}} \sum_{j=1}^{N_{at}} \sum_L \left( \frac{C_{6ij}}{r_{ij,L}^6} f_{d,6}(r_{ij,L}) \right)$$

**Equation 30**

where the summations are over all atoms  $N_{at}$  and in calculations, the sum is truncated. The number indicates that  $i \neq j$  for  $L = 0$ ,  $C_{6ij}$  denotes the dispersion coefficient for the atom pair  $ij$ ,  $r_{ij,L}$  is the distance between atom  $i$  located in the reference cell  $L=0$  and atom  $j$  in the cell  $L$  and the term  $f(r_{ij})$  is a damping function whose role is to scale the force field such as to minimize the contributions from interactions within typical bonding distances. In practice, the terms in the equation for  $E_{disp}$  corresponding to interactions over distances longer than a certain suitably chosen cutoff radius contribute only negligibly to  $E_{disp}$  and can be ignored. Parameters  $C_{6ij}$  and  $R_{0ij}$  are computed using the following combination rules:

$$C_{6ij} = \sqrt{C_{6ii}C_{6jj}}$$

**Equation 31**

and

$$R_{0ij} = R_{0i} + R_{0j}$$

**Equation 32**

The values for  $C_{6ij}$  and  $R_{0ij}$  are tabulated for each element and are insensitive to the particular chemical situation. In the original method described by Grimme et al. [14], a Fermi-type damping function is used:

$$f_{d,6}(r_{ij}) = \frac{s_6}{1 + e^{-d(\frac{r_{ij}}{s_R R_{0ij}} - 1)}}$$

**Equation 33**

whereby the global parameter  $s_6$  has been optimized for several different DFT functionals. The  $s_R$  is usually fixed at 1.

For the DFT-D3 method of Grimme [13], the following vdW energy expression is used instead:

$$E_{disp} = -\frac{1}{2} \sum_{i=1}^{N_{at}} \sum_{j=1}^{N_{at}} \sum_L \left( f_{d,6}(r_{ij,L}) \frac{C_{6ij}}{r_{ij,L}^6} + f_{d,8}(r_{ij,L}) \frac{C_{8ij}}{r_{ij,L}^8} \right)$$

**Equation 34**

Unlike in the method DFT-D2 reported in previous **Equation 30**, this time the dispersion coefficients  $C_{6ij}$  are geometry-dependent as they are adjusted on the basis of local geometry (coordination number) around atoms  $i$  and  $j$ . In the zero damping DFT-D3 method, the damping function is expressed as follows:

$$f_{d,n}(r_{ij}) = \frac{s_n}{1 + 6 \left( \frac{r_{ij}}{s_{R,n} R_{0ij}} \right)^{-\alpha_n}}$$

**Equation 35**

where  $R_{0ij} = \sqrt{\frac{c_{8ij}}{c_{6ij}}}$ , the parameters  $\alpha_6$ ,  $\alpha_8$ ,  $s_{R,s}$ ,  $s_6$  are fixed at values of 14, 16, 1 and 1 respectively, and  $s_8$  and  $s_{R,6}$  are adjustable parameters whose values depend on the choice of exchange-correlation functional.

For this thesis, we chose to employ the zero damping DFT-D3 of Grimme [13] reported in **Equation 34-Equation 35**.

### 2.4.5 DFT calculation of the total electron energy

The most basic type of DFT calculation is to compute the total energy of a set of atoms at prescribed positions in space. The main aim of a DFT calculation is to find the electron density that corresponds to the ground state configuration of the system,  $\rho(\mathbf{r})$ . Below we introduce an alternative form of the electron density and of the Kohn-Sham formalism (§2.3.1), defining the first in terms of the solutions to the latter as follows:

$$\rho(\mathbf{r}) = \sum_j \psi_j(\mathbf{r})\psi_j^*(\mathbf{r})$$

**Equation 36**

The Kohn-Sham equations being:

$$-\frac{\hbar^2}{2m}\nabla^2\psi_j(\mathbf{r}) + v^{eff}(\mathbf{r})\psi_j(\mathbf{r}) = \epsilon_j\psi_j(\mathbf{r})$$

**Equation 37**

The fact that makes these equations difficult to solve directly is that the effective potential is itself a complicated function of  $\rho(\mathbf{r})$ . Therefore, a commonly-used general strategy for solving this problem would be the attempt to solve it iteratively. We start this iterative process by estimating the overall electron density, then use this trial density to define the effective potential. The Kohn-Sham equations with this effective potential are then solved numerically with this effective potential, defining a new electron density. If the new electron density and the old electron density do not match, then we have not solved the overall problem. The old and new

electron densities are then combined in some way to give a new trial electron density. This new trial density is then used to define a new effective potential from which an updated electron density is found, and so on. If successful, this iterative process will lead to a self-consistent solution. However, we need to think about how to start our iterative process; in fact, in absence of other information, the electron density can be initially approximated by superimposing the electron densities appropriate for each atom in its isolated state. This is typically the default initialization used in most DFT packages. If a better initial approximation is available, a self-consistent solution should be reached more quickly (i.e. in fewer iterations).

Another important aspect of this iterative procedure is to understand how we stop it. However, it is not always convenient to directly compare two solutions for the electron density and determine their similarity, even though this may represent the most direct way to find out if a self-consistent solution is reached. In fact, a method that is easier to interpret is to calculate the energy corresponding to the electron density after each iteration. After all, this coincides precisely with the quantity which we are interested in finding. If our iterations are converging, then the difference in energy between consecutive iterates will approach to zero. This suggests that the iterations can be stopped once the magnitude of the energy difference between iterates falls below an appropriately chosen tolerance parameter.

### **2.4.6 Geometry optimization of molecular structures**

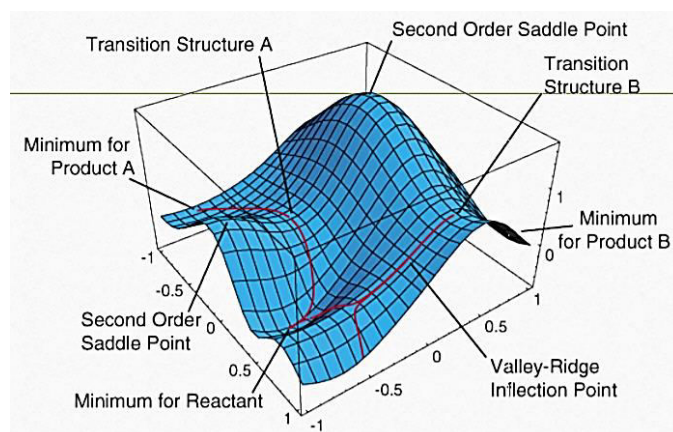
In the field of computational chemistry, energy minimization represents the process of finding an arrangement in space of a collection of atoms where, according to the implemented QM computational model, the net interatomic force on each atom is acceptably close to zero and the position on the potential energy surface (PES) is a stationary point. The collection of atoms may be identified by a single molecule, a condensed phase, a transition state or even a collection of any of these.

The motivation for performing a geometry optimization is the physical significance of the obtained structure; in fact, optimized structures often correspond to a substance as it is found in nature and the geometry of such a structure can be used in a variety of experimental and

theoretical investigation in the fields of chemical structure, thermodynamics, chemical kinetics, spectroscopy and others.

Typically, the process seeks to find the geometry of a particular arrangement of the atoms that represents a local or global energy minimum. Instead of searching for global energy minimum, it might be desirable to optimize to a transition state.

The principal terms describing a PES are: the gradient, which represents the first derivative of the energy with the respect to geometry ( $x,y,z$ ), in particular the negative of the gradient is termed the force; the stationary points, which identify the points on the PES where the force is zero, corresponding to maxima, minima, transition states (corresponding to first order saddle points) and higher order saddle points.



**Figure 20 : 3D scheme of features of Potential Energy Surface (PES) [70].**

In order to distinguish among the latter, one must examine the second derivatives of the PES with respect to geometry. The matrix of the second derivatives is termed a Hessian (or force constant) matrix. The diagonalization of this matrix yields eigenvectors which are normal modes of vibration; their eigenvalues are proportional to the square of the vibrational frequency (from which IR spectra can be derived).

Through the sign of the second derivative, it is possible to distinguish between the maxima and minima on the PES; minima on the PES have only positive eigenvalues (vibrational frequencies), while maxima or saddle points (i.e. maximum in one direction and minimum in the other direction) have one or more negative (imaginary) frequencies.

From a mathematical point of view, the geometry of a set of atoms or molecules can be described by Cartesian coordinates of the atoms or *internal coordinates* formed from a set of bond lengths, bond angles and dihedral angles. Given a set of atoms and a vector  $\mathbf{r}$  describing the atoms positions, one can introduce the concept of the energy as a function of the positions,  $E(\mathbf{r})$ .

Geometry optimization is then a mathematical optimization problem, in which it is desired to find the value of  $\mathbf{r}$  for which  $E(\mathbf{r})$  is at a local minimum, that is, the derivative of the energy with the respect to the position of the atoms,  $\frac{\partial E}{\partial \mathbf{r}}$ , is the zero vector.

The computational model that provides an approximate  $E(\mathbf{r})$  could be based on quantum-mechanics (like DFT or semi-empirical methods), force fields or a combination of both in case of QM/MM models.

Some methods such as quantum-mechanics methods can be used to calculate the energy,  $E(\mathbf{r})$ , the gradient of the PES, that is, the derivative of the energy with the respect to the position of the atoms,  $\frac{\partial E}{\partial \mathbf{r}}$ . An optimization algorithm can use some or all of  $E(\mathbf{r})$ ,  $\frac{\partial E}{\partial \mathbf{r}}$  and  $\frac{\partial^2 E}{\partial r_i \partial r_j}$  to try to minimize the forces and this could in theory be any method, such as gradient descent, conjugate gradient or Newton's method.

### 2.4.7 Nudged Elastic Band method

The Nudged Elastic Band (NEB) [15] is an efficient method for finding the minimum energy path (MEP) for a transition between a given initial and final states[16]. This method has been used both in conjunction with electronic structure calculations (in particular plane wave based DFT calculations [17, 18] and in combination with empirical potentials [19, 20]).

The MEP is found by constructing a set of images (replicas) of the system, typically on the order of 4-20, between the initial and final images. A spring interaction between adjacent images is added to ensure that images are held equidistant, thus mimicking an elastic band.

Practically, the NEB method is implemented for finding saddle points and minimum energy paths between known reactants and products. The NEB method works by optimizing a number of intermediate images along the reaction path. Each image finds the lowest energy possible while

maintaining equal spacing to neighboring images. This method is implemented in the VASP package [5].

## 2.5 Relative energy calculations

Within our DFT simulations, we used the Vienna Ab initio Simulation Package (VASP 5.4.1) and calculated the adsorption energy ( $\Delta E_{ads}$ ) according to the following equation:

$$\Delta E_{ads} = E_{molecule+slab} - E_{slab} - E_{molecule}$$

Equation 38

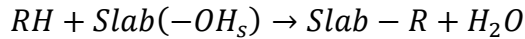
Where  $E_{molecule+slab}$  represents the total energy of the optimized structure formed after the molecule is (chemically) absorbed on the oxide slab and  $E_{molecule}$  and  $E_{slab}$  are the total energies of the non-interacting molecule and the slab, respectively.

Furthermore, the adsorption energy was decomposed in two contributions: the  $E_{ads}^{vdW}$  energy resulting from the dispersion interactions (as calculated using Grimme's zero damping DFT-D3 method [13]), and the "pure" DFT energy ( $E_{ads}^{DFT}$ ), corresponding to DFT total energy computed using a given exchange-correlation functional as defined in **Equation 39** below :

$$\Delta E_{ads}^{DFT} = \Delta E_{ads} - \Delta E_{ads}^{vdW}$$

Equation 39

In this thesis, we also considered the case study where an adsorbate species  $RH$  is substituted with a water molecule  $H_2O$ , as defined below:



Equation 40

Where  $(-OH_s)$  represents a hydroxyl group of the hydroxylated surface that picks up the proton from the adsorbate in the exchange reaction. The substitution energy was calculated as:

$$\Delta E_{subst}(RH) = E_{slab-R} - E_{RH} - E_{slab(-OH_s)} + E_{H2O}$$

**Equation 41**

It is to be noticed that the absolute and relative electronic energies do not take into temperature effects nor entropies. Such thermodynamic corrections can be calculated using statistical mechanics and more particularly the partition functions, which will be described in the next paragraph.

## 2.6 Thermodynamic calculations

The calculated energy mentioned in the previous paragraph are considered for systems at 0 K. However, we are usually interested in the study of molecular systems which undergo physical or chemical processes at different temperature than 0 K, thus it is essential to consider standard thermodynamic relationships in order to provide the necessary connections:

$$\Delta G = \Delta H - T\Delta S$$

**Equation 42**

$$\Delta H = \Delta U + P\Delta V$$

**Equation 43**

Where  $G$  is the free energy,  $H$  is the enthalpy,  $S$  is the entropy,  $U$  is the internal energy and  $T$ ,  $P$  and  $V$  are the temperature, pressure and volume, respectively. The absolute entropy may be written as a sum of multiple terms as follows:

$$S = S_{tr} + S_{rot} + S_{vib} + S_{el} - nR[\ln(nN_0) - 1]$$

**Equation 44**

$$S_{tr} = nR \left\{ \frac{3}{2} + \ln \left[ \left( \frac{2\pi mkT}{h^2} \right)^{3/2} \left( \frac{nRT}{P} \right) \right] \right\}$$

**Equation 45**

$$S_{rot} = nR \left\{ \frac{3}{2} + \ln \left[ \frac{(\pi v_A v_B v_C)^{1/2}}{s} \right] \right\} (\text{valid for non linear molecules})$$

**Equation 46**

$$S_{vib} = nR \sum_i \left\{ (u_i e^{u_i} - 1)^{-1} - \ln(1 - e^{-u_i}) \right\}$$

**Equation 47**

$$S_{el} = nR \ln(\omega_{el})$$

**Equation 48**

Where

$$v_A = \frac{h^2}{8\pi I_A kT}; v_B = \frac{h^2}{8\pi I_B kT}; v_C = \frac{h^2}{8\pi I_C kT}$$

**Equation 49**

$$\mu_i = \frac{h v_i}{kT}$$

**Equation 50**

$n$  is the number of moles,  $M$  is the molecular mass,  $I_A, I_B, I_C$  are the principal moments of inertia,  $s$  is the rotational symmetry number,  $v_i$  are the vibrational frequencies and  $\omega_{el}$  is the degeneracy of the electronic ground state.  $R, k$  and  $h$  are the gas constant, Boltzmann's constant and Planck's constant respectively, and  $N_0$  is the Avogadro's number.

Molecular structure enters the rotational entropy component and vibrational frequencies into the vibrational entropy component.

In case our system is at a finite temperature, we must adopt a correction for the expression of the enthalpy to change it from 0 K at the aforementioned finite  $T$ , given by:

$$\Delta H(T) = H_{trans}(T) + H_{rot}(T) + \Delta H_{vib}(T) + RT$$

**Equation 51**

$$H_{trans}(T) = \frac{3}{2} RT$$

**Equation 52**

$$H_{rot}(T) = \frac{3}{2}RT \text{ (valid for non linear molecules)}$$

**Equation 53**

$$\Delta H_{vib}(T) = H_{vib}(T) - H_{vib}(0) = Nh \sum_i^{normal\ modes} \frac{v_i}{(e^{hv_i/kT} - 1)}$$

**Equation 54**

Where the residual vibrational energy of a molecule at 0 K is given by:

$$H_{vib}(0) = \varepsilon_{zero-point} = \frac{1}{2}h \sum_i^{normal\ modes} v_i$$

**Equation 55**

Which is also known as the “Zero Point Energy” or ZPE.

On the basis of the adsorption energies calculated according to **Equation 38**, we may estimate the desorption temperatures for each adsorbed species as the temperature where  $\Delta G_{ads} = 0$  or  $\Delta H_{ads} = T\Delta S_{ads}$ . Assuming that  $\Delta H_{ads} \approx \Delta E_{ads}$  and that the loss in entropy upon adsorption is solely due to the complete loss of translational and rotational entropy, while  $\Delta S_{vib} = 0$ , the desorption temperature equals to:

$$T_{desorb} = \frac{\Delta E_{ads}}{S_{trans} + S_{rot}}$$

**Equation 56**

Where  $S_{trans}$  and  $S_{rot}$  are respectively the translational and rotational entropy contribution of the adsorbate in the gas phase. These entropic contributions were calculated at  $T = 298$  K and  $P = 1$  atm at the B3LYP/6-311G(d,p) level with Gaussian 16 [21].

## 2.7 Implemented QM based softwares

Modern electronic structure methods fall into two broad classes, depending on the choice of the basis set for the expansion of the valence orbitals, charge densities and potentials: plane-wave methods (e.g. VASP [22, 23]) or methods using some kind of localized basis functions (e.g. Gaussian 16 [21]).

The Vienna Ab initio Simulation Package (VASP) developed by Kresse et al. [22, 23] is a plane-wave code for ab initio density functional calculations. It attempts to match the accuracy of the most advanced all-electron codes by using a projector-augmented-wave approach (PAW [10]) for describing the electron-ion interaction. A stable and accurate solution of the Kohn-Sham equations, as well as a favorable scaling of the computational effort with system size, are achieved by adopting iterative diagonalization techniques. This code uses fast iterative techniques for the diagonalization of the DFT Hamiltonian and allows to perform total-energy calculations and structural optimization for systems with thousands of atoms. In VASP the following GGA functionals are implemented: the PW91 proposed by Perdew et al. [3], the Perdew-Burke-Ernzerhof (PBE) [4] functional (which was implemented in the DFT calculations of this thesis), its revised form proposed by Hansen et al. (RPBE) [24] and the functional proposed by Armiento and Mattson (AM05) [25].

The Gaussian 16 [21] is a quantum-mechanical computational software package that is mostly used for the predictions of the energies, molecular structures, vibrational frequencies and molecular properties of compounds and reactions in a wide variety of chemical environments. This software offers a wide range of methods for modeling compounds and chemical processes, including the DFT method.

In the framework of this thesis, we chose to implement VASP for the obtention of the optimized molecular structures (since our heterogeneous systems counted more than 500 atoms), while we preferred to implement Gaussian 16 for the acquisition of the thermodynamic data obtained for each one of the examined adsorbed species on the basis of the substrate (i.e. dry or fully-hydroxylated alumina/chromia surfaces).

## 2.8 Bader charge calculation

In this thesis, charge analyses were implemented through the Bader's charge analysis program, developed by the research Henkelman group [26]. This program (which reads electronic density reported in the VASP CHGCAR file) consists into an intuitive way of dividing molecules into atoms through the identification of an atom based purely on the electronic charge density. Bader's charge analysis uses what are called zero flux surfaces to divide atoms. A zero-flux surface is a 2-D surface on which the charge density is a minimum perpendicular to the surface. Typically, in molecular systems the charge density reaches a minimum between atoms and this is a natural place to separate atoms from each other.

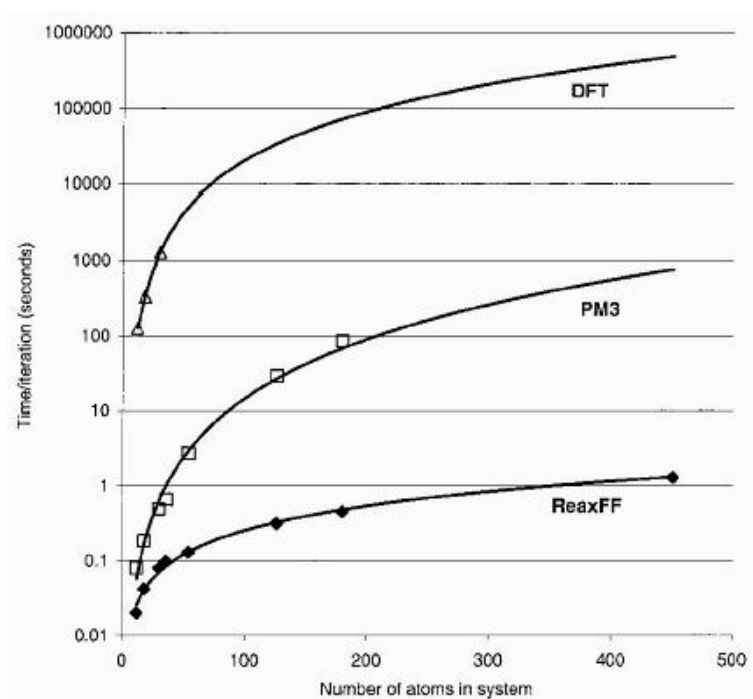
Bader's definition is often useful for charge analysis and it was used in this thesis. For this method, the charge enclosed within the Bader volume is a good approximation to the total electronic charge of an atom. The charge distribution can be used to determine multipole moments of interacting atoms or molecules.

## 2.9 From ab-initio to empirical molecular dynamics

Simulations methods based on quantum-mechanics have proven to be particularly relevant to explore structural material properties and in recent years they have been used for this means mostly as theoretical guide and screening tool [27–29].

From **Figure 21** it is noticed that indeed quantum-mechanical (QM) calculations performed via DFT are the slowest compared to semi-empirical methods (e.g. PM3) and empirical in spite being the most accurate in the description of geometries, energies and vibrational energies for characterized systems.

Furthermore, the empirical MD method provides a means to explore the phase space of a system without *a priori* knowledge of the phase diagram of the given system, thus making it a powerful low-CPU-cost tool when searching for novel system properties.



**Figure 21 : Comparison in terms of computational methods at increasing atoms number. Figure taken from Ref. [30]**

Specifically about empirical MD approaches, force-fields refer to the functional form and parameter sets used to calculate the potential energy of a system of interacting atoms; eventually the parameters of the energy functions may be derived from physical or chemical experiments or, like for the case of this thesis, from QM calculations.

## 2.10 Force field (FF) methods

As already mentioned, quite often the spatial and/or time scales needed are prohibitively expensive for ab initio MD (AIMD) simulations and in these cases we are obliged to use a higher level of approximation and make recourse to empirical force fields (FF) based methods. These methods allow to simulate systems containing hundreds of thousands of atoms during times of several nanoseconds.

Although the empirical force field present conspicuous advantages in terms of affordable sizes and time scales compared to the AIMD simulations, their implementation show some intrinsic limitations that are not negligible. In particular, they cannot provide any information about the electronic structure and they are unable to handle reactions such as the breaking and formation of bonds, electron excitations, charge transfers, etc.

In the last years, several specialized groups have started working actively in developing new methods to overcome some of the limitations of the empirical force fields, a good example being the development of the reactive force field (ReaxFF).

## **2.11 ReaxFF (Reactive Force Field) methods**

The reactive Force Field (ReaxFF) method developed by van Duin et al. [30] represents a new generation force field for modeling reactive chemical systems. The dynamic chemical bonds in a reactive system are modeled based on a the physically intuitive concept of bond order of a chemical bond. By making each atomic interaction bond order dependent, it can be possible to attain a dynamic description of each atomic and molecular interaction; to do so, a detailed parameterization of the atomic, bonding, angle and torsion properties of each particle and interaction within the system against quantum mechanical and experimental data is necessary. In this way, the implementation of ReaxFF allows to obtain a highly accurate, reactive and dynamic model of atomic systems that can be in the order of hundreds of thousands particles and timescales on the order of nanoseconds; this features acts as discriminator between ReaxFF and DFT methods because simulating so large systems would be computationally impractical or even impossible by using QM methods[31]. ReaxFF allows to describe non-reactive interactions between all atoms of the given system, thanks to the integration of Coulomb and Morse (van der Waals) potentials.

Furthermore, ReaxFF enables simulations involving reactive events at the interface between solid, liquid and gas phases [32] and this aspect is crucial for this thesis, since the interactions occurring at the liquid/solid interface are to be explored in depth in this study.

The description of the bond-order formalism that ReaxFF uses to describe each atomic interaction occurring within the system through the calculation of the forces acting on each atom, can be derived from the energy expression given in the following equation:

$$E_{system} = E_{bond} + E_{angle} + E_{lp} + E_{over} + E_{under} + E_{val} + E_{tors} + E_{vdW} + E_{Coulomb}$$

Equation 57

In this empirical many-body description of energy  $E_{bond}$ ,  $E_{angle}$  and  $E_{tors}$  are bond, angular and torsional energy terms, respectively. The terms  $E_{vdW}$ ,  $E_{Coulomb}$  are the two-body van der Waals and Coulombic contributions that are calculated for all pairs, regardless of their connectivity. The terms  $E_{over}$  and  $E_{under}$  contain the energy penalties for over or under- coordination of atoms, while the terms  $E_{lp}$  and  $E_{val}$  define the contributions of lone-pair and valence angle energies, respectively. [30, 33, 34] The general scheme of how each computational iteration is performed during the ReaxFF simulation is illustrated in the scheme reported below:

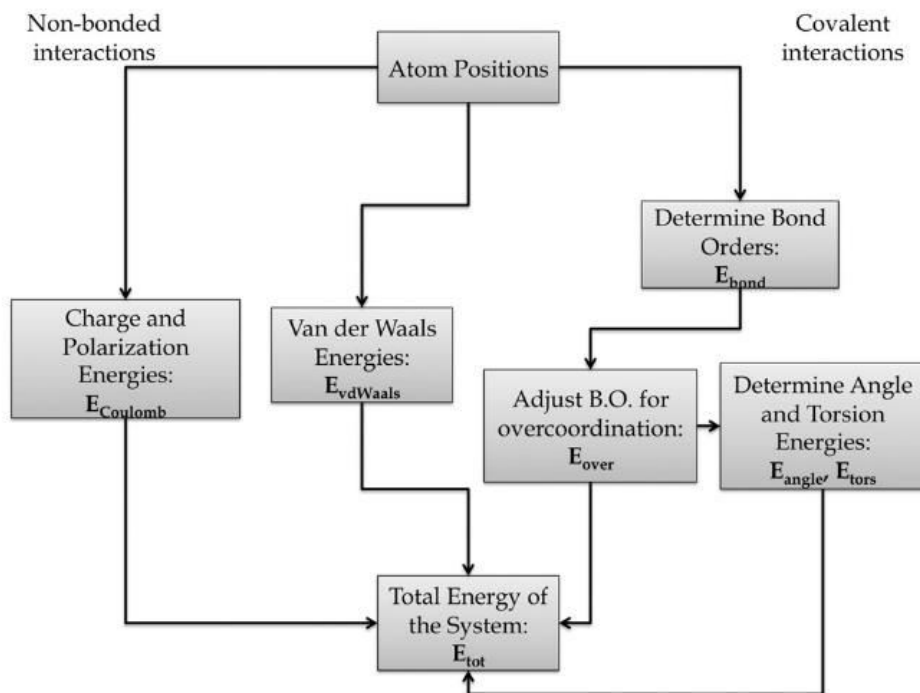


Figure 22: schematic of the ReaxFF iteration. The non-bonded interactions are on the left and the covalent/bonded interactions are on the right. Figure taken from Ref. [31]

As depicted in **Figure 22**, the potential is divided into bond-order-dependent and independent contributions.

A fundamental assumption of ReaxFF is that bond order (BO) between a pair of atoms can be obtained directly from the interatomic distance as given by **Equation 58**. In calculating the bond orders, ReaxFF distinguishes between contributions from sigma bonds, pi-bonds and double pi-bonds.

$$BO'_{ij} = BO_{ij}^{\sigma} + BO_{ij}^{\pi} + BO_{ij}^{\pi\pi}$$

$$= \exp \left[ p_{bo,1} * \left( \frac{r_{ij}}{r_0^{\sigma}} \right)^{p_{bo,2}} \right] + \exp \left[ p_{bo,3} * \left( \frac{r_{ij}}{r_0^{\pi}} \right)^{p_{bo,4}} \right] + \exp \left[ p_{bo,5} * \left( \frac{r_{ij}}{r_0^{\pi\pi}} \right)^{p_{bo,6}} \right]$$

**Equation 58**

The term  $BO'_{ij}$  is the bond order between atoms  $i$  and  $j$ ,  $r_{ij}$  is their interatomic distance,  $r_0$  terms are equilibrium bond lengths and  $p_{bo}$  terms are empirical parameters.

The “bo” subscript in the  $p_{bo}$  terms stands for “bond order” and these empirical parameters are necessary in order to obtain the “corrected” bond orders ( $BO_{ij}$ ) from the “uncorrected” bond order term  $BO'_{ij}$  as defined in **Equation 58**. From these empirical parameters, it is possible to calculate the corrected  $BO_{ij}^{\sigma}$ ,  $BO_{ij}^{\pi}$  and  $BO_{ij}^{\pi\pi}$  defining the  $\sigma$ ,  $\pi$  and  $\pi\pi$  bonds (**Equation 58**) that are consequently implemented to calculate all the energetic terms defined in **Equation 57**.

### 2.11.1 ReaxFF parametrization

In the recent years, many research works that envisaged the use and development of ReaxFF provided new ReaxFF parameter sets for a large number of elements of the periodic table [30, 35–39], as we can see from **Figure 23**.

Although a ReaxFF description exists for these elements, it is also true that one cannot simply use these parameter sets in any combination and expect to obtain a satisfactory transferability.

To better comprehend the concept of ReaxFF transferability, we will briefly introduce an overview of ReaxFF parameterization and development branches.

H																	He
Li	Be											B	C	N	O	F	Ne
Na	Mg											Al	Si	P	S	Cl	Ar
K	Ca	Sc	Ti	V	Cr	Mn	Fe	Co	Ni	Cu	Zn	Ga	Ge	As	Se	Br	Kr
Rb	Sr	Y	Zr	Nb	Mo	Tc	Ru	Rh	Pd	Ag	Cd	In	Sn	Sb	Te	I	Xe
Cs	Ba	* Lu	Hf	Ta	W	Re	Os	Ir	Pt	Au	Hg	Tl	Pb	Bi	Po	At	Rn
Fr	Ra	** Lr	Rf	Db	Sg	Bh	Hs	Mt	Ds	Rg	* La, Ce, Pr-Yb ** Ac-No						

**Figure 23: Elements currently described in available parameter sets. Image taken from ref. [32]**

Firstly, we should precise that there are currently two major groupings (i.e. ReaxFF branches) of parameter sets that are intra-transferable with one another: (1) the combustion branch and (2) the aqueous branch. To explain the existence of branches within a common functional form, we must consider that ReaxFF does not employ atom typing strategy, in contrast to popular non-reactive force-fields like AMBER [40] and CHARMM [41].

For example, there is only one oxygen type in ReaxFF regardless of the chemical environment in which the oxygen atom finds itself. On one hand, this feature is quite helpful because it allows atoms to migrate between phases during a simulation. On the other hand, this results in a significantly more complex force-field development process. The lack of transferability between branches is evident in the performance of the 2008-C/H/O combustion force field developed by Chenoweth et al. [35], which accurately describes water as a gas-phase molecule yet fails to describe water as a liquid. This happens because, during the development at that time, describing liquid water was not a particular aim for ReaxFF and, since all intended applications were at temperatures well above the water boiling point, this was not a major development concern. In 2009, efforts were initiated to redevelop ReaxFF for aqueous chemistry and it became clear that the 2008-C/H/O combustion force field, which at that time was extended to a significant range of metal oxide (Me = V/Bi/Mo/Nb/Si) materials and catalysts [42–44] could not be parametrized to the liquid water without changing general-ReaxFF and atomic-specific parameters. As such, the decision was made to initiate a new branch (e.g. the aqueous branch) that employs the same

functional form of the 2008-C/H/O description, but with different O/H atom and bond parameters.

This resulted in the creation of a number of parameter sets that are not directly transferable with those on the pre-existing combustion branches, thus leading to the new aqueous branch.

Parameter sets on the same development branch can be directly combined, where the required force-field fitting consists only of parameterizing bond and angular terms between newly combined elements. Transferring parameters between branches, however, requires more extensive refitting.

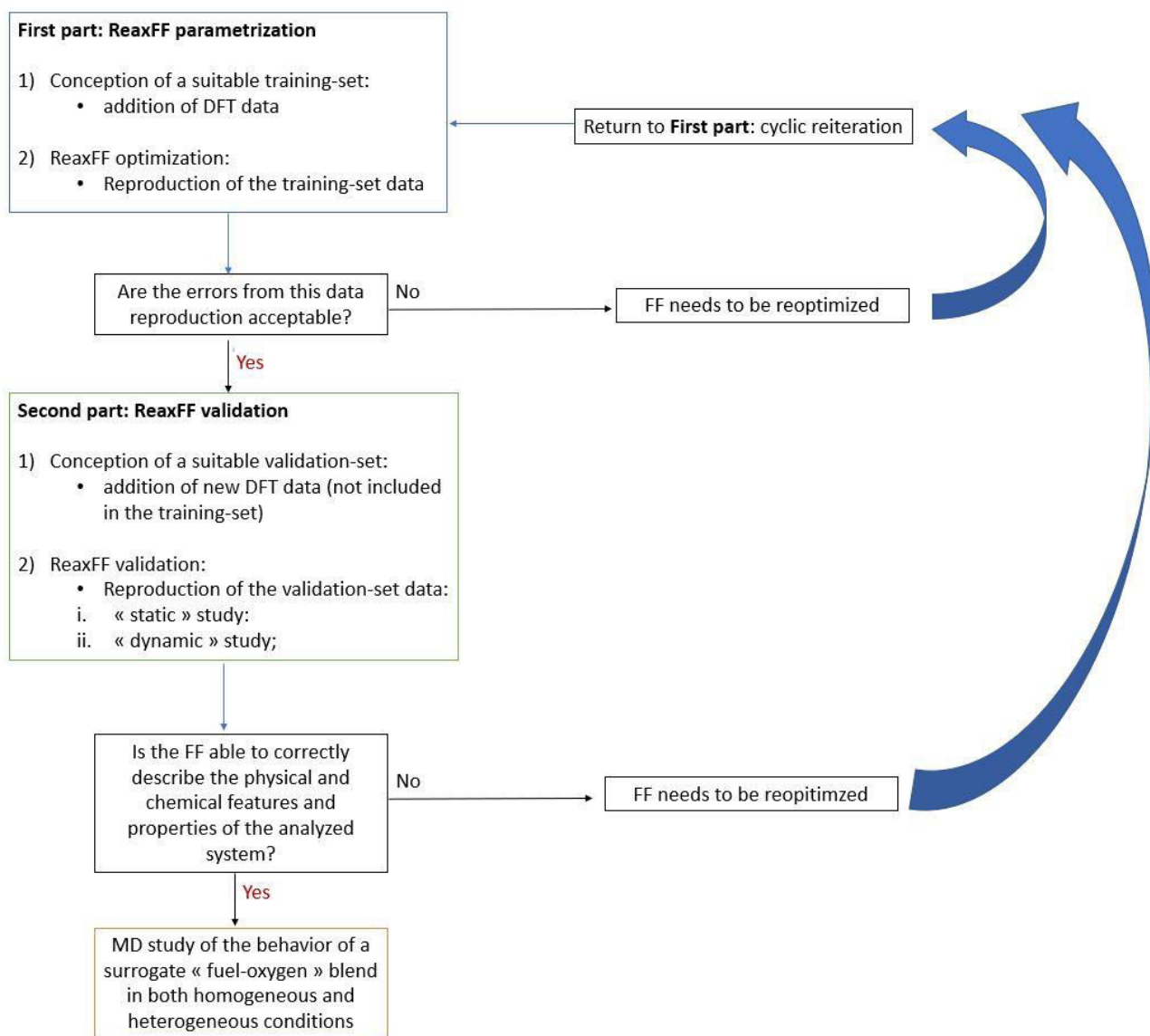
We can then conclude that, given the difficulty to have a reparametrized force field able to reproduce the description of different molecular systems (even when sharing similar atomic compositions) it emerges the necessity to reparametrize a suitable reactive force field in order to reach an accurate representation of the physics and chemistry of a molecular system of interest.

In the framework of this thesis, our main interest falls in finding a way to correctly describe the interface interactions between a liquid organic phase and a solid phase represented by aluminium and stainless steel materials. We acknowledge a certain difficulty in this scope since in literature the number of available force field that can describe aluminum and chromium-based systems is still very limited [45–49].

For this reason, we chose to use the DFT results obtained from the preliminary theoretical study as input data to parametrize ReaxFF through their addition to the training-set. To attain a force field able to correctly describe the properties and features of the molecular systems of interest, the training-set must include the ensemble of the optimized DFT configurations that better represent the overall analyzed chemical system. In our case, since we were interested in the description of the phenomena related to the fuel deposit formation, we chose to add to our training-set mainly the DFT optimized adsorption configurations of the model molecules representing the deposit precursors on the top of the aluminum and stainless steel surrogates in both anhydrous and hydroxylated conditions.

For this thesis, the training-set was composed mainly of the adsorption configurations of a large variety of model molecules to ensure a higher possibility for the reactive force field to be well fitted for correctly predicting the analyzed molecular systems. This implemented methodology for the improvement of the ReaxFF into describing the chemical properties and reactivities of our systems envisaged an iterative cycle, where we can say that the two major parts may be defined

as the “ReaxFF parameterization” and the “ReaxFF validation”. The first part, as it was already mentioned above, the objective was to define a suitable training-set that would aid us to improve the implemented force fields, while the second part of this cycle was conceived to validate them. This iterative scheme can be described in the following **Figure 24** reported below; from this simplified scheme, we can easily understand that the first part of this methodology consisting in the ReaxFF parameterization is crucial. In fact, if at the end of the ReaxFF parametrization we observe that after the optimization step the reactive force field is not yet able to predict the inserted DFT data in the training-set, we cannot access to the second part of this methodology.



**Figure 24: Simplified scheme of the ReaxFF methodology implemented in this thesis.**

In the following paragraphs, each of the steps shown in **Figure 24** will be addressed following the order of the used methodology. In this section of our work, we chose to implement the AMS 2019 [50] modeling package for the ReaxFF calculations.

### 2.11.2 ReaxFF optimization algorithms

To find new parameters in ReaxFF, a new training-set must be constructed, which consists of reference properties,  $x_{i,ref}$ , of molecules relevant to the chemistry interest. The standalone ReaxFF provides an optimization scheme consisting of *successive one-parameter parabolic extrapolation* (SOPPE) [51], in which the calculated predictions for these properties,  $x_{i,calc}(\{p_j\})$ , are determined by parameters,  $p_j$ , which can be adjusted to minimize the deviation from the training data. The quality of a parameter vector is quantified by an objective function, from this point referred to as error and given by:

$$error(\{p_j\}) = \sum_{i=1}^n \left( \frac{x_{i,calc}(\{p_j\}) - x_{i,ref}}{\sigma_i} \right)^2$$

**Equation 59**

Where the sum runs over all the training data points. In each term,  $\sigma_i$  is an estimate of acceptable deviations between a ReaxFF calculation and its corresponding reference value. Note that reference values can be obtained either from experiment or from ab initio calculations (as in this thesis). The aim of the optimization is to find a parameter set that minimizes the objective function (error) defined in **Equation 59**.

The SOPPE algorithm attempts to arrive at an optimally configured parameter set by fine tuning each parameter individually. However, using this optimization method becomes laborious as parameters in the potential energy model are often related, such that the optimal value of each parameter may shift if another one is changed.

Another solution for better parameter optimization is represented by the class of stochastic-heuristic global optimization methods known as the *genetic algorithm* (GA) [52]. Next to GA, many other techniques were proposed, such as *multi-objective evolutionary strategy* [53], a

*parallel local search algorithm*[54], *Taguchi method-based optimization*[55], a *Monte-Carlo FF optimizer* (MCFF) [56, 57] and a *covariance matrix adaptation evolutionary strategy* (CMA-ES) [58, 59].

### 2.11.3 ReaxFF optimization via CMA-ES optimizer

Once the training-set data is constructed, the next step is the force field optimization. In the AMS 2019 software, the implementation of this operation is run by the *FF Optimizer* module. The base *FFOptimizer* module offers methods to compute the cost function (**Equation 59**) and its first and second derivatives with respect to the force-field parameter values. Besides that, there are two extensions available that implement global optimization methods: Monte-Carlo (MCFF) and Covariance Matrix Adaptation Evolution Strategy (CMA-ES), the second being employed in this thesis framework. This choice may be justified by the fact that the CMA-ES optimizer proves to be more efficient than the MCFF if we compare them in terms of computational cost, as reported in the work of Shchygol et. al [60], where they conducted a comparative study of the MCFF, the CMA-ES and GA optimizations methods.

The CMA-ES (Covariance Matrix Adaptation Evolution Strategy) is an evolutionary algorithm for difficult non-linear non-convex black-box optimization problems in continuous domain. The CMA-ES is considered as state-of-the-art in evolutionary computation and has been adopted as one of the standard tools for continuous optimization in various research and industrial environments. The CMA-ES is typically applied to unconstrained or bounded constraint optimization problems and search space dimensions between three and a hundred. The method should be applied if derivative based methods (e.g. quasi-Newton, BFGS or conjugate gradient) supposedly fail due to a rugged search landscape (such as discontinuities, sharp bends or ridges, noise, local optima, outliers). If second order derivative based methods are successful, they are usually faster than the CMA-ES.

Similar to quasi-Newton methods, the CMA-ES is a second order approach estimating a positive definite matrix within an iterative procedure (more precisely: a covariance matrix, that is, on convex-quadratic functions, closely related to the inverse Hessian). This makes the method feasible on non-separable and/or badly conditioned problems. In contrast to quasi-Newton

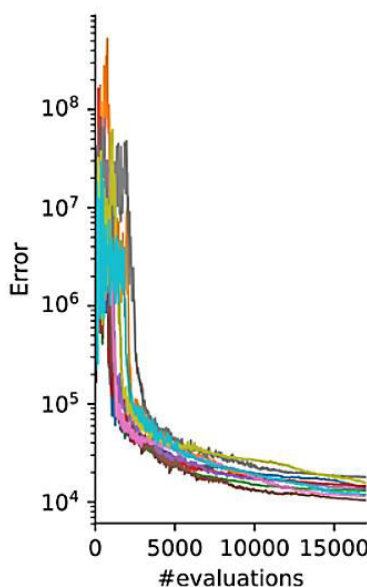
methods, the CMA-ES does not use or approximate gradients and does not even presume or require their existence. This makes the method feasible on non-smooth and even non-continuous problems, as well as on multimodal and/or noisy problems. It turns out to be a particularly reliable and highly competitive evolutionary algorithm for local optimization [61] and, surprising at first sight, also for global optimization [62].

The CMA-ES has several invariance properties; two of them, inherited from the plain evolution strategy, are (i) invariance to order preserving (i.e. strictly monotonic) transformations of the objective function value and (ii) invariance to angle preserving (rigid) transformations of the search space (including rotation, reflection, and translation), if the initial search point is transformed accordingly. Invariances are highly desirable: they imply uniform behavior on classes of functions and therefore imply the generalization of empirical results.

In addition, the CMA-ES does not require a tedious parameter tuning for its application. In fact, the choice of strategy internal parameters is not left to the user (arguably with the exception of population size  $\lambda$ ). Finding good (default) strategy parameters is considered as part of the algorithm design, and not part of its application—the aim is to have a well-performing algorithm as is. The default population size  $\lambda$  is comparatively small to allow for fast convergence. Restarts with increasing population size [63] improve the global search performance. For the application of the CMA-ES, an initial solution, an initial standard deviation (step-size, variables should be defined such that the same standard deviations can be reasonably applied to all variables, see also here) and, possibly, the termination criteria (e.g. a function tolerance) need to be set by the user. The most common applications are model calibration (e.g. curve fitting) and shape optimization.

In regards of FF parametrization [59, 64–66], the CMA-ES FF optimizer is implemented to find the best fit force field for the given training-set. This FF optimizer represents a stochastic gradient-free optimization algorithm proposed by Hansen et al. [58]. Starting from a user-provided initial guess, CMA-ES iteratively tries to estimate the reference values of each training-set parameter in order to reach the lowest error function value (**Equation 59**) of the implemented force field. To achieve an efficient force field optimization, multiple parallel runs by the CMA-ES optimizer are suggested, because in this way we could reduce the risk of reaching a convergence on a higher local minimum. A good example of ReaxFF optimization via multiple runs of the CMA-ES optimizer is reported in the **Figure 25** below taken from the work of

Shchygol et al. [60], where the error function values produced by 10 different CMA-ES optimization runs were plotted against the number of calculated iterations. From **Figure 25** we can see that all the error function values started as very high ( $10^6$ - $10^8$  order) but lowered of many orders already after the first thousands of iterations. We can see that most of the runs gave an error value around the  $10^4$  order, which is not so negligible compared to the first error values.



**Figure 25: Plots of the error as a function of the number of error evaluations for the CMA-ES optimizer taken from ref. [60]**

In our adopted methodology, we chose to verify the good fit of the optimized force field showing the lowest error function value through the run of a new type of optimization run, in which this time the force field had to predict different reference data from the training-set.

#### 2.11.4 Required files for ReaxFF training-set

As stated before, the construction of a suitable training-set is fundamental to ensure a good force field optimization. In the AMS 2019 modeling package that we employed for this thesis, the training-set data (which is defined in the *training\_data* dossier) requires four different files, namely the *.trainset.in*, the *.ffield*, the *.geo* and the *.params* files respectively. The *.trainset.in* file contains the training set data and tells the program how to calculate the cost function (**Equation**

59) which is used to optimize the force field parameters. The *.ffield* file defines the original force field integrated to be optimized, the *.geo* file contains the training-set geometries (in our case the adsorption configurations derived from DFT) and finally the *.params* file contains the information of which training-set parameters should be optimized (e.g. bonds, atoms, angles).

### 2.11.5 ReaxFF validation-set

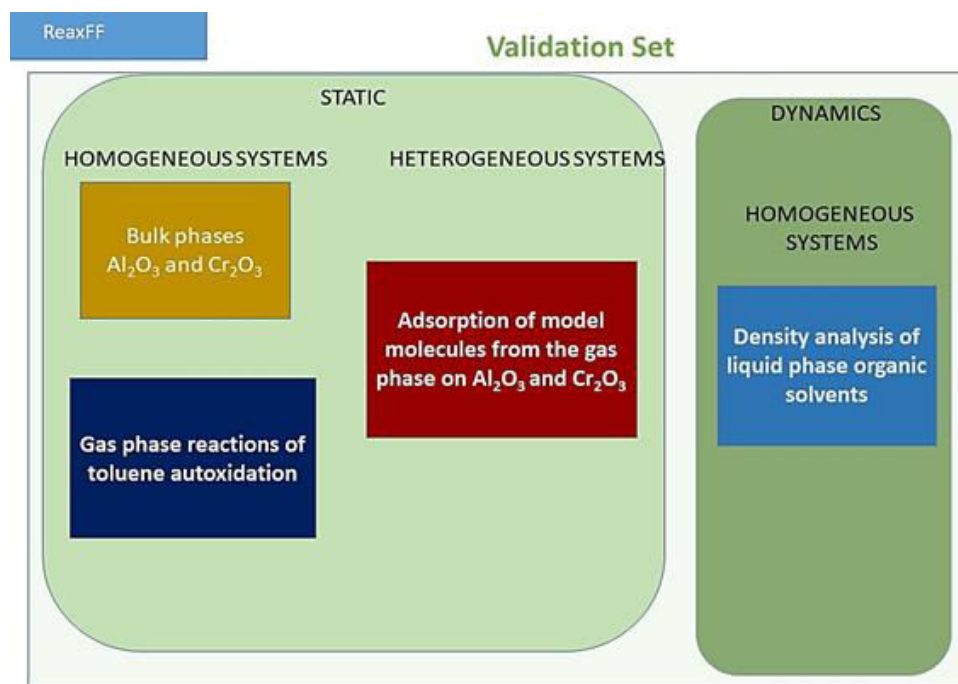
The validation-set has a very similar setting with the training-set previously described, with the only exception given by the reference data added in it. The strategy adopted in this study was to add a larger variety of molecular optimized configurations in the training-set to ensure a higher capability of a correct prediction of the chemical systems for the new optimized force field. Instead, we chose to add a more “restricted” variety of molecular data in the validation-set since in this step the aim was to verify and possibly confirm that the optimized ReaxFF was fit good enough to well describe the overall ensemble of our molecular systems.

Once confirmed that the optimized ReaxFF is able to correctly reproduce the training-set data, we go towards the ReaxFF validation step. Here, if we observe that the ReaxFF estimations are not accurate enough compared to the validation-set DFT data, then the iteration cycle of ReaxFF reparametrization-optimization starts again. On the other hand, if the ReaxFF predictions proved to be close to the reference values, then we validate ReaxFF and go forward to the ReaxFF data production, which envisages the MD investigation of a surrogate liquid “fuel-oxygen” blend in both homogeneous (i.e. liquid-phase) and heterogeneous (i.e. liquid/solid interface) conditions.

### 2.11.6 ReaxFF validation

Once verified that the optimized ReaxFF can well describe the molecular systems of the training-set in terms of molecular structure (bonds and angles) and energies (adsorption energies), the following step is the validation of the optimized force field. In this study, the ReaxFF validation step was divided into two different parts: a “static” study and a “dynamic” study (as reported in **Figure 24**).

The main stages of the “static” and “dynamic” studies carried out in our ReaxFF validation are resumed in **Figure 26**.



**Figure 26:** Simplified scheme depicting the main “static” and “dynamic” studies envisaged in the ReaxFF validation carried out in this study.

The “static” study is represented by two main categories of systems: the homogeneous (i.e. gas-phase) and heterogeneous (gas/solid interface) systems, respectively.

For the homogeneous systems, we carry out the following calculations:

- i. The ReaxFF geometry optimizations of the bulk lattice parameters for both  $\alpha$ - $\text{Al}_2\text{O}_3$  and  $\alpha$ - $\text{Cr}_2\text{O}_3$  compared with the corresponding DFT results and experimental data.
- ii. The ReaxFF geometry optimizations of the gas-phase reactions that describe the toluene autoxidation mechanism compared with the corresponding DFT results.

For the heterogeneous systems, we carry out the ReaxFF calculations of the adsorption of surrogates of deposit precursors (molecules not included in the previous training-set) on both  $\alpha$ - $\text{Al}_2\text{O}_3$  and  $\alpha$ - $\text{Cr}_2\text{O}_3$  (in dry and hydroxylated conditions). These ReaxFF results are compared with the corresponding DFT values to be validated.

The “dynamic” study envisages the ReaxFF MD calculation of the densities of common liquid solvents selected among our model molecules: acetic acid, acetone and ethanol (as aliphatic molecules) and benzaldehyde and benzyl alcohol (as aromatic molecules) at ambient conditions ( $P = 1$  bar and  $T = 20^{\circ}\text{C}$ ). Also water was included since it is hugely present in the systems represented by the fully-hydroxylated surface layer. These ReaxFF densities are compared with experimental data.

## 2.12 Molecular Dynamics

A Molecular Dynamics (MD) simulation consists of the numerical, step-by-step, solution of the classical equation of motion, which for a simple atomic system may be written:

$$m_i \left( \frac{d^2 \mathbf{r}_i}{dt^2} \right) = \mathbf{f}_i$$

**Equation 60**

Where  $m_i$  is the mass of the  $i$ -th particle,  $\mathbf{f}_i$  is the force on it and  $\mathbf{r}_i$  represents its position coordinates. The computation of the force  $\mathbf{f}_i$  involves the calculation of the derivative of the interacting potential,  $U(\mathbf{r}_1, \mathbf{r}_2, \dots, \mathbf{r}_N)$ :

$$\mathbf{f}_i = - \left( \frac{\partial U(\mathbf{r}_1, \mathbf{r}_2, \dots, \mathbf{r}_N)}{\partial \mathbf{r}_i} \right)$$

**Equation 61**

In each time step of the simulation, one needs to compute the force  $\mathbf{f}_i$  and, using this force, the position  $\mathbf{r}_i$  gets updated. To solve the second order differential equation as in **Equation 60**, there are several numerical schemes available, which are based on finite difference methods. The integration algorithms often include the Verlet algorithm, which several variations are the most widely used in the MD calculation framework.

The integration of **Equation 61** in the Verlet algorithm involves the computation of the positions at different times using the Taylor expansion about  $\mathbf{r}(t)$ , where  $\Delta t$  is the time step. Thus:

$$\mathbf{r}(t + \Delta t) = \mathbf{r}(t) + \Delta t \mathbf{v}(t) + \frac{1}{2}(\Delta t^2) \mathbf{a}(t) + \dots$$

**Equation 62**

$$\mathbf{r}(t - \Delta t) = \mathbf{r}(t) - \Delta t \mathbf{v}(t) + \frac{1}{2}(\Delta t^2) \mathbf{a}(t) - \dots$$

**Equation 63**

Making use of these two expressions, the next step position  $\mathbf{r}(t + \Delta t)$  is easily found:

$$\mathbf{r}(t + \Delta t) = 2\mathbf{r}(t) - \mathbf{r}(t - \Delta t) + (\Delta t^2) \mathbf{a}(t)$$

**Equation 64**

Although the velocities  $\mathbf{v}(t)$  are not required to compute trajectories, those are useful for the computation of kinetic energy (hence, total energy) and the velocity auto-correlation functions. We can then write:

$$\mathbf{v}(t) = \left( \frac{1}{2\Delta t} \right) [\mathbf{r}(t + \Delta t) - \mathbf{r}(t - \Delta t)]$$

**Equation 65**

In the Verlet integration scheme, the errors in calculated positions  $\mathbf{r}(t)$  are of the order of  $\Delta t^4$ , while those in calculated velocities  $\mathbf{v}(t)$  are of the order of  $\Delta t^2$ .

The integration of motion gives the constant-energy surface of the system. However, in most of the cases, we seek to run MD simulations in a particular thermodynamic ensemble at a particular state point (e.g. target energy, temperature and pressure). Under these conditions, the total energy of system varies. To control the fluctuations in different state variables, different statistical ensembles have been formulated. The state variables are defined as the energy ( $E$ ), temperature ( $T$ ), volume ( $V$ ), number of particles ( $N$ ), enthalpy ( $H$ ) and pressure ( $P$ ). The structural, energetic

and several dynamic properties are calculated by taking average of these properties through all the ensembles generated. Depending on the state variable maintained constant during the simulation, we can define the following thermodynamic ensembles:

1. NVE ensemble, where the number of atoms, the volume and the energy remain constant (micro-canonical ensemble).
2. NVT ensemble, where the number of atoms, the volume and the temperature remain constant (canonical ensemble).
3. NPT ensemble, where the number of atoms, the pressure and the temperature remain constant (isothermal-isobaric ensemble).

In the “dynamic” section of the ReaxFF validation, for the “physico-chemistry” study we performed MD simulations through the implementation of the NPT ensemble since we wanted to set a system where pressure and temperature were fixed ( $P = 1$  bar and  $T = 20^{\circ}\text{C}$ ). In this way, we could verify if the reparametrized FF could be able to describe some of the model molecules from a macroscopic point of view (e.g. density).

On the other hand, for the “chemical reactivity” study, we run MD simulations through the NVT. In both cases, we selected the Nosé-Hoover chain (NHC) [67] as thermostat, while in NPT case we used the implemented Martina-Tobias-Klein (MTK) [68] barostat.

### 2.12.1 Radial distribution function (RDF)

In the MD simulations, we obtain the trajectory of the particles composing the molecular system. We can make use of this obtained trajectory by calculating a structural quantity of the system, such as the radial distribution function (RDF). The RDF is represented by the function  $g(r)$  and it is defined as:

$$g(r) = \frac{V}{N^2} \langle \sum_i \sum_j \delta(r - r_{ij}) \rangle$$

**Equation 66**

where  $N$  is the total number of particles present in a volume  $V$ ,  $r_{ij}$  is the distance between a pair of particles,  $\delta(x)$  is a delta function and the angular brackets represent ensemble average. In the

MD simulations, we compute the  $r_{ij}$  values of all the particle pairs from the trajectories and this is then used to calculate the RDF.

From the  $g(r)$ , we can also calculate its integral, which corresponds to the mean number of atoms around a specific type of atom at distance  $r$ . The integral is defined as:

$$N(r) = \int_0^r 4\pi r^2 g(r) \rho \, dr$$

**Equation 67**

Where  $\rho$  represents the atomic density of the surrounding atoms.

## References

- 1 Warren J. Hehre (2003) *A Guide to Molecular Mechanics and Quantum Chemical Calculations*, 18401 Von Karman Ave., Suite 370 Irvine, CA 92612. ISBN: SBN 1-890661-18-X.
- 2 Parr R.G., Yang W. (1989) *Density functional theory of atoms and molecules*.
- 3 Perdew J. P., Wang J., Perdew, Wang (1992) Accurate and simple analytic representation of the electron-gas correlation energy, *Phys. Rev. B* **45**, 23, 13244–13249. DOI: 10.1103/PhysRevB.45.13244.
- 4 John P. Perdew, K. Burke, M. Ernzerhof (1996) Generalized Gradient Approximation Made Simple, *Phys. Rev. Lett.* **77**, 18, 3865–3868. DOI: 10.1103/PhysRevLett.77.3865.
- 5 Hafner J. (2008) Ab-initio simulations of materials using VASP: Density-functional theory and beyond, *Journal of computational chemistry* **29**, 13, 2044–2078. DOI: 10.1002/jcc.21057.
- 6 Moroni E.G., Kresse G., Hafner J., Furthmüller J. (1997) Ultrasoft pseudopotentials applied to magnetic Fe, Co, and Ni: From atoms to solids, *Physical review. B, Condensed matter* **56**, 24, 15629–15646. DOI: 10.1103/PhysRevB.56.15629.
- 7 R. Hafner et al. (2002) Ab initio local-spin-density study of oscillatory exchange coupling in Fe/Au multilayers, *J. Phys.: Condens. Matter* **14**, 4297–4307.
- 8 Sholl D.S., Steckel J.A. (eds.) (2009) *Density functional theory: A practical introduction*, Wiley, Hoboken N.J.
- 9 Vanderbilt D. (1997) First-principles based modelling of ferroelectrics, *Curr Opin Solid State Mater Sci* **2**, 6, 701–705. DOI: 10.1016/S1359-0286(97)80013-7.
- 10 Blöchl P.E (1994) Projector augmented-wave method, *Phys. Rev. B* **50**, 24, 17952–17979. DOI: 10.1007/BF02712785.
- 11 Kresse G., Joubert D. (1999) From ultrasoft pseudopotentials to the projector augmented-wave method, *Phys. Rev. B* **59**, 3, 1758–1775. DOI: 10.1103/PhysRevB.59.1758.
- 12 Dudarev et al (1997) Electron-energy-loss spectra and the structural stability of nickel oxide: an LSDA+U study, *Phys. Rev. B* **57**, 1505–1509. DOI: 10.1103/PhysRevB.57.1505.
- 13 Grimme S., Antony J., Ehrlich S., Krieg H. (2010) A consistent and accurate ab initio parametrization of density functional dispersion correction (DFT-D) for the 94 elements H-Pu, *J. Chem. Phys.* **132**, 15, 154104. DOI: 10.1063/1.3382344.
- 14 Stephan Grimme (2006) Semiempirical GGA-type density functional constructed with a long-range dispersion correction, *Journal of computational chemistry* **Volume 27, Issue 15**, 1787–1799.
- 15 Henkelman G., Jónsson H. (2000) Improved tangent estimate in the nudged elastic band method for finding minimum energy path and saddle points // Improved tangent estimate in the nudged elastic band method for finding minimum energy paths and saddle points, *J. Chem. Phys.* **113**, 22, 9978–9985. DOI: 10.1063/1.1323224.
- 16 Hannes Jónsson, Greg Mills, Karsten W. Jacobsen (385) *Nudged Elastic Band Method for Finding Minimum Energy Paths of Transitions*.
- 17 Uberuaga, Leskovaar, Smith, Jonsson, Olmstead (2000) uuberu // Diffusion of Ge below the Si(100) surface: theory and experiment, *Physical Review Letters* **84**, 11, 2441–2444. DOI: 10.1103/PhysRevLett.84.2441.
- 18 Shen T.-C., Steckel J.A., Jordan K.D. (2000) Electron-stimulated bond rearrangements on the H/Si(100)-3×1 surface, *Surface Science* **446**, 3, 211–218. DOI: 10.1016/S0039-6028(99)01147-4.
- 19 Mads R. Sorensen, 1 Karsten W. Jacobsen, 1, 2 and Hannes Jonsson 1, 3, Sorensen, Jacobsen, Jónsson (1996) Thermal Diffusion Processes in Metal-Tip-Surface Interactions: Contact Formation and Adatom Mobility, *Physical Review Letters* **77**, 25, 5067–5070. DOI: 10.1103/PhysRevLett.77.5067.
- 20 Villarba M., Jónsson H. (1995) Atomic exchange processes in sputter deposition of Pt on Pt(111), *Surface Science* **324**, 1, 35–46. DOI: 10.1016/0039-6028(94)00631-8.
- 21 M.J. Frisch, G.W. Trucks, H.B. Schlegel, G.E. Scuseria, M.A. Robb, J.R. Cheeseman, G. Scalmani, V. Barone, G.A. Petersson, H. Nakatsuji, X. Li, M. Caricato, A.V. Marenich, J. Bloino, B.G. Janesko, R. Gomperts, B. Mennucci, H.P. Hratchian, J.V. Ortiz, Izmaylov, A. F., Sonnenberg, J. L., Williams, F. Ding, F. Lipparini, F. Egidi, J. Goings, B. Peng, A. Petrone, T. Henderson, D. Ranasinghe, V.G. Zakrzewski, J. Gao, N. Rega, G. Zheng, W. Liang, M. Hada, M. Ehara, K. Toyota, R. Fukuda, J. Hasegawa, M. Ishida, T. Nakajima, Y. Honda, O. Kitao, H. Nakai, T. Vreven, K. Throssell, J.A. Montgomery Jr., Peralta, J. E., F. Ogliaro, M.J. Bearpark,

- Heyd, J. J., E.N. Brothers, K.N. Kudin, Staroverov, V. N., T.A. Keith, R. Kobayashi, J. Normand, K. Raghavachari, A.P. Rendell, J.C. Burant, S.S. Iyengar, J. Tomasi, M. Cossi, J.M. Millam, M. Klene, C. Adamo, R. Cammi, J.W. Ochterski, R.L. Martin, K. Morokuma, O. Farkas, J.B. Foresman, D.J. Fox (2016) *Gaussian 16 Rev. C.01*, Wallingford, E.U.A.
- 22 Kresse, Furthmüller (1996) Efficient iterative schemes for ab initio total-energy calculations using a plane-wave basis set, *Phys. Rev. B* **54**, 16, 11169–11186. DOI: 10.1103/physrevb.54.11169.
  - 23 Kresse G., Furthmüller J. (1996) Efficiency of ab-initio total energy calculations for metals and semiconductors using a plane-wave basis set, *Comput. Mater. Sci.* **6**, 15–50. DOI: 10.1016/0927-0256(96)00008-0.
  - 24 Hammer B., Hansen L.B., Nørskov J.K. (1999) Improved adsorption energetics within density-functional theory using revised Perdew-Burke-Ernzerhof functionals, *Phys. Rev. B* **59**, 11, 7413–7421. DOI: 10.1103/PhysRevB.59.7413.
  - 25 Armiento R., Mattsson A.E. (2005) Functional designed to include surface effects in self-consistent density functional theory, *Phys. Rev. B* **72**, 8. DOI: 10.1103/PhysRevB.72.085108.
  - 26 W. Tang, E. Sanville, and G. Henkelman. (2009) A grid-based Bader analysis algorithm without lattice bias, *J. Phys.: Condens. Matter* **21**, 084204.
  - 27 Gouron A., Kittel J., Bruin T. de, Diawara B. (2015) Density Functional Theory Study of Monoethanolamine Adsorption on Hydroxylated Cr 2 O 3 Surfaces, *J. Phys. Chem. C* **119**, 40, 22889–22898. DOI: 10.1021/acs.jpcc.5b05375.
  - 28 Costa D., Garrain P.-A., Baaden M. (2013) Understanding small biomolecule-biomaterial interactions: A review of fundamental theoretical and experimental approaches for biomolecule interactions with inorganic surfaces, *J. Biomed. Mater. Res. Part A* **101**, 4, 1210–1222. DOI: 10.1002/jbm.a.34416.
  - 29 Nigussa K.N., Nielsen K.L., Borck Ø., Støvneng J.A. (2011) Adsorption of hydrogen, chlorine, and sulfur atoms on  $\alpha$ -Cr<sub>2</sub>O<sub>3</sub>(0001) surfaces: A density functional theory investigation, *Corros. Sci.* **53**, 11, 3612–3622. DOI: 10.1016/j.corsci.2011.07.005.
  - 30 van Duin A.C.T., Dasgupta S., Lorant F., Goddard W.A. (2001) ReaxFF: A Reactive Force Field for Hydrocarbons, *J. Phys. Chem. A* **105**, 41, 9396–9409. DOI: 10.1021/jp004368u.
  - 31 Russo M.F., van Duin A.C. (2011) Atomistic-scale simulations of chemical reactions: Bridging from quantum chemistry to engineering, *Nucl. Instrum. Methods Phys. Res.* **269**, 14, 1549–1554. DOI: 10.1016/j.nimb.2010.12.053.
  - 32 Senftle T.P., Hong S., Islam M.M., Kylasa S.B., Zheng Y., Shin Y.K., Junkermeier C., Engel-Herbert R., Janik M.J., Aktulga H.M., Verstraelen T., Grama A., van Duin A.C.T. (2016) The ReaxFF reactive force-field: Development, applications and future directions, *NPJ Comput. Mater.* **2**, 1, 9396. DOI: 10.1038/npjcompumats.2015.11.
  - 33 van Duin A.C., Damsté J.S. (2003) Computational chemical investigation into isorenieratene cyclisation, *Org. Geochem.* **34**, 4, 515–526. DOI: 10.1016/S0146-6380(02)00247-4.
  - 34 Chen N., Lusk M.T., van Duin A.C.T., Goddard W.A. (2005) Mechanical properties of connected carbon nanorings via molecular dynamics simulation, *Phys. Rev. B* **72**, 8, 29. DOI: 10.1103/PhysRevB.72.085416.
  - 35 Chenoweth K., van Duin A.C.T., Goddard W.A. (2008) ReaFF Potential Functions: Supporting Information for the manuscript "A ReaxFF Reactive Force Field for Molecular Dynamics Simulations of Hydrocarbon Oxidation", *J. Phys. Chem. A* **112**, 5, 1–10. DOI: 10.1021/jp709896w.
  - 36 Castro-Marciano F., Kamat A.M., Russo M.F., van Duin A.C., Mathews J.P. (2012) Combustion of an Illinois No. 6 coal char simulated using an atomistic char representation and the ReaxFF reactive force field, *Combustion and Flame* **159**, 3, 1272–1285. DOI: 10.1016/j.combustflame.2011.10.022.
  - 37 Rahaman O., van Duin A.C.T., Goddard W.A., Doren D.J. (2011) Development of a ReaxFF reactive force field for glycine and application to solvent effect and tautomerization, *The journal of physical chemistry. B* **115**, 2, 249–261. DOI: 10.1021/jp108642r.
  - 38 Monti S., Corozzi A., Fristrup P., Joshi K.L., Shin Y.K., Oelschlaeger P., van Duin A.C.T., Barone V. (2013) Exploring the conformational and reactive dynamics of biomolecules in solution using an extended version of the glycine reactive force field, *Phys. Chem. Chem. Phys.* **15**, 36, 15062–15077. DOI: 10.1039/c3cp51931g.
  - 39 Raymand D., van Duin A.C., Spångberg D., Goddard W.A., Hermansson K. (2010) Water adsorption on stepped ZnO surfaces from MD simulation, *Surface Science* **604**, 9-10, 741–752. DOI: 10.1016/j.susc.2009.12.012.

- 40 Case D.A., Cheatham T.E., Darden T., Gohlke H., Luo R., Merz K.M., Onufriev A., Simmerling C., Wang B., Woods R.J. (2005) The Amber biomolecular simulation programs, *Journal of computational chemistry* **26**, 16, 1668–1688. DOI: 10.1002/jcc.20290.
- 41 B. R., Brooks C.L., Mackerell A.D., Nilsson L., Petrella R.J., Roux B., Won Y., Archontis G., Bartels C., Boresch S., Caflisch A., Caves L., Cui Q., Dinner A.R., Feig M., Fischer S., Gao J., Hodoscek M., Im W., Kuczera K., Lazaridis T., Ma J., Ovchinnikov V., Paci E., Pastor R.W., Post C.B., Pu J.Z., Schaefer M., Tidor B., Venable R.M., Woodcock H.L., Wu X., Yang W., York D.M., Karplus M. (2009) CHARMM: the biomolecular simulation program, *Journal of computational chemistry* **30**, 10, 1545–1614. DOI: 10.1002/jcc.21287.
- 42 Chenoweth K., van Duin A.C.T., Goddard W.A. (2009) The ReaxFF Monte Carlo reactive dynamics method for predicting atomistic structures of disordered ceramics: application to the Mo(3)VO(x) catalyst, *Angewandte Chemie (International ed. in English)* **48**, 41, 7630–7634. DOI: 10.1002/anie.200902574.
- 43 Chenoweth K., van Duin A.C.T., Goddard W.A. (2008) ReaxFF reactive force field for molecular dynamics simulations of hydrocarbon oxidation, *J. Phys. Chem. A* **112**, 5, 1040–1053. DOI: 10.1021/jp709896w.
- 44 Buehler M.J., Tang H., van Duin A.C.T., Goddard W.A. (2007) Threshold crack speed controls dynamical fracture of silicon single crystals, *Physical Review Letters* **99**, 16, 165502. DOI: 10.1103/PhysRevLett.99.165502.
- 45 Jiang X., Hu Y., Ling L., Wang X. (2021) The initial wet oxidation process on Fe-Cr alloy surface: Insights from ReaxFF molecular dynamic simulations, *Applied Surface Science* **548**, 149159. DOI: 10.1016/j.apsusc.2021.149159.
- 46 Shin Y.K., Kwak H., Vasenkov A.V., Sengupta D., van Duin A.C. (2015) Development of a ReaxFF Reactive Force Field for Fe/Cr/O/S and Application to Oxidation of Butane over a Pyrite-Covered Cr<sub>2</sub>O<sub>3</sub> Catalyst, *ACS Catal.* **5**, 12, 7226–7236. DOI: 10.1021/acscatal.5b01766.
- 47 Dabaghmanesh S., Neek-Amal M., Partoens B., Neyts E.C. (2017) The formation of Cr<sub>2</sub>O<sub>3</sub> nanoclusters over graphene sheet and carbon nanotubes, *Chemical Physics Letters* **687**, 188–193. DOI: 10.1016/j.cplett.2017.09.005.
- 48 Zeng H., Cheng X., Zhang C., Lu Z. (2018) Responses of Core–Shell Al/Al<sub>2</sub>O<sub>3</sub> Nanoparticles to Heating: ReaxFF Molecular Dynamics Simulations, *J. Phys. Chem. C* **122**, 16, 9191–9197. DOI: 10.1021/acs.jpcc.8b01088.
- 49 Soleymanibrojeni M., Shi H., Liu F., Han E.-H. (2019) Atomistic simulations of Epoxy/Water/Aluminum systems using the ReaxFF method, *Computational Materials Science*, 109424. DOI: 10.1016/j.commatsci.2019.109424.
- 50 Rüger R., Franchini M., Trnka T., Yakovlev A., van LentheAMS 2019, T. SCM, Theoretical Chemistry, Vrije Universiteit: Amsterdam, The Netherlands.
- 51 van Duin A.C.T., Baas J. M. A., van de Graal B. (1994) Delft molecular mechanics : a new approach to hydrocarbon force fields, *J. Chem. Soc. Faraday Trans.* **90**, 19, 2881–2895. DOI: 10.1039/FT9949002881.
- 52 Holland J.H. (1992) *Adaptation in natural and artificial systems: An introductory analysis with applications to biology, control, and artificial intelligence*, The MIT Press, Cambridge (Mass.) London. ISBN: 9780262581110.
- 53 Larentzos J.P., Rice B.M., Byrd E.F.C., Weingarten N.S., Lill J.V. (2015) Parameterizing Complex Reactive Force Fields Using Multiple Objective Evolutionary Strategies (MOES). Part 1: ReaxFF Models for Cyclotrimethylene Trinitramine (RDX) and 1,1-Diamino-2,2-dinitroethene (FOX-7), *J. Chem. Theory Comput.* **11**, 2, 381–391. DOI: 10.1021/ct500788c.
- 54 Deetz J.D., Faller R. (2014) Parallel optimization of a reactive force field for polycondensation of alkoxysilanes, *The journal of physical chemistry. B* **118**, 37, 10966–10978. DOI: 10.1021/jp504138r.
- 55 Hu X., Schuster J., Schulz S.E. (2017) Multiparameter and Parallel Optimization of ReaxFF Reactive Force Field for Modeling the Atomic Layer Deposition of Copper, *J. Phys. Chem. C* **121**, 50, 28077–28089. DOI: 10.1021/acs.jpcc.7b09948.
- 56 Iype E., Hütter M., Jansen A.P.J., Nedeia S.V., Rindt C.C.M. (2013) Parameterization of a reactive force field using a Monte Carlo algorithm, *Journal of computational chemistry* **34**, 13, 1143–1154. DOI: 10.1002/jcc.23246.
- 57 Kirkpatrick S., Gelatt C. D., Vecchi M. P. (1983) Optimization by simulated annealing, *Science* **220**, 4598, 671–680. DOI: 10.1126/science.220.4598.671.

- 58 Lozano J.A., Larrañaga P., Inza I., Bengoetxea E. (2006) *Towards a New Evolutionary Computation: Advances in the Estimation of Distribution Algorithms*, Springer Berlin Heidelberg, Berlin, Heidelberg. ISBN: 9783540324942.
- 59 Trnka T., Tvaroška I., Koča J. (2018) Automated Training of ReaxFF Reactive Force Fields for Energetics of Enzymatic Reactions, *Journal of chemical theory and computation* **14**, 1, 291–302. DOI: 10.1021/acs.jctc.7b00870.
- 60 G. Shchygol, A. Yakovlev, T. Trnka, A.C.T van Duin, T. Verstraelen ReaxFF parameter optimization with Monte Carlo and Evolutionary Algorithms: Guidelines and Insights Center for Molecular Modeling (CMM), Ghent University, Technologiepark 903, B-9052,
- 61 Hansen N., Ostermeier A. (2001) Completely derandomized self-adaptation in evolution strategies, *Evolutionary computation* **9**, 2, 159–195. DOI: 10.1162/106365601750190398.
- 62 N. Hansen, S. Kern (2004) *Evaluating the CMA Evolution Strategy on Multimodal Test Functions: Parallel problem solving from nature*, Springer, Berlin. ISBN: 978-3-540-23092-2.
- 63 A. Auger, N. Hansen (2005, 2003) *Proceeding of the IEEE Congress on Evolutionary Computation, CEC 2005*, IEEE, Piscataway NJ. ISBN: 0-7803-9363-5.
- 64 Dürholt J.P., Fraux G., Coudert F.-X., Schmid R. (2019) Ab Initio Derived Force Fields for Zeolitic Imidazolate Frameworks: MOF-FF for ZIFs, *Journal of chemical theory and computation* **15**, 4, 2420–2432. DOI: 10.1021/acs.jctc.8b01041.
- 65 Verstraelen T., Bultinck P. (2015) Can the electronegativity equalization method predict spectroscopic properties?, *Spectrochimica acta. Part A, Molecular and biomolecular spectroscopy* **136 Pt A**, 76–80. DOI: 10.1016/j.saa.2013.10.124.
- 66 Semino R., Dürholt J.P., Schmid R., Maurin G. (2017) Multiscale Modeling of the HKUST-1/Poly(vinyl alcohol) Interface: From an Atomistic to a Coarse Graining Approach, *J. Phys. Chem. C* **121**, 39, 21491–21496. DOI: 10.1021/acs.jpcc.7b07090.
- 67 W. G. Hoover, B. L. Holian (1996) Kinetic moments method for the canonical ensemble distribution, *Phys. Rev. A (Physical Review A)* **211**, 253–257. DOI: 10.1016/0375-9601(95)00973-6.
- 68 Martyna G.J., Tuckerman M.E., Tobias D.J., Klein M.L. (1996) Explicit reversible integrators for extended systems dynamics, *Molecular Physics* **87**, 5, 1117–1157. DOI: 10.1080/00268979600100761.
- 69 Kim, Y. M., Cho, K.-B., Cho, J., Wang, B., Li, C., Shaik, S., et al. (2013). A mononuclear non-heme high-spin iron(III)–hydroperoxo complex as an active oxidant in sulfoxidation reactions. *J. Am. Chem. Soc.* **135**, 8838–8841. doi: 10.1021/ja404152qX.
- 70 Shubin L., Research Computing Center, ITS University of North Carolina at Chapel Hill “Gaussia & GaussianView” (lecture), <https://www.slideserve.com/vin/gaussian-gaussview>.

## Chapter 3. Studied surfaces

### 3.1 Choice of corundum $\alpha$ -Al<sub>2</sub>O<sub>3</sub> and $\alpha$ -Cr<sub>2</sub>O<sub>3</sub> surfaces

The major interest of this thesis is the study on the interactions occurring between an organic liquid phase, surrogate of the deposit precursors, and a metal-oxide solid phase, representative of the metallic materials commonly coating the engine injection systems.

In the previous sections, firstly we reported the bibliographic review on the occurrence of the formation of liquid deposits, followed by an overview of the main experimental and theoretical works centered on the adsorption of an organic phase above metal-oxide substrates. In this section, we will focus more on the metallic surfaces considered in this study and how we chose to model them accordingly in our simulations.

As metallic surfaces, we opted for aluminium and stainless steel since both materials are hugely used as coatings in the transport sector. They both exhibit corrosion resistance due to the presence of a protective passive oxide film [1, 2].

The aluminum oxide known as alumina (Al<sub>2</sub>O<sub>3</sub>) represents one of the most important materials in earth's surface while aluminium (Al) is one of the most abundant elements in the earth's crust [3]. Alumina has a high insulating property (ceramic) and structural stability over a large temperature range and presents a versatility for a wide range of scientific and technological applications [4, 5].

Alumina is found in nature in the crystallographic structure of corundum, represented as  $\alpha$ -Al<sub>2</sub>O<sub>3</sub>. In its pure form,  $\alpha$ -Al<sub>2</sub>O<sub>3</sub> (or corundum) is an important ceramic material. The  $\alpha$ -Al<sub>2</sub>O<sub>3</sub> is widely used in a range of industrial areas, such as optics, electronics and ceramic applications [6]. For instance,  $\alpha$ -alumina is widely used as a substrate for the growth of thin metal, semiconductor and insulator films in the microelectronics industry [7, 8].

The chromium oxide known as chromia ( $\text{Cr}_2\text{O}_3$ ) is an antiferromagnetic insulator that can also be found with the corundum crystallographic structure  $\alpha\text{-Cr}_2\text{O}_3$ . Very similarly to its aluminium counterpart, the corundum-type  $\alpha\text{-Cr}_2\text{O}_3$  has a variety of applications in various technologies, as catalyst [9, 10], protective layer (corrosion and wear resistance of stainless steel [11]), as an adhesion promoter [11] to cite a few of them. The protective passive film layer on Fe-Cr stainless steel alloys is composed of an inner  $\text{Cr}_2\text{O}_3$  oxide film layer and an outer hydroxylated layer [12]; also, according to ref. [12], model studies on monocrystalline Fe-22Cr alloys have evidenced the formation of an inner  $\alpha\text{-Cr}_2\text{O}_3$  (0001) oxide film at the interface with water.

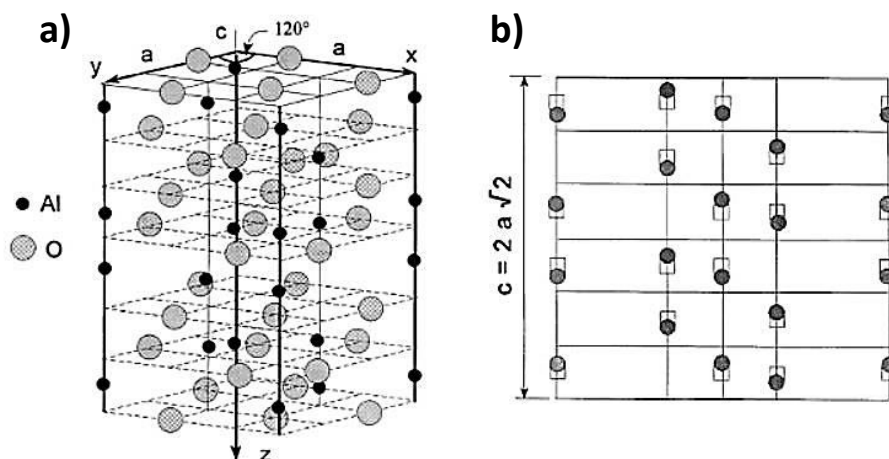
In the next paragraph, we proceed the description of these two metal-oxides with the introduction of the  $\alpha$ -(0001)  $\text{Al}_2\text{O}_3$  and  $\alpha$ -(0001)  $\text{Cr}_2\text{O}_3$  surfaces.

## **3.2 Introduction to $\alpha$ -(0001) $\text{Al}_2\text{O}_3$ and $\alpha\text{-Cr}_2\text{O}_3$ surfaces**

### **3.2.1 Bulk structures of $\alpha\text{-Al}_2\text{O}_3$ and $\alpha\text{-Cr}_2\text{O}_3$**

Bulk  $\alpha\text{-Al}_2\text{O}_3$  (space group  $R3c$  [13]) can be described as a hexagonal unit cell containing six formula units. It is also frequently described by a rhombohedral unit cell containing two formula units of  $\text{Al}_2\text{O}_3$ .

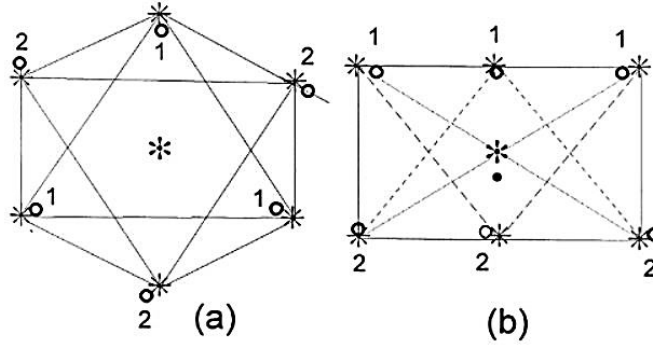
The structure of  $\alpha\text{-Al}_2\text{O}_3$  is closely related to the ideal corundum structure ( $c/a = 2\sqrt{2}$ ) shown in **Figure 27a**.



**Figure 27: a) Idealized corundum structure for alumina showing the location of the aluminium and oxygen ions in the hexagonal unit cell. The angle between the x- and y- axes is  $120^\circ$ . The aluminium ions are located on the heavy vertical lines, while the oxygen ions are located in the intersection of horizontal (dashed) lines. b) Cross-section of the idealized (white squares) and real (dark circles) arrangement of aluminium ions in the hexagonal unit cell of alumina. The value  $c = 2a\sqrt{2}$  is used for the idealized structure. Images taken from ref. [13].**

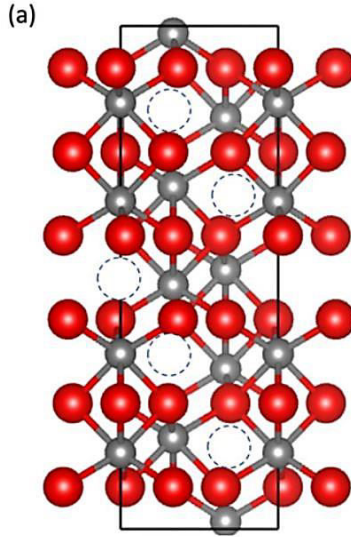
Here, the  $\text{Al}^{3+}$  ions lie along the c-axis in coplanar layers, filling  $2/3$  of the octahedral holes between layers of  $\text{O}^{2-}$  ions. These oxide layers are equidistant from each other, spaced  $1/6$  of the unit cell side  $c$  apart. In this structure, the  $\text{Al}^{3+}$  ions are situated halfway between two oxide layers. In the oxygen layers themselves, the  $\text{O}^{2-}$  ions are equidistant from each other, forming an exactly hexagonal arrangement.

In reality, the  $\text{Al}^{3+}$  ions in  $\text{Al}_2\text{O}_3$  do not form coplanar layers, but are buckled as shown in **Figure 27b**. As a result, the two neighboring oxide layers to each  $\text{Al}^{3+}$  ion are located at different distances, as can be clearly seen in the cross-section shown in **Figure 28b**. This displacement divides the six nearest neighbor oxygen ions into two triads of equivalent ions located in two adjacent layers. In the oxide layers, the  $\text{O}^{2-}$  ions are also slightly shifted laterally away from the ideal positions. In the  $\text{O}^{2-}$  layer furthest from  $\text{Al}^{3+}$  ion, each triad of oxide ions shrinks evenly towards the c-axis. In the other layer, closest to  $\text{Al}^{3+}$  ion, each triad is expanded and twisted about the c-axis (**Figure 28a**).



**Figure 28:** Top (a) and cross-section (b) of a set of O-Al-O layers in the ideal and real alumina hexagonal unit cell showing the octahedron of the nearest O neighbors [idealized (\*) and real (°) case] to an Al ion [idealized (\*) and real (•) case]. Image taken from ref. [13].

The  $\alpha$ -Cr<sub>2</sub>O<sub>3</sub> bulk is antiferromagnetic oxide with the corundum structure and space group R3c [14] (same as  $\alpha$ -Al<sub>2</sub>O<sub>3</sub>). **Figure 29** shows the  $\alpha$ -Cr<sub>2</sub>O<sub>3</sub> unit cell comprised of a hexagonal closed-packed O matrix where two thirds of the octahedral sites are occupied by Cr cations and one third are vacant, similarly to what shown in **Figure 27a** for the  $\alpha$ -Al<sub>2</sub>O<sub>3</sub>. An O anion in the crystal structure is enclosed by four nearest neighboring Cr cations forming four-fold (tetrahedral) coordination. The Cr ions in the  $\alpha$ -Cr<sub>2</sub>O<sub>3</sub> have an antiferromagnetic spin configuration below 307 K [15] and a magnetic structure corresponding to (++--) spin sequence along the [111] axis and overall zero magnetic moment for the unit cell [16].

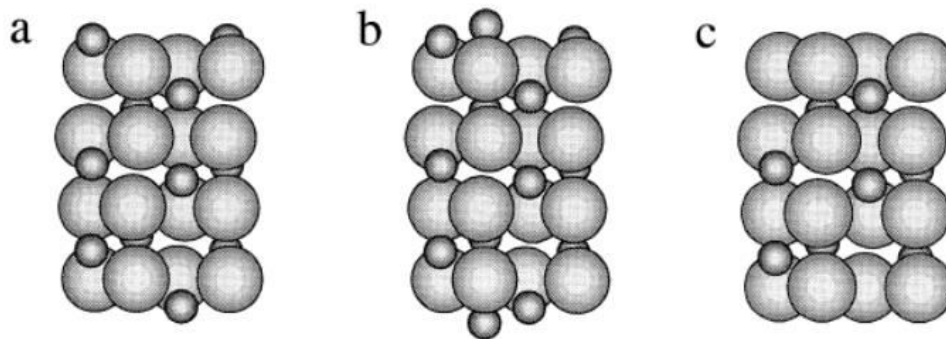


**Figure 29:** Atomistic structure presenting  $\alpha$ - $\text{Cr}_2\text{O}_3$  unit cell where unoccupied octahedral sites are shown in dashed circles. Image taken from ref. [17]

### 3.2.2 Surface terminations of $\alpha$ -(0001) $\text{Al}_2\text{O}_3$ and $\text{Cr}_2\text{O}_3$

Both  $\alpha$ - $\text{Al}_2\text{O}_3$  and  $\alpha$ - $\text{Cr}_2\text{O}_3$  corundum structure in the [0001] direction can be depicted as a hexagonal planar layers of O being separated by two closely-spaced layers of  $M$ , where  $M$  represents the metal cation characterizing the given metal oxide. For these corundum-type oxides, in order to maintain the  $M_2\text{O}_3$  stoichiometry in their (0001) surface, each O layer has to contain 3 times as many atoms as each  $M$  layer; thus in this (0001) direction, the stacking can be simply represented as  $-\text{O}_3\text{-}M\text{-}M\text{-}\text{O}_3\text{-}M\text{-}M\text{-}$ .

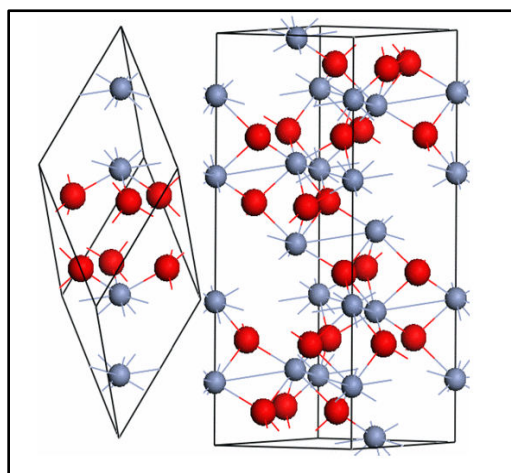
In the case where the (0001) surface maintains a structure similar to the bulk, three potential terminations can be found: metal-single-layer-terminated  $-M\text{-}\text{O}_3\text{-}M\text{-}$ , oxygen-terminated  $-\text{O}_3\text{-}M\text{-}M\text{-}$ , metal-bilayer-terminated  $-M\text{-}M\text{-}\text{O}_3$  (**Figure 30** below).



**Figure 30: Representations of three distinct surfaces that can be obtained by  $M_2O_3$  (0001) perpendicular to the [0001] direction shown along [2110]: a) the stoichiometric, or metal-single-layer-terminated (-M-O<sub>3</sub>-M-); b) the oxygen-rich, or oxygen-terminated (-O<sub>3</sub>-M-M-); c) The M-rich, or metal-bilayer-terminated (-M-M-O<sub>3</sub>). Large ball : Cr or Al, small balls : O. Image taken from ref.[18]**

By exploring their electrostatic features, it can be found that both the -O<sub>3</sub>-M-M- and -M-M-O<sub>3</sub> surfaces present polarity that lead to a divergent electrostatic potential in the bulk; by contrast, the -M-O<sub>3</sub>-M- surface does not [18–22].

Corundum-type surfaces such as  $\alpha$ -Cr<sub>2</sub>O<sub>3</sub> and  $\alpha$ -Al<sub>2</sub>O<sub>3</sub> crystallize in a structure which can be described by a conventional hexagonal unit with six  $M_2O_3$  formula units (30 atoms). Each hexagonal unit cell contains 12 metallic atoms, among which every four atoms form a subunit corresponding to the rhombohedral primitive cell. For the hexagonal unit cell (**Figure 31** below), the atoms are stacked along the (0001) direction according to the sequence R-M-M-O<sub>3</sub>-M-M-O<sub>3</sub>-R, where  $R$  represents the continuing sequence in the bulk.



**Figure 31: Rhombohedral primitive cell of Cr<sub>2</sub>O<sub>3</sub> and Al<sub>2</sub>O<sub>3</sub> (left) together with the hexagonal unit cell (right). Smaller blue (lighter) spheres represent Cr/Al atoms; larger red (darker) spheres display the O atom. Figure taken from ref. [35]**

### 3.2.3 Experimental studies of $\alpha$ -(0001) $\text{Al}_2\text{O}_3$ and $\text{Cr}_2\text{O}_3$ surfaces

Even though the corundum surface  $\alpha\text{-Al}_2\text{O}_3$  covers a huge importance in many different usages, the surface structure and even the structure stoichiometry still represents a matter of strong controversy. According to ref. [22], the principal reason for this inconvenience is traceable from the difficulty to prepare a clean and uniform surface with specific, well-defined structures and stoichiometries.

For Goniakowski et al. [20], (0001) surfaces of alumina have been the subject of numerous experimental and theoretical studies in the past. From the experimental point of view, earlier ion-scattering [23, 24] and x-ray [24] experiments concluded that under UHV and ambient conditions the surface was unreconstructed ( $1 \times 1$ ) and Al-terminated.

In their work, Ahn et al. [23] implemented the techniques of time-of-flight scattering and recoiling spectrometry (TOF-SARS), LEED and classical ion trajectory simulations in their analyses with the aim to characterize the elemental composition in the outermost two atomic layers of  $\alpha\text{-Al}_2\text{O}_3$ . From their analyses, they found that hydrogen was detected on the surface by TOF-SARS and these H atoms were proposed to come from the bulk.

Soares et al. [25] confirmed from their LEED analysis on  $\alpha\text{-Al}_2\text{O}_3$  (0001) that hydrogen adsorption on Al-terminated surface reduced the interlayer contraction at the surface, which was also reported by Ahn et al. [23].

The conclusion on Al-terminated surface as the most stable surface termination under UHV and ambient condition for corundum  $\alpha\text{-Al}_2\text{O}_3$  was also reached by the ion-scattering experiments carried out by Suzuki et al. [26]. While earlier tensor-LEED analysis [13] proposed a mixture of Al- and O- terminated terraces as a best fit of the experimental data, a more recent analysis [25, 27] strongly favors the Al termination.

About corundum-type  $\alpha\text{-Cr}_2\text{O}_3$  surface, Priyantha et al. [28] studied the epitaxial growth of chromium oxide films on Ag(111) and characterized them through LEED, X-ray photoelectron spectroscopy (XPS) and X-ray photoelectron diffraction (XPD). From their analyses, they found that chromium oxide with thickness greater than approximately  $12 \text{ \AA}$  show a pattern consistent

with  $\alpha$ -Cr<sub>2</sub>O<sub>3</sub> (0001) surface, conclusion further confirmed by their XPD results that identified the surface termination as a single Cr layer with an inward relaxation of 50%.

In the work of Bikondoa et al. [29], surface X-ray diffraction (SXRD) was employed to quantitatively assess the surface structure of  $\alpha$ -Cr<sub>2</sub>O<sub>3</sub> as a function of oxygen partial pressure at room temperature. From their analysis, they found that the surface geometry can be modified in the presence of oxygen at room temperature; a Cr<sub>0,22</sub>-Cr<sub>0,31</sub>-O<sub>3</sub>- termination was seen at UHV conditions and a chromyl-topped O<sub>0,38</sub>=Cr<sub>0,38</sub>-O<sub>3</sub>- structure was observed at an O<sub>2</sub> partial pressure of  $1 \times 10^{-2}$  mbar. However, they stated ab-initio theoretical calculations [30, 31] have not predicted either of the two oxygen-terminated surfaces.

In the work of Rohr et al. [32], the surface structure of Cr<sub>2</sub>O<sub>3</sub> (0001) was investigated by quantitative LEED in UHV conditions and molecular dynamics simulations. From their LEED analysis, the surface was found as chromium terminated and, furthermore, they found that both experimental and numerical methods indicated the presence of strong vertical relaxations at and near the surface. According to Rohr et al. [32], these relaxations were concomitant with a charge reduction and depolarization, which stabilized the surface and yielded energies close to values found for non-polar oxide surfaces.

### 3.2.4 DFT modeling of $\alpha$ -(0001) Cr<sub>2</sub>O<sub>3</sub> and Al<sub>2</sub>O<sub>3</sub> surfaces

In the literature, it is possible to find several theoretical studies carried out with the intent of investigating about surface properties of Al<sub>2</sub>O<sub>3</sub> and Cr<sub>2</sub>O<sub>3</sub> [18, 22, 30, 34–36]. The main objective of these researches was to determine the surface terminations of  $\alpha$ -(0001)Al<sub>2</sub>O<sub>3</sub> and  $\alpha$ -(0001)Cr<sub>2</sub>O<sub>3</sub> as a function of the chemical potential (corresponding to the partial pressure) of both oxygen [22, 37] or water [34, 38].

The existence of one chromium or aluminium terminations is well established in the literature for both  $\alpha$ -Al<sub>2</sub>O<sub>3</sub> and  $\alpha$ -Cr<sub>2</sub>O<sub>3</sub> surfaces [18, 22, 30, 35–37].

In their work Tepesch et al. [18] examined different  $\alpha$ -(0001)Al<sub>2</sub>O<sub>3</sub> surface terminations, confirming that the  $\alpha$ -(0001)Al<sub>2</sub>O<sub>3</sub> stoichiometric surface is the lowest energy surface relative to the oxygen-terminated or 2-Al-terminated surfaces and that their result was in agreement with

ion-scattering results by Ahn et al. [23]. Tepesch et al. [18] concluded their analysis by confirming that the most stable surface termination for the  $\alpha$ -Al<sub>2</sub>O<sub>3</sub> represented by the Al-terminated.

According to Wang et al.[22], for the systems containing just aluminum and oxygen the only one low energy surface stoichiometry is given by the AlO<sub>3</sub>Al-R structure. They concluded that this stability extends across the entire range of the oxygen chemical potential, even up to the limit where an O<sub>2</sub> condensate would form on the surface.

For surfaces like  $\alpha$ -Cr<sub>2</sub>O<sub>3</sub> and  $\alpha$ -Fe<sub>2</sub>O<sub>3</sub>, the main interest lies in the role of their strong electronic correlations that significantly characterize their physical properties since they have antiferromagnetic and insulator features. However, it is well-known that DFT experiences considerable difficulties when trying to achieve a correct description of such strongly-correlated materials [30, 39]. To correct the strong electronic correlation describing these kind of materials, the DFT+*U* method in the form proposed by Liechtenstein and Dudarev et al.[39–41] is generally used (cf.§2.4.3).

Since the DFT+*U* method ensured to better depict the electronic and magnetic nature of chromia, also for this thesis when speaking about the DFT method implemented, it will be implicitly reminded to the DFT+*U* method.

The hexagonal lattice characterizing Cr<sub>2</sub>O<sub>3</sub>-Cr (0001) surface consists of three rhombohedral primitive cells, in which only three antiferromagnetic spin configurations are possible: A (+ + – –), B (+ – – +) and C (+ – + –). As verified in multiple works [30, 34, 37], the spin ground state of Cr<sub>2</sub>O<sub>3</sub> is identified with the (CCC), which results in a total magnetic moment equal to zero.

Rohrbach et al. [30] analyzed the structural, electronic and magnetic properties of the polar (0001) surface of  $\alpha$ -Cr<sub>2</sub>O<sub>3</sub> through DFT+*U* approach, obtaining reasonable results for the description of the behavior of 3d Cr electrons present in the band structure. In their work, they concluded that the most stable surface of Cr<sub>2</sub>O<sub>3</sub> is Cr-terminated [30].

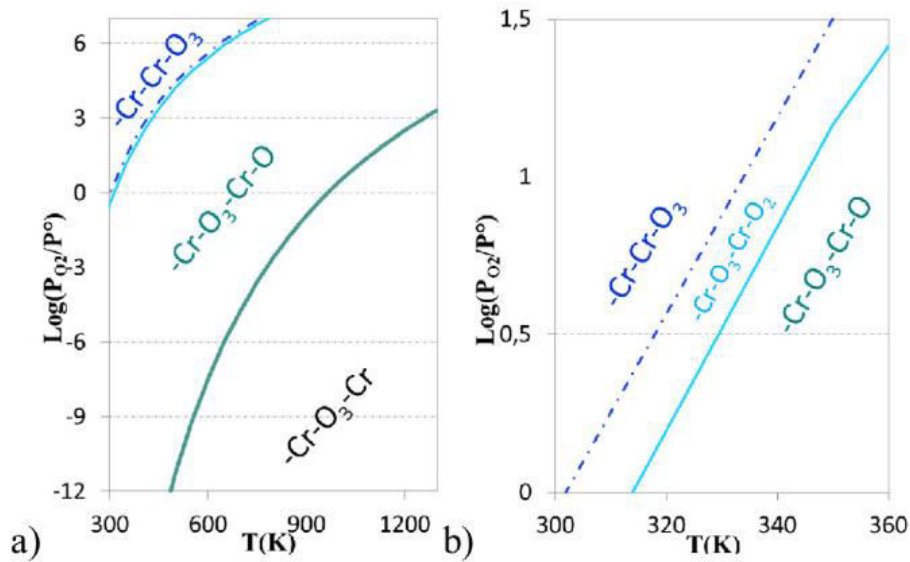
In the work of Souvi et al. [37], different  $\alpha$ -(0001)Cr<sub>2</sub>O<sub>3</sub> surface terminations were considered in order to find the most stable one. Their results confirmed that between the two stoichiometric Cr<sub>2</sub>O<sub>3</sub> configurations (the Cr-terminated and O-terminated respectively), the oxygen terminated surface presented an energy surface greater than the chromium terminated, thus the latter being the most stable.

From this literature study of  $\alpha$ -(0001)  $\text{Al}_2\text{O}_3$  and  $\text{Cr}_2\text{O}_3$  surfaces, we decided in this thesis to consider only the Al-terminated and Cr-terminated surfaces as reference for the study of the adsorption of the organic molecules on the metallic surface.

Both references [37, 42] for  $\alpha$ - $\text{Al}_2\text{O}_3$  and  $\alpha$ - $\text{Cr}_2\text{O}_3$  conducted a theoretical study by calculating the Gibbs free energy of both (0001) surfaces in equilibrium with a realistic environment containing both oxygen and hydrogen species. Their objective was to determine the stability of the surface terminations of  $\alpha$ -(0001)  $\text{Al}_2\text{O}_3$  and  $\alpha$ -(0001)  $\text{Cr}_2\text{O}_3$  as a function of the partial pressure of oxygen and hydrogen, respectively.

About the  $\alpha$ -(0001) $\text{Al}_2\text{O}_3$  surface, Marmier et al. [42] confirmed that the O-terminated surface can only be stabilized in the presence of hydrogen and this same conclusion was also made by Wang et al. [22].

About the  $\alpha$ -(0001) $\text{Cr}_2\text{O}_3$  surface, Souvi et al. [37] discovered that below 600 K the adsorption of  $\text{O}_2$  is favored whatever the measured oxygen partial pressure and this would lead to the formation of a chromyl termination  $\text{CrO}_3\text{-Cr-O}$ . However, in case of low oxygen partial pressures, the Cr-terminated surface remains the most stable one. Similarly, in case of higher temperature (>1200 K), the only stable termination surface is  $\text{-CrO}_3\text{-Cr}$  whatever the oxygen partial pressure is (Figure 32).

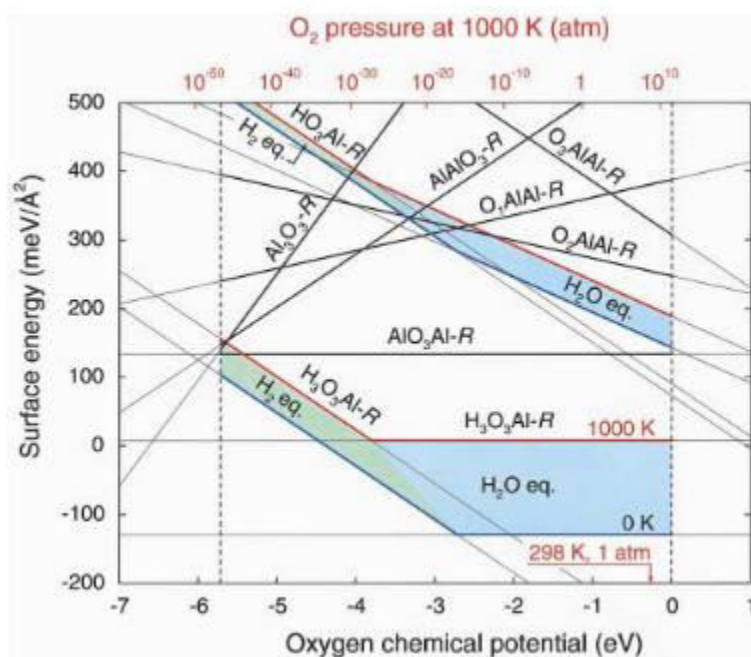


**Figure 32:** a) (P,T) phase diagram of chromia in presence of  $\text{O}_2$  and b) a zoom to show the domain stability of the 3 different chromia terminations. Dotted blue curve:  $\text{-Cr-Cr-O}_3$ ; Light-blue curve:  $\text{-Cr-O}_3\text{-Cr-O}_2$ ; Green curve:  $\text{-Cr-O}_3\text{-Cr-O}$ . Figure taken from ref. [11]

### 3.2.5 Hydration condition

It is indeed well-known that, when certain oxide surfaces are exposed to water, they tend to react with water molecules that in turn dissociate and form hydroxyl groups at the surface [43–45] and, from what has been mentioned above, this behavior certainly concerns both the aluminum (which is modeled by  $\text{Al}_2\text{O}_3$ ) and the stainless steel (being its protective layer composed by  $\text{Cr}_2\text{O}_3$  [34, 45–48]).

As already stated before, for Wang et al. [22] the addition of hydrogen to the surface dramatically lowers the free energy and this new surface results to be much more stable than the O<sub>3</sub>-terminated surface at all oxygen partial pressures. As observed in **Figure 33**, the saturation of all surface oxygens with hydrogen as indicated by the H<sub>3</sub>O<sub>3</sub>Al-R line results in the lowest free energy and greatest stability across the entire range of physically realistic conditions.



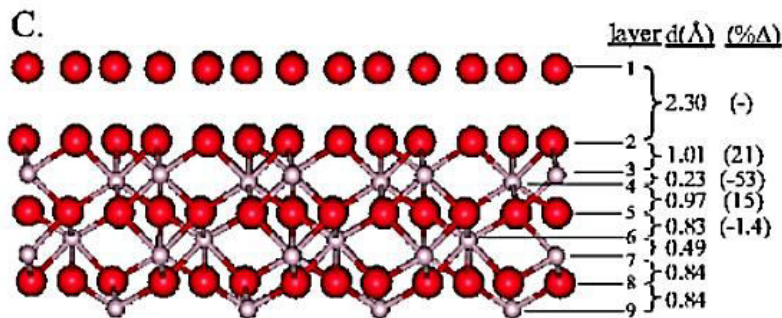
**Figure 33: Surface energies of different  $\text{Al}_2\text{O}_3$  (0001) surface terminations. The dashed vertical lines indicate the allowed range of the oxygen chemical potential,  $\mu_{\text{O}}$ . Values in red indicate examples of higher temperatures and pressures. The green and blue regions indicate the range where hydrogen on the surface is in equilibrium with  $\text{H}_2$  and  $\text{H}_2\text{O}$ , respectively, from 0 K up to 1000 K and 1 atm pressure (red lines). Figure taken from ref. [22]**

For  $\alpha$ -Al<sub>2</sub>O<sub>3</sub> (0001) surface, many experimental works have been conducted to investigate the structural changes in case of water adsorption, pointing out that the surface structure of  $\alpha$ -Al<sub>2</sub>O<sub>3</sub> could be fairly different under UHV and in ambient conditions [20].

An example is the study conducted by Eng et al. [49], where the structure of the hydrated  $\alpha$ -Al<sub>2</sub>O<sub>3</sub> (0001) surface was determined in the presence of water vapor at 300 K by crystal truncation rod (CTR) diffraction. From their analysis, it appeared that the structure of the hydrated  $\alpha$ -Al<sub>2</sub>O<sub>3</sub> (0001) was found to correspond to a fully hydrogenated O-terminated surface, with a 53% contracted double aluminium layer directly below (**Figure 34**).

This results obtained from Eng et al. [49] differed markedly from previous studies of the UHV-prepared clean  $\alpha$ -Al<sub>2</sub>O<sub>3</sub> (0001) surface in which the best model was the single Al-terminated surface [23]. However, it has also been shown that the clean  $\alpha$ -Al<sub>2</sub>O<sub>3</sub> (0001) surface readily reacts with water [50].

A more recent work on the investigation of the adsorption and reaction of water on a single crystal  $\alpha$ -Al<sub>2</sub>O<sub>3</sub> (0001) in UHV and ambient conditions was led by Petrik et al. [51]. For their study, they employed TPD, infrared reflection absorption spectroscopy (IRAS) and diffuse reflectance infrared Fourier transform spectra (DRIFTS) and other surface science techniques.



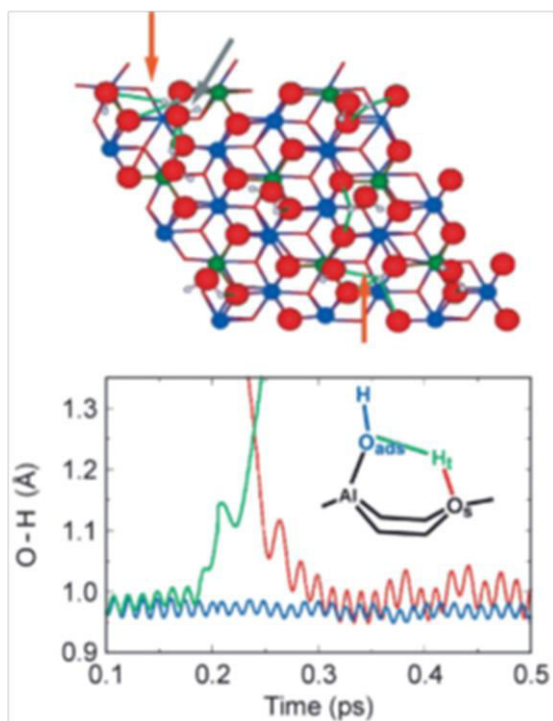
**Figure 34:** Slide view of a section of the  $\alpha$ -Al<sub>2</sub>O<sub>3</sub> unit cell showing the atomic layering sequence and layer spacings ( $d$ ) along the [0001] direction of the best fit relaxed surface model for the oxygen terminated surface from reference [49] including the oxygen overlayer.

From their results on water adsorption on  $\alpha$ -Al<sub>2</sub>O<sub>3</sub> (0001) in UHV, IR spectroscopy showed that molecular water is present at coverages as low as 1 water molecule per surface aluminium ion, but at the same time their results showed no evidence of the surface hydroxyls expected from

dissociation. Also, they found that water films completely cover the  $\alpha\text{-Al}_2\text{O}_3$  (0001) when the coverage reached  $\sim 1\text{ML}$  and the films grew layer-by-layer for at least the first two layers. They observed that water desorbed from  $\alpha\text{-Al}_2\text{O}_3$  (0001) over a wide temperature range, leaving a hydroxyl-free surface after heating above  $\sim 800\text{ K}$ .

Along with the aforementioned experimental studies, in the last decades many ab-initio works have been conducted on the hydration states of  $\alpha\text{-Al}_2\text{O}_3$  (0001) surface [38, 52, 53].

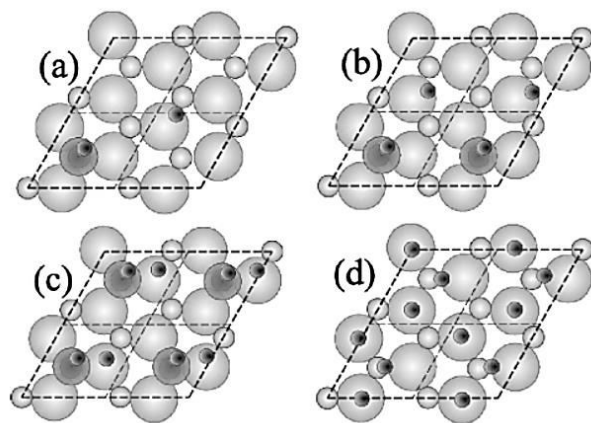
According to the work of Hass and coworkers [52] on the  $\alpha\text{-Al}_2\text{O}_3$  (0001) surface, both molecular and dissociative  $\text{H}_2\text{O}$  adsorption modes were identified, with the latter favored by  $\sim 10\text{ kcal/mol}$ . Plus, they conducted simulations at intermediate  $\text{H}_2\text{O}$  coverages, where the following trends were reported: (1) spontaneous unimolecular and (2)  $\text{H}_2\text{O}$ -mediated dissociation events, as well as (3) the diffusion and hydrogen bonding of physisorbed  $\text{H}_2\text{O}$  and (4) an additional proton transfer reaction between adsorbed  $\text{H}_2\text{O}$  and OH species. The authors also conducted ab initio molecular dynamics [54] at the coverage of 1 ML (one water molecule per surface Al) during 1 ps at 300 K (**Figure 35**).



**Figure 35:** Snapshot of the 300 K dynamical simulation of an  $\alpha\text{-Al}_2\text{O}_3$  (0001) surface plus nine  $\text{H}_2\text{O}$  molecules taken after 1 ns. Red, blue and green spheres indicate O, interior Al and surface Al atoms respectively. Green line indicates H bonds; orange arrows indicate the 1-4 chemisorbed species. Image taken from ref. [54].

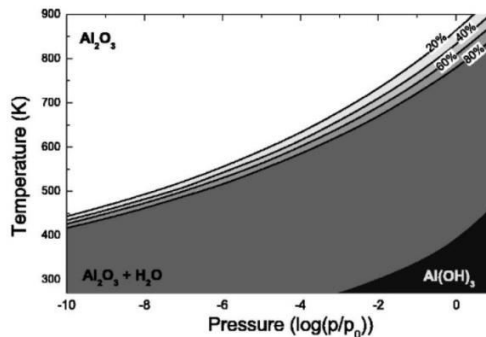
They found that the molecular state of water was the most frequent. They also evidenced two types of surface H bonds stabilizing the OH groups: a H bond acceptor from a proton adsorbed on a surface oxygen, and also a H bond acceptor from a vicinal physisorbed water molecule. The authors also observed that during the run, one H<sub>2</sub>O molecule “desorbed” early on from its molecular adsorption site and began to diffuse laterally along the surface in a precursor-like physisorbed state.

Łodziana et al. [53] implemented DFT calculations for the investigation of the stability of the hydroxylated (0001) surface of  $\alpha$ -Al<sub>2</sub>O<sub>3</sub>. They reported the most stable configurations at different water coverages by using a (2x2) supercell (**Figure 36** below).



**Figure 36:** Surface of corundum at various water coverages considered in reference [53]: (a) 2.6 OH/nm<sup>2</sup>, (b) 5 OH/nm<sup>2</sup>, (c) 10.0 OH/nm<sup>2</sup>, (d) gibbsite-like surface terminated by hydrogen. Large spheres represent oxygen, small grey spheres are for aluminium and dark grey are hydrogen. The darker larger spheres represent adsorbed oxygen.

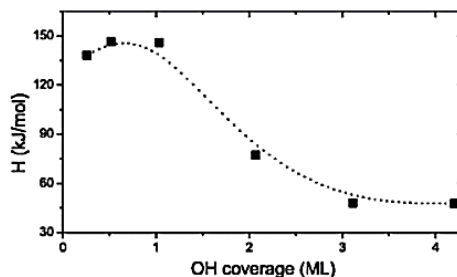
According to Łodziana et al. [53], for coverages lower than 1 ML, water dissociates on the surface and also water adsorption creates a large surface distortion accompanied by migration of the aluminium cations into the subsurface region. Plus, at 1 ML every surface Al cation is already saturated with one OH group, giving a total coverage of 10 OH/nm<sup>2</sup>. This surface was referred to as fully-hydroxylated surface [53]. In addition to the corundum hydroxylated surface, they consider a gibbsite-like surface, named Al(OH)<sub>3</sub>. The authors also propose a phase diagram of the different terminations [53] (**Figure 37**).



**Figure 37:** The phase diagram of the  $\alpha$ - $\text{Al}_2\text{O}_3$  (0001) surface with respect to the pressure of water vapor and temperature. White region is a clean Al-terminated surface. The contours are plotted at every 1/5 ML. The black region represents thermodynamic conditions where the  $\text{Al}(\text{OH})_3$  surface is dominating. Image taken from ref. [53].

If we refer to the  $P_{\text{H}_2\text{O}}/P^\circ$  value corresponding to the experimental conditions we are interested in (e.g. water content of 1000ppm, which corresponds to a  $P_{\text{H}_2\text{O}}/P^\circ = 0.0035$  atm) in the temperature range 400-500 K, we observe that the termination is the  $\text{Al}_2\text{O}_3 + \text{H}_2\text{O}$ , meaning that the surface is of corundum type (i.e. Al terminated) covered with a mixed OH and water layer. For this reason, in the framework of this thesis we decided to study the (0001)- $\text{Al}_2\text{O}_3$ - $\text{Al}(\text{OH})_3$  surface where each  $\text{Al}_s$  atom of the outermost surface layer is linked with three chemisorbed water molecules.

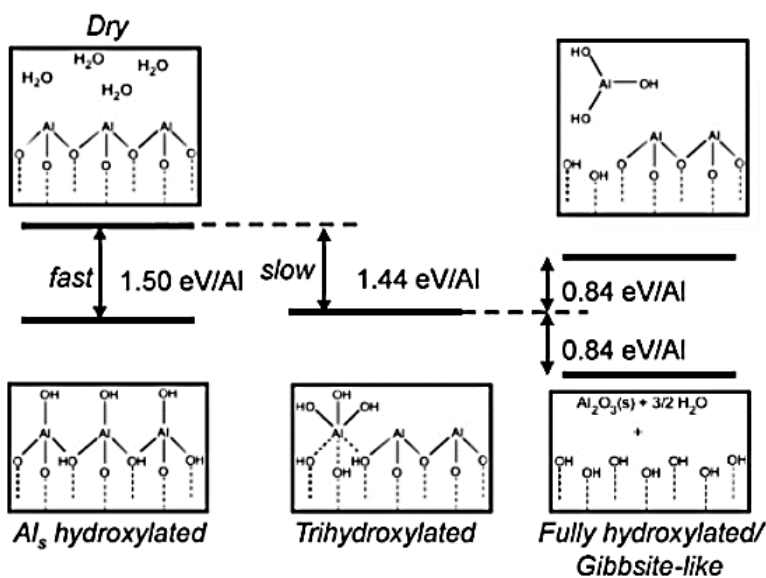
In addition, Łodziana et al. [53] calculated the heat of adsorption of water on the (0001) surface of  $\alpha$ - $\text{Al}_2\text{O}_3$  and  $\text{Al}(\text{OH})_3$  that are reported in **Figure 38** below. They observed two distinct regions for the  $\alpha$ - $\text{Al}_2\text{O}_3$  (0001) surface: below 1 ML, where water dissociates and forms a strong bond with the surface and above 1 ML, where a rapid drop of adsorption energy reflects weakly physisorbed molecules.



**Figure 38:** The differential heat of adsorption of water on the (0001) surface of  $\alpha$ - $\text{Al}_2\text{O}_3$  (0001). Dissociation adsorption occurs at coverage from 0 to 10  $\text{OH}/\text{nm}^2$  (0 to 1 ML); at higher coverages, molecular adsorption is preferred. Image taken from ref.[53].

Another noteworthy ab-initio work to mention in the merits of DFT investigation of  $\alpha$ - $\text{Al}_2\text{O}_3$  (0001) hydroxylation is the led by Ranea et al. [38]. They implemented progressive multiple water dissociation steps starting from the hydrogen-free stoichiometric surface to the fully-hydroxylated, gibbsite-like surface, aiming to report the different energies barriers calculated at each successive hydroxylation step.

They reported an overall picture (**Figure 39** below) which summarizes what they observed from their DFT results. According to them [38], the hydrogen-free, dry  $\alpha$ - $\text{Al}_2\text{O}_3$  (0001) surface readily adsorbs and reacts one water per surface Al site with a nearly coverage-independent energy. This obtained surface can then adsorb molecular water exothermically, but dissociative adsorption to a more highly hydrated surface sites has a small thermodynamic driving force and is relatively slow. The energetics of the final removal of fully reacted  $\text{Al}_s$  depends on the disposition of the hydrated aluminium and could be endo- or exothermic. Once the surface becomes fully hydroxylated, reconstitution of the dry surface proceeds only by transport of Al from the bulk or solution; processes that are likely to have high activation energies.



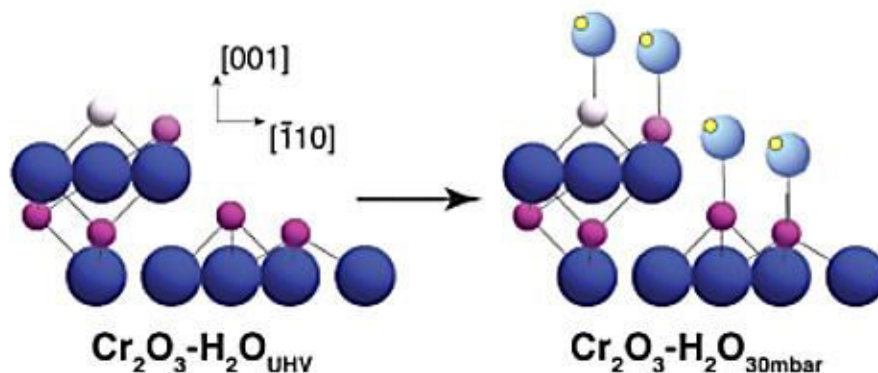
**Figure 39:** Schematic of overall  $\alpha$ - $\text{Al}_2\text{O}_3$  (0001) reaction landscape reported in ref. [38].

In the work of Henderson and Chambers [55] the interaction of water with the (0001) surface of  $\alpha$ - $\text{Cr}_2\text{O}_3$  was examined with temperature programmed desorption (TPD), high resolution electron energy-loss spectroscopy (HREELS) and XPS. From their results, they observed that the  $\alpha$ - $\text{Cr}_2\text{O}_3$

(0001) surface is very active for dissociation of water under UHV conditions, where it adsorbs on  $\alpha\text{-Cr}_2\text{O}_3$  (0001) in both molecular and dissociative states, with the former desorbing in TPD at 295 K and the latter at 345 K. In addition, their TPD measurements and XPS data suggested that each surface  $\text{Cr}^{+3}$  atom had the capacity to bind two water molecules, one in a molecular state and one in a dissociative state. According to their HREELS analysis, the water in dissociative state was observed to be comprised of two distinct OH groups, one of which is a terminal group and the other of which is presumably a bridging group.

More recently, the research group of Ahmed et al. [56] employed the surface X-ray diffraction (SXRD) to investigate the surface structure of  $\alpha\text{-Cr}_2\text{O}_3$  (0001) as a function of water partial pressure at room temperature. They addressed that, till the date of their work, most of the measurements have been conducted in ultra-high vacuum (UHV), limiting their relevance to the understanding of corrosion performance of stainless steel alloys in engineering environments.

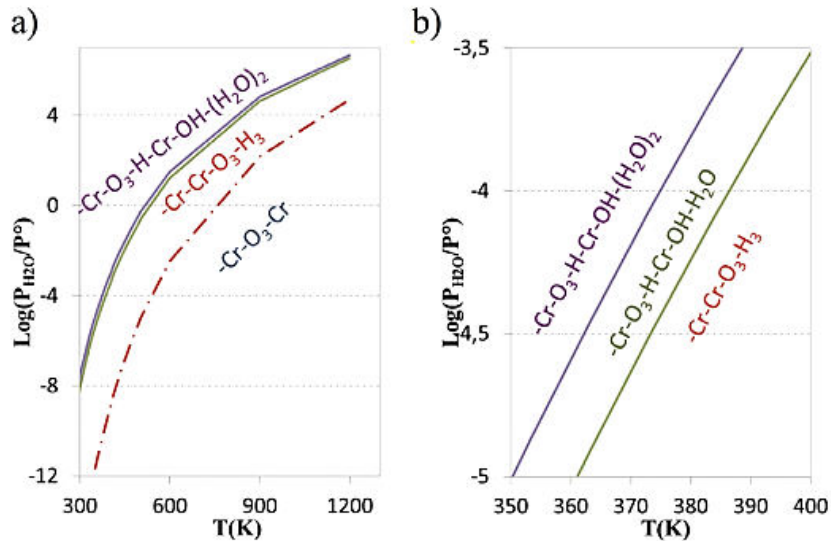
Ahmed et al. [56] compared their results to the theoretical work conducted by Sharkas et al. [34] since they studied the structural changes of  $\alpha\text{-Cr}_2\text{O}_3$  (0001) surface as a function of both  $\text{H}_2\text{O}$  partial pressure and temperature through an ab-initio modeling approach. Ahmed et al. [56] stated in their work that the theoretical structures obtained by Sharkas et al. [34] are found to be consistent with experimental characterization conducted under UHV conditions in thin films of  $\alpha\text{-Cr}_2\text{O}_3$  (0001) exposed to  $\text{H}_2\text{O}$  at room temperature, observing that water dissociation was evident in these conditions. In addition, the existence of two distinct OH species and of interadsorbate hydrogen bonding seemed to be apparent from their vibrational data.



**Figure 40: Cartoon of the variation in surface termination of  $\alpha\text{-Cr}_2\text{O}_3$  (0001) with water partial pressure, as determined through analysis of the SXRD data acquired from  $\text{Cr}_2\text{O}_3\text{-H}_2\text{O}_{\text{UHV}}$  and  $\text{Cr}_2\text{O}_3\text{-H}_2\text{O}_{30\text{mbar}}$ . Larger (smaller) spheres are oxygen (chromium) atoms; the smallest spheres are hydrogen atoms, which are employed to indicate location of adsorbed OH/ $\text{H}_2\text{O}$  [56].**

With all these considerations, Ahmed et al. [56] tried to validate experimentally the validity of the theoretical study of Costa et al. [34] and conducted a SXRD analysis at UHV and at H<sub>2</sub>O partial pressure of 30 mbar on the  $\alpha$ -Cr<sub>2</sub>O<sub>3</sub> (0001) at room temperature, the first examined system labeled as Cr<sub>2</sub>O<sub>3</sub>-H<sub>2</sub>O<sub>UHV</sub> and the second system as Cr<sub>2</sub>O<sub>3</sub>-H<sub>2</sub>O<sub>30mbar</sub>, respectively (see **Figure 40** below).

From their SXRD data, they observed that in the presence of 30 mbar of water (i.e. Cr<sub>2</sub>O<sub>3</sub>-H<sub>2</sub>O<sub>30mbar</sub> system), each under-coordinated surface Cr atom becomes decorated with a single atop OH/H<sub>2</sub>O species; however, they observed an unexpected lack of OH/H<sub>2</sub>O on Cr<sub>2</sub>O<sub>3</sub>-H<sub>2</sub>O<sub>UHV</sub> system since according to Henderson and Chambers [55] the presence of adsorbed OH at room temperature was found even in the UHV in case of H<sub>2</sub>O adsorption on  $\alpha$ -Cr<sub>2</sub>O<sub>3</sub> (0001). Ahmed et al. [56] hypothesized that this discrepancy could be due to the fact that the work mentioned in reference [55] was undertaken on thin films of  $\alpha$ -Cr<sub>2</sub>O<sub>3</sub> (0001) rather than suitable oriented single crystal, thus concluding that this difference in substrate could lead to variation in H<sub>2</sub>O adsorption, i.e. thin films of  $\alpha$ -Cr<sub>2</sub>O<sub>3</sub> (0001) may display significant concentration of sites active for dissociative adsorption of H<sub>2</sub>O that are not present to any significant extent on the single crystal substrate.

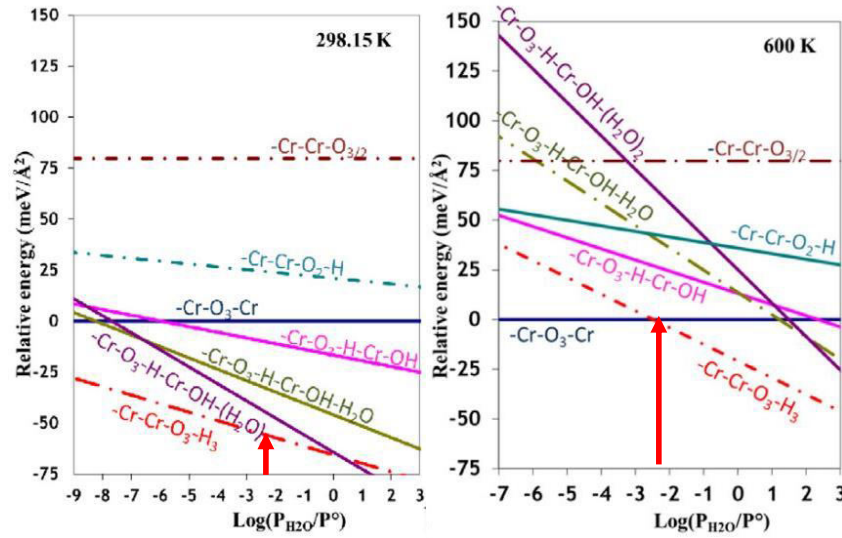


**Figure 41: a) (P,T) phase diagram of chromia in presence of H<sub>2</sub>O and b) a zoom to show the domain stability of the 3 different chromia terminations. Figure taken from ref. [11]**

The hydration states of  $\alpha$ -(0001) Cr<sub>2</sub>O<sub>3</sub> surface were also studied in the theoretical study of ref. [37], where the chromia most stable terminations in the case of water adsorption were

investigated in detail (**Figure 41**). The results of Souvi et al. [37] showed that in the thermal range of 300-900 K hydrated surfaces have to be necessarily considered and a new termination notes as Cr-Cr-O<sub>3</sub>-H<sub>3</sub> was identified as the most stable one. In this newfound configuration, the two outermost chromium atoms will be saturated with OH groups, which will cause an unavoidable decreasing of the acidic (Lewis) character of the chromia surface.

Considering the operating conditions of our interest as we did for the alumina case, we followed the example of the work conducted by Benoit Darenne [57], where he traced a vertical red arrow representing the fixed experimental conditions of the system (i.e. T = [298.15 K – 600 K], P = 1 atm and water content of 1000ppm) on the chromia phase diagrams of ref. [37] (**Figure 42**) to find the corresponding hydrated surface termination.



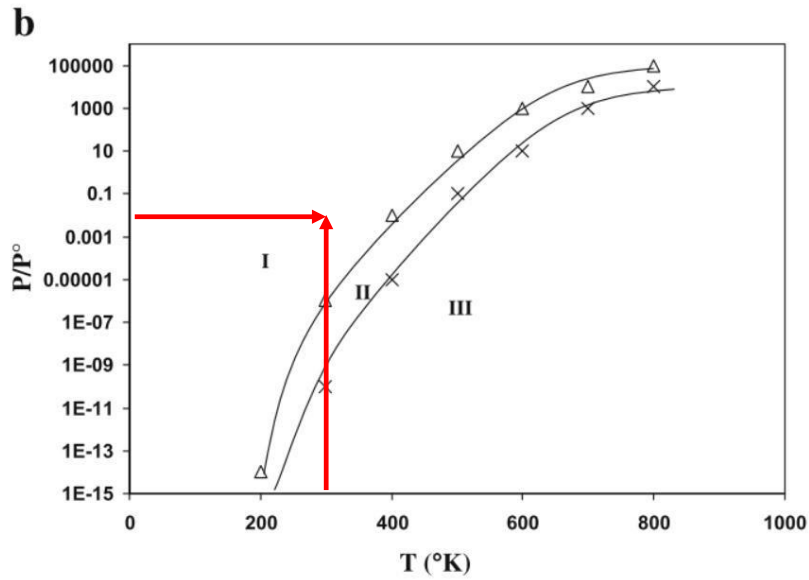
**Figure 42:** Stability diagram of different hydrated surfaces at 298K (on the left) and at 600K (on the right) as reported in ref. [37]. The red arrow corresponding to a  $\log(P_{H_2O}/P^\circ) = 2,5$  marks the operating conditions describing our system.

In these conditions of temperature, pressure and water content (corresponding in our case to a water pressure  $P_{H_2O} = 0,0035$  atm), we can see on the phase diagram reported in **Figure 42** that for the chromia hydrated surface the most stable surface termination is depicted by the -Cr-Cr-O<sub>3</sub>-H<sub>3</sub> surface termination, confirming what was mentioned above.

However, because the more stable termination of  $\alpha$ -Al<sub>2</sub>O<sub>3</sub> is the -Al-(OH)<sub>3</sub> one, also called the corundum-H<sub>2</sub>O termination, we preferred to compare the results on chromia with those of alumina for the same termination, i.e. the corundum one. This surface is documented in the work

of Sharkas et al. [34], where for each Cr atom of the Cr-terminated layer was saturated with three water molecules (i.e. a water coverage  $\theta = 14.1 \text{ H}_2\text{O}/\text{nm}^2$ ). In this configuration, the Cr coordination sphere is saturated to six as in the bulk.

If we look at the phase diagram obtained by Sharkas et al. [34] and we trace again with red arrows our  $P/P^\circ$  ratio corresponding to 300 K (**Figure 43**), we fall in the (I) zone which corresponds to the (0001)- $\text{Cr}_2\text{O}_3$ - $\text{Cr}(\text{OH})_3$  surface. In the zone of experimental conditions, for T around 400K-500K, we should take in consideration that the surface might be not totally hydroxylated.



**Figure 43:** (T,P) phase diagram of the different surface terminations (I, II, III) for the (0001)-Cr- $\text{Cr}_2\text{O}_3$ -water system. (I):  $-\text{Cr}(\text{OH})_3$ -like termination with water coverage of  $14.1 \text{ H}_2\text{O}/\text{nm}^2$ , (II):  $-\text{Cr}(\text{OH})_2$  termination with water coverage of  $9.4 \text{ H}_2\text{O}/\text{nm}^2$ , (III): dry Cr-terminated surface. Image taken from ref. [34].

We conclude this paragraph reaffirming that the behavior encountered for both metallic surfaces when coming in contact with water is very significant for this thesis since, according to many experimental studies related to injection systems performances, a certain water content has been found inside the pipelines of fuel injection circuits[58–60]. For this reason, we decided to model the reactivity of the stainless steel and aluminum in their hydration states with the fully-hydroxylated  $-\text{Cr}(\text{OH})_3$  and  $-\text{Al}(\text{OH})_3$  terminated surfaces. To consider the possibility of dehydration, we also address the dry surfaces,  $\alpha\text{-Al}_2\text{O}_3$  and  $\alpha\text{-Cr}_2\text{O}_3$ .

## References

- 1 Zhang C.-H., Liu M., Jin Y., Sun D.-B. The corrosive influence of chloride ions preference adsorption on  $\alpha$ -Al<sub>2</sub>O<sub>3</sub> (0 0 1) surface, *Applied Surface Science* **347** (2015), 386–391. DOI: 10.1016/j.apsusc.2015.04.088.
- 2 Massoud T., Maurice V., Klein L. H., Seyeux A., Marcus P. Nanostructure and local properties of oxide layers grown on stainless steel in simulated pressurized water reactor environment, *Corros. Sci.* **84** (2014), 198–203. DOI: 10.1016/j.corsci.2014.03.030.
- 3 Piispanen R. Principles and applications of Inorganic Geochemistry. A comprehensive textbook for geology students, *Lithos* **29**, 1-2 (1992), 160–161. DOI: 10.1016/0024-4937(92)90042-w.
- 4 Dingemans G., Kessels W.M.M. Status and prospects of Al<sub>2</sub>O<sub>3</sub>-based surface passivation schemes for silicon solar cells, *Journal of Vacuum Science & Technology A: Vacuum, Surfaces, and Films* **30**, 4 (2012), 40802. DOI: 10.1116/1.4728205.
- 5 French R.H. Electronic Band Structure of Al<sub>2</sub>O<sub>3</sub>, with Comparison to Alon and AlN, *J. Am. Ceram. Soc.* **73**, 3 (1990), 477–489. DOI: 10.1111/j.1151-2916.1990.tb06541.x.
- 6 Boettger J.C. High-precision, all-electron, full-potential calculation of the equation of state and elastic constants of corundum, *Physical review. B, Condensed matter* **55**, 2 (1997), 750–756. DOI: 10.1103/PhysRevB.55.750.
- 7 Godin, LaFemina Atomic and electronic structure of the corundum (alpha -alumina) (0001) surface, *Physical review. B, Condensed matter* **49**, 11 (1994), 7691–7696. DOI: 10.1103/PhysRevB.49.7691.
- 8 T. Fujii, D. Alders, F.C. Voogt, T. Hibma, B.T. Thole, G.A. Sawatzky, Fujii T., Alders D., Voogt F.C., Hibma T., Thole B.T., Sawatzky G.A. In situ RHEED and XPS studies of epitaxial thin  $\alpha$ -Fe<sub>2</sub>O<sub>3</sub> (0001) films on sapphire // In situ RHEED and XPS studies of epitaxial thin  $\alpha$ -Fe<sub>2</sub>O<sub>3</sub>(0001) films on sapphire, *Surf. Sci.* **366**, 3 (1996), 579–586. DOI: 10.1016/0039-6028(96)00844-8.
- 9 Huš M., Kopač D., Likožar B. Kinetics of non-oxidative propane dehydrogenation on Cr<sub>2</sub>O<sub>3</sub> and the nature of catalyst deactivation from first-principles simulations, *J. Catal.* **386** (2020), 126–138. DOI: 10.1016/j.jcat.2020.03.037.
- 10 Chang Q.-Y., Yin Q., Ma F., Zhu Y.-A., Sui Z.-J., Zhou X.-G., de Chen, Yuan W.-K. Tuning Adsorption and Catalytic Properties of  $\alpha$ -Cr<sub>2</sub>O<sub>3</sub> and ZnO in Propane Dehydrogenation by Creating Oxygen Vacancy and Doping Single Pt Atom: A Comparative First-Principles Study, *Ind. Eng. Chem. Res.* **58**, 24 (2019), 10199–10209. DOI: 10.1021/acs.iecr.9b01143.
- 11 Marcus P. *Corrosion Mechanisms in Theory and Practice*, CRC Press (2011). ISBN: 9780429143564.
- 12 Maurice V., Yang W.P., Marcus P. XPS and STM Study of Passive Films Formed on Fe-22Cr(110) Single-Crystal Surfaces, *J. Electrochem. Soc.* **143**, 4 (1996), 1182–1200. DOI: 10.1149/1.1836616.
- 13 Toofan J., Watson P. The termination of the  $\alpha$ -Al<sub>2</sub>O<sub>3</sub> (0001) surface: a LEED crystallography determination, *Surface Science* **401**, 2 (1998), 162–172. DOI: 10.1016/S0039-6028(97)01031-5.
- 14 Finger L.W., Hazen R.M. Crystal structure and isothermal compression of Fe<sub>2</sub>O<sub>3</sub>, Cr<sub>2</sub>O<sub>3</sub>, and V<sub>2</sub>O<sub>3</sub> to 50 kbars, *J. Appl. Phys.* **51**, 10 (1980), 5362. DOI: 10.1063/1.327451.
- 15 Shi S., Wysocki A.L., Belashchenko K.D. Magnetism of chromia, *Phys. Rev. B* **79**, 10 (2009), 537. DOI: 10.1103/PhysRevB.79.104404.
- 16 Bruce R.H., Cannell D.S. Specific heat of Cr<sub>2</sub>O<sub>3</sub> near the Néel temperature, *Phys. Rev. B* **15**, 9 (1977), 4451–4459. DOI: 10.1103/PhysRevB.15.4451.
- 17 Oware Sarfo K., Isgor O., Santala M.K., Tucker J.D., Árnadóttir L. Bulk Diffusion of Cl through O Vacancies in  $\alpha$ -Cr<sub>2</sub>O<sub>3</sub>: A Density Functional Theory Study, *J. Electrochem. Soc.* **168**, 7 (2021), 71503. DOI: 10.1149/1945-7111/ac0ec9.
- 18 Tepesch P. D., Quong A. A First-Principles Calculations of  $\alpha$ -Alumina (0001) Surfaces Energies with and without Hydrogen, *Phys. Stat. Sol (b)* **217**, 377 (2000), 377–387. DOI: 10.1002/(SICI)1521-3951(200001)217:1%3C377:AID-PSSB377%3E3.0.CO;2-B.

- 19 Wysocki A.L., Shi S., Belashchenko K.D. Microscopic origin of the structural phase transitions at the Cr<sub>2</sub>O<sub>3</sub> (0001) surface, *Phys. Rev. B* **86**, 16 (2012). DOI: 10.1103/PhysRevB.86.165443.
- 20 Goniakowski J., Finocchi F., Noguera C. Polarity of oxide surfaces and nanostructures, *Rep. Prog. Phys.* **71**, 1 (2008), 16501. DOI: 10.1088/0034-4885/71/1/016501.
- 21 Kaspar T.C., Chamberlin S.E., Chambers S.A. Surface structure of  $\alpha$ -Cr<sub>2</sub>O<sub>3</sub>(0001) after activated oxygen exposure, *Surf. Sci.* **618** (2013), 159–166. DOI: 10.1016/j.susc.2013.09.005.
- 22 X-G. Wang, A. Chaka, M. Scheffler Effect of the Environment on  $\alpha$ -Al<sub>2</sub>O<sub>3</sub> (0001) Surface Structures, *Phys. Rev. Lett.* **84**, 16 (2000), 3650–3653. DOI: 10.1103/PhysRevLett.84.3650.
- 23 J. Ahn J., W. Rabalais Composition and structure of the Al<sub>2</sub>O<sub>3</sub>{0001}-(1 × 1) surface, *Surf. Sci.* **388**, Issue 1-3 (1997), 121–131. DOI: 10.1016/S0039-6028(97)00383-X.
- 24 Guenard P., Renaud G., Barbier A., Gautier-Soyer M. Determination Of The  $\alpha$ -Al<sub>2</sub>O<sub>3</sub> (0001) Surface Relaxation and Termination by Measurements of Crystal Truncation Rods, *MRS Proc.* **437** (1996). DOI: 10.1557/PROC-437-15.
- 25 Soares E.A., van Hove M.A., Walters C.F., McCarty K.F. Structure of the  $\alpha$ -Al<sub>2</sub>O<sub>3</sub>(0001) surface from low-energy electron diffraction: Al termination and evidence for anomalously large thermal vibrations, *Phys. Rev. B* **65**, 19 (2002). DOI: 10.1103/PhysRevB.65.195405.
- 26 Suzuki T., Hishita S., Oyoshi K., Souda R. PII: S0039-6028(99)00706-2 // Structure of  $\alpha$ -Al<sub>2</sub>O<sub>3</sub> (0001) surface and Ti deposited on  $\alpha$ -Al<sub>2</sub>O<sub>3</sub> (0001) substrate, *Surface Science* **437**, 3 (1999), 289–298. DOI: 10.1016/S0039-6028(99)00706-2.
- 27 Walters C.F., McCarty K.F., Soares E.A., van Hove M.A. The surface structure of  $\alpha$ -Al<sub>2</sub>O<sub>3</sub> determined by low-energy electron diffraction: aluminum termination and evidence for anomalously large thermal vibrations, *Surface Science* **464**, 2-3 (2000), L732-L738. DOI: 10.1016/S0039-6028(00)00687-7.
- 28 Priyantha W., Waddill G.D. Structure of chromium oxide ultrathin films on Ag(111), *Surface Science* **578**, 1-3 (2005), 149–161. DOI: 10.1016/j.susc.2005.01.028.
- 29 Bikondoa O., Moritz W., Torrelles X., Kim H.J., Thornton G., Lindsay R. Impact of ambient oxygen on the surface structure of  $\alpha$ -Cr<sub>2</sub>O<sub>3</sub>(0001), *Phys. Rev. B* **81**, 205439 (2010). DOI: 10.1103/PhysRevB.81.205439.
- 30 Rohrbach A., Hafner J., Kresse G. Ab initio study of the (0001) surfaces of hematite and chromia: Influence of strong electronic correlations, *Phys. Rev. B* **70**, 12 (2004), 13. DOI: 10.1103/PhysRevB.70.125426.
- 31 Cline J.A., Rigos A.A., Arias T.A. Ab Initio Study of Magnetic Structure and Chemical Reactivity of Cr<sub>2</sub>O<sub>3</sub> and Its (0001) Surface, *J. Phys. Chem. B* **104**, 26 (2000), 6195–6201. DOI: 10.1021/jp9943474.
- 32 Rohr F., Bäumer M., Freund H.-J., Mejias J.A., Staemmler V., Müller S., Hammer L., Heinz K. Strong relaxations at the Cr<sub>2</sub>O<sub>3</sub> (0001) surface as determined via low-energy electron diffraction and molecular dynamics simulations, *Surf. Sci.* **372**, 1-3 (1997), 291-197. DOI: 10.1016/S0039-6028(96)01255-1.
- 33 Henderson M.A., Chambers S.A. HREELS, TPD and XPS study of the interaction of water with the  $\alpha$ -Cr<sub>2</sub>O<sub>3</sub>(001) surface, *Surface Science* **449**, 1-3 (2000), 135–150. DOI: 10.1016/S0039-6028(99)01246-7.
- 34 Costa D., Sharkas K., Islam M.M., Marcus P. Ab initio study of the chemical states of water on Cr<sub>2</sub>O<sub>3</sub>(0001): From the isolated molecule to saturation coverage, *Surf. Sci.* **603**, 16 (2009), 2484–2493. DOI: 10.1016/j.susc.2009.05.037.
- 35 Costa D., Marcus P. Electronic core levels of hydroxyls at the surface of chromia related to their XPS O 1s signature: A DFT+U study, *Surf. Sci.* **604**, 11-12 (2010), 932–938. DOI: 10.1016/j.susc.2010.02.023.
- 36 Siegel D.J., Hector L.G., Adams J.B. Adhesion, atomic structure, and bonding at the Al(111)/ $\alpha$ -Al<sub>2</sub>O<sub>3</sub>(0001) interface: A first principles study, *Phys. Rev. B* **65**, 8 (2002). DOI: 10.1103/PhysRevB.65.085415.
- 37 Souvi S.M., Badawi M., Virot F., Cristol S., Cantrel L., Paul J.-F. Influence of water, dihydrogen and dioxygen on the stability of the Cr<sub>2</sub>O<sub>3</sub> surface: A first-principles investigation, *Surf. Sci.* **666** (2017), 44–52. DOI: 10.1016/j.susc.2017.08.005.
- 38 Ranea V.A., Carmichael I., Schneider W.F. DFT Investigation of Intermediate Steps in the Hydrolysis of  $\alpha$ -Al<sub>2</sub>O<sub>3</sub> (0001), *J. Phys. Chem. C* **113**, 6 (2009), 2149–2158. DOI: 10.1021/jp8069892.
- 39 Anisimov et al. First-principles calculations of the electronic structure and spectra of strongly correlated systems: the LDA+U method, *J. Phys.: Condens. Matter* **9** (1997), 767–808. DOI: 10.1088/0953-8984/9/4/002.
- 40 S.L. Dudarev, A.I. Liechtenstein, M.R. Castell, G.A.D. Briggs, A.P. Sutton Surface states on NiO (100) and the origin of the contrast reversal in atomically resolved scanning tunnelling microscope images, *Phys. Rev. B* **56**, 8 (1997), 4900–4908. DOI: 10.1103/PhysRevB.56.4900.

- 41 Dudarev et al Electron-energy-loss spectra and the structural stability of nickel oxide: an LSDA+U study, *Phys. Rev. B* **57** (1997), 1505–1509. DOI: 10.1103/PhysRevB.57.1505.
- 42 Marmier A., Parker S.C. Ab initio morphology and surface thermodynamics of  $\alpha$ -Al<sub>2</sub>O<sub>3</sub>, *Phys. Rev. B* **69**, 11 (2004). DOI: 10.1103/PhysRevB.69.115409.
- 43 Arrouvel C., Diawara B., Costa D., Marcus P. DFT Periodic Study of the Adsorption of Glycine on the Anhydrous and Hydroxylated (0001) Surfaces of  $\alpha$ -Alumina, *J. Phys. Chem. C* **111**, 49 (2007), 18164–18173. DOI: 10.1021/jp0741408.
- 44 Hémeryck A., Motta A., Swiatowska J., Pereira-Nabais C., Marcus P., Costa D. Diaminoethane adsorption and water substitution on hydrated TiO<sub>2</sub>: A thermochemical study based on first-principles calculations, *Phys. Chem. Chem. Phys.* **15**, 26 (2013), 10824–10834. DOI: 10.1039/c3cp44498h.
- 45 Garrain P.-A., Costa D., Marcus P. Biomaterial–Biomolecule Interaction: DFT-D Study of Glycine Adsorption on Cr<sub>2</sub>O<sub>3</sub>, *J. Phys. Chem. C* **115**, 3 (2011), 719–727. DOI: 10.1021/jp109704b.
- 46 Gouron A., Kittel J., Bruin T. de, Diawara B. Density Functional Theory Study of Monoethanolamine Adsorption on Hydroxylated Cr<sub>2</sub>O<sub>3</sub> Surfaces, *J. Phys. Chem. C* **119**, 40 (2015), 22889–22898. DOI: 10.1021/acs.jpcc.5b05375.
- 47 Dabaghmanesh S., Neyts E.C., Partoens B. van der Waals density functionals applied to corundum-type sesquioxides: Bulk properties and adsorption of CH<sub>3</sub> and C<sub>6</sub>H<sub>6</sub> on (0001) surfaces, *Phys. Chem. Chem. Phys.* **18**, 33 (2016), 23139–23146. DOI: 10.1039/c6cp00346j.
- 48 Lebreau F., Islam M.M., Diawara B., Marcus P. Structural, Magnetic, Electronic, Defect, and Diffusion Properties of Cr<sub>2</sub>O<sub>3</sub>: A DFT+ U Study, *J. Phys. Chem. C* **118**, 31 (2014), 18133–18145. DOI: 10.1021/jp5039943.
- 49 Eng P.J., Trainor T.P., Brown G.E. JR., Waychunas G.A., Newville M., Sutton N.R., Rivers M., Eng, Trainor, Brown, Waychunas, Newville, Sutton, Rivers Structure of the Hydrated  $\gamma$ -Al<sub>2</sub>O<sub>3</sub> (0001) Surface Measured by Crystal Truncation Rod Diffraction // Structure of the hydrated alpha-Al(2)O(3) (0001) surface, *Science* **288**, 5468 (2000), 1029–1033. DOI: 10.1126/science.288.5468.1029.
- 50 Liu P., Kendelewicz T., Brown G.E., Nelson E.J., Chambers S.A. Reaction of water vapor with  $\alpha$ -Al<sub>2</sub>O<sub>3</sub>(0001) and  $\alpha$ -Fe<sub>2</sub>O<sub>3</sub>(0001) surfaces: synchrotron X-ray photoemission studies and thermodynamic calculations, *Surface Science* **417**, 1 (1998), 53–65. DOI: 10.1016/S0039-6028(98)00661-X.
- 51 Petrik N.G., Huestis P.L., LaVerne J.A., Aleksandrov A.B., Orlando T.M., Kimmel G.A. Molecular Water Adsorption and Reactions on  $\alpha$ -Al<sub>2</sub>O<sub>3</sub> (0001) and  $\alpha$ -Alumina Particles, *J. Phys. Chem. C* **122**, 17 (2018), 9540–9551. DOI: 10.1021/acs.jpcc.8b01969.
- 52 Hass K.C., Schneider W.F., Curioni A., Andreoni W. First-Principles Molecular Dynamics Simulations of H<sub>2</sub>O on  $\alpha$ -Al<sub>2</sub>O<sub>3</sub> (0001), *J. Phys. Chem. B* **104**, 23 (2000), 5527–5540. DOI: 10.1021/jp000040p.
- 53 Łodziana Z., Nørskov J.K., Stoltze P. The stability of the hydroxylated (0001) surface of  $\alpha$ -Al<sub>2</sub>O<sub>3</sub>, *J. Chem. Phys.* **118**, 24 (2003), 11179–11188. DOI: 10.1063/1.1574798.
- 54 Hass, Schneider, Curioni, Andreoni The chemistry of water on alumina surfaces: reaction dynamics from first principles, *Science* **282**, 5387 (1998), 265–268. DOI: 10.1126/science.282.5387.265.
- 55 Micheal A. Henderson HREELS, TPD and XPS study of the interaction of water with the Cr<sub>2</sub>O<sub>3</sub>(001) surface, *Surf. Sci.* **449** (2000), 135–150. DOI: 10.1016/S0039-6028(99)01246-7.
- 56 Ahmed M.H.M., Torrelles X., Treacy J.P.W., Hussain H., Nicklin C., Wincott P.L., Vaughan D.J., Thornton G., Lindsay R. Geometry of  $\alpha$ -Cr<sub>2</sub>O<sub>3</sub>(0001) as a Function of H<sub>2</sub>O Partial Pressure, *J. Phys. Chem. C* **119**, 37 (2015), 21426–21433. DOI: 10.1021/acs.jpcc.5b04607.
- 57 Darenne B Modélisation de l'interaction des agrégats hydrocarbonés avec les parois, *These de Doctorat*, ENSPC-Chimie ParisTech (2018).
- 58 R. G. Larsen, R. E. Thorpe, and F. A. Armfield, Larsen R.G., Thorpe R.E., Armfield F.A. Oxidation Characteristics of Pure Hydrocarbons, *Ind. Eng. Chem. Res.* **34**, 2 (1942), 183-193. DOI: 10.1021/ie50386a012.
- 59 McCormick R.L., Ratcliff M., Moens L., Lawrence R. Several factors affecting the stability of biodiesel in standard accelerated tests, *Fuel Processing Technology* **88**, 7 (2007), 651–657. DOI: 10.1016/j.fuproc.2007.01.006.
- 60 M. Sicard, J. Boulicault, K. Coulon, C. Thomasset, K. Ancelle, B. Raepsaet, F. Ser (ed.) *Oxidation stability of jet fuel model molecules evaluated by rapid small scale oxidation tests: Handling and Use of Liquid Fuels 2013 IASH 2013*, RHODES, Greece (2013).

## Chapter 4. DFT study: analysis of gas-phase reactions and gas-solid interface interactions

### 4.1 Introduction

In the previous **Chapter 3** we discussed about the features and properties of the metal-oxides surfaces that were chosen in the framework of this thesis. In this chapter, we move the focus on the theoretical study carried out to gain the necessary input data for ReaxFF optimization.

We focused our ab-initio study on two main systems:

- i. The homogeneous systems represented by the gas-phase autoxidation reactions.
- ii. The heterogeneous systems represented by the molecules/surfaces interactions.

For the study of the gas-phase reactions, we selected a set of reactions describing the toluene autoxidation mechanism. The main objective was the obtention of the  $\Delta E_r$  energies of these reactions in order to gain useful data on the molecular reactivity in the gas phase. The reaction energies were calculated with Gaussian 16 [1].

For the study of the molecule-surface interactions, we chose model molecules as surrogates of the deposit precursors and analyzed their reactivity when adsorbed on the  $\alpha$ -Al<sub>2</sub>O<sub>3</sub> and  $\alpha$ -Cr<sub>2</sub>O<sub>3</sub> either in their anhydrous and hydroxylated state. In addition, two substitution reactions where the organic adsorbates replace a surface H<sub>2</sub>O/OH are discussed. These calculations were implemented with the VASP package [2]. Similarly to the gas-phase study, the main objective of this study was to gain useful insights on the interface interactions occurring between the organic gas-phase (i.e. deposit precursors) and the metallic solid phase (i.e. aluminium and stainless steel surfaces).

Complementary thermodynamic calculations were implemented to corroborate the theoretical results: the analysis of the desorption temperatures calculated for all the molecule/surface configurations was carried out with Gaussian 16 [1] and the results are reported in **Table A4-5** in the **Annex**.

Both these studies provided important input data to implement for the successive ReaxFF: the autoxidation reactions provided a mean for ReaxFF to predict the chemical reactivity in the gas-phase, while the adsorption configurations contributed to aid the reactive force field to estimate the nature of the gas-solid interface interactions. Both energetic data were fundamental for the achievement of the ReaxFF optimization and validation implemented in this thesis.

In the next paragraph, we introduce the organic molecules that we selected as surrogates of the oxygenated precursors of fuel deposits, on their autoxidation reaction pathway in the gas phase and on their interactions on the dry and fully hydroxylated substrates. We will also address certain thermodynamic properties of these molecules that we acquired in the course of the preliminary theoretical study.

## 4.2 Model of deposit surrogate

As previously discussed, the main products sorted out from fuel autoxidation are oxygenated compounds like alcohols, aldehydes, ketones, epoxides and carboxylic acids. Based on the previous experimental work of K. Bacha [3], the XPS results of real biofuels deposits over different surfaces (alumina, stainless steel, gold, polymer) showed that the chemical bond between deposits and surface was made through the oxygenated head of the molecule under study. In addition, the study conducted by Mei et al. [4] showed that the increase of the adsorption energy of the fuel on the surface was exclusively dependent of the ester amount in the fuel.

For these reasons, in the present study small oxygenated molecules have been preferred as model molecules on the basis of their chemical functional group, i.e. ethanol for the alcohol family, acetaldehyde and acetone to represent aldehydes and ketones respectively, 2-ethyl-3-methyloxirane for the epoxides and acetic acid for the carboxylic acids.



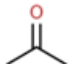
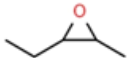
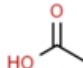

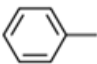
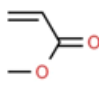
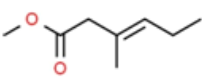
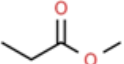

In addition, three other types of chemical families have been considered:

(1) aromatic species since they are found in diesel refined from crude oil, and so they are present in the diesel/biodiesel blends in the market. Here we consider benzene and toluene as model aromatic compounds.

(2) ester species: methyl propionate, unsaturated methyl esters (e.g. methylacrylate and methyl-3-trans-hexenoate), as representatives of deposits derived from biodiesel blends.

(3) alkanes since they are the main component of petrodiesel. Here we consider n-propane as surrogate of alkyl-chain deposits produced from n-alkanes degradation.

The listed model molecules are reported in **Table 2**, where they have been matched with the corresponding configuration optimized via DFT (last right column):

Chemical family	Model molecule	Molecule 2-D structure
Alcohol	Ethanol	
Aldehyde	Acetaldehyde	
Ketone	Acetone	
Epoxide	2Ethyl-3methyloxirane	
Carboxylic acid	Acetic acid	
Aromatic compounds	1) Benzene	1) 
	2) Toluene	2) 
Methyl esters	1) Methylacrylate	1) 
	2) Methyl-3-trans-hexenoate	2) 
	3) Methyl propionate	3) 
Alkane	n-Propane	

**Table 2: Organic molecules selected as models for representing the precursors of the liquid deposits coming from the fuel autoxidation process.**

In the next paragraph, we will introduce the main kinetic reaction steps related to the autoxidation process in the gas phase that we studied through a theoretical approach and that we used in the next MD study for ReaxFF parametrization.

### 4.3 Gas phase autoxidation reactions

We chose the model molecules, what we did as the next step was to choose a set of gas phase reactions describing the autoxidation mechanism. Taking in mind the fuel autoxidation mechanism introduced in section 1.3.1 (taken from ref. [3]), we firstly had to choose at which point of the reaction phases we wanted to focus our analysis. Since we wanted to investigate on oxygenated deposit precursors interacting either in their homogeneous liquid phase and in the heterogeneous phase with the alumina and chromia surfaces, we focused on the propagation step of the reaction mechanism, where alkyl radicals start reacting with molecular oxygen and then proceeding to the formation of the peroxy-radical that transform into hydroperoxides species by reacting with the present hydrocarbon compounds (**Equation 6-Equation 7** in section 1.3.1).

In this thesis, we decided to correlate the referential reaction mechanism to the one describing the toluene autoxidation (e.g. RH = toluene). This choice is due to the fact that aromatic compounds represent a major constituent of petrodiesel and toluene is often in literature taken as model molecule for fuel autoxidation studies [5–7]. The reactions are described in **Eq. 68-Eq. 78** below.

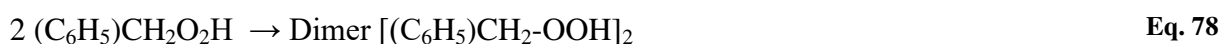
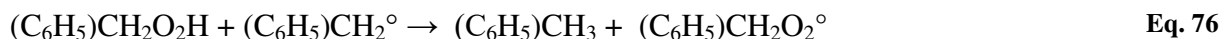
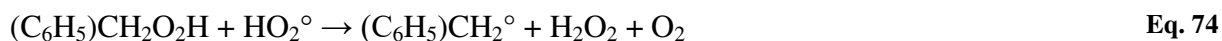
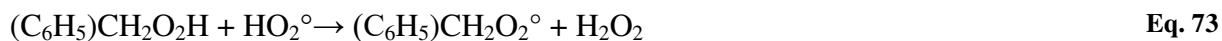
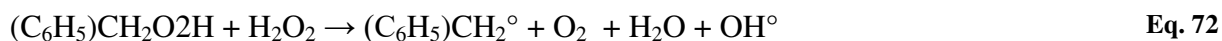
Our focus in this reaction mechanism is centered on the hydroperoxide  $(\text{C}_6\text{H}_5)\text{CH}_2\text{O}_2\text{H}$ , which corresponds to the ROOH species in reference to the mechanism mentioned in section 1.3.1. The hydroperoxide species are fundamental in this mechanism since, starting from their decomposition, the future oxygenated precursors are produced (e.g. alcohols, carboxylic acids, aldehydes, etc.) [8].

Da Silva et al. [6] reported in their work a simplified scheme for the mechanism of benzyl +  $\text{HO}_2^\circ$  reaction, which is reported below in **Figure 44**.

According to Da Silva et al. [6], the addition of  $\text{HO}_2^\circ$  to the methylene site in the benzyl radical is calculated to be exothermic (-253 kJ/mol) and it corresponds to the most favorable  $\text{HO}_2^\circ$  addition since the ones to the ortho and para ring sites produce weak adducts (-67 and -79.5

kJ/mol, respectively). The HO<sub>2</sub><sup>°</sup> addition to the methylene site provides the formation of an excited benzyl hydroperoxide adduct (denoted with the \*), which possess a significant amount of energy for use in further unimolecular isomerization and dissociation reactions.

From this activated benzyl hydroperoxide adduct, seven different reaction pathways are possible according to Da Silva et al. [6]. These different pathways lead towards six different products.



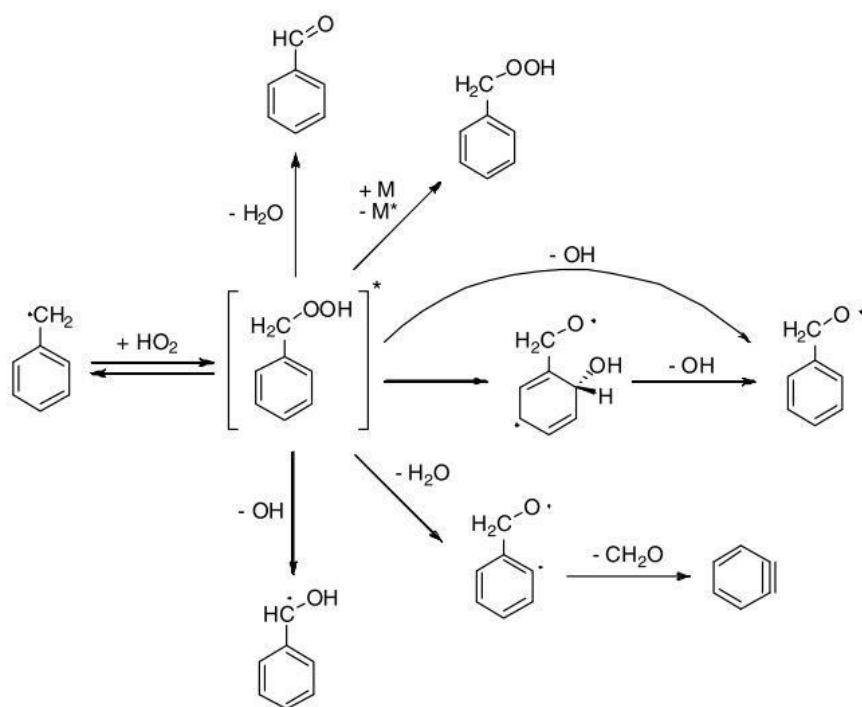
From **Figure 44**, we can observe that the activated benzyl hydroperoxide adduct can react to produce the benzoyl radical (C<sub>6</sub>H<sub>5</sub>CH<sub>2</sub>O<sup>°</sup>) + OH<sup>°</sup>. Concerning our study, this reaction pathway leading to the formation of the benzoyl radical + OH<sup>°</sup> represents one of the major focuses in the analysis of the system reactivity.

### 4.3.1 Computational details

To calculate the reaction energies for the reactions reported in **Eq. 68-Eq. 78**, we implemented calculations through Gaussian 16 package [1]. For these calculations, we implemented the M06-2X functional coupled with the 6-311G(d,p) basis set with the following convergence criteria: 10<sup>-</sup>

<sup>8</sup> Hartree for the energy, 0.0045 and 0.0030 Hartree/Bohr for the maximal and average forces, 0.018 and 0.0012 Bohr for the maximal and average displacement, respectively. We chose to implement this hybrid meta-GGA functional for the calculation of the reaction energies since it has been confirmed in recent studies about the thermochemistry of hydrocarbon radicals [25-26] that the Minnesota functional M06-2X coupled with the 6-311G(d,p) basis set has been proven to be one of the best performers in the prediction of the energetic data. A comparison between the energetic results obtained with the M06-2X functional and the corresponding ones calculated instead via the PBE-GGA functional has been reported in **Table A4-3** in the **Annex**.

Firstly, we run geometry optimizations of each single species to obtain the corresponding electronic energies and secondly we calculated the reaction energies for each specific reaction.



**Figure 44: Elementary mechanism for the benzyl + HO<sub>2</sub> reaction from reference [6].**

We also calculated the relative bond dissociation energies for the scission of the (C<sub>6</sub>H<sub>5</sub>)CH<sub>2</sub>-OOH and (C<sub>6</sub>H<sub>5</sub>)CH<sub>2</sub>O-OH bonds respectively. To acquire this result, we run the potential energy surface (PES) scans with Gaussian 16 package [1] to obtain the energetic profile at varying bond lengths.

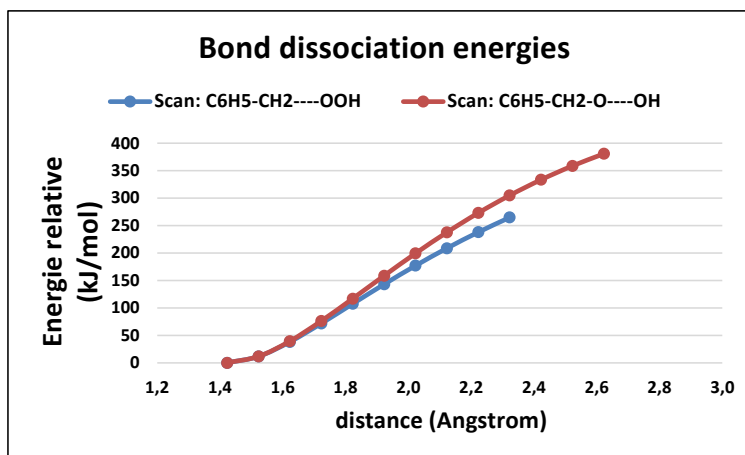
### 4.3.2 Results and discussion

The results of the electronic reaction energies are reported in **Table 3**. The majority of these reactions are linked to the bond dissociation of the benzyl hydroperoxide (C<sub>6</sub>H<sub>5</sub>)CH<sub>2</sub>O<sub>2</sub>H.

**Table 3: Reaction energies (in kJ/mol) for the reaction mechanism of toluene autoxidation used in this thesis. The reaction 5) with four products is a non-elementary reaction.**

Reactions	$\Delta E_r$ (kJ/mol)
1) (C <sub>6</sub> H <sub>5</sub> )CH <sub>2</sub> O <sub>2</sub> H → (C <sub>6</sub> H <sub>5</sub> )CH <sub>2</sub> O <sub>2</sub> ° + H°	374,4
2) (C <sub>6</sub> H <sub>5</sub> )CH <sub>2</sub> O <sub>2</sub> H → (C <sub>6</sub> H <sub>5</sub> )CH <sub>2</sub> O° + HO°	194,7
3) (C <sub>6</sub> H <sub>5</sub> )CH <sub>2</sub> O <sub>2</sub> H → (C <sub>6</sub> H <sub>5</sub> )CH <sub>2</sub> ° + HO <sub>2</sub> °	264,0
4) (C <sub>6</sub> H <sub>5</sub> )CH <sub>2</sub> O <sub>2</sub> H → (C <sub>6</sub> H <sub>5</sub> )CH <sub>2</sub> ° + H° + O <sub>2</sub>	638,3
5) (C <sub>6</sub> H <sub>5</sub> )CH <sub>2</sub> O <sub>2</sub> H + H <sub>2</sub> O <sub>2</sub> → (C <sub>6</sub> H <sub>5</sub> )CH <sub>2</sub> ° + O <sub>2</sub> + H <sub>2</sub> O + OH°	353,8
6) (C <sub>6</sub> H <sub>5</sub> )CH <sub>2</sub> O <sub>2</sub> H + HO <sub>2</sub> ° → (C <sub>6</sub> H <sub>5</sub> )CH <sub>2</sub> O <sub>2</sub> ° + H <sub>2</sub> O <sub>2</sub>	-2,7
7) (C <sub>6</sub> H <sub>5</sub> )CH <sub>2</sub> O <sub>2</sub> H + HO <sub>2</sub> ° → (C <sub>6</sub> H <sub>5</sub> )CH <sub>2</sub> ° + H <sub>2</sub> O <sub>2</sub> + O <sub>2</sub>	261,2
8) (C <sub>6</sub> H <sub>5</sub> )CH <sub>2</sub> O <sub>2</sub> ° → (C <sub>6</sub> H <sub>5</sub> )CH <sub>2</sub> ° + O <sub>2</sub>	263,9
9) (C <sub>6</sub> H <sub>5</sub> )CH <sub>2</sub> O <sub>2</sub> H + (C <sub>6</sub> H <sub>5</sub> )CH <sub>2</sub> ° → (C <sub>6</sub> H <sub>5</sub> )CH <sub>3</sub> + (C <sub>6</sub> H <sub>5</sub> )CH <sub>2</sub> O <sub>2</sub> °	-33,4
10) HO <sub>2</sub> ° → O <sub>2</sub> + H°	374,4
11) 2 (C <sub>6</sub> H <sub>5</sub> )CH <sub>2</sub> O <sub>2</sub> H → Dimer [(C <sub>6</sub> H <sub>5</sub> )CH <sub>2</sub> -OOH] <sub>2</sub>	-68,9

**Figure 45** below reports the PES scans results for C-OOH and CO-OH bond dissociation energies in the benzyl hydroperoxide molecules. We chose to run relaxed coordinate scans for both cases.



**Figure 45:** PES scans for relative bond dissociation energies of -C-OOH bond scission (blue curve) and of -CO-OH bond scission (red curve) respectively.

From **Figure 45** we can see that the two curves are almost overlapping on each other till the bond distance of 1.8 Å, then they start to diverge and to culminate towards two different energetic maxima. However, in this calculation we were not able to reach the energetic maximum for either of the bonds and the reason is because the molecule started to contract inwardly once the examined bond started to stretch further and this effect caused difficulty for us to continue the scan.

## 4.4 Adsorption on $\alpha$ -(0001) $\text{Al}_2\text{O}_3$ and $\alpha$ -(0001) $\text{Cr}_2\text{O}_3$ surfaces

### 4.4.1 Computational details

Total energy calculations were performed within the density functional theory (DFT) and the generalized gradient Perdew-Burke-Ernzerhof (PBE [9]) exchange correlation functional was used for the whole study. To solve the Kohn-Sham equations we use the Vienna Ab initio Simulation Package (version 5.4.1) [2, 10–12]. VASP performs an iterative diagonalization of the Kohn-Sham Hamiltonian via unconstrained band-by-band minimization of the norm of the residual vector to each eigenstate and via optimized charge density mixing routines. A smearing of 0.1 eV was used. We used a cut-off energy of 520 eV for the total energy calculations. The electronic optimizations were done up to a convergence of  $10^{-5}$  eV for the self-consistent loop and until all forces on the atoms were lower than 0.02 eV/Å for the geometry relaxations. The Brillouin zone was sampled with an appropriated Monkhorst-Pack k-point mesh (vide infra)

[13]. To account for the strong correlation between the d-electrons of the chromium, an on-site coulomb repulsion U-term is added to the DFT Hamiltonian, turning into DFT + U method. [14] Subsequently, this formalization impacts on the cell dimensions, band gap and, magnetic moment. Herewith, we have considered U and J parameters to be 5 eV and 1 eV respectively as reported in the literature [15, 16].

To account for the antiferromagnetic state of  $\text{Cr}_2\text{O}_3$ , spin-polarised calculations were performed. The van der Waals corrections are calculated with DFT-D3 method of Grimme [17] at each electronic step, implying that the geometry is optimized with the dispersion forces included.

The rhomboidal (R3c) unit cell of  $\alpha\text{-Al}_2\text{O}_3$  and  $\alpha\text{-Cr}_2\text{O}_3$  was taken as the starting point for the calculations of the bulk oxide. For the corundum-type surfaces, the hexagonal unit cell reported in **Figure A41** in the **Annex** contains 12 metallic atoms among which every four atoms form a subunit corresponding to the rhombohedral primitive cell. In particular for  $\alpha\text{-Cr}_2\text{O}_3$ , only three antiferromagnetic spin configurations are possible: A (+ + - -), B (+ - - +) and C (+ - + -). We agree with Rohrbach et al. [16] and Costa et al. [18] about the spin ground state of  $\text{Cr}_2\text{O}_3$ , which is (CCC) and results in a total magnetic moment equal to zero. The electronic energy convergence was obtained with k-points grids of (3×3×1) for the bulk and of (1×1×1) for the (4×4) supercell of  $\alpha\text{-Al}_2\text{O}_3$  and  $\alpha\text{-Cr}_2\text{O}_3$ . The unit cell was relaxed by alternating a cell parameter optimization and ion relaxation until convergence criteria for the forces and energies were obtained (*vide supra*). The results are shown in the **Table A41-A42 (Annex)**.

For  $\alpha$ -alumina and  $\alpha$ -chromia, both the Al(Cr)-terminated dry surface (Bulk-Al-O-Al) (respectively Bulk-Cr-O-Cr) and the fully hydrated Bulk-Al-O-Al-(OH)<sub>3</sub> and Bulk-Cr-O-Cr-(OH)<sub>3</sub> surfaces were considered. The oxide slab thicknesses correspond to six and seven layers, respectively. We validated our calculation methodology, by verifying that for the dry surfaces, the calculated surface energy of  $\alpha\text{-Al}_2\text{O}_3$  1.55 J/m<sup>2</sup> is in good adequacy with the literature [19] value of 1.66 J/m<sup>2</sup>.

The lattice parameters and surface areas for the examined surfaces are grouped in **Table 4-Table 5**. For the  $\alpha\text{-Cr}_2\text{O}_3(0001)\text{-Cr}$  and  $\alpha\text{-Al}_2\text{O}_3(0001)\text{-Al}$  surfaces, we considered a supercell (4×4) large enough to adsorb molecules without lateral interactions (**Table 4**). Seen the large size of the cells, the calculations were performed at the Gamma point.

The fully hydrated  $\alpha$ -Al<sub>2</sub>O<sub>3</sub>-Al(OH)<sub>3</sub> termination, corresponding to 8.7 OH/nm<sup>2</sup>, was considered stable over a large temperature and partial water pressure range, based on the ones reported in the literature [20]. According to Ranea et al. [21], the final configuration Al(OH)<sub>3</sub> generated from three successive water dissociations shows an approximately trigonal coordination on the Al<sub>s</sub> center and its formation energy from the dry surface is calculated to be −139.9 kJ/mol.

A (4×4) cell was used (**Table 4**), at the exception of the study of the substitution of water (OH) by methyl propionate (respectively acetate) which was performed on (2×2) cells of the corundum surfaces (**Table 5**). It should be noticed that in all molecule/surface interactions calculations, only the four top layers were relaxed for  $\alpha$ -alumina and  $\alpha$ -chromia.

**Table 4: Lattice parameters for the DFT computed (4x4) slabs for  $\alpha$ -Cr<sub>2</sub>O<sub>3</sub> (001) and  $\alpha$ -Al<sub>2</sub>O<sub>3</sub> (001) respectively.**

Surfaces (4x4) slab	a [Å]	b [Å]	Number of layers	Supercell surface area [Å <sup>2</sup> ]	Slab thickness [Å]	Vacuum thickness [Å]	K-points mesh
$\alpha$ -Cr <sub>2</sub> O <sub>3</sub> (0001)	20.29	20.29	6	356.58	13.85	14.59	1×1×1
$\alpha$ -Cr <sub>2</sub> O <sub>3</sub> (001)-Cr(OH) <sub>3</sub>	20.29	20.29	7	356.58	15.27	13.17	1×1×1
$\alpha$ -Al <sub>2</sub> O <sub>3</sub> (001)	19.14	19.14	6	317.25	13.07	14.51	1×1×1
$\alpha$ -Al <sub>2</sub> O <sub>3</sub> (001)-Al(OH) <sub>3</sub>	19.14	19.14	7	317.25	14.71	12.86	1×1×1

**Table 5: Lattice parameters for the DFT computed (2x2) slabs for the hydroxylated  $\alpha$ -Cr<sub>2</sub>O<sub>3</sub> (0001) and  $\alpha$ -Al<sub>2</sub>O<sub>3</sub> (0001).**

Surfaces (2x2) slabs	a [Å]	b [Å]	Number of layers	Supercell surface area [Å <sup>2</sup> ]	Slab thickness [Å]	Vacuum thickness [Å]	K-points mesh
$\alpha$ -Cr <sub>2</sub> O <sub>3</sub> (0001)-Cr(OH) <sub>3</sub>	10.15	10.15	6	89.15	15.27	13.17	1×1×1
$\alpha$ -Al <sub>2</sub> O <sub>3</sub> (0001)-Al(OH) <sub>3</sub>	9.57	9.57	6	79.31	14.72	12.86	1×1×1

## 4.4.2 Results and discussion

To rigorously compare the reactivity of both corundum surfaces, the starting adsorption configurations of the molecules on dry surfaces have been maintained identical.

First, we started our study by experimenting different molecule positions and orientations above the oxide surfaces. In fact, some of the smaller molecules (such as ethanol, acetone and acetaldehyde) were placed in a tilted fashion on top of the surface by promoting a stronger interaction between the molecule O atom and the metallic surface layer and, at the same time, by allowing the molecule hydrocarbon chain to also interact with the surface layer through weaker dispersion forces.

For flatter molecules such as the aromatic compounds, we opted to arrange them parallel to the surface layer in order to favor van der Waals interactions, which are prominent for polarizable molecules.

In the case of bigger molecules, as methyl-3-trans-hexenoate and the 2-ethyloxirane, we chose to arrange them perpendicular to the surface in a monodentate adsorption configuration, in this way favoring the bonding between the adsorbate O atom and the outermost M cation.

In the case of dissociative adsorption, for both dry surfaces, the dissociated adsorption configuration was formed by imposing from the beginning the transfer of the H atom on a O<sub>s</sub> atom on the surface outermost layer. Several locations of the proton on surface Oxygens were considered and the most stable are retained here.

A similar reasoning has been done to study the adsorption on the hydroxylated corundum-type surfaces, since we wanted to explore the difference in reactivity of both substrates under the same conditions of hydroxylation state and organic adsorbates. As a starting point, the molecules were placed in a similar position as that obtained on the anhydrous surfaces, but farther from the surface.

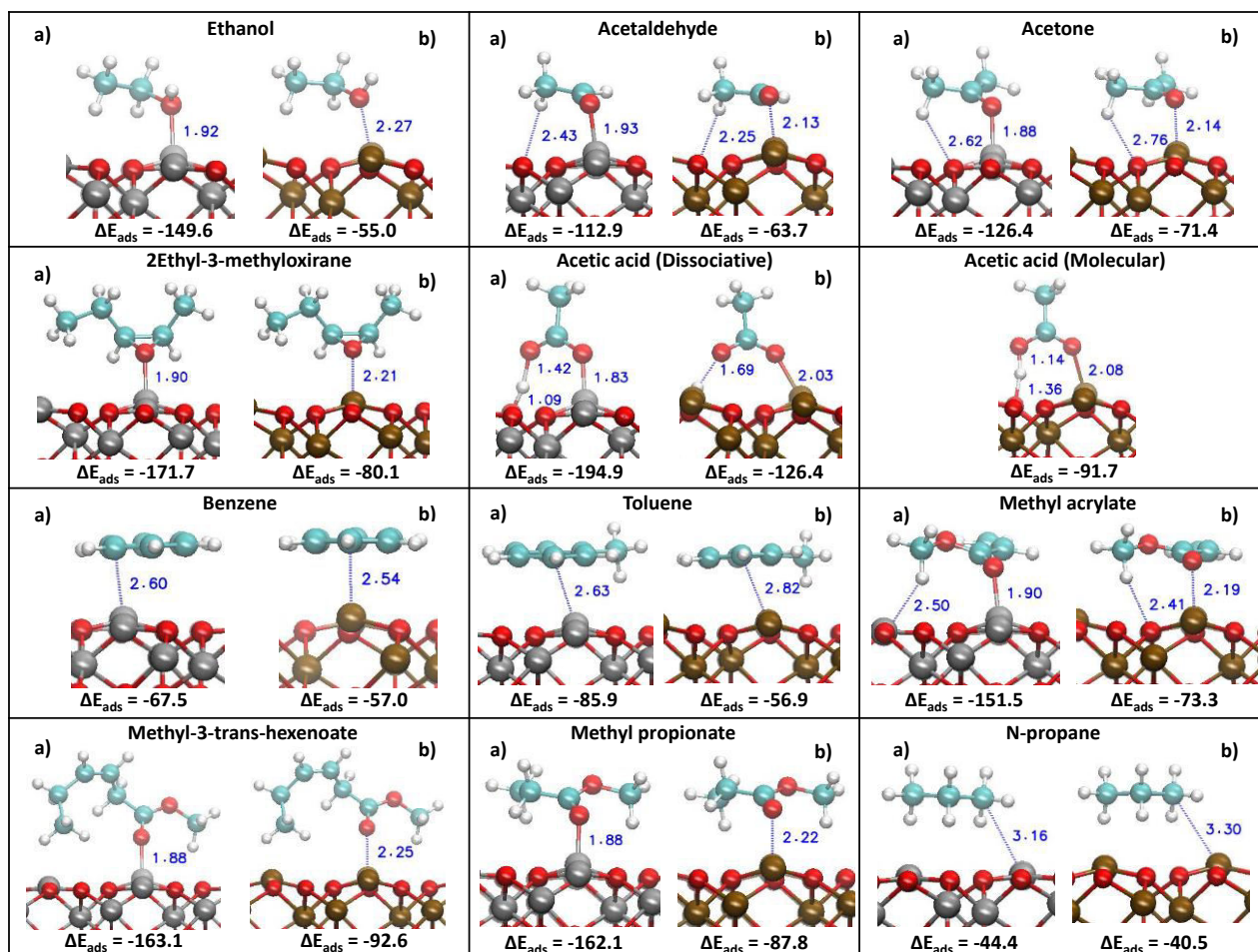
In the first part, we screen several model molecules on the dry and hydroxylated  $\alpha$ -Al<sub>2</sub>O<sub>3</sub> and  $\alpha$ -Cr<sub>2</sub>O<sub>3</sub> surfaces. Then, we study whether some molecules might substitute surface OH groups. The results are summarized in **Figure 46-Figure 48**.

**Figure 46** shows the optimized configurations obtained for the molecules on the dry corundum surfaces, respectively  $\alpha$ -Al<sub>2</sub>O<sub>3</sub> (a) and  $\alpha$ -Cr<sub>2</sub>O<sub>3</sub> (b). From **Figure 46** it appears that the final configurations are very similar for Al<sub>2</sub>O<sub>3</sub> and Cr<sub>2</sub>O<sub>3</sub>. For both metal-oxide surfaces the strongest interactions are represented by the metal-oxygen covalent bonds that are formed between the

oxygenated polar groups (hydroxyl and carbonyl groups), acting as a Lewis base, of the adsorbate and the metallic atoms (Al/Cr), terminating the surfaces, acting as Lewis acids.

Apolar molecules such as alkanes (n-propane) and aromatic compounds (benzene and toluene) do not form covalent bonds with the oxides and essentially associate by induction and dispersion forces. Indeed, the Al-C and Cr-C bonds formed are 2.60 and 2.54 Å respectively, suggesting weak interactions. These values are in good agreement with those calculated by Dabaghmanesh et al. [22], 2.82 and 2.68 Å respectively. The adsorption energies calculated by the authors, -53.1 kJ/mol and -50.2 kJ/mol for Al<sub>2</sub>O<sub>3</sub> and Cr<sub>2</sub>O<sub>3</sub>, are also in good correlation with our calculations, -67.5 and -57.0 kJ/mol.

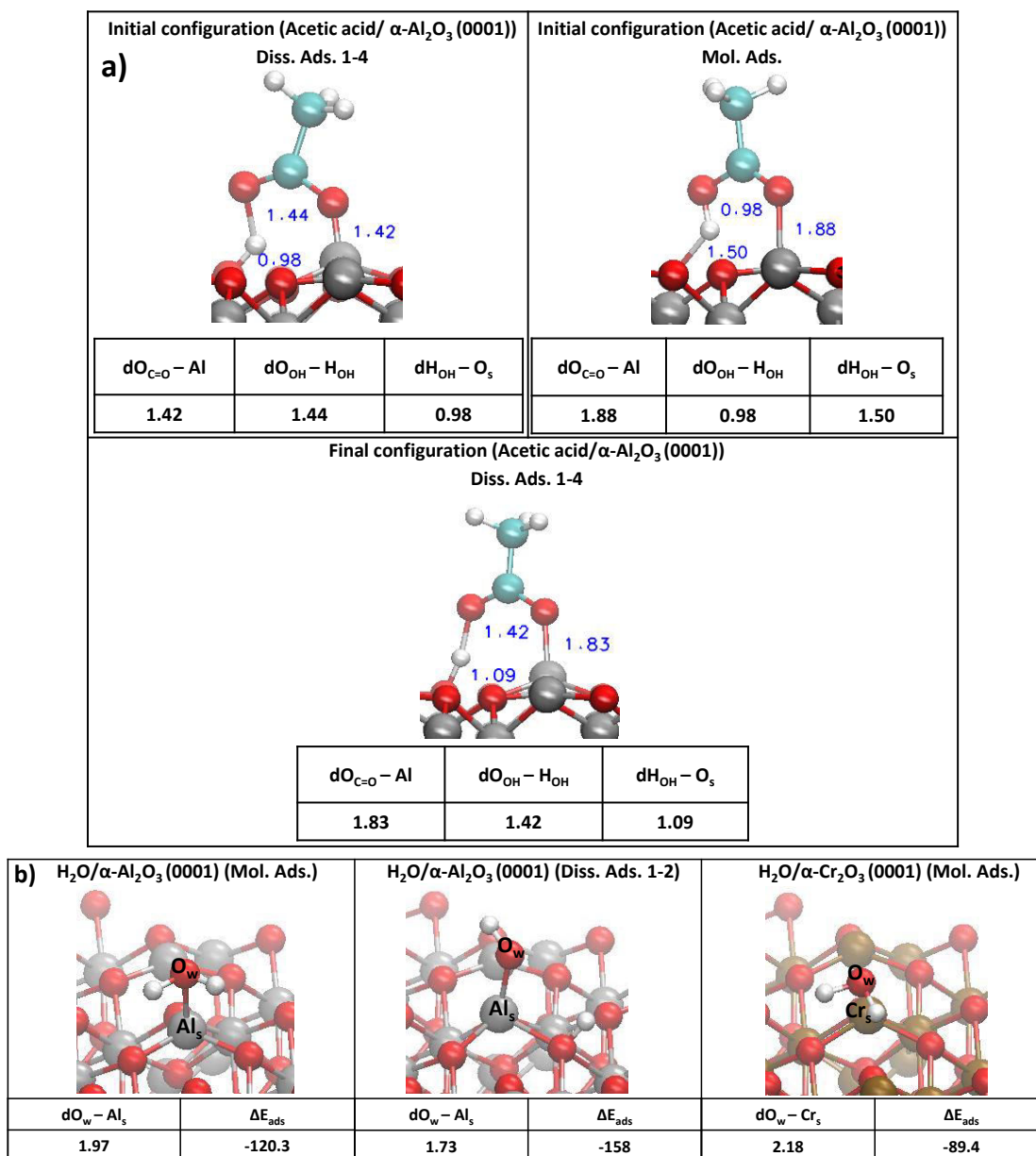
For water and acetic acid, both the associative (molecular) and dissociative adsorption have been considered (**Figure 47**). On Al<sub>2</sub>O<sub>3</sub> the non-dissociative adsorption evolves during the geometry optimization towards a dissociative adsorption, through a proton transfer to a surface O atom (see **Figure 46**). For the chromia case, acetic acid can adsorb molecularly and dissociatively, the second case being more exothermic by 34.7 kJ/mol. The barrier from the molecular to the dissociative adsorption was evaluated to 20.3 kJ/mol (the barrier was calculated using the Nudged Elastic Band approach).



**Figure 46:** Optimized adsorption configurations on anhydrous surfaces with their corresponding adsorption energies calculated via DFT approach of different model molecules on dry  $\alpha$ -Al<sub>2</sub>O<sub>3</sub> (a) and  $\alpha$ -Cr<sub>2</sub>O<sub>3</sub> (b) surfaces, respectively. The bond distances are reported in Angstrom [Å] and the adsorption energies in [kJ/mol]. Color code: red = O; light-blue = C; white: H; grey = Al; brown = Cr.

We considered for the Al<sub>2</sub>O<sub>3</sub> surface two different dissociative configurations: the “1-2” dissociation for water and the “1-4” dissociation for acetic acid, *cf.* **Figure A4-2** in the **Annex** for the nomenclature. It appears that a small molecule like water, preferentially adsorbs in the 1-2 position, in agreement with literature data [81], while for the larger acetic acid, the 1-4 position is most stable. In fact, the 1-2 (respectively 1-4) position maximizes the hydrogen bond interactions between the O from the OH (respectively -COO) group and the adsorbed proton.

We report in **Figure 47a** the comparison between their initial configurations, in this way highlighting the differences in their calculation starting-points.

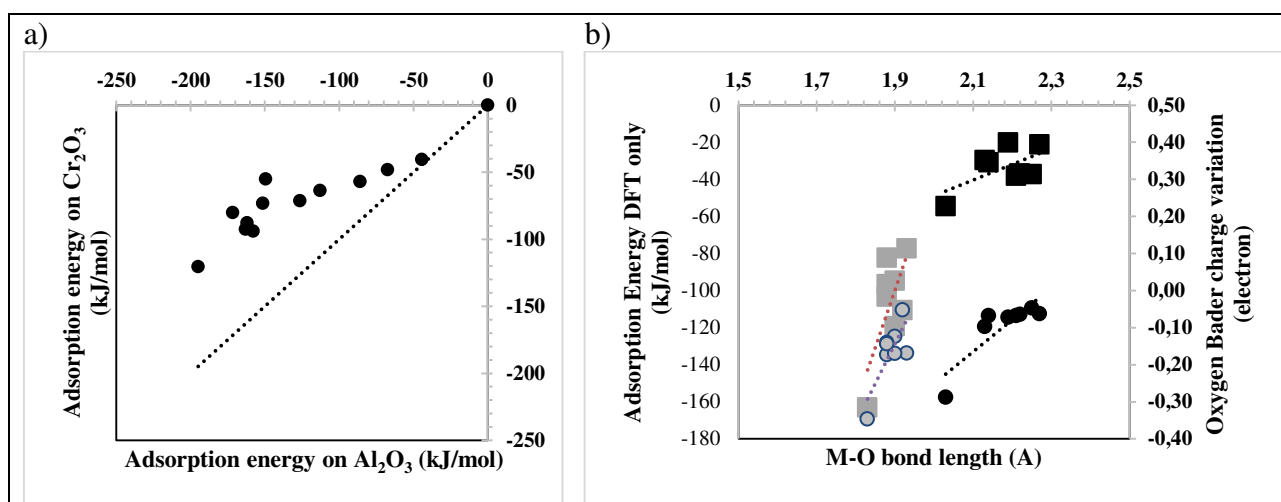


**Figure 47:** a) Starting and final configurations of the acetic acid dissociative 1-4 and molecular adsorptions on dry  $\alpha$ -Al<sub>2</sub>O<sub>3</sub>. b) configurations of the water dissociative and molecular adsorptions on dry  $\alpha$ -Al<sub>2</sub>O<sub>3</sub> and Cr<sub>2</sub>O<sub>3</sub>. The bond distances are reported in Angstrom [Å] and the adsorption energies in [kJ/mol]. Color code: red = O; light-blue = C; white: H; grey = Al; brown = Cr.

From **Figure 47a**, we find the dissociation of the acetic acid on dry  $\alpha$ -Al<sub>2</sub>O<sub>3</sub> also in the molecular adsorption case, leading us to the conclusion that the acetic acid spontaneously dissociates on  $\alpha$ -Al<sub>2</sub>O<sub>3</sub>. However, the same cannot be said for the acetic acid adsorbed on  $\alpha$ -Cr<sub>2</sub>O<sub>3</sub> (**Figure 46**), where the dissociative and associative configurations show a marked difference in terms of adsorption energies (-126.4 kJ/mol for the dissociative case against -91.7 kJ/mol for the associative case) and also in terms of bond lengths.

For water, (**Figure 47b**) we calculated associative and dissociative adsorption energy that fit well with the literature data: -158 and -120.3 kJ/mol for dissociative and molecular adsorption of water on  $\text{Al}_2\text{O}_3$ [23], and around -90 kJ/mol for water (molecular) adsorption on  $\text{Cr}_2\text{O}_3$ [18]. We indeed found that for water adsorbed on  $\text{Cr}_2\text{O}_3$ , starting from the 1-4 dissociative adsorption, the system evolves towards the molecular adsorption mode. This result agrees with that of Sharkas et al. [18], where the molecular and dissociative adsorption modes of water were found iso energetics.

**Figure 48a** compares for all molecules, the adsorption energies on  $\text{Al}_2\text{O}_3$  and  $\text{Cr}_2\text{O}_3$ . It appears clearly that  $\text{Al}_2\text{O}_3$  is more reactive than  $\text{Cr}_2\text{O}_3$  since it presents more negative adsorption energies for all molecules.

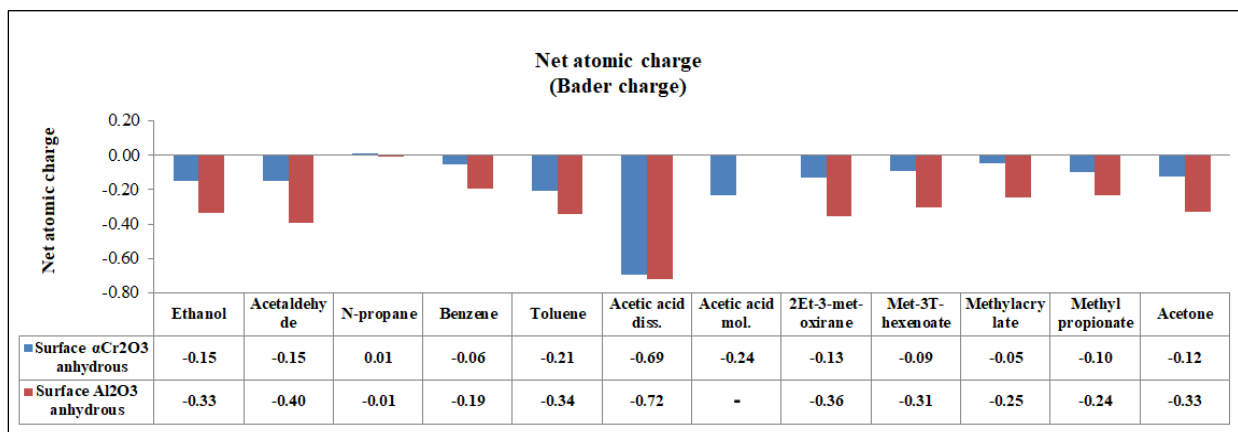


**Figure 48:** a) Adsorption energies on  $\text{Cr}_2\text{O}_3$  versus  $\text{Al}_2\text{O}_3$  (kJ/mol). The dashed line is the identity function ( $y=x$ ). b) DFT interaction contribution (e.g. covalent and H-bonds) plotted against Al-O (grey squares) and Cr-O (black squares) bonds respectively for oxygen-containing molecules adsorbed on anhydrous  $\text{M}_2\text{O}_3$  ( $\text{M}=\text{Al}, \text{Cr}$ ). Bader charge variation of the adsorbed O atom is reported (black circles:  $\text{M}=\text{Cr}$ ; grey circles:  $\text{M}=\text{Al}$ ).

The M-O bond lengths formed for the O-containing adsorbates, are smaller for  $\alpha\text{-Al}_2\text{O}_3$  than for  $\alpha\text{-Cr}_2\text{O}_3$ . **Figure 48b** shows that the DFT energy contribution  $E_{ads}^{DFT}$  (thus without van der Waals contributions) is well correlated to the M-O bond length: the shorter the bond length, the more exothermic the adsorption energy. The slopes of the trends for  $\alpha\text{-Al}_2\text{O}_3$  and  $\alpha\text{-Cr}_2\text{O}_3$  are different. For Al, the Al-O bond is in a narrow range around 1.9 Å, and  $E_{ads}^{DFT}$  adsorption energies are strong, (between -80 kJ/mol and -160 kJ/mol), while the slope is less steep for  $\text{Cr}_2\text{O}_3$ , where

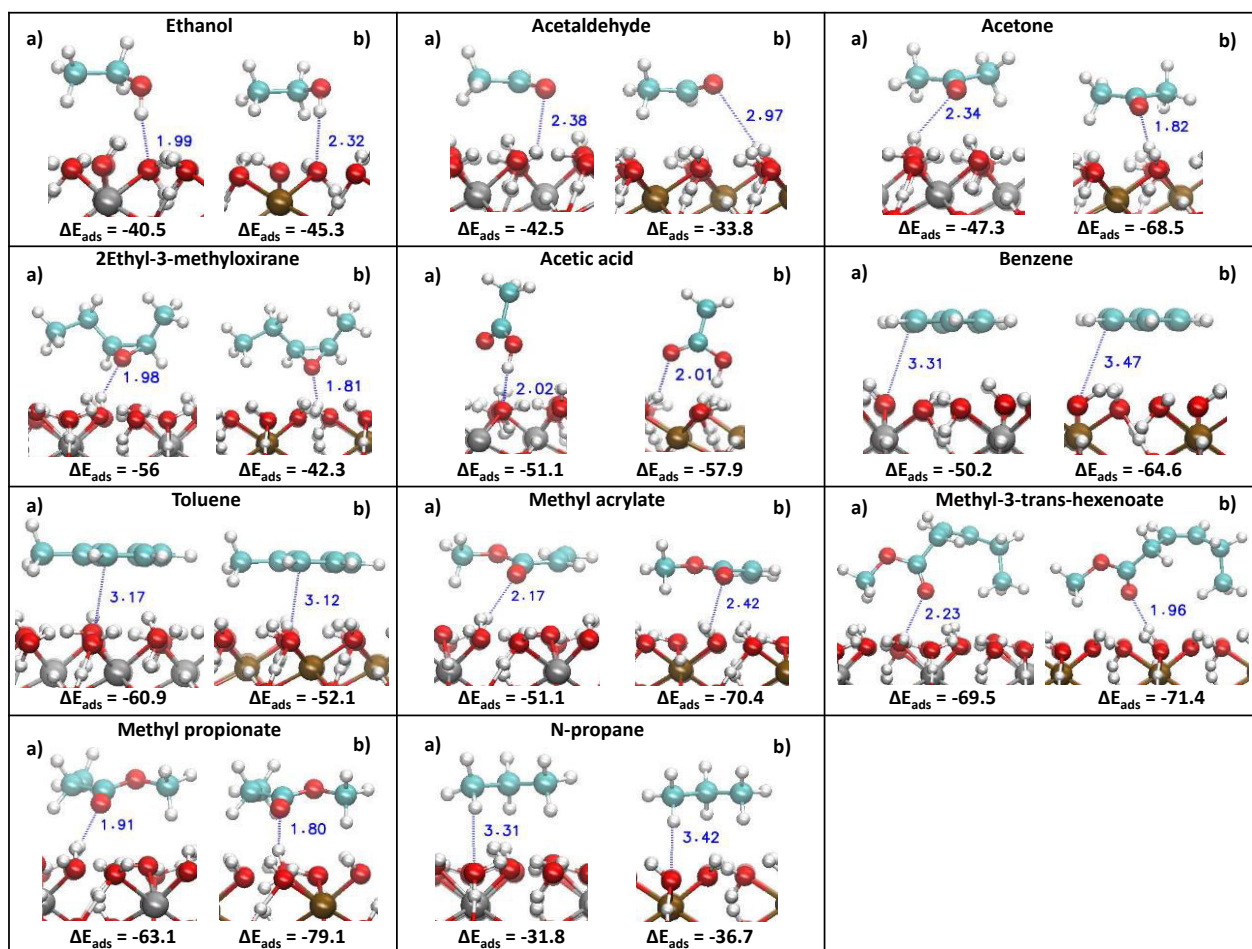
the bond length interval is larger [2.1 Å – 2.3 Å] and associated with less exothermic  $E_{ads}^{DFT}$  (between -20 kJ/mol and -60 kJ/mol).

The charge transfer  $\Delta\rho$  from the surface to the molecules (including non O-containing molecules) for each adsorbed molecule on dry  $\alpha$ -Al<sub>2</sub>O<sub>3</sub> and  $\alpha$ -Cr<sub>2</sub>O<sub>3</sub> is reported in **Figure 49** below. At the exception of the dissociative adsorption of the acetic acid, the charge transfer to the molecule is weak (see the detailed values in the inset below **Figure 49**). For acetic acid, for which the adsorption is dissociative on alumina, the calculated charge is the charge variation of the anionic part of the molecule (the charge difference of the proton from the molecule to the adsorption on the surface is not considered). The charge transferred is higher (in absolute value) for Al<sub>2</sub>O<sub>3</sub> than Cr<sub>2</sub>O<sub>3</sub>, in line with the slightly larger electropositivity (or smaller electronegativity:  $X=1.61$ ) of Al with respect to Cr ( $X=1.66$ ).



**Figure 49:** Electronic charge transfer  $\Delta\rho$  (electron) of the molecules adsorbed on dry  $\alpha$ -Al<sub>2</sub>O<sub>3</sub> and (orange dots) and on dry  $\alpha$ -Cr<sub>2</sub>O<sub>3</sub> (blue dots) respectively. A minus charge corresponds to an increase in negative charge of the molecule.

To understand the role of the water activity on the molecule/surface interaction, the adsorption of the molecules on the hydroxylated surfaces is discussed. **Figure 50** shows the optimized configurations obtained for the molecules on the hydroxylated corundum surfaces. As for the dry corundum-type surfaces, we placed the molecules on top of the surface in the same initial arrangement to compare how the same molecule interacts with the two different substrates with the same initial configuration.

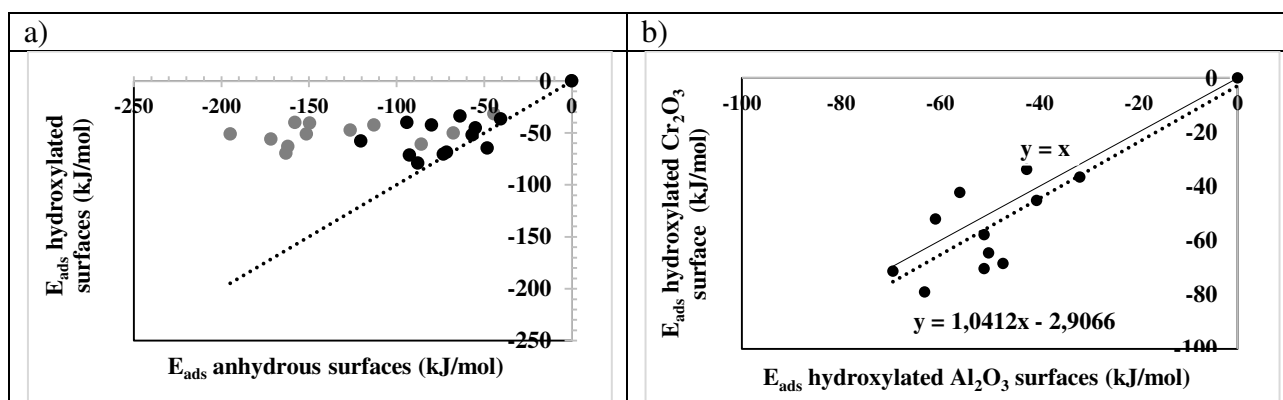


**Figure 50:** Optimized adsorption configurations on hydroxylated surfaces with their corresponding adsorption energies calculated via DFT approach of different model molecules on fully-hydroxylated  $\alpha$ -Al<sub>2</sub>O<sub>3</sub> (a) and  $\alpha$ -Cr<sub>2</sub>O<sub>3</sub> (b) surfaces. The bond distances are reported in Angstrom [Å] and the adsorption energies in [kJ/mol]. Color code: red = O; light-blue = C; white: H; grey = Al; brown = Cr.

From **Figure 50a** it is noticed that the hydration layer attenuates the adsorption energies, especially in the case of alumina. For chromia, the obtained trend is very similar to that observed by Blanck et al, for hematite. The attenuation of the adsorption energy with the hydration layer depends however on the nature of the molecule-surface interaction. This is, for example, illustrated for the adsorption of ethanol. Whereas for the anhydrous surfaces adsorption energies are calculated of  $-149.6$  and  $-55$  kJ/mol for alumina and chromia, respectively, these values reduce to practically equal values of  $-40.5$  and  $-45.3$  kJ/mol for the fully hydrated surfaces. Similar trends are observed for the aldehyde, ketone, epoxide, and esters, which coordinate with a polar oxygen atom (or group) to the surface.

Such polar groups are missing in benzene and toluene, where the attenuation effect due to the hydration layer is almost absent.

**Figure 51b** compares the adsorption energies on hydroxylated  $\text{Cr}_2\text{O}_3$  and  $\text{Al}_2\text{O}_3$ . The average value is very near the  $y = x$  line, suggesting that it is principally the hydration layer that now determines the adsorption energy, and the underlying oxide only plays a secondary role. The charge transfers between the surface and the adsorbed molecules have been calculated and are found to be negligible, ranging between -0.03 and +0.02 electrons.



**Figure 51:** a) Adsorption energies (kJ/mol) on the hydroxylated surfaces versus the anhydrous surfaces, black: Cr, grey: Al; b) Adsorption energies (kJ/mol) on hydroxylated  $\text{Cr}_2\text{O}_3$  versus hydroxylated  $\text{Al}_2\text{O}_3$ . The linear average curve is plotted in black, dotted line. The identity curve  $y = x$  is plotted in black, solid line.

## 4.5 Surface impact on intramolecular distortion

To have an idea on the effect of the surface on the adsorption process, in **Table 6** below, we report the intramolecular bonds of each compound that presented the highest distortion from the consequent adsorption above the dry  $\alpha$ -(0001)  $\text{Al}_2\text{O}_3$ .

We chose to report the values related to the adsorption on dry  $\alpha$ -alumina since in our study this substrate was observed to be the most reactive, thus the one that could provide the highest variations between the pre and post-adsorption conditions. We can notice that the general trend confirms the weak impact of surface on the intramolecular distortion, at the exception of the dissociated case of the acetic acid, where indeed we see a  $\Delta_{\text{O-H}} = 0.44 \text{ \AA}$ , which confirms the proton transfer from the molecule towards the surface oxygen atom (**Figure 46**).

**Table 6: Intramolecular bonds presenting the highest distortion after adsorption of each molecule on top of the dry  $\alpha$ -(0001)  $\text{Al}_2\text{O}_3$**

Molecules	MAX $\Delta d_{\text{mol}}$ (Ads - Gas) [Angstrom]	Intramol. Bond
Acetic acid (Diss. Ads)	<b>0.44</b>	O-H
Ethanol	0.05	C-O
Acetaldehyde	0.03	C-C
Acetone	0.03	C-C
Benzene	0.01	C=C
Toluene	0.01	C-C
Methyl Acrylate	0.03	C=O
Methyl-3T-Hexenoate	0.03	C=O
Methyl propionate	0.04	C=O
2Ethyl-3methyl-oxirane	0.04	C-O
N-propane	0.00	-

## 4.6 Water/OH substitution on corundum surfaces

In addition to the adsorption configurations reported in the previous paragraphs, in this work we also treated another type of configuration, where a water molecule or a OH group is substituted with an organic adsorbate. In our case, two cases were examined: the water substitution with an acetate molecule and a OH substitution with a methyl propionate molecule.

### 4.6.1 Implemented scheme

The surface OH substitution can be described through an acid base mechanism resumed in the equation below:



Equation 79

where **Slab-HY** is the hydroxylated surface and the (**–OH<sub>s</sub>**) coincides with the substituted –OH surface termination (**Figure 52**).

In reference to the adsorption mechanism for this dissociative configuration, what happens between the acetic acid and the OH<sub>s</sub> can be described as a Brønsted-Lowry reaction reported in **Figure 52** below, where the acetic acid represents the proton donor (Brønsted-Lowry acid) and the OH<sub>s</sub> represents the proton acceptor (Brønsted-Lowry base). In fact, when the acetic acid reacts with the OH<sub>s</sub> through the H atom of its hydroxyl group, the result is the formation of its conjugate base (acetate) and of a released water molecule.

The substitution energy  $\Delta E_{\text{subst}}[\text{kJ/mol}]$  was calculated as:

$$\Delta E_{\text{subst}}(\text{RH}) = E_{\text{slab-R}} - E_{\text{RH}} - E_{\text{Slab-HY}(-\text{OH}_s)} + E_{\text{H}_2\text{O}}$$

Equation 80

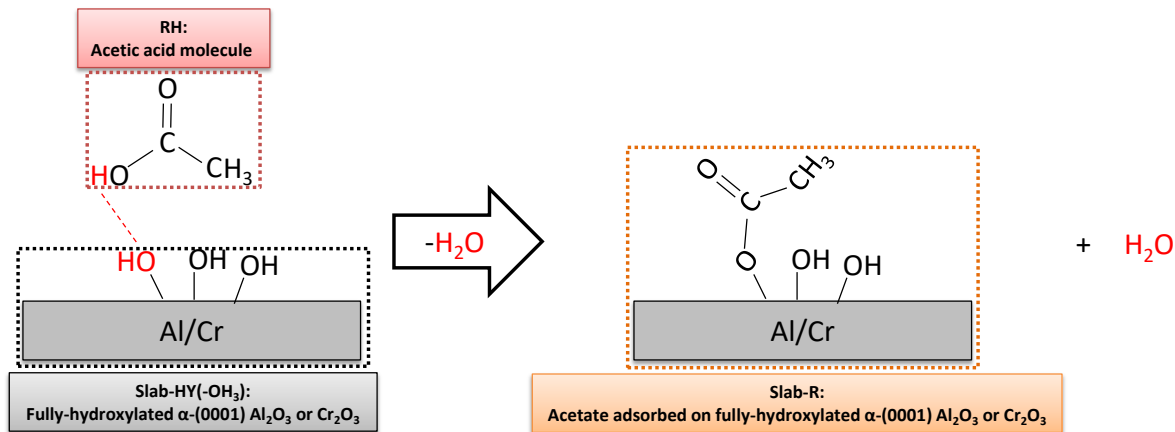
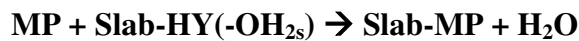


Figure 52: Simplified scheme for the substitution OH reaction with an acetate molecule described as a Brønsted-Lowry reaction.

For the methyl propionate (MP) case, instead of the substitution of a superficial –OH<sub>s</sub>, we preferred to study the substitution of an entire chemisorbed water molecule at the surface; in this case, we have :



Equation 81

and

$$\Delta E_{\text{subst}} = E_{\text{slab-MP}} - E_{\text{MP}} - E_{\text{Slab-HY(-OH}_2\text{s)}} + E_{\text{H}_2\text{O}}$$

Equation 82

where in this case the **Slab-HY** is characterized by a chemisorbed water termination ( $-\text{OH}_2\text{s}$ ).

We can analyze further these results in calculating the different components of the substitution energy: water desorption energy and molecule/surface binding energy. We have, if X is the adsorbed moiety, either R or MP,

$$\Delta E_{\text{subst}} = \Delta E_{\text{H}_2\text{O}}^{\text{desorb}} + E_{\text{slab-X}}^{\text{binding}} + \Delta E_{\text{Slab-HY-minus-H}_2\text{O}}^{\text{relaxation}}$$

Equation 83

With

$$\Delta E_{\text{H}_2\text{O}}^{\text{desorb}} = E_{\text{Slab-HY-minus-H}_2\text{O}} - E_{\text{Slab-HY}} + E_{\text{H}_2\text{O}}$$

Equation 84

And

$$E_{\text{slab-X}}^{\text{binding}} = E_{\text{slab-X}}^{\text{optimized}} - E_X - E_{\text{Slab-HY-minus-H}_2\text{O}}^{\text{in the geometry of the adsorption}}$$

Equation 85

And

$$\Delta E_{\text{Slab-HY-minus-H}_2\text{O}}^{\text{relaxation}} = E_{\text{Slab-HY-minus-H}_2\text{O}}^{\text{optimized}} - E_{\text{Slab-HY-minus-H}_2\text{O}}^{\text{in the geometry of the adsorption}}$$

Equation 86

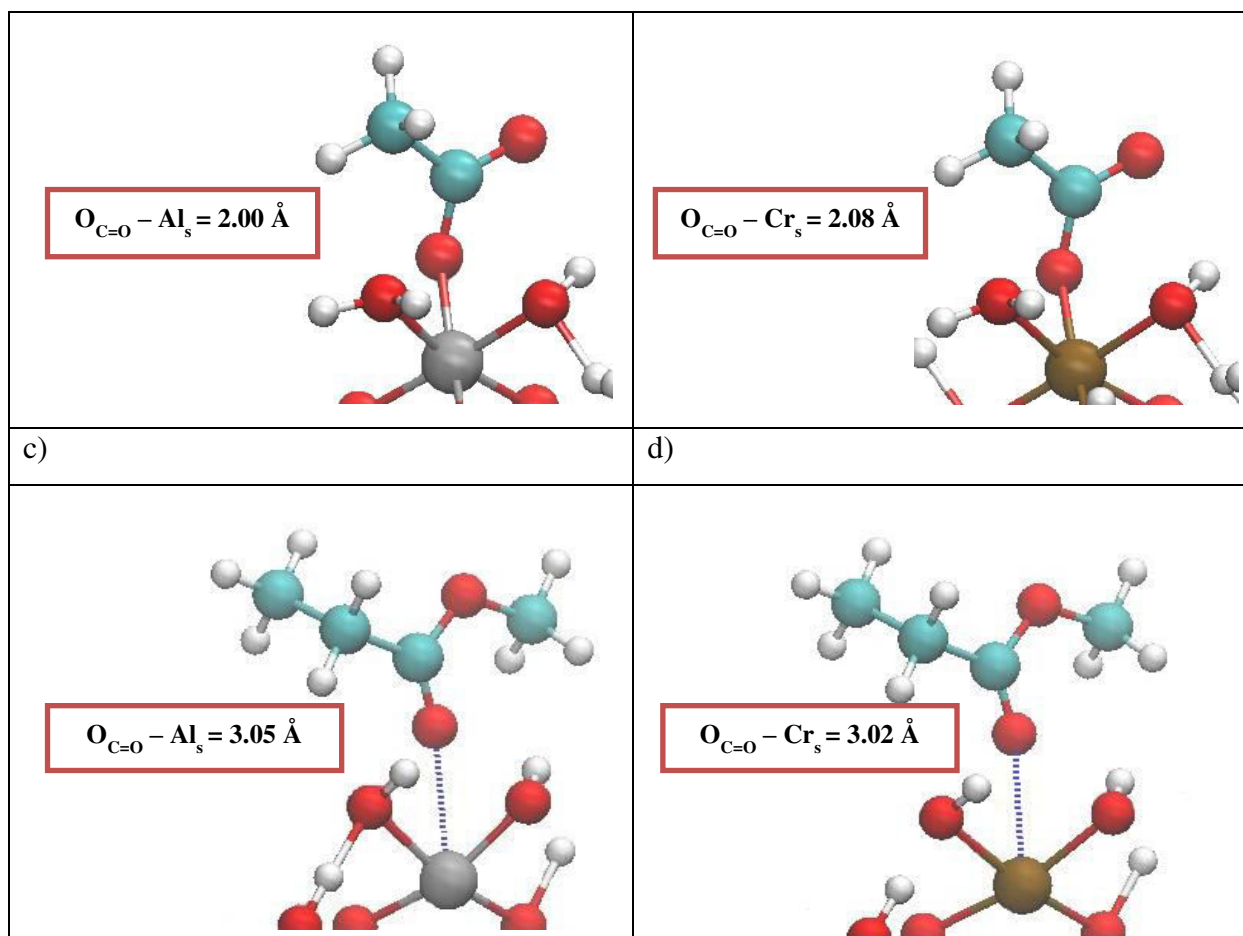
## 4.6.2 Results and discussion

Now we will study explicitly acetic acid that has a marked affinity with the anhydrous surfaces, to which extent water molecule can be exchanged. The results are compared with that on methyl propionate, which, according to our first estimation, is not expected to substitute water at the corundum surfaces. In **Figure 53a-b** are reported the optimized configurations of the dissociative adsorptions of the acetic acid molecules on fully-hydroxylated  $\alpha$ -Cr<sub>2</sub>O<sub>3</sub>-Cr(OH)<sub>3</sub> and  $\alpha$ -Al<sub>2</sub>O<sub>3</sub>-Al(OH)<sub>3</sub>. The substitution reaction of an OH group by an acetate anion is described by **Equation 80** and consists of an acid-base mechanism with formation of a Cr-molecule adduct and the release of a water molecule in the gas phase. The substitution energy is -43.8 kJ/mol for chromia, and -17.5 kJ/mol for Al<sub>2</sub>O<sub>3</sub>. The substitution of OH by acetate is thus an exothermic process for both surfaces, a trend in agreement with the conclusions of the preceding paragraph.

The results of the substitution reaction of water by methyl propionate are shown in **Figure 53c-d**. It can easily be observed that methyl propionate does not get very close to the surfaces. Starting with the Cr-O and Al-O bond lengths obtained on the anhydrous surfaces, 1.88 Å for Al<sub>2</sub>O<sub>3</sub> and 2.22 Å for Cr<sub>2</sub>O<sub>3</sub> (**Figure 46**), we observe that the M-O distances increase on the hydroxylated surfaces to 3.05 Å (**Figure 53c**) and 3.02 Å (**Figure 53d**), respectively. Complementary calculations of adsorption on partially hydroxylated surfaces were performed in the case of methyl propionate. We found that methyl propionate forms a bond with surface Al only in the totally dehydrated case, but not on the Al-OH and Al-(OH)<sub>2</sub> terminations, confirming that methyl propionate binds a bond with Al<sub>4c</sub> (four fold coordinated) only. The substitution energies are -34.7 and 17 kJ/mol for Cr<sub>2</sub>O<sub>3</sub> and Al<sub>2</sub>O<sub>3</sub>, respectively. The water substitution by methyl propionate is endothermic for Al<sub>2</sub>O<sub>3</sub>, as expected from the preceding paragraph, while slightly exothermic on Cr<sub>2</sub>O<sub>3</sub>.

We can analyze further these results in calculating the different components of the substitution energy: water desorption energy and molecule/surface binding energy, and **Table A4-3** in the **Annex** summarizes the values obtained for energy decomposition for MP and acetic acid.

a)	b)
----	----



**Figure 53: a-b) Optimized adsorption configurations calculated via DFT approach of a substitution reaction between an acetic acid and a water molecule on fully hydroxylated corundum-type  $\alpha$ - $\text{Al}_2\text{O}_3$ - $\text{Al}(\text{OH})_3$  (a) and  $\alpha$ - $\text{Cr}_2\text{O}_3$ - $\text{Cr}(\text{OH})_3$  (b) respectively. The background atoms of both configurations have been removed for clarity.**

**Color code: Red = O; light-blue = C; white = H; Brown = Cr; Grey = Al. c-d) Optimized adsorption configurations calculated via DFT approach of a substitution reaction between a methylpropionate molecule and a water molecule on fully hydroxylated corundum-type  $\alpha$ - $\text{Al}_2\text{O}_3$ - $\text{Al}(\text{OH})_3$  (a) and  $\alpha$ - $\text{Cr}_2\text{O}_3$ - $\text{Cr}(\text{OH})_3$  (b) respectively. The background atoms of both configurations have been removed for clarity. Colour code: Red = O; light-blue = C; white = H; Brown = Cr; Grey = Al.**

## 4.7 Conclusion

To improve our understanding of undesired deposit formations observed for biodiesels in engine fuel circuits, we have conducted a quantum mechanical study using density functional theory calculations considering the molecular interactions established by these fuel deposits in both homogeneous conditions (i.e. their gas-phase) and heterogeneous conditions (i.e. their contact with the solid surfaces).

In regards of the deposits reactivity in the gas-phase, a set of representative reactions describing the toluene autoxidation process was considered (**Eq. 68-Eq. 78**). We proposed the toluene autoxidation mechanism because aromatic compounds represent a major constituent of petrodiesel and toluene is often in literature taken as model molecule for fuel autoxidation studies [5–7]. In this thesis, our focus was set on the hydroperoxide  $(\text{C}_6\text{H}_5)\text{CH}_2\text{O}_2\text{H}$  because, starting from their decomposition, the future oxygenated precursors are produced (e.g. alcohols, carboxylic acids, aldehydes, etc.) [8].

Through ab-initio calculations, we obtained the  $\Delta E_r$  of these autoxidation reactions. Also, we run a PES scan for the for C-OOH and CO-OH bond dissociation energies in the benzyl hydroperoxide molecules, where we found that the two curves almost overlap on each other till the bond distance of 1.8 Å. However, the energetic maximum for either of the bonds was not reached in our calculations because of intramolecular contractions that prevented us to analyze further the stretching for both C-OOH and CO-OH bonds.

About the interface interactions occurring between the gas-phase molecules and the alumina and chromia surfaces, we studied the adsorption of small representative organic molecules on representative aluminum and stainless steel surfaces. The investigated organic compounds comprise hydrocarbons like n-alkanes and aromatic molecules, as well as oxygen containing molecules including an alcohol, aldehyde, ketone, epoxide, carboxylic acid, and esters. Whereas the stainless-steel fuel circuit was represented by  $\alpha\text{-Cr}_2\text{O}_3$  and aluminum-based circuits by  $\alpha\text{-Al}_2\text{O}_3$ , in which each studied surface orientation was either anhydrous or fully hydroxylated.

From this heterogeneous study we determined that:

1. Anhydrous surfaces are more reactive towards the organic molecules than their fully hydroxylated counterparts as seen from the more negative adsorption energies.
2. Aluminum anhydrous surfaces show a higher reactivity as compared to anhydrous chromia, while this difference vanishes upon fully hydroxylating the surfaces.
3. Oxygen containing organic compounds show more negative adsorption energies independent of the nature of the inorganic surface.
4. Except for the dissociative adsorption of acetic acid on anhydrous  $\alpha\text{-Al}_2\text{O}_3$  no other significant geometrical changes, e.g. bond elongations, in the organic molecules were observed due to adsorption on the oxide surfaces.

5. Bader charge analyses show that there are only weak charge transfers between the different oxides and organic molecules, except for the dissociative adsorption of acetic acid on dry alumina.

Since under operational conditions each of the oxide surfaces is at least partially or fully hydroxylated, the difference in nature of the oxides vanishes with respect to its reactivity towards the investigated organic compounds. In other words, based on this study, stainless-steel circuits which is the surface that is more problematic since it is material of injectors, would not play a more important role in the autoxidation reactions as compared to aluminum-based circuits. This finding is important since it corroborates that fuel oxidation product aggregates seem to be mainly formed in the liquid phase further being deposited on a surface by different mechanisms [24]. Furthermore, the relatively weak interactions ( $-30$  to  $-70$  kJ/mol) between surface and molecule seem to be insufficient to provoke significant distortions in the organic molecule itself, which in turn could lead to higher reactivity and rendering the molecule more prone to autoxidation reactions in liquid phase.

We conclude this chapter by emphasizing that both homogeneous and heterogeneous studies were carried out to provide important input data to use for the ReaxFF discussed in the next chapter. The autoxidation reactions as a mean for ReaxFF to predict the chemical reactivity in the gas-phase, while the adsorption configurations to aid the reactive force field to estimate the nature of the gas-solid interface interactions. Both energetic data were fundamental for the achievement of the ReaxFF optimization and validation implemented in this thesis.

## References

- 1 M.J. Frisch, G.W. Trucks, H.B. Schlegel, G.E. Scuseria, M.A. Robb, J.R. Cheeseman, G. Scalmani, V. Barone, G.A. Petersson, H. Nakatsuji, X. Li, M. Caricato, A.V. Marenich, J. Bloino, B.G. Janesko, R. Gomperts, B. Mennucci, H.P. Hratchian, J.V. Ortiz, Izmaylov, A. F., Sonnenberg, J. L., Williams, F. Ding, F. Lipparini, F. Egidi, J. Goings, B. Peng, A. Petrone, T. Henderson, D. Ranasinghe, V.G. Zakrzewski, J. Gao, N. Rega, G. Zheng, W. Liang, M. Hada, M. Ehara, K. Toyota, R. Fukuda, J. Hasegawa, M. Ishida, T. Nakajima, Y. Honda, O. Kitao, H. Nakai, T. Vreven, K. Throssell, J.A. Montgomery Jr., Peralta, J. E., F. Ogliaro, M.J. Bearpark, Heyd, J. J., E.N. Brothers, K.N. Kudin, Staroverov, V. N., T.A. Keith, R. Kobayashi, J. Normand, K. Raghavachari, A.P. Rendell, J.C. Burant, S.S. Iyengar, J. Tomasi, M. Cossi, J.M. Millam, M. Klene, C. Adamo, R. Cammi, J.W. Ochterski, R.L. Martin, K. Morokuma, O. Farkas, J.B. Foresman, D.J. Fox *Gaussian 16 Rev. C.01*, Wallingford, E.U.A. (2016).
- 2 Kresse, Furthmüller Efficient iterative schemes for ab initio total-energy calculations using a plane-wave basis set, *Phys. Rev. B***54**, 16 (1996), 11169–11186. DOI: 10.1103/physrevb.54.11169.
- 3 Bacha K. These de Doctorat "Etude de l'interaction entre le carburant diesel et les composants su systèmes d'injection diesel, *Physique des matériaux*, Université de Haute Alsace (2016).
- 4 Mei D., Dai S., Chen T., Wang H., Yuan Y. Absorption of fuel containing esters on iron surface based on molecular simulation and its effects on lubricity, *Energ. Sources, Part A* (2020), 1–12. DOI: 10.1080/15567036.2020.1783395.
- 5 Mielczarek D.C., Matrat M., Amara A.B., Bouyou Y., Wund P., Starck L. Toward the Accurate Prediction of Liquid Phase Oxidation of Aromatics: A Detailed Kinetic Mechanism for Toluene Autoxidation, *Energy Fuels***31**, 11 (2017), 12893–12913. DOI: 10.1021/acs.energyfuels.7b00416.
- 6 da Silva G., Bozzelli J.W. Kinetic modeling of the benzyl+HO<sub>2</sub> reaction, *Proceedings of the Combustion Institute***32**, 1 (2009), 287–294. DOI: 10.1016/j.proci.2008.05.040.
- 7 da Silva G., Hamdan M.R., Bozzelli J.W. Oxidation of the Benzyl Radical: Mechanism, Thermochemistry, and Kinetics for the Reactions of Benzyl Hydroperoxide, *Journal of chemical theory and computation***5**, 12 (2009), 3185–3194. DOI: 10.1021/ct900352f.
- 8 Bacha K., Ben-Amara A., Vannier A., Alves-Fortunato M., Nardin M. Oxidation Stability of Diesel/Biodiesel Fuels Measured by a PetroOxy Device and Characterization of Oxidation Products, *Energy Fuels***29**, 7 (2015), 4345–4355. DOI: 10.1021/acs.energyfuels.5b00450.
- 9 John P. Perdew, K. Burke, M. Ernzerhof Generalized Gradient Approximation Made Simple, *Phys. Rev. Lett.***77**, 18 (1996), 3865–3868. DOI: 10.1103/PhysRevLett.77.3865.
- 10 Kresse G., Hafner J. Ab initio molecular dynamics for liquid metals, *Phys. Rev. B***47**, 558 (1993). DOI: 10.1103/PhysRevB.47.558.
- 11 Kresse G., Hafner J. Ab initio molecular-dynamics simulation of the liquid-metal-amorphous-semiconductor transition in germanium, *Phys. Rev. B***49**, 20 (1994), 12252–14269. DOI: 10.1103/PhysRevB.49.14251.
- 12 Kresse G., Furthmuller J. Efficiency of ab-initio total energy calculations for metals and semiconductors using a plane-wave basis set, *Comput. Mater. Sci.***6** (1996), 15–50. DOI: 10.1016/0927-0256(96)00008-0.
- 13 Monkhorst H. J., Pack J. D Special points for Brouillon-zone integrations, *Phys. Rev. B***13** (1976), 5188–5192. DOI: 10.1103/PhysRevB.13.5188.
- 14 Anisimov et al. First-principles calculations of the electronic structure and spectra of strongly correlated systems: the LDA+U method, *J. Phys.: Condens. Matter***9** (1997), 767–808. DOI: 10.1088/0953-8984/9/4/002.
- 15 Souvi S.M., Badawi M., Virot F., Cristol S., Cantrel L., Paul J.-F. Influence of water, dihydrogen and dioxygen on the stability of the Cr 2 O 3 surface: A first-principles investigation, *Surf. Sci.***666** (2017), 44–52. DOI: 10.1016/j.susc.2017.08.005.
- 16 Rohrbach A., Hafner J., Kresse G. Ab initio study of the (0001) surfaces of hematite and chromia: Influence of strong electronic correlations, *Phys. Rev. B***70**, 12 (2004), 13. DOI: 10.1103/PhysRevB.70.125426.
- 17 Grimme S., Antony J., Ehrlich S., Krieg H. A consistent and accurate ab initio parametrization of density functional dispersion correction (DFT-D) for the 94 elements H-Pu, *J. Chem. Phys.***132**, 15 (2010), 154104. DOI: 10.1063/1.3382344.

- 18 Costa D., Sharkas K., Islam M.M., Marcus P. Ab initio study of the chemical states of water on Cr<sub>2</sub>O<sub>3</sub>(0001): From the isolated molecule to saturation coverage, *Surf. Sci.* **603**, 16 (2009), 2484–2493. DOI: 10.1016/j.susc.2009.05.037.
- 19 Arrouvel C., Diawara B., Costa D., Marcus P. DFT Periodic Study of the Adsorption of Glycine on the Anhydrous and Hydroxylated (0001) Surfaces of  $\alpha$ -Alumina, *J. Phys. Chem. C* **111**, 49 (2007), 18164–18173. DOI: 10.1021/jp0741408.
- 20 Łodziana Z., Nørskov J.K., Stoltze P. The stability of the hydroxylated (0001) surface of  $\alpha$ -Al<sub>2</sub>O<sub>3</sub>, *The Journal of Chemical Physics* **118**, 24 (2003), 11179–11188. DOI: 10.1063/1.1574798.
- 21 Ranea V.A., Carmichael I., Schneider W.F. DFT Investigation of Intermediate Steps in the Hydrolysis of  $\alpha$ -Al<sub>2</sub>O<sub>3</sub> (0001), *J. Phys. Chem. C* **113**, 6 (2009), 2149–2158. DOI: 10.1021/jp8069892.
- 22 Dabaghmanesh S., Neyts E.C., Partoens B. van der Waals density functionals applied to corundum-type sesquioxides: Bulk properties and adsorption of CH<sub>3</sub> and C<sub>6</sub>H<sub>6</sub> on (0001) surfaces, *Phys. Chem. Chem. Phys.* **18**, 33 (2016), 23139–23146. DOI: 10.1039/c6cp00346j.
- 23 Heiden S., Usvyat D., Saalfrank P. Theoretical Surface Science Beyond Gradient-Corrected Density Functional Theory: Water at  $\alpha$ -Al<sub>2</sub>O<sub>3</sub> (0001) as a Case Study, *J. Phys. Chem. C* **123**, 11 (2019), 6675–6684. DOI: 10.1021/acs.jpcc.9b00407.
- 24 Alves-Fortunato M., Ayoub E., Bacha K., Mouret A., Dalmazzone C. Fatty Acids Methyl Esters (FAME) autoxidation: New insights on insoluble deposit formation process in biofuels, *Fuel* **268** (2020), 117074. DOI: 10.1016/j.fuel.2020.117074.
- 25 Wodrich M. D., Corminboeuf C., Wheeler S. E. Accurate Thermochemistry of Hydrocarbon Radicals via an Extended Generalized Bond Separation Scheme (2012) *J. Phys. Chem. A*, **116**, 13, 3436–3447. DOI: 10.1021/jp212209q
- 26 Zhao Y, Thrular D. G. Density Functional Theory for Reaction Energies: Test of Meta and Hybrid Meta Functionals, Range-Separated Functionals, and Other High-Performance Functionals (2011) *J. Chem. Theory Comput.* 2011, **7**, 3, 669–676. DOI: 10.1021/ct1006604

## Chapter 5. ReaxFF development and validation

### 5.1 Introduction

As mentioned in the previous **Chapter 4**, the next step in our multi-scale molecular modeling approach is the use of an empirical reactive force field, ReaxFF, to run molecular dynamics simulations on systems that are larger and more representative than one could model with DFT. As detailed in (cf.§2.11.1) there is no unique ReaxFF force field and its parameters often need to be adjusted or optimized to accurately describe the chemistry of the system of interest. The number of available force fields that can describe aluminum and chromium-based systems is very limited in the literature [1–5]. In fact, in the PhD of Benoît Darenne [6] a force field describing both alumina and chromia was put in place. Logically, we first tested its applicability to the systems of our interest, by reproducing the adsorption energies for the molecules on chromia and alumina (cf.§4.4.2). We refer to the implemented force field of the work [6] as FF0.

On the basis of these results (see **Figure A5-3** in the **Annex**) and the observation of the formation of lactones during molecular dynamics simulations of acetic acid on hydroxylated alumina, which is highly endothermic at ambient temperatures (see **A5.2.2-Figure A5-6** in the **Annex**), it was decided to readjust certain ReaxFF parameters using the CMA-ES algorithm (cf.§2.11.3).

However, preliminary calculations with this optimized force field (see **Annex A5.6.2**) showed us that it was not able to correctly reproduce adsorption geometries and energies for  $\alpha$ -Cr<sub>2</sub>O<sub>3</sub>, as a consequence of the fact that optimizing this FF to improve the description of  $\alpha$ -Al<sub>2</sub>O<sub>3</sub> decreased the accuracy to describe  $\alpha$ -Cr<sub>2</sub>O<sub>3</sub> systems.

Therefore, in this chapter we start a new cycle of ReaxFF reparametrization by using two different force fields: FFA for the Al<sub>2</sub>O<sub>3</sub> systems and FFB for the Cr<sub>2</sub>O<sub>3</sub> systems. These two different force fields are both based on the force field of Benoît Darenne [6], with the difference that in FFB we chose to substitute the ReaxFF parameters of H and O atoms by inserting the values of the “CHON-2017\_weak.ff” force field developed by Zhang and van Duin [18].

The FFA and FFB parametrizations will be discussed in the following paragraphs.

The quality of the obtained force fields is evaluated in two steps. In the first step, called training set, we tested how the force field is able to reproduce a set of DFT data. In the second step, called validation set, we tested how the force-field is able to reproduce the other DFT data (data that are not included in the training set). The validation set includes the reproduction of the cell parameters of the bulk, adsorption energies and curves of similar but different organic molecules that were used in the training set, representative reactions of the autoxidation of toluene, and the dynamic structuration of pure organic liquids (mass/volume density, radial distribution functions). Since the latter requires molecular dynamic simulations that are relatively time consuming as opposed to geometry optimizations, these MD simulations were only performed once the preceding steps were validated.

A simplified scheme resuming the implemented ReaxFF parametrization and validation is reported in **Figure 24** (*cf.* §2.11.1), while another scheme detailing the “static” and “dynamic” studies of the ReaxFF validation is reported in **Figure 26** (*cf.* §2.11.6).

## 5.2 FFA and FFB reparametrizations

In this section, we discuss the new cycle of ReaxFF reparametrization by using these two different force fields: FFA for the  $\text{Al}_2\text{O}_3$  systems (*cf.* §4.4.2) and FFB for the  $\text{Cr}_2\text{O}_3$  systems (*cf.* §4.4.2). The choice to optimize two different force fields was to ensure a more reliable description of the interactions on the two metal-oxide substrates, since they present different features as well as different reactivities towards the organic adsorbates, as it was observed in the previous **Chapter 4**.

In the next paragraph, we discuss how we carried out the optimization of both implemented force fields, reporting the selection of the parameters that were reparametrized and the conclusion that we reached from this optimization procedure.

### 5.2.1 Computational details

For the FFA training-set, all the DFT alumina adsorption configurations (cf.§4.4.2) were considered, conversely for the FFB training-set, all the DFT chromia adsorption configurations were taken into account (cf.§4.4.2), accompanied by the geometries of the single molecules (cf.§4.2) and dry and hydroxylated surfaces (cf.§4.4.1). However, both training-sets shared some DFT data, such as the lactone reaction coordinate (see **Figure A5-6** in the **Annex**).

Aiming to reach a higher reproducibility of the surrogate/surface interactions for both implemented force fields (see **Annex A5.6.2**), we selected the force field parameters that could majorly impact on the molecule/surface interactions, characterizing these molecular systems in order to reparametrize them. In **Table 7-Table 8** we report the selected ReaxFF parameters.

For both FFA and FFB we selected the following parameters for the C-C, C-H and C-O bonds:  $E(\sigma)$ ,  $pbo1$ ,  $pbo2$ ,  $povun1$  and  $pbe1$  and  $pbe2$ . These parameters correspond to the sigma bond dissociation energy  $E(\sigma)$ , the sigma bond orders  $pbo1$  and  $pbo2$  (cf.§2.11), the overcoordination penalty  $povun1$  and the bond energies  $pbe1$  and  $pbe2$ . In the FFA case, we selected only alumina-based parameters (e.g. C-Al and Al-O bonds) and conversely only chromia-based parameters for FFB (e.g. C-Cr and Cr-O bonds). For the C-O, C-Al (C-Cr), H-O and Al-O (Cr-O) bonds, we also selected the ReaxFF parameters linked to the van der Waals dispersion forces: the vdW energy  $E(vdW)$ , the vdW radius  $R(vdW)$ , the vdW coefficient  $\alpha(vdW)$  and the sigma bond length  $R(\sigma)$ . The formalism linked to these parameters is taken from reference [13].

The decision behind this selection of parameters was made because we wanted to achieve a better description of the interface. By “activating” the parameters linked to the bond orders and bond energies for C-Cr, Cr-O, C-Al, Al-O and O-H, we thought that we could gain an improvement in the ReaxFF description of the interface interactions since from the DFT calculations we observed that the main interactions are established either through polar covalent bonds (e.g. oxygenated molecules on dry substrates) or through vdW forces (e.g. hydrocarbon molecules like benzene, toluene and n-propane) or finally H-bonds (e.g. molecules on both hydroxylated surfaces).

We imposed 1000 fit iterations for the CMA-ES FF optimizer. For supplementary information regarding the functioning of the CMA-ES algorithm, see the **Annex A5** section. For the geometry optimization setup, we implemented the “Conjugate Gradient” (CG) algorithm and imposed the number of maximum iterations up to 1000 iterations for the adsorption configurations.

**Table 7: Reparametrized ReaxFF parameters for FFA.**

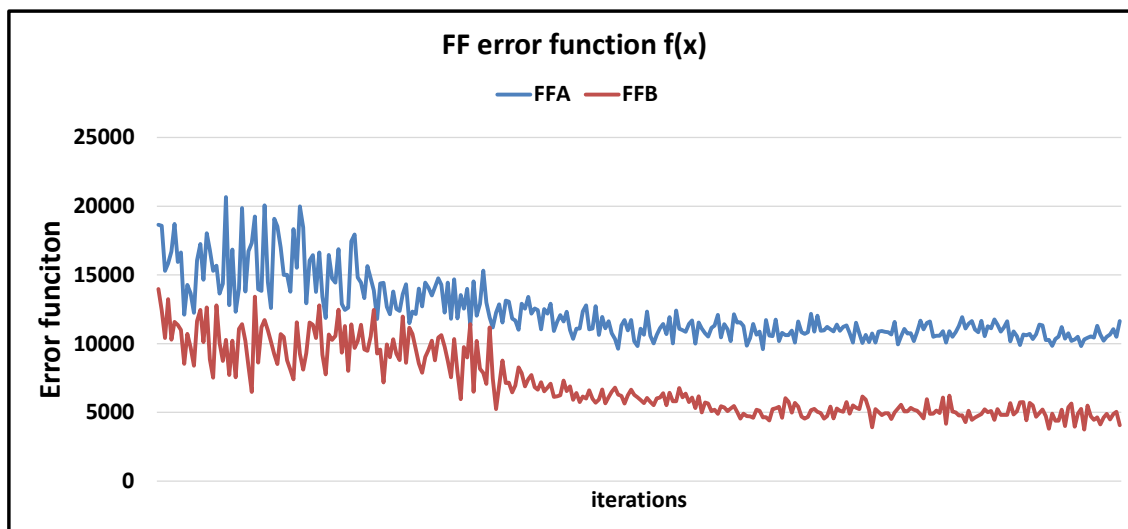
<b>Optimized parameters</b>	<b>C-C</b>	<b>C-H</b>	<b>C-O</b>	<b>C-Al</b>	<b>H-O</b>	<b>Al-O</b>
E(sigma)	✓	✓	✓	✓	✓	✓
pbe1	✓	✓	✓	✓	✓	✓
povun1	✓	✓	✓	✓	✓	✓
pbe2	✓	✓	✓	✓	✓	✓
pbo1	✓	✓	✓	✓	✓	✓
pbo2	✓	✓	✓	✓	✓	✓
E(vdW)	-	-	✓	✓	✓	✓
R(vdW)	-	-	✓	✓	✓	✓
Alpha(vdW)	-	-	✓	✓	✓	✓
R(sigma)	-	-	✓	✓	✓	✓

**Table 8: Reparametrized ReaxFF parameters for FFB.**

<b>Optimized parameters</b>	<b>C-C</b>	<b>C-H</b>	<b>C-O</b>	<b>C-Cr</b>	<b>H-O</b>	<b>Cr-O</b>
E(sigma)	✓	✓	✓	✓	✓	✓
pbe1	✓	✓	✓	✓	✓	✓
povun1	✓	✓	✓	✓	✓	✓
pbe2	✓	✓	✓	✓	✓	✓
pbo1	✓	✓	✓	✓	✓	✓
pbo2	✓	✓	✓	✓	✓	✓
E(vdW)	-	-	✓	✓	✓	✓
R(vdW)	-	-	✓	✓	✓	✓
Alpha(vdW)	-	-	✓	✓	✓	✓
R(sigma)	-	-	✓	✓	✓	✓

### 5.2.2 Results and discussion

The new optimized FFA and FFB force fields were obtained at the end of the FF CMA-ES run, which gave the error function value (*cf.* §2.11.2) displayed in **Figure 54** below.



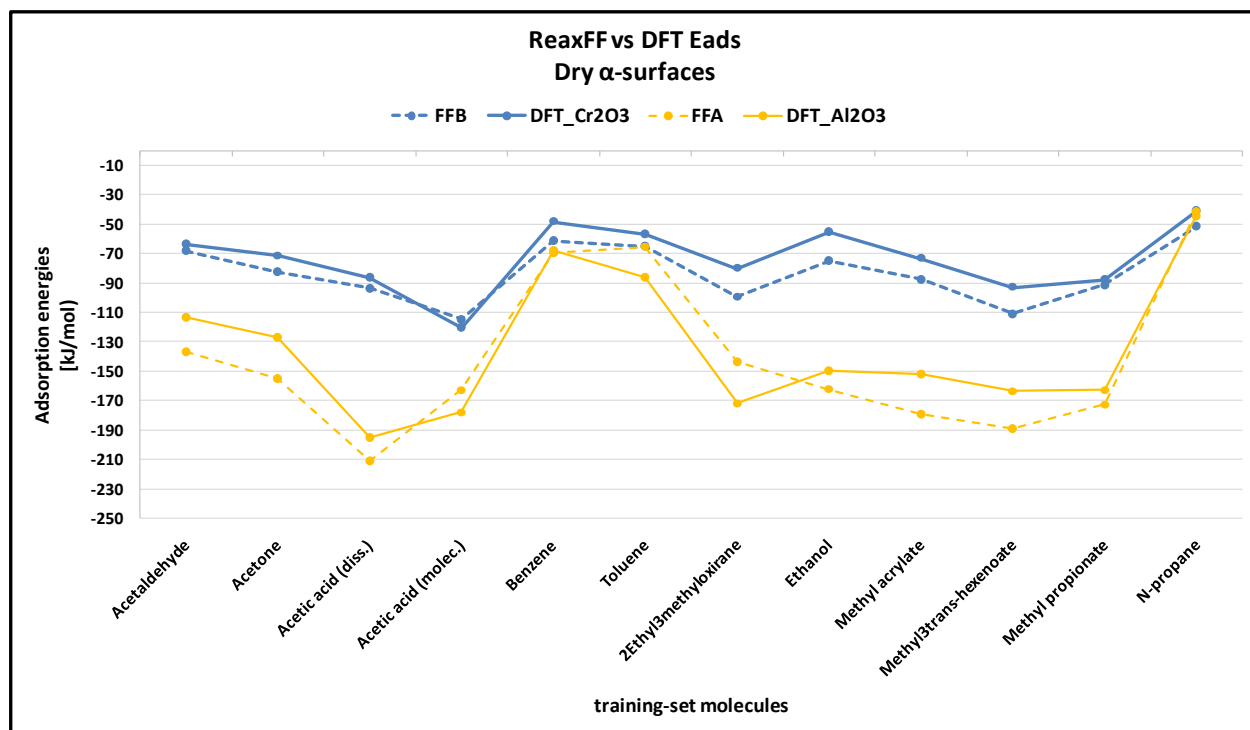
**Figure 54:** Error functions  $f(x)$  obtained from FFA (blue curve) and FFB (red curve) optimizations.

We can see from **Figure 54** that both FFA and FFB reached a plateau at the end of the ReaxFF optimization, in particular FFB reached a value around 5000 and FFA around 10'000 respectively.

In regards of the geometry optimization run with CG, the convergence for the majority of the analyzed configurations was not reached. We concluded that a better option for the geometry optimization calculated via the force fields could be by changing the CG with another algorithm that could aid us reaching the convergence for all the configurations. For this reason, we chose to implement the “Fast Inertial Relaxation Engine” (FIRE) algorithm since this algorithm guarantees a faster resolution than CG solver.

For this new geometry optimization campaign, we imposed the following convergence criteria for the FIRE algorithm in the AMS2019 package: we selected an energy criterion equal to  $10^{-4}$  eV ( $\approx 0.00965$  kJ/mol), a gradient criterion step of  $10^{-3}$  eV/Å ( $\approx 0.0965$  kJmol<sup>-1</sup>/Å) and a maximum number of iteration equal to 4000 steps.

In **Figure 55**, we reported the results of the optimized configurations for the training-set molecules (*cf.* §4.2) when adsorbed on both dry  $\alpha$ -surfaces. It is possible to observe that the FFB predictions for the dry  $\alpha$ -Cr<sub>2</sub>O<sub>3</sub> configurations are fairly better than the FFA predictions for the dry  $\alpha$ -Al<sub>2</sub>O<sub>3</sub>.



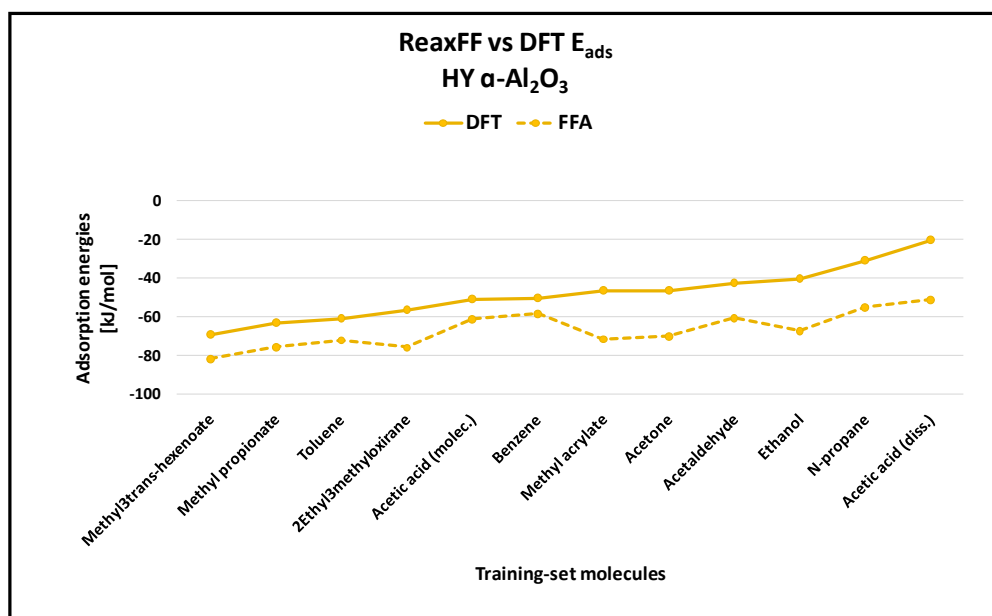
**Figure 55:** Comparison of the adsorption energies of the training-set molecules (*cf.* §4.2) on dry  $\alpha$ -surfaces calculated via ReaxFF geometry optimization (with FIRE algorithm) and DFT, respectively.

FFB accurately predicts the adsorption energies on dry  $\alpha$ -Cr<sub>2</sub>O<sub>3</sub> for acetaldehyde, acetic acid (in both dissociative and molecular configurations), methyl propionate and n-propane, while FFA accurately predicts the adsorption energies on dry  $\alpha$ -Al<sub>2</sub>O<sub>3</sub> for benzene, methyl propionate and n-propane. The maximal energetic difference between ReaxFF predictions against DFT data was equal to 20 kJ/mol for FFB (e.g. 2-ethyloxirane, ethanol and methyl-3-trans-hexenoate) and to 30 kJ/mol for FFA predictions (e.g. methyl acrylate and methyl-3-trans-hexenoate).

Given the fact that these maximal energetic differences observed for the dry surfaces refer to a small portion of the overall training-set molecules, we decided to retain these results as valid for the both reactive force field optimizations. This decision was further confirmed by the fact that

we observed an average % error smaller than 25%, threshold that we decided beforehand as criterion for a good approximation of the used force field when predicting the DFT results. In particular, we measured a 13% and 17% average for the FFA predictions of DFT results related to dry alumina configurations and for FFB predictions of the corresponding DFT results related to dry chromia, respectively. With this result, we evaluated both force fields as well-fitted for this training-set.

In **Figure 56**, we reported the results of the optimized configurations for the training-set molecules (*cf.* §4.2) when adsorbed on hydroxylated  $\alpha$ -Al<sub>2</sub>O<sub>3</sub> surface. We can notice that the majority of the FFA energetic estimations are not very close to DFT results, registering a maximal energetic difference between FFA predictions and DFT data of 30 kJ/mol (e.g. acetic acid dissociative case, ethanol and methyl acrylate).

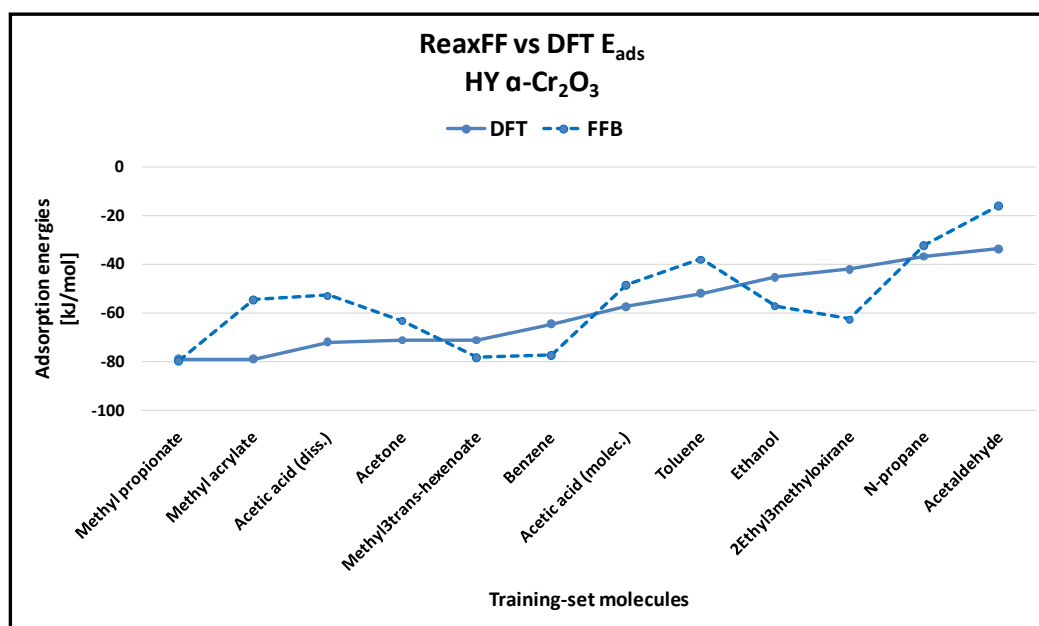


**Figure 56:** Comparison of the adsorption energies of the training-set molecules (*cf.* §4.2) on hydroxylated  $\alpha$ -Al<sub>2</sub>O<sub>3</sub> surface calculated via ReaxFF geometry optimization (with FIRE algorithm) and DFT, respectively.

At the same time, representative surrogates such as acetone, acetic acid (molecular adsorption), benzene, toluene, methyl-3-trans-hexenoate and methyl propionate show a good correspondence between the two methods, confirming the FFA capacity to reproduce molecular systems with these features.

A similar tendency is depicted also in **Figure 57**, where this time the FFB estimations on the fully-hydroxylated  $\alpha$ -Cr<sub>2</sub>O<sub>3</sub> surface are reported. Here we can still notice that some FFB estimations are not on point with their DFT references, registering a maximal energetic difference between FFA predictions and DFT data of 20 kJ/mol (e.g. acetic acid dissociative case, 2-ethyl-3-methyloxirane and methyl acrylate).

At the same time, representative surrogates such as acetone, acetic acid (molecular adsorption), methyl-3-trans-hexenoate, methyl propionate and n-propane show a good correspondence between the two methods, confirming the FFB capacity to reproduce molecular systems with these features.



**Figure 57:** Comparison of the adsorption energies of the training-set molecules (*cf.* §4.2) on hydroxylated  $\alpha$ -Cr<sub>2</sub>O<sub>3</sub> surface calculated via ReaxFF geometry optimization (with FIRE algorithm) and DFT, respectively.

Despite these non negligible energetic discrepancies between ReaxFF predictions and DFT data observed for the hydroxylated surfaces, we decided to retain these results as valid for the both reactive force field optimizations. Therefore, we proceed towards the next step: the ReaxFF validation. As we did for the cases related to the dry surfaces, we considered as criterion for a good approximation of the used force field when predicting the DFT results a maximal average % error of 25%. In particular, we measured a 23% average for both FFA and FFB predictions of

DFT results related to both hydroxylated alumina and chromia configurations, respectively. With this result, we evaluated both force fields as well-fitted for this training-set.

### 5.3 FFA and FFB validation: “Static” study

As already mentioned in section 5.1, the ReaxFF validation consists in the reproduction of the data contained in the validation set, which were not included in the training set.

The reproduction of those new data goes by the following order (see **Figure 26**, *cf.* §2.11.6):

- i. The homogeneous systems, which include: a) the cell parameters of the bulk of  $\alpha$ - $\text{Al}_2\text{O}_3$  and  $\alpha$ - $\text{Cr}_2\text{O}_3$  and b) the gas-phase reactions of toluene autoxidation.
- ii. The heterogeneous systems, consisting in the adsorption energies of similar but different organic molecules that were used in the training-set.

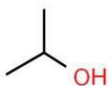
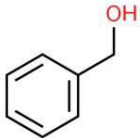
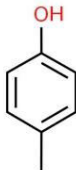
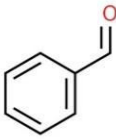
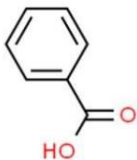
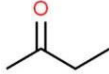
To achieve this goal, we added to both FFA and FFB validation-sets representative toluene autoxidation reactions (*cf.* §4.3), reported in **Table 9** and adsorption configurations of supplementary deposit precursors surrogates ([22, 23]) reported in **Table 10**.

**Table 9:** Scheme of the toluene autoxidation reactions inserted in the training-set for ReaxFF optimization.

Reaction label	Reactions	$\Delta E_r$ (kJ/mol)
R1	$(\text{C}_6\text{H}_5)\text{CH}_2\text{O}_2\text{H} + (\text{C}_6\text{H}_5)\text{CH}_2^\circ \rightarrow (\text{C}_6\text{H}_5)\text{CH}_3 + (\text{C}_6\text{H}_5)\text{CH}_2\text{O}_2^\circ$	-33.4
R2	$(\text{C}_6\text{H}_5)\text{CH}_2\text{O}_2\text{H} \rightarrow (\text{C}_6\text{H}_5)\text{CH}_2\text{O}^\circ + \text{HO}^\circ$	194.7
R3	$(\text{C}_6\text{H}_5)\text{CH}_2\text{O}_2\text{H} \rightarrow (\text{C}_6\text{H}_5)\text{CH}_2\text{O}_2^\circ + \text{H}^\circ$	374.4
R4	$(\text{C}_6\text{H}_5)\text{CH}_2\text{O}_2\text{H} \rightarrow (\text{C}_6\text{H}_5)\text{CH}_2^\circ + \text{HO}_2^\circ$	264.0
R5	$(\text{C}_6\text{H}_5)\text{CH}_2\text{O}_2\text{H} \rightarrow (\text{C}_6\text{H}_5)\text{CH}_2^\circ + \text{H}^\circ + \text{O}_2$	638.3
R6	$(\text{C}_6\text{H}_5)\text{CH}_2\text{O}_2\text{H} + \text{HO}_2^\circ \rightarrow (\text{C}_6\text{H}_5)\text{CH}_2\text{O}_2^\circ + \text{H}_2\text{O}_2$	-2.7
R7	$(\text{C}_6\text{H}_5)\text{CH}_2\text{O}_2\text{H} + \text{HO}_2^\circ \rightarrow (\text{C}_6\text{H}_5)\text{CH}_2^\circ + \text{H}_2\text{O}_2 + \text{O}_2$	261.2
R8	$(\text{C}_6\text{H}_5)\text{CH}_2\text{O}_2^\circ \rightarrow (\text{C}_6\text{H}_5)\text{CH}_2^\circ + \text{O}_2$	263.9
R9	$\text{HO}_2^\circ \rightarrow \text{O}_2 + \text{H}^\circ$	374.4

The surrogates adsorption on alumina were added to the FFA validation-set, while the ones related to chromia were added to the FFB validation-set. For both cases, the alumina and chromia surfaces were considered in both anhydrous and hydroxylated states, as for the surrogates of the training-set.

**Table 10: Organic molecules added to the validation-set as supplementary models for fuel deposit precursors.**

Chemical family	Model molecule	Molecule 2-D structure
Aliphatic alcohol	Isopropyl alcohol	
Aromatic alcohol	Benzyl alcohol	
Phenol	P-cresol	
Aromatic aldehyde	Benzaldehyde	
Aromatic carboxylic acid	Benzoic acid	
Aliphatic ketone	2-butanone	

### 5.3.1 Comparison of the lattice parameters

To validate the FFA and FFB, we verified if they were able to replicate the lattice parameters of both bulk and surfaces of  $\alpha$ -Al<sub>2</sub>O<sub>3</sub> and  $\alpha$ -Cr<sub>2</sub>O<sub>3</sub> respectively. We run geometry optimization calculations for the  $\alpha$ -Al<sub>2</sub>O<sub>3</sub> via FFA and for the  $\alpha$ -Cr<sub>2</sub>O<sub>3</sub> via FFB.

#### 5.3.1.1 Computational details

The geometry optimizations were carried out with AMS2019 package [7] with the implementation of the FIRE algorithm. We selected the following convergence criteria: the energy criterion of  $10^{-5}$  Hartree ( $\approx 0.0263$  kJ/mol), the gradient convergence of  $10^{-3}$  Hartree/Å ( $\approx 2.626$  kJmol<sup>-1</sup>/Å) and a maximum number of iterations of 5000 steps.

We proceeded by following this sequence of calculations: first, we run a geometry optimization with FFA for the alumina bulk and surface and with FFB for the chromia bulk and surface. With the obtained optimized geometry, we selected the option to optimize the lattice, in this way obtaining new lattice parameters a, b, c and cell volume. The last step was to optimize this updated lattice configuration but enabling the change in the atoms position inside the new optimized lattice. This last configuration was compared with the original lattice optimized via DFT for both  $\alpha$ -Al<sub>2</sub>O<sub>3</sub> and  $\alpha$ -Cr<sub>2</sub>O<sub>3</sub> to verify if both force fields were able to reproduce the surfaces relaxations.

For the bulk geometries, (1x1x1) cells were used for bulk  $\alpha$ -Al<sub>2</sub>O<sub>3</sub> and  $\alpha$ -Cr<sub>2</sub>O<sub>3</sub>, while for the surface geometries we considered the (4x4) slabs used in our DFT study (*cf.* §4.4.1).

#### 5.3.1.2 Results and discussion

The results of these geometry optimizations for the bulk lattices of  $\alpha$ -Al<sub>2</sub>O<sub>3</sub> and  $\alpha$ -Cr<sub>2</sub>O<sub>3</sub> are resumed in **Table 11** and **Table 12**, where in **Table 11** we compared our DFT and ReaxFF results for bulk  $\alpha$ -Al<sub>2</sub>O<sub>3</sub> lattice parameters with experimental values of references [19, 20] and conversely in **Table 12** we compared our DFT and ReaxFF results for bulk  $\alpha$ -Cr<sub>2</sub>O<sub>3</sub> lattice parameters with experimental values of reference [21]. We found a good agreement between our simulated results and the reported experimental data.

In **Table 11** we report the a,b,c lattice vectors calculated via FFA for the bulk  $\alpha$ -Al<sub>2</sub>O<sub>3</sub>. In this case, we registered a further relaxation for the ReaxFF calculation, which resulted in a cell volume difference between DFT and FFA of  $\Delta V_{\text{cell}} = 2.8\%$ . Being this difference not too impactful, we regarded the FFA as validated in regards of the Al<sub>2</sub>O<sub>3</sub> bulk system.

In **Table 12** we report the a,b,c lattice vectors calculated via FFB for the bulk  $\alpha$ -Cr<sub>2</sub>O<sub>3</sub>. For this case, we registered a cell volume difference between DFT and FFB of  $\Delta V_{\text{cell}} = 1.4\%$ , which allowed us to validate the FFB.

**Table 11: Lattice parameters for bulk  $\alpha$ -Al<sub>2</sub>O<sub>3</sub>: a) experimental data; b) DFT data and c) FFA data.**

	Bulk $\alpha$ -Al <sub>2</sub> O <sub>3</sub>		
	a) Experimental <sup>[19]</sup>	b) Calc. Bulk DFT (this work)	c) Calc. Bulk FFA (this work)
<b>a = b (Å)</b>	4.76	4.79	4.76
<b>c (Å)</b>	12.99	13.07	12.82
<b>c/a (Å)</b>	2.73	2.73	2.69
<b>V (Å<sup>3</sup>)</b>	254.93	259.11	251.80
<b>Al-O<sub>1</sub> (Å)</b>	1.85 <sup>[20]</sup>	1.87	1.87
<b>Al-O<sub>2</sub> (Å)</b>	1.97 <sup>[20]</sup>	1.98	1.93

**Table 12: Lattice parameters for bulk  $\alpha$ -Cr<sub>2</sub>O<sub>3</sub>: a) experimental data; b) DFT data and c) FFB data.**

	Bulk $\alpha$ -Cr <sub>2</sub> O <sub>3</sub>		
	a) Experimental <sup>[21]</sup>	b) Calc. Bulk DFT (this work)	c) Calc. Bulk FFB (this work)
<b>a = b (Å)</b>	4.95	5.07	5.08
<b>c (Å)</b>	13.57	13.85	14.02
<b>c/a (Å)</b>	2.74	2.73	2.76
<b>V (Å<sup>3</sup>)</b>	-	308.75	313.10
<b>Cr-O<sub>1</sub> (Å)</b>	-	2.05	2.05
<b>Cr-O<sub>2</sub> (Å)</b>	-	2.01	2.03

Analogously, we also implemented the geometry optimizations for the lattice parameters of both corundum surfaces, which are resumed in **Table 13** and **Table 14**. In **Table 13** we compared the DFT calculated  $\alpha$ -Al<sub>2</sub>O<sub>3</sub> lattice parameters with those calculated through FFA and in **Table 14** we compared instead the DFT calculated  $\alpha$ -Cr<sub>2</sub>O<sub>3</sub> lattice parameters with those calculated through FFB.

**Table 13:** Comparison of lattice parameters and surface energies of dry  $\alpha$ -Al<sub>2</sub>O<sub>3</sub> between: a) literature , b) DFT; c) FFA.

	$\alpha$ -Al <sub>2</sub> O <sub>3</sub> lattice		
	a) Literature	b) Calculated DFT (this work)	c) Calculated FFA (this work)
<b>a = b (Å)</b>	4.76 <sup>[19]</sup>	4.79	4.76
<b>E<sub>surface</sub> (J/m<sup>2</sup>)</b>	1.66 <sup>[28]</sup>	1.55	1.74

**Table 14:** Comparison of lattice parameters and surface energies of dry  $\alpha$ -Cr<sub>2</sub>O<sub>3</sub> between: a) literature , b) DFT; c) FFB.

	$\alpha$ -Cr <sub>2</sub> O <sub>3</sub> lattice		
	a) Literature	b) Calculated DFT (this work)	c) Calculated FFB (this work)
<b>a = b (Å)</b>	4.95 <sup>[21]</sup>	5.07	5.08
<b>E<sub>surface</sub> (J/m<sup>2</sup>)</b>	1.70 <sup>[29]</sup>	1.85	1.15

In **Table 13** we can see that the a and b lattice parameters calculated via FFA for the  $\alpha$ -Al<sub>2</sub>O<sub>3</sub> surface did not differ a lot from the corresponding DFT values and neither did not the surface energy.

In **Table 14** we can observe that the a and b lattice parameters calculated via FFB  $\alpha$ -Cr<sub>2</sub>O<sub>3</sub> surface are very close to the corresponding DFT values and so does the surface energy.

From this analysis, we conclude that both force fields are able to accurately describe both bulk and surface structures for  $\alpha$ -Al<sub>2</sub>O<sub>3</sub> and  $\alpha$ -Al<sub>2</sub>O<sub>3</sub>, thus we continued our ReaxFF validation by analyzing the energetics.

### 5.3.2 Comparison of the energies

In this paragraph, we proceed through the ReaxFF validation by the comparison between the energetic data calculated via DFT and the one calculated via ReaxFF. We examined the energetic data related to the gas-phase reactions (**Table 9**) and to the adsorptions of the supplementary surrogates (**Table 10**) on the  $\alpha$ -(0001) surfaces.

In support to these calculations, we also calculated the dissociation curves obtained from the binding energies between the organic adsorbates and the dry  $\alpha$ -Al<sub>2</sub>O<sub>3</sub> surface.

#### 5.3.2.1 Computational details

In regards of the calculation of the gas-phase reaction energies, geometry optimizations of the molecules involved in the toluene oxidation mechanism were carried out. Since here only single molecules were optimized, the following convergence criteria set by default in the AMS2019 were sufficient to reach the convergence of these systems: the energy criterion was set on the default value of  $10^{-5}$  Hartree ( $\approx 0.0263$  kJ/mol) and the gradient convergence on the default value of  $10^{-3}$  Hartree/Å ( $\approx 2.626$  kJmol<sup>-1</sup>/Å), with a maximum number of iteration set on 5000 iterations.

For the calculation of the adsorption energies, we imposed the following convergence criteria for the FIRE algorithm in the AMS2019 package: we selected an energy criterion equal to  $10^{-4}$  eV ( $\approx 0.00965$  kJ/mol), a gradient criterion step of  $10^{-3}$  eV/Å ( $\approx 0.0965$  kJmol<sup>-1</sup>/Å) and a maximum number of iteration equal to 4000 steps.

Supplementary energetic calculations were carried out to better describe the molecule-surface interactions, completing the study of the adsorption energies by a study of molecule-surface

binding energies. The dissociation curves of all the studied model molecules adsorbed on the dry alumina were considered.

To conduct this study, we proceeded in this way: we fixed a rigid coordinate in the z direction identifying the vertical molecule-surface bond distance, leaving the remaining molecules' atoms as relaxed. Instead, the surface structure was completely fixed. The rigid coordinate scan between the molecule and the surface was gradually increased: we started from the optimized bond distances of each adsorbate to the final molecule/surface distance of 6 Å.

We thereby define  $E_{binding}$  as follows:

$$E_{binding} = E_{ads_{mol}^*} - E_{surface^*} - E_{mol}$$

**Equation 87**

The energetic term  $E_{surface^*}$  corresponds to the energy of the optimized fixed structure of the dry alumina surface, while the energetic term  $E_{mol}$  identifies the energy of the optimized molecule. The  $E_{ads_{mol}^*}$  is the energy of the system where the surface is completely fixed and the molecule's atoms are relaxed, at the exception of the atom involved in the molecule/surface bond. For supplementary information regarding the definitions of the  $E_{ads_{mol}^*}$ ,  $E_{surface^*}$  and  $E_{binding}$  energetic terms, see the **Annex A5** section.

### 5.3.2.2 Results and discussion

The first examined case is the calculation of the  $\Delta E_r$  of the gas-phase autoxidation reaction (R1 – R9) (**Table 9**). These results are reported in **Figure 58** for the FFA implementation and in **Figure 59** for the one related to FFB.

We can see that both reactive force fields are capable to predict fairly well these reaction energies, in particular the FFB appears to be even more precise than FFA (from R1 to R5 reactions). However, they both seem to have a remaining difficulty to approach to the last three points (e.g. R7, R8 and R9 reactions).

The second examined case is the calculation of the adsorptions of the supplementary surrogates (**Table 10**) on the  $\alpha$ -surfaces. In the following figures, all the converged optimized configurations are reported.

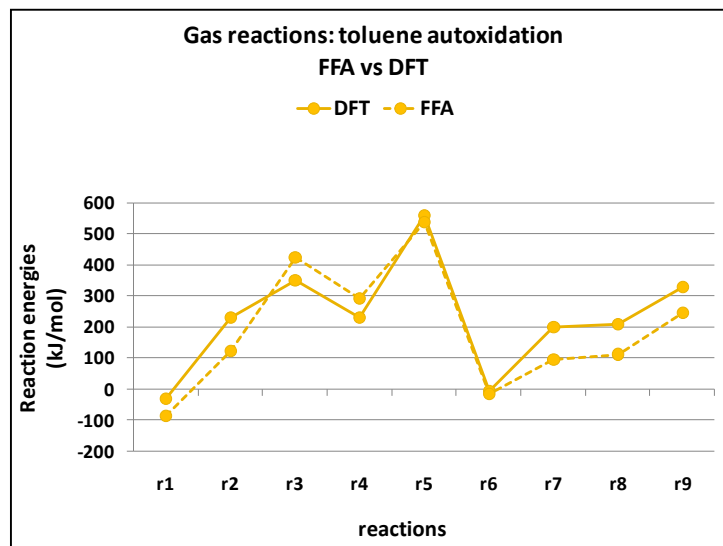


Figure 58: Comparison of the reaction energies of toluene oxydation mechanism obtained through ReaxFF geometry optimization (with FIRE algorithm) and DFT, respectively.

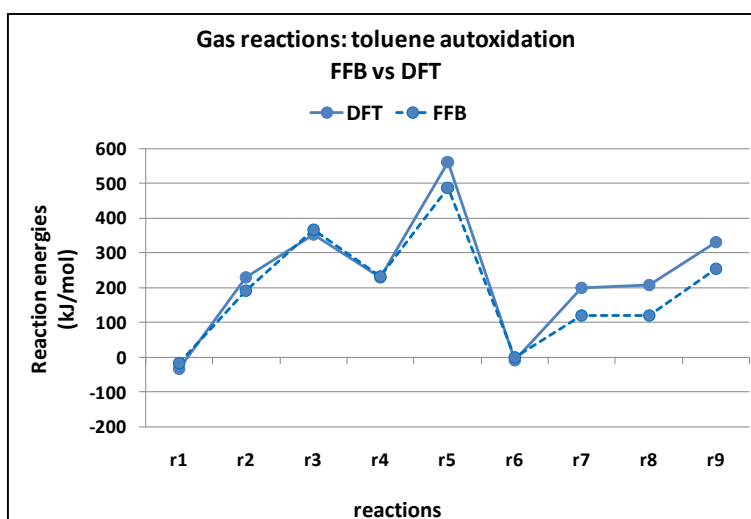
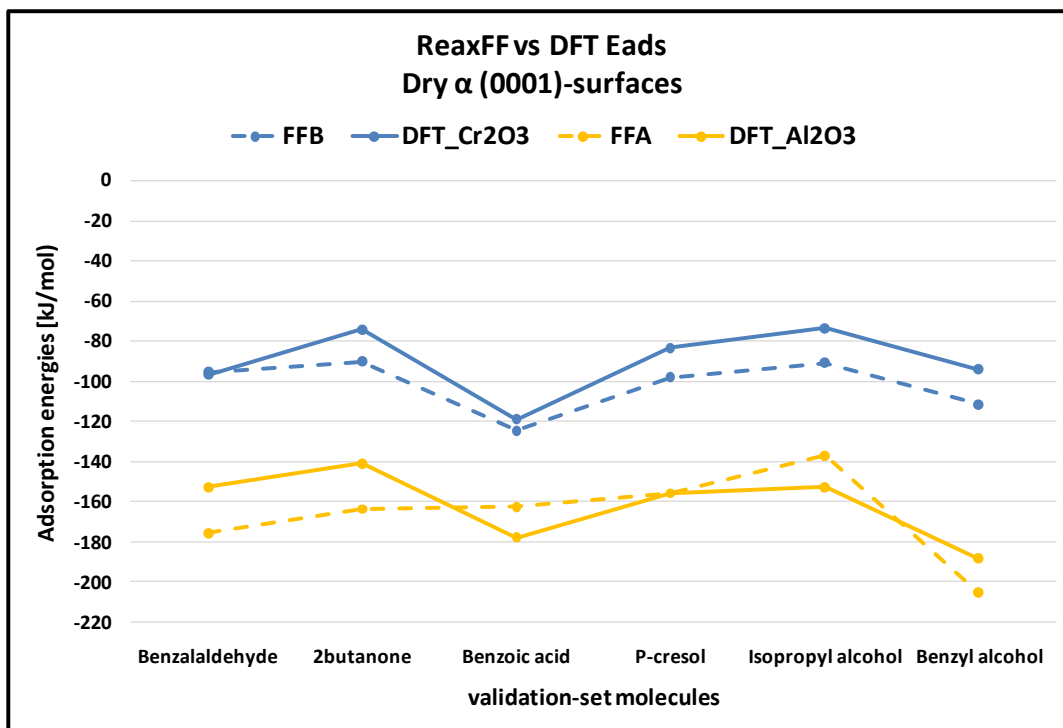


Figure 59: Comparison of the reaction energies of toluene oxydation mechanism obtained through ReaxFF geometry optimization (with FIRE algorithm) and DFT, respectively.

In **Figure 60** are shown the results of the adsorption energies for the dry  $\alpha$ -(0001) surfaces calculated with FFA and FFB.



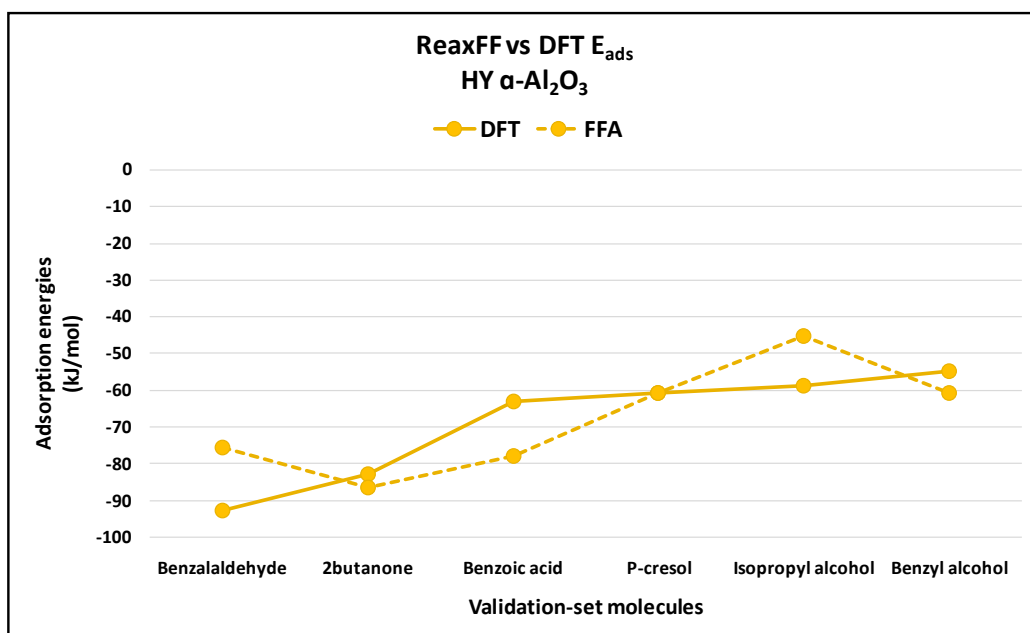
**Figure 60:** Comparison of the adsorption energies on dry  $\alpha$ -surfaces calculated via ReaxFF geometry optimization (with FIRE algorithm) and DFT, respectively.

In **Figure 60**, among the validation-set molecules (**Table 10**), we can notice a very accurate FFB description for the adsorption on dry  $\alpha$ -Cr<sub>2</sub>O<sub>3</sub> of the benzaldehyde and the benzoic acid, while for the FFA a very accurate description is noted for the adsorption on dry  $\alpha$ -Al<sub>2</sub>O<sub>3</sub> of the benzoic acid and the p-cresol.

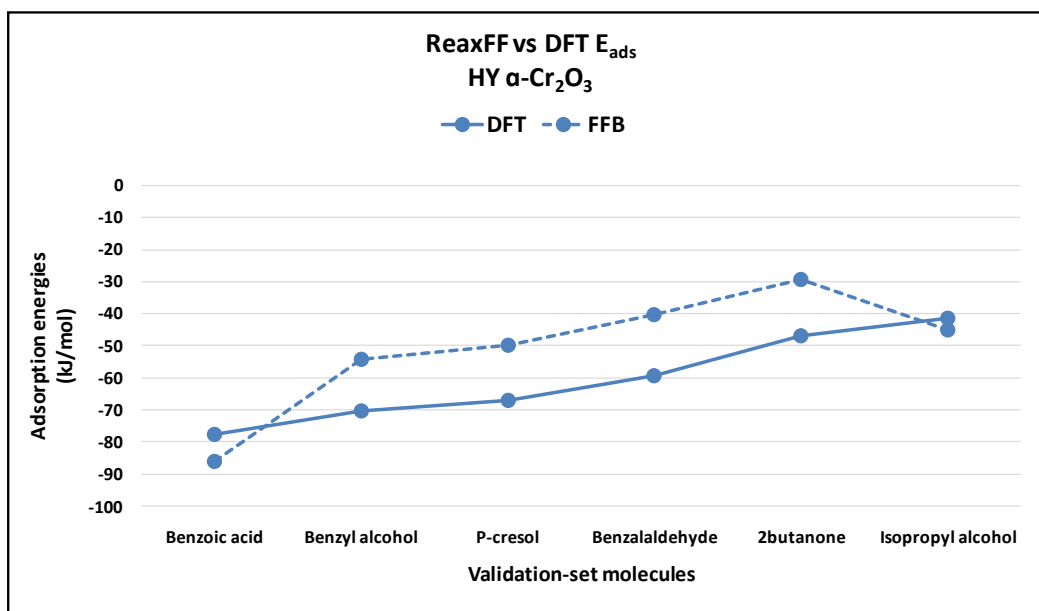
The maximal energetic difference between ReaxFF predictions against DFT data was equal to 20 kJ/mol for FFB (e.g. p-cresol and isopropyl alcohol) and to 25 kJ/mol for FFA predictions (e.g. benzaldehyde and 2-butanone).

As we did for the cases related to the dry surfaces when considering the training-set molecules, we considered as criterion for a good approximation of the used force field when predicting the DFT results a maximal average % error of 25%. In particular, we measured a 9% for the FFA predictions of DFT results related to dry alumina and 15% average and FFB predictions of DFT results related to dry chromia configurations, respectively. With this result, we evaluated both force fields as well-fitted for this training-set.

**Figure 61** reports instead the results obtained from the geometry optimizations run with the FFA for the fully-hydroxylated  $\alpha$ -Al<sub>2</sub>O<sub>3</sub> surface confronted with their corresponding DFT results.



**Figure 61:** Comparison of the adsorption energies on hydroxylated  $\alpha$ -Al<sub>2</sub>O<sub>3</sub> surfaces calculated via ReaxFF geometry optimization (with FIRE algorithm) and DFT, respectively.



**Figure 62:** Comparison of the adsorption energies on hydroxylated  $\alpha$ -Cr<sub>2</sub>O<sub>3</sub> surfaces calculated via ReaxFF geometry optimization (with FIRE algorithm) and DFT, respectively.

Among the validation-set molecules (**Table 10**) we can notice a very accurate FFA description for the adsorption on hydroxylated  $\alpha$ -Al<sub>2</sub>O<sub>3</sub> of the benzaldehyde, the 2-butanone and the benzoic acid.

A similar tendency is depicted also in **Figure 62**, where this time the FFB estimations on the fully-hydroxylated  $\alpha$ -Cr<sub>2</sub>O<sub>3</sub> surface are reported. Among the validation-set molecules (**Table 10**) we can notice a very accurate FFB description for the adsorption on hydroxylated  $\alpha$ -Cr<sub>2</sub>O<sub>3</sub> of the isopropyl alcohol and the benzoic acid.

The maximal energetic difference between ReaxFF predictions against DFT data was equal to 20 kJ/mol for both FFA (e.g. p-cresol) and FFB predictions (e.g. benzaldehyde and 2-butanone and p-cresol).

Despite these non negligible energetic discrepancies between ReaxFF predictions and DFT data observed for the hydroxylated surfaces, we decided to retain these results as valid for both reactive force field validations. As we did for the cases related to the hydroxylated surfaces when considering the training-set molecules, we considered as criterion for a good approximation of the used force field when predicting the DFT results a maximal average % error of 25%. In particular, we measured a 14% for the FFA predictions of DFT results related to hydroxylated alumina and 21% average and FFB predictions of DFT results related to hydroxylated chromia configurations, respectively. With this result, we evaluated both force fields as well-fitted for this training-set.

We conclude this energetic analysis by reporting below the binding energy curves related to the training-set molecules (*cf.* §4.2) and the validation-set molecules (**Table 10**) when adsorbed on the dry  $\alpha$ -Al<sub>2</sub>O<sub>3</sub> surface. The curves referring to the training-set molecules are reported in **Figure 63** and the ones calculated for the validation-set molecules are reported in **Figure 64**.

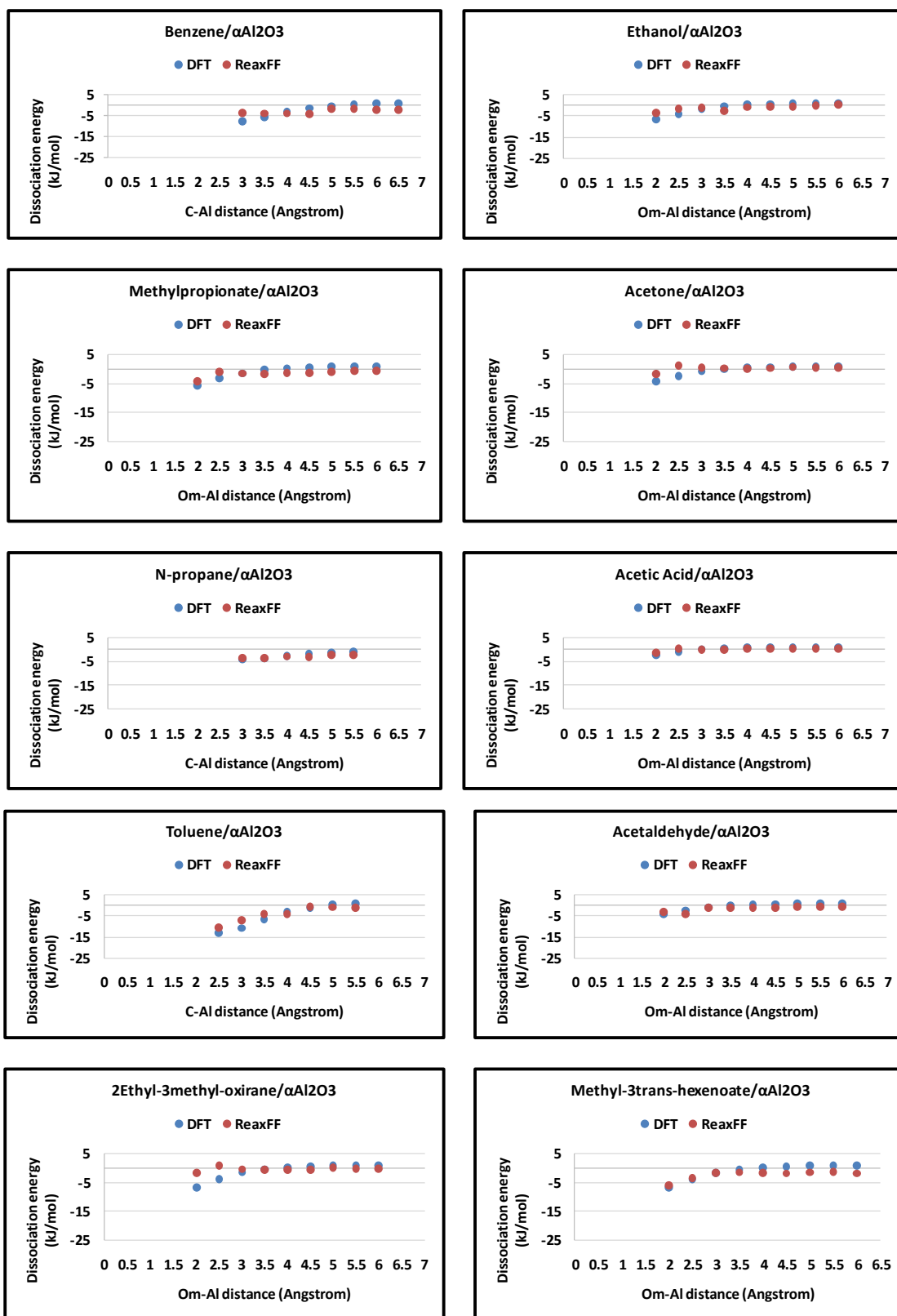
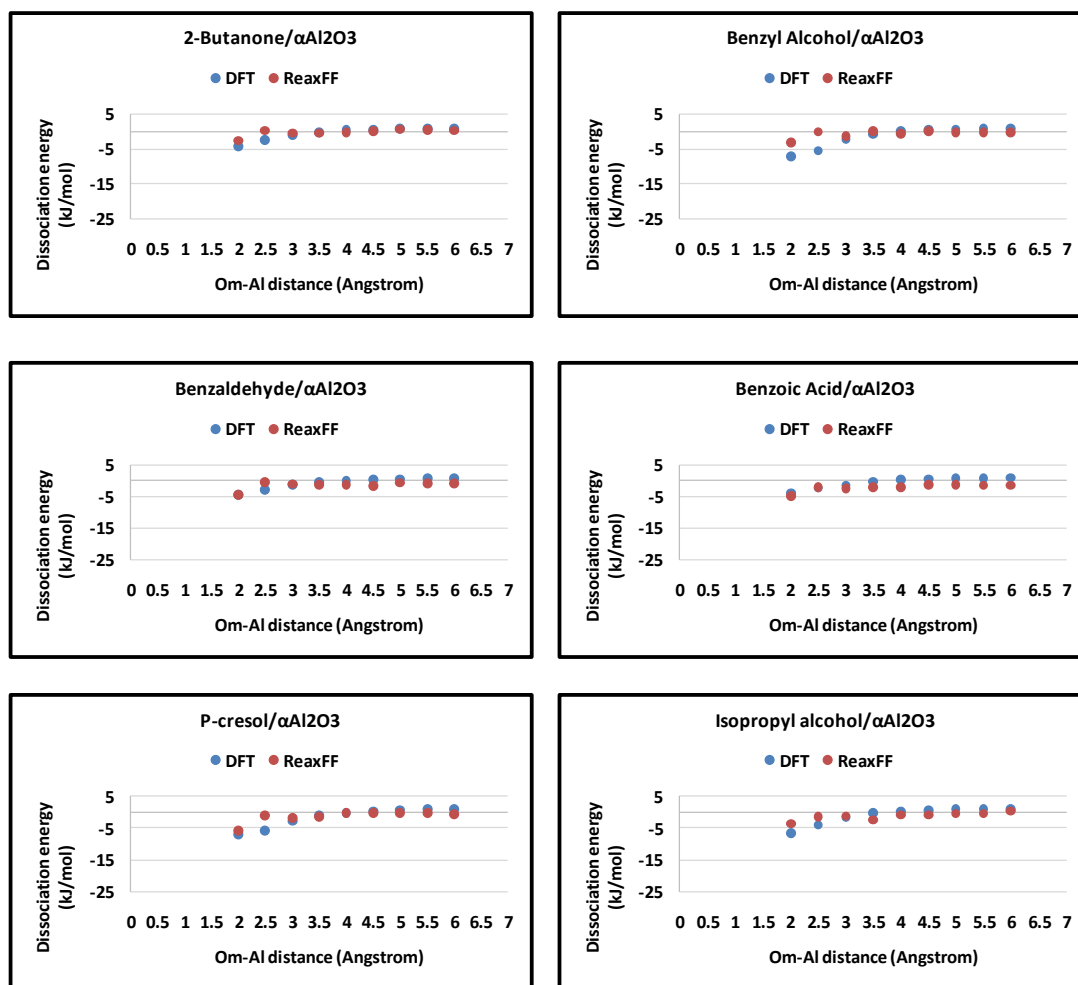


Figure 63: Dissociation curves obtained from the binding energies calculated between the training-set molecules (*cf.* §4.2) and the dry alumina surface. The binding energies calculated via DFT are reported in blue dots, the values obtained via FFA in red dots.



**Figure 64:** Dissociation curves obtained from the binding energies calculated between the validation-set molecules (Table 10) and the dry alumina surface. The binding energies calculated via DFT are reported in blue dots, the values obtained via FFA in red dots.

These binding energy calculations allowed us to scrutinize the attractive potential between the surface and the molecule, a very important aspect if one is interested in finite temperature effects as adsorption/desorption. We chose to calculate the binding energies for these adsorbates on dry alumina because our prior DFT study (**Chapter 4**) evidenced a higher reactivity for this molecule/substrate system rather than the one concerning the dry chromia. For this reason, we wanted to further ascertain that our reactive force field was capable to accurately predict the binding energies describing the molecule/dry alumina systems.

As shown by **Figure 63**, a very accurate FFA description is achieved for the following deposit precursor surrogates: the acetaldehyde, the n-propane, the methyl acrylate, the methyl propionate

and the acetic acid. For these training-set molecules, the FFA dissociation curve is almost overlapped to the one calculate with DFT.

In **Figure 64**, the dissociative curves displaying the binding energies between the validation-set molecules and the dry alumina surface are shown. Here, a particularly good accuracy of the FFA estimation is reached for the benzoic acid, the 2-butanone and the isopropyl alcohol.

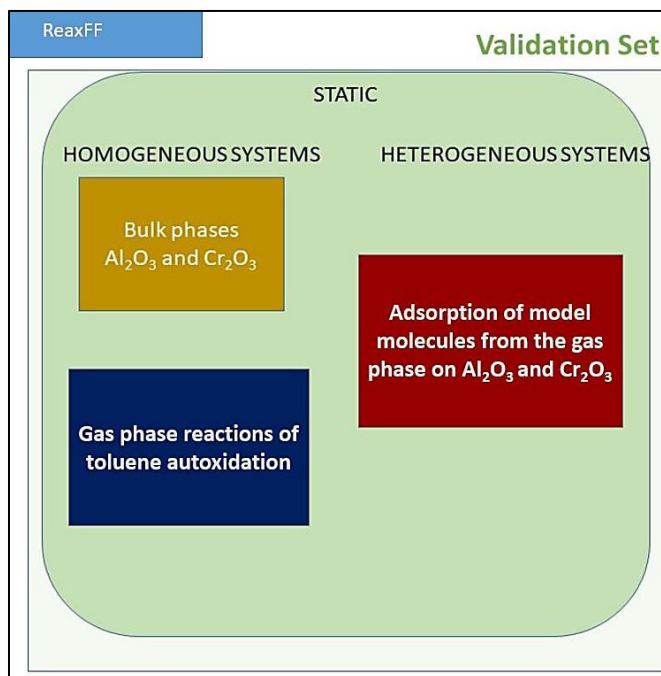
From the analysis of **Figure 63-Figure 64**, we can conclude that overall a very accurate correspondence of the potential landscape obtained with FFA with respect to DFT was achieved, thus further validating FFA.

### 5.3.3 Conclusion of the “static” study

In this section **5.3**, procedures and corresponding results related to the “static” study of the two force fields FFA and FFB validation were discussed. We recapitulate here the different steps we followed in **Figure 65**.

The first “static” test (section**5.3.1**) envisaged geometry optimization runs for bulk and surface structures of  $\alpha$ -Al<sub>2</sub>O<sub>3</sub> and  $\alpha$ -Cr<sub>2</sub>O<sub>3</sub>, respectively, calculated through FFA and FFB. The objective was to validate both force fields by verifying their capacity to reproduce the surface relaxation states for both corundum surfaces. Our analysis point out a good correspondence between bulk lattice parameters calculated via DFT and ReaxFF and also a good agreement with experimental data.

The second “static” test (section**5.3.2**) envisaged geometry optimization runs with the aim to calculate the energetics of our systems: the reaction energies of the gas-phase reactions (**Table 9**) and the adsorption energies of the supplementary surrogates (**Table 10**) on the  $\alpha$ -surfaces. We also reported the dissociation curves obtained from the binding energies between the organic adsorbates and the dry  $\alpha$ -Al<sub>2</sub>O<sub>3</sub> surface. All the geometry optimizations were carried out through the implementation of the FIRE algorithm.



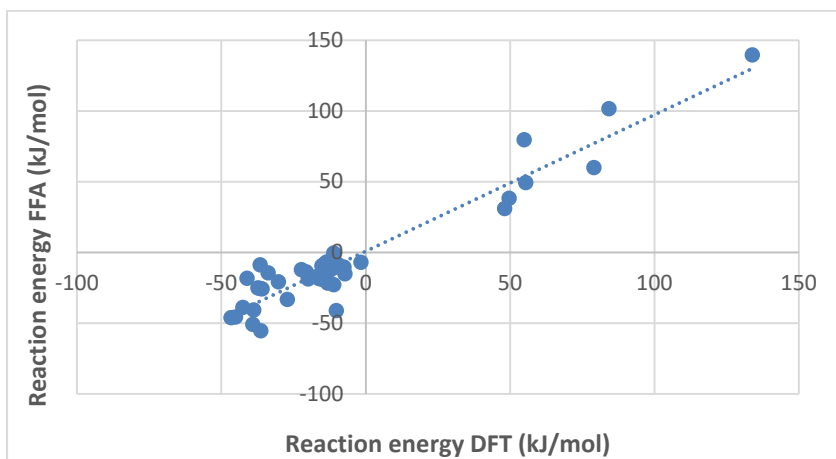
**Figure 65: Simplified scheme of our ReaxFF validation strategy where the static study is evidenced with the dotted red square.**

From the gas-phase reaction analysis, we found that both reactive force fields are capable to predict fairly well the reaction energies, in particular the FFB appears to be even more precise than FFA (from R1 to R5 reactions). However, they both seem to have a remaining difficulty to approach to the last three points (e.g. R7, R8 and R9 reactions).

From the adsorption analysis, a good correspondence was achieved for the FFA description of the alumina-based configurations and conversely for the FFB in correspondence of chromia-based systems. For the dry surface configurations, the maximal energetic difference between ReaxFF predictions against DFT data was equal to 20 kJ/mol for FFB (e.g. p-cresol and isopropyl alcohol) and to 25 kJ/mol for FFA predictions (e.g. benzaldehyde and 2-butanone). For the hydroxylated surface configurations, the maximal energetic difference between ReaxFF predictions against DFT data was equal to 20 kJ/mol for both FFB (e.g. benzaldehyde and 2-butanone and p-cresol) and FFA predictions (e.g. p-cresol). Despite these not negligible energetic discrepancies between ReaxFF predictions and DFT data, we decided to retain these results as valid for both reactive force field validations.

We concluded this energetic analysis with the results of the binding energy curves calculated between all the studied model molecules and the dry  $\alpha$ -Al<sub>2</sub>O<sub>3</sub> surface. We observed a very accurate correspondence of the potential landscape obtained with FFA and DFT.

Furthermore, we report here the FFA versus DFT set of results (**Figure 66**). One can observe that FFA is able to fit DFT data on a wide range of energies. This gives us confidence that FFA can produce semi-quantitative data with a safe predictive character.



**Figure 66: Reaction energies calculated with FFA, versus the same reactions energies calculated with DFT for the alumina system.**

We overall conclude this ReaxFF “static” analysis by validating both FFA and FFB. Now we proceed to the successive “dynamic” validation step.

## 5.4 FFA and FFB validation: “Dynamic” study

In this section, we report the “dynamic” study of the ReaxFF validation, where we carried out different MD calculations.

We carried out MD simulations where the densities of common liquid solvents at ambient conditions ( $T = 20^{\circ}\text{C}$  and  $P = 1\text{ atm}$ ) were calculated through both FFA and FFB. The objective of this test was to verify if both reactive force fields were able to reproduce the macroscopic properties (e.g. density) of well-known compounds in realistic ambient conditions.

In addition, MD simulations where the desorption temperatures (**Chapter 4**) of certain model molecules were calculated via ReaxFF are reported in the **Annex-A5.8**. The objective was to confirm the validity and correspondence between the “static” dimension (e.g. DFT + atomistic thermodynamics) and the “dynamic” one (e.g. MD).

### 5.4.1 Liquid-phase solvents at ambient conditions

Here, we carried out MD simulations where the densities of liquid solvents such as acetic acid, acetone, ethanol, benzaldehyde, benzyl alcohol and water were calculated at ambient conditions ( $T = 20^{\circ}\text{C}$  and  $P = 1\text{ atm}$ ) by employing both FFA and FFB.

#### 5.4.1.1 Computational details

For the MD study on densities, we implemented the NPT ensemble. Here, we selected the Martyna-Tobias-Klein (MTK) barostat [24] and the Nosé-Hoover Chain (NHC) thermostat [15]. We selected a pressure  $P = 1\text{ atm}$  and  $T = 293\text{ K}$  ( $= 20^{\circ}\text{C}$ ), with a damping constant of 500 fs for the barostat and of 100 fs for the thermostat, respectively. The NHC length was set at 10 (coinciding with AMS2019 default value). The total number of steps was set to  $2 \cdot 10^6$ , with a time step of 0.25 fs, obtaining a total calculation time of 500 ps. The initial temperature was set to 293 K.

The simulated MD boxes contained about 200 molecules of each compound at the exception of the water, where instead we had 300 molecules.

For the production data of these simulations, we considered the average density value measured on the last 100'000 steps.

#### 5.4.1.2 Results and discussion

These results are reported in **Table 15a-b** below. **Table 15a** (on the left) includes the FFA densities estimations. If we look at the percentage errors reported in the last column on the right, we can notice that the maximal value is almost 9% and it is given by the FFA estimation of the benzaldehyde density. Overall, we can observe that the FFA estimations appear close enough to the experimental densities, in particular the acetic acid, acetone and water give a percentage error below 5%.

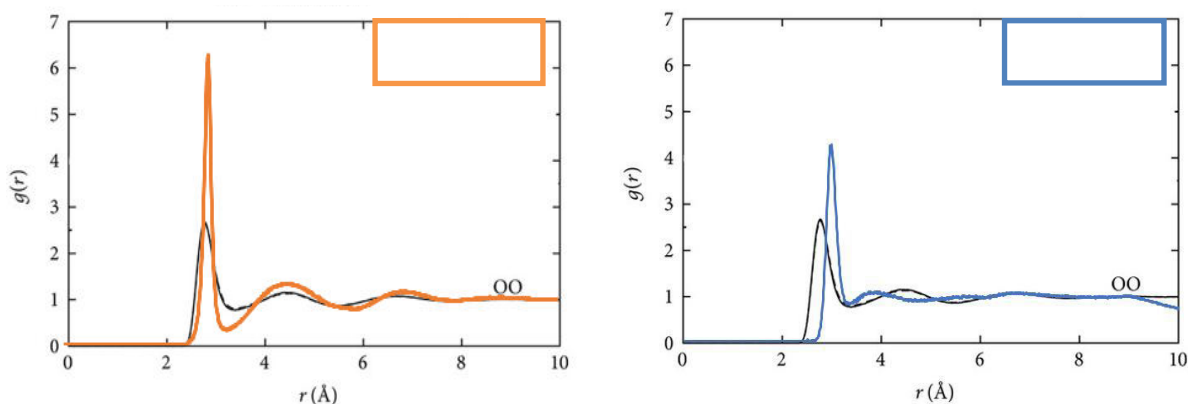
**Table 15b** (on the right) includes instead the FFB densities estimations. Here we can see that the percentage errors are higher than the FFA case, showing a weaker capacity for FFB to accurately predict the same densities. Apart from the ethanol and water densities, FFB exhibits a very poor estimation of the densities of both aliphatic and aromatic compounds, which are not acceptable. We will see later in the manuscript that this force field does not give reasonable results.

**Table 15: Densities of liquid solvents calculated at T=20°C and P=1atm with a) FFA force field (on the left), b) FFB force field (on the right).**

Molecules	Exp. Density @ 1 bar, 20 °C [g/cm <sup>3</sup> ]	FFA Density @ 1 bar, 20 °C [g/cm <sup>3</sup> ]	Error%	Exp. Density @ 1 bar, 20 °C [g/cm <sup>3</sup> ]	FFB Density @ 1 bar, 20 °C [g/cm <sup>3</sup> ]	Error%
Acetic acid	1.05 <sup>[25]</sup>	1.05	0.3%	1.05 <sup>[25]</sup>	1.62	54.2%
Acetone	0.79 <sup>[25]</sup>	0.81	2.7%	0.79 <sup>[25]</sup>	1.10	38.6%
Ethanol	0.79 <sup>[25]</sup>	0.74	6.1%	0.79 <sup>[25]</sup>	0.83	5.2%
Benzaldehyde	1.05 <sup>[16]</sup>	1.14	8.9%	1.05 <sup>[16]</sup>	1.28	22.5%
Benzyl alcohol	1.04 <sup>[25]</sup>	1.11	7.1%	1.04 <sup>[25]</sup>	1.16	11.9%
Water	1.00 <sup>[26]</sup>	0.97	3.1%	1.00 <sup>[26]</sup>	1.00	0.0%

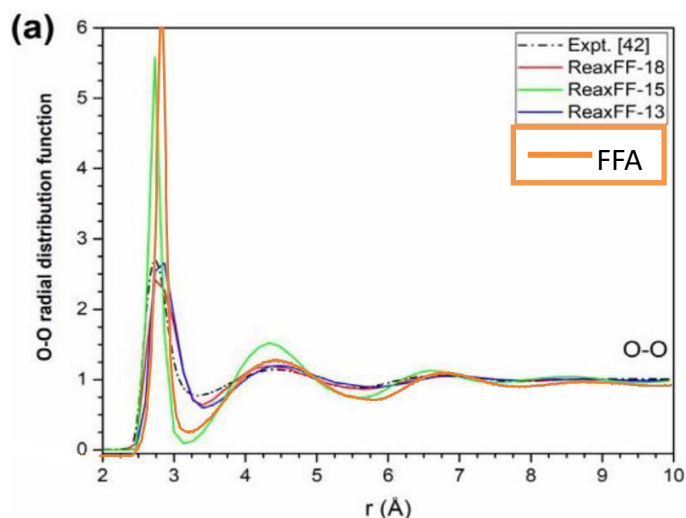
To complement the density analysis through ReaxFF, we also calculated the radial distribution function (RDF)  $g(r)$  (cf.§2.12.1) of the O-O bond of water (at T = 293 K and P = 1 atm) for both FFA and FFB, showed in **Figure 67a-b** respectively. In a system of particles (atoms, molecules, colloids, etc.), the RDF describes how density varies as a function of distance from a reference particle.

**Figure 67a** (on the left) shows the RDF of the O-O bond of water calculated with the FFA. This estimated RDF is compared with the experimental result reported in the work of Soper et al. [27], where they obtained the water RDF at 315 K. We can notice that the orange line depicting the RDF calculated with FFA almost overlaps the experimental reference, implying that FFA accurately describes the structure of liquid water. The location of the peaks indicating first and second neighbors are well reproduced, indicating a nice description of the H bonding. However, the MAX/MIN ratio is higher than the experimental value. This overstructuration can be due to a too short accumulation statistics of the dynamics. It could also be corrected by increasing gently the temperature of simulation.



**Figure 67:** RDFs of the O-O bond of water calculated via: a) FFA (orange line on the left), b) and FFB (blue line on the right) with the NPT ensemble at 293 K and 1 atm. The black line showed corresponds to the experimental RDF result taken from reference [27].

In **Figure 68** below we report the RDF for O-O bond in water as measured by three different ReaxFF in the study of Soleymanibrojeni et al. [5]. We overlapped above their figure our RDF calculated with the FFA because we wanted to evaluate how accurate was our ReaxFF in comparison to their different predictions. According to their results, the sharp peaks seen for the ReaxFF-15 of the O-O pair indicate that the representation of water with the ReaxFF-15 at 298.2 K is an amorphous solid rather than a liquid, while the ReaxFF-13 and ReaxFF-18 seem to better align with their referential experimental curve. The prediction made by our FFA overlaps the curve defining ReaxFF-15 estimation, which resembles the behavior of an amorphous solid.



**Figure 68:** RDF of the O-O pair of water calculated by Soleymanibrojeni et al. [5] with three different force fields: ReaxFF-13 (blue curve), ReaxFF-15 (green curve) and ReaxFF-18 red curve). The curve obtained in our study with the FFA is defined by the orange curve.

**Figure 67b** (on the right) shows the RDF of the O-O bond of water calculated with the FFB. The FFB estimation is again compared with the reference [27]. We can see that in this case, the first peak indicating the first neighbor interaction in the RDF calculated with FFB is slightly shifted to larger distances from the experimental reference, suggesting that the H bonds are too weak. Moreover, the second neighbor seems to be at too short distances. Thus, albeit the overall water density is correct (**Table 15**), the local water interactions are not correctly described.

From these results, we can conclude that the FFA is able to describe more accurately than FFB the physicochemical properties of the liquid solvents by the evaluation of their densities. Moreover, the examination of the O-O RDF of water reveals that the H bonds are correctly described by FFA, and not by FFB.

For this reason, we evaluated FFA as fully validated and employable in the next MD production study, while FFB cannot be considered as validated.

## 5.5 Final conclusion

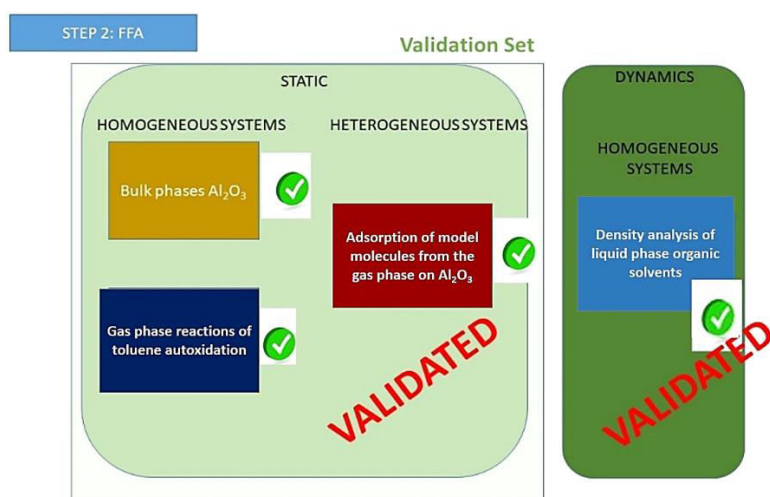
In this chapter, we introduced our ReaxFF study aimed at the implementation of a reactive force field able to describe the chemistry of the solid, the liquids, the gas phase and some interfacial systems. To achieve this goal, we consider the obtained DFT results shown in **Chapter 4** as input data to parametrize ReaxFF. In this way, we “train” our reactive force field to reproduce the energetics and molecular structures of the optimized DFT configurations. As a sort of a preliminary step, we decided to “test” a force field (“FF0”) that was used in the work of Benoît Darenne [1] since our context study and objective is aligned with his work.

However, preliminary results of this optimized force field (**Annex A5.6.2**) showed us that it was not able to correctly reproduce adsorption geometries and energies for  $\alpha$ -Cr<sub>2</sub>O<sub>3</sub>, as a consequence of the fact that optimizing this FF to improve the description of  $\alpha$ -Al<sub>2</sub>O<sub>3</sub> decreased the accuracy to describe  $\alpha$ -Cr<sub>2</sub>O<sub>3</sub> systems.

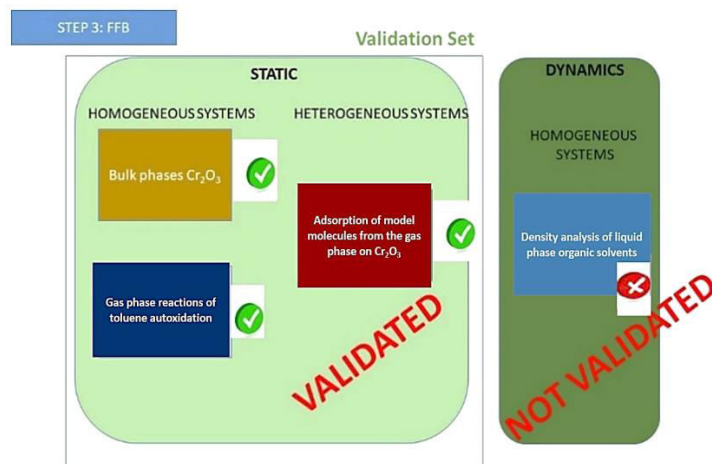
Therefore, we started a new cycle of ReaxFF reparametrization by using two different force fields: FFA for the Al<sub>2</sub>O<sub>3</sub> systems and FFB for the Cr<sub>2</sub>O<sub>3</sub> systems. These two different force fields are both based on the force field of Benoît Darenne [6], with the difference that in FFB we chose to change the ReaxFF parameters of H and O atoms by inserting the values of the “CHON-2017\_weak.ff” force field developed by Zhang and van Duin [18].

The two force field optimizations were evaluated through the reproduction of the data in the training set used to reparametrize the force fields. Here, the convergence for the majority of the analyzed configurations was not reached. This result led us to run again geometry optimizations with the FIRE algorithm since this algorithm guarantees a faster resolution than CG solver. In this new geometry optimization campaign, we observed that the maximal energetic difference between ReaxFF predictions against DFT data was equal to 20 kJ/mol for FFB and to 30 kJ/mol for FFA predictions either in the anhydrous or hydroxylated surface condition. However, these non negligible energetic discrepancies between ReaxFF predictions and DFT data were contained only for a small portion of the training-set molecules, which led us to accept the two force fields as optimized. We therefore proceed towards the next step: the ReaxFF validation.

The FFA and FFB validation was evaluated through the reproduction of data of a validation set (data that are not included in the training set), which included the reproduction of the cell parameters of the bulk, adsorption energies and curves of similar but different organic molecules that were used in the training set, representative reactions of the autoxidation of toluene, and the dynamic structuration of pure organic liquids (mass/volume density, radial distribution functions). Supplementary calculations that provided the comparison between the desorption temperatures of certain model molecules between DFT (**Chapter 4**) and FF were reported in the **Annex-A5.8**.



**Figure 69:** Simplified scheme for the achieved ReaxFF validation of the FFA (sections 5.2-5.4).



**Figure 70:** Simplified scheme for the unachieved ReaxFF validation of the FFB (sections 5.2-5.4).

The achieved FFA validation and unachieved FFB validations are reported in the simplified schemes in **Figure 69** and **Figure 70**, respectively.

From the first “static” test (section **5.3.1**), we concluded that both FFA and FFB gave a good correspondence with bulk lattice values calculated via DFT, together with the experimental values. Therefore, both force fields “passed” this first static validation test.

From the second “static” test (section **5.3.2**), we found that both reactive force fields are capable to predict fairly well the reaction energies, in particular the FFB appears to be even more precise than FFA (from R1 to R5 reactions). However, they both seem to have a remaining difficulty to approach to the last three points (e.g. R7, R8 and R9 reactions). In addition, a good correspondence was achieved for the FFA description of the alumina-based configurations and conversely for the FFB in correspondence of chromia-based systems. We concluded this energetic analysis with the results of the binding energy curves calculated between all the studied model molecules and the dry  $\alpha$ -Al<sub>2</sub>O<sub>3</sub> surface, where a very accurate correspondence of the potential landscape obtained with FFA with respect to DFT was also observed.

Therefore, both force fields “passed” this second static validation test.

We thereby concluded that both FFA and FFB are validated from our “static” study and can be further employed for the successive “dynamic” validation step.

From section **5.4.1**, overall we observed that the FFA density estimations appear close enough to the experimental data. The same could not be said for FFB, since the percentage errors are higher than for the FFA case, showing a weaker capacity for FFB to accurately predict experimental densities. This trend is further confirmed by the water RDFs plotted for the O-O pair, where we confirmed that the FFA estimation is more accurate than the one obtained with FFB.

Therefore, FFA “passed” this dynamic validation test, while FFB did not.

For this reason, only FFA will be further implemented in our successive ReaxFF study, where we aim to describe the dynamic behavior of a surrogate “fuel-oxygen” blend either in homogeneous conditions (e.g. only organic liquid phase) or in heterogeneous conditions (e.g. organic liquid phase in contact with alumina surfaces).

## References

- 1 Jiang X., Hu Y., Ling L., Wang X. The initial wet oxidation process on Fe-Cr alloy surface: Insights from ReaxFF molecular dynamic simulations, *Applied Surface Science***548** (2021), 149159. DOI: 10.1016/j.apsusc.2021.149159.
- 2 Shin Y.K., Kwak H., Vasenkov A.V., Sengupta D., van Duin A.C. Development of a ReaxFF Reactive Force Field for Fe/Cr/O/S and Application to Oxidation of Butane over a Pyrite-Covered Cr<sub>2</sub>O<sub>3</sub> Catalyst, *ACS Catal.***5**, 12 (2015), 7226–7236. DOI: 10.1021/acscatal.5b01766.
- 3 Dabaghmanesh S., Neek-Amal M., Partoens B., Neyts E.C. The formation of Cr<sub>2</sub>O<sub>3</sub> nanoclusters over graphene sheet and carbon nanotubes, *Chemical Physics Letters***687** (2017), 188–193. DOI: 10.1016/j.cplett.2017.09.005.
- 4 Zeng H., Cheng X., Zhang C., Lu Z. Responses of Core–Shell Al/Al<sub>2</sub>O<sub>3</sub> Nanoparticles to Heating: ReaxFF Molecular Dynamics Simulations, *J. Phys. Chem. C***122**, 16 (2018), 9191–9197. DOI: 10.1021/acs.jpcc.8b01088.
- 5 Soleymanibrojeni M., Shi H., Liu F., Han E.-H. Atomistic simulations of Epoxy/Water/Aluminum systems using the ReaxFF method, *Comput. Mater. Sci.***173** (2020), 109424. DOI: 10.1016/j.commatsci.2019.109424.
- 6 Darenne B Modélisation de l'interaction des agrégats hydrocarbonés avec les parois, *These de Doctorat*, ENSPC-Chimie ParisTech (2018).
- 7 Rüger R., Franchini M., Trnka T., Yakovlev A., van Lenthe AMS 2019, T. SCM, Theoretical Chemistry, Vrije Universiteit: Amsterdam, The Netherlands.
- 8 Bitzek E., Koskinen P., Gähler F., Moseler M., Gumbusch P. Structural relaxation made simple, *Physical review letters***97**, 17 (2006), 170201. DOI: 10.1103/PhysRevLett.97.170201.
- 9 Berendsen H.J.C., Postma J.P.M., van Gunsteren W.F., DiNola A., Haak J.R. Molecular dynamics with coupling to an external bath, *The Journal of chemical physics***81**, 8 (1984), 3684–3690. DOI: 10.1063/1.448118.
- 10 T. W. Graham Solomons *Organic Chemistry (11th Ed)*.
- 11 Bacha K. These de Doctorat "Etude de l'interaction entre le carburant diesel et les composants du système d'injection diesel", *Physique des matériaux*, Université de Haute Alsace (2016).
- 12 Kresse G., Joubert D. From ultrasoft pseudopotentials to the projector augmented-wave method, *Phys. Rev. B***59**, 3 (1999), 1758–1775. DOI: 10.1103/PhysRevB.59.1758.
- 13 van Duin A.C.T., Dasgupta S., Lorant F., Goddard W.A. ReaxFF: A Reactive Force Field for Hydrocarbons, *J. Phys. Chem. A***105**, 41 (2001), 9396–9409. DOI: 10.1021/jp004368u.
- 14 Mielczarek D.C., Matrat M., Amara A.B., Bouyou Y., Wund P., Starck L. Toward the Accurate Prediction of Liquid Phase Oxidation of Aromatics: A Detailed Kinetic Mechanism for Toluene Autoxidation, *Energy Fuels***31**, 11 (2017), 12893–12913. DOI: 10.1021/acs.energyfuels.7b00416.
- 15 W. G. Hoover, B. L. Holian Kinetic moments method for the canonical ensemble distribution, *Phys. Rev. A (Physical Review A)***211** (1996), 253–257. DOI: 10.1016/0375-9601(95)00973-6.
- 16 *Chemical Hazards Response Information System (CHRIS) Hazardous Chemical Data*.
- 17 Bacha K., Ben-Amara A., Vannier A., Alves-Fortunato M., Nardin M. Oxidation Stability of Diesel/Biodiesel Fuels Measured by a PetroOxy Device and Characterization of Oxidation Products, *Energy Fuels***29**, 7 (2015), 4345–4355. DOI: 10.1021/acs.energyfuels.5b00450.
- 18 Zhang W., van Duin A.C.T. Improvement of the ReaxFF Description for Functionalized Hydrocarbon/Water Weak Interactions in the Condensed Phase, *J. Phys. Chem. B***122**, 14 (2018), 4083–4092. DOI: 10.1021/acs.jpcc.8b01127.
- 19 C. B. Alcock *Crystallographic data on minerals: CRC Handbook of Chemistry and Physics*, FL (2003–2004).
- 20 Y. M. DE HAAN Refinement of the Al<sub>2</sub>O<sub>3</sub>, Ti<sub>2</sub>O<sub>3</sub>, V<sub>2</sub>O<sub>3</sub> and Cr<sub>2</sub>O<sub>3</sub> structures, *Zeitschrift für Kristallographie - Crystalline Materials*, 1-6 (1962), 235–237.

- 21 Finger L.W., Hazen R.M. Crystal structure and isothermal compression of Fe<sub>2</sub>O<sub>3</sub>, Cr<sub>2</sub>O<sub>3</sub>, and V<sub>2</sub>O<sub>3</sub> to 50 kbars, *J. Appl. Phys.* **51**, 10 (1980), 5362. DOI: 10.1063/1.327451.
- 22 Chatelain K., Nicolle A., Ben Amara A., Catoire L., Starck L. Wide Range Experimental and Kinetic Modeling Study of Chain Length Impact on n -Alkanes Autoxidation, *Energy Fuels* **30** (2016), 1294–1303. DOI: 10.1021/acs.energyfuels.5b02470.
- 23 Mielczarek D.C., Matrat M., Amara A.B., Bouyou Y., Wund P., Starck L. Toward the Accurate Prediction of Liquid Phase Oxidation of Aromatics: A Detailed Kinetic Mechanism for Toluene Autoxidation, *Energy Fuels* **31**, 11 (2017), 12893–12913. DOI: 10.1021/acs.energyfuels.7b00416.
- 24 Martyna G.J., Tuckerman M.E., Tobias D.J., Klein M.L. Explicit reversible integrators for extended systems dynamics, *Molecular Physics* **87**, 5 (1996), 1117–1157. DOI: 10.1080/00268979600100761.
- 25 W.M. Haynes *CRC handbook of chemistry and physics: A ready-reference book of chemical and physical data*, CRC Press, Boca Raton, Fla. (2013).
- 26 M. J. O'Neil The Merck Index: An Encyclopedia of Chemicals, Drugs, and Biologicals, 15th Edition Edited by M.J.O'Neil, Royal Society of Chemistry, Cambridge, UK ISBN 9781849736701; 2708 pages. April 2013, \$150 with 1-year free access to The Merck Index Online, *Drug Dev. Res.* **74**, 5 (2013), 339. DOI: 10.1002/ddr.21085.
- 27 A.K. Soper The radial distribution functions of water and ice from 220 to 673 K and at pressures up to 400 MPa, *Chemical Physics*, 121–137. DOI: 10.1016/S0301-0104(00)00179-8.
- 28 Arrouvel C., Diawara B., Costa D., Marcus P. DFT Periodic Study of the Adsorption of Glycine on the Anhydrous and Hydroxylated (0001) Surfaces of  $\alpha$ -Alumina, *J. Phys. Chem. C* **111**, 49 (2007), 18164–18173. DOI: 10.1021/jp0741408.
- 29 Costa D., Sharkas K., Islam M.M., Marcus P. Ab initio study of the chemical states of water on Cr<sub>2</sub>O<sub>3</sub>(0001): From the isolated molecule to saturation coverage, *Surf. Sci.* **603**, 16 (2009), 2484–2493. DOI: 10.1016/j.susc.2009.05.037.

## Chapter 6. ReaxFF study of biofuel-alumina interactions

### 6.1 Liquid-phase “fuel-oxygen” mixture

In the previous section, we provided the description of the NPT results for common liquid-phase solvents like acetic acid, ethanol, water of which we compared the densities calculated through FFA and FFB against the experimental values. In addition, we also reported the RDF of the O-O pair of water for both FFA and FFB to verify if both reactive force fields were able to describe the water density. From these two “dynamic” study, we concluded that only FFA can be further implemented in the following ReaxFF study, where we aim to describe the dynamic behavior of a surrogate “fuel-oxygen” blend either in homogeneous conditions (e.g. only organic liquid phase) or in heterogeneous conditions (e.g. organic liquid phase in contact with alumina surfaces).

In the framework of this thesis, we examined a surrogate “fuel-oxygen” blend where the fuel (i.e. the solvent) is modeled by toluene molecules, while the oxygen (i.e. the solute) is instead modeled by benzyl hydroperoxide molecules (the skeletal structure of benzyl hydroperoxide molecule is shown in **Figure 44** in section 4.3.1).

The choice of these molecules defining our surrogate “fuel-oxygen” blend is given by the fact that on one hand we wanted to simulate an organic blend that would be a good representation of a liquid-phase fuel already undergoing an oxidative degradation and on the other hand we wanted to link this phenomenon to the toluene autoxidation process. For this reason, we selected the toluene as our solvent and the benzyl hydroperoxide, a well-known intermediate in the toluene autoxidation process [1–3], as our solute.

The “fuel-oxygen” mixture simulated in this study is composed by a 95% mol of toluene and 5% mol of benzyl hydroperoxide. For this “fuel-oxygen” composition, we took inspiration from the predictions of the species concentration profiles calculated with the RMG model by Mielczarek and Matrat [1], where both toluene and hydroperoxide profiles were seen right at the beginning of the autoxidation mechanism. Our main objective was to observe the behavior of the fuel when the autoxidation process is already seen at its propagation state (i.e. relevant intermediates are already being formed, for example the benzyl hydroperoxide). The selection of the benzyl

hydroperoxide as intermediate for the toluene oxidation was studied in previous theoretical studies such as for references [4, 5], where da Silva and coworkers tried to further investigate the kinetic steps describing the toluene autoxidation.

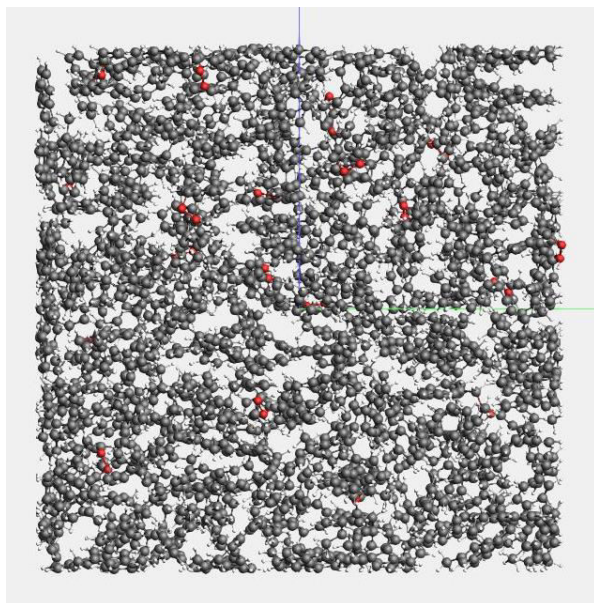
### 6.1.1 Computational details

The simulated box contains 450 toluene molecules and 25 benzyl hydroperoxide molecules respecting the 95:5 molar ratio. The cell used was a cell with an initial volume  $V^0$  fixed to 85184 Å<sup>3</sup>, corresponding to an initial liquid density  $\rho_l^0 \approx 0.87$  g/cm<sup>3</sup> (i.e. toluene density at T = 25 °C and P = 1 atm [6]).

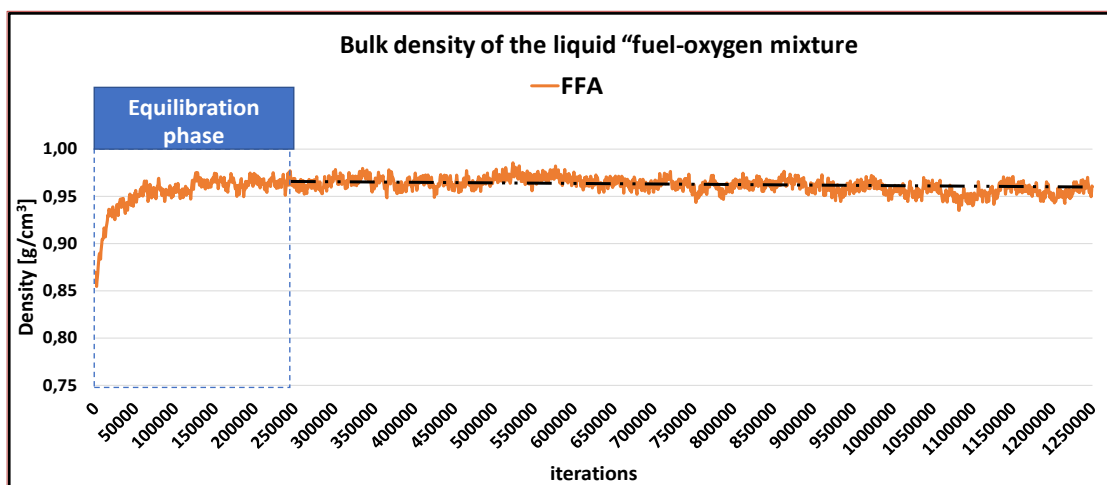
To verify the good reproducibility of the density through the implementation of both reactive force fields, we run a NPT simulation where T= 298 K and P = 1 atm. We selected the MKT barostat [7] and the NHC thermostat [8], with a damping constant of 500 fs and of 100 fs for the barostat and thermostat, respectively. The torsion 2013-correction was not applied in this simulation. The sample frequency was imposed to be registered every 500 steps. The total number of steps was set to  $1.25 \cdot 10^6$  with a time step of 0.25 fs, giving a total simulation time of 312.5 ps, where the first 62.5 ps were of equilibration and the final 250 ps of production. In other words, we considered as valid the data results taken after the first 250'000 iterations, which in our case coincided with the first 500 frames of the NPT simulations (see **Annex-Figure A6-1**).

### 6.1.2 Results and discussion: physico-chemical analysis

In **Figure 71** we report the cubic box containing our “fuel-oxygen” mixture surrogate. In **Figure 72** we report the plot of the bulk density as function of the NPT iterations for the FFA, where we chose to take data after the first 250'000 steps (corresponding to the first 62.5 ps). As we observed for the energy in the **Annex-Figure A6-1**, we can also see in **Figure 72** that we reached a plateau for the slab density in the equilibration phase. In the last 50'000 iterations, the bulk density converged at the average value of 0.96 g/cm<sup>3</sup> (**Figure 72**). We can then calculate a  $\Delta\rho_l\%$  = 9% between the new and the original density value.



**Figure 71:** Simulated cubic box containing the “fuel-oxygen” mixture of 95% mol toluene and 5% mol benzyl hydroperoxide.



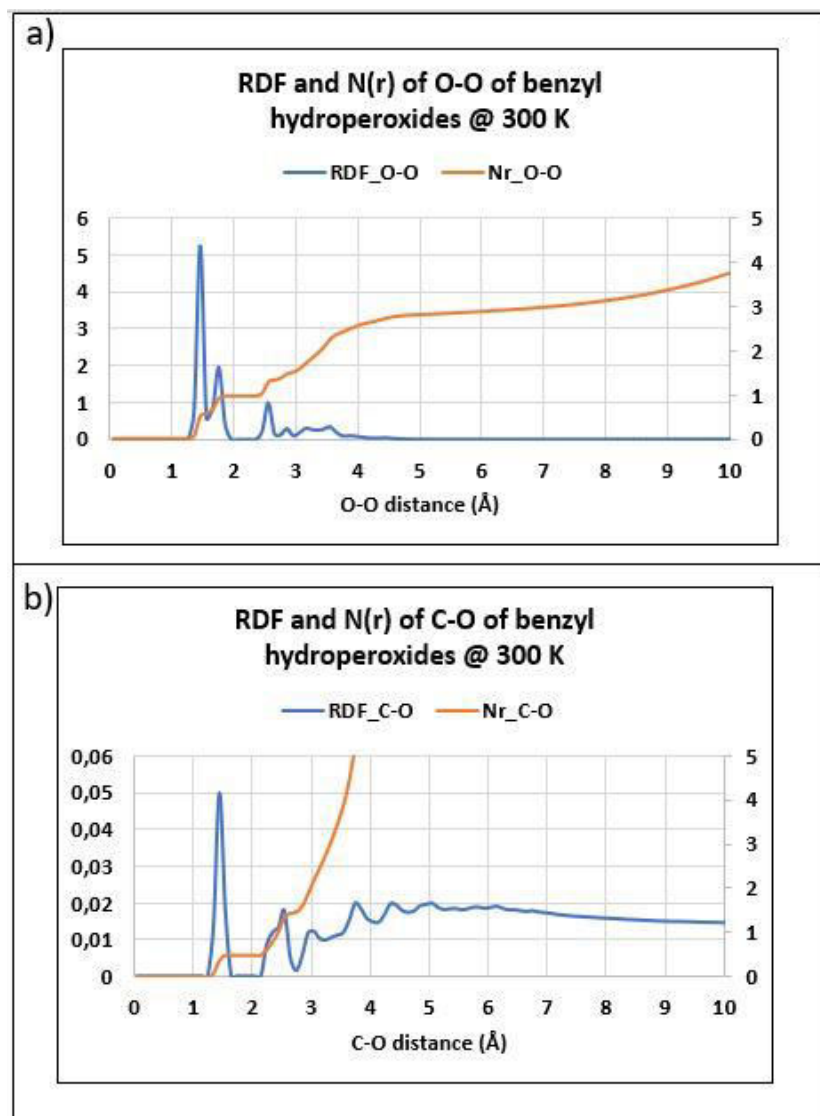
**Figure 72:** Bulk density increase measured during the NPT simulation with the FFA implementation.

Similarly to the density plateau reported in **Figure 72** in the equilibration phase, we also found a plateau for the system temperature and pressure (see **Annex-Figure A6-2**).

Now we will discuss the analysis of the reactivity of this organic mixture, with a particular focus on the benzyl hydroperoxides.

### 6.1.3 Results and discussion: reactivity analysis

The aspect of the chemical reactivity was taken in consideration for this organic “toluene-benzyl hydroperoxide” mixture, especially focusing on the oxygenated solute since it represents a well-known reactive intermediate for the toluene autoxidation [1, 4]. In **Figure 73** we report the RDF and N(r) plots for the O-O and C-O intramolecular bonds of the benzyl hydroperoxides calculated for the entire NPT calculation.

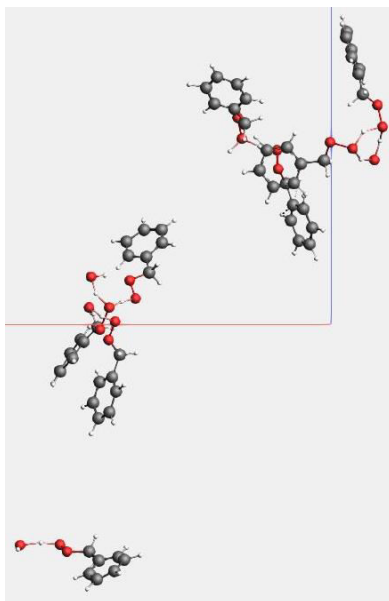


**Figure 73:** RDF and N (r) plots of benzyl hydroperoxide molecules regarding: a) O-O pair and b) C-O pair.

From **Figure 73a**, we observe the highest peak in correspondence of 1.5 Å, which coincides with the O-O bond length for the benzyl hydroperoxides. Minor peaks are observed for 1.7 Å and 2.5 Å, which are representative of H-bonds. The g(r) integral, N(r), corresponds to the mean number

of atoms around a specific type of atom at a distance  $r$ ; for the O-O pair, we obtained a mean value of 1 for the O-O bond length of 1.7-1.8 Å, meaning that we have only one benzyl hydroperoxide molecule in correspondence to that distance (i.e. no bond dissociation is observed). Concerning the intramolecular C-O bond of benzyl hydroperoxides, from **Figure 73b** we observe the highest peak in correspondence of 1.45 Å, which coincides with the C-O bond length for the benzyl hydroperoxides. Again, minor peaks are observed for 2.55 Å and 3 Å, representatives of weaker interactions. For the  $N(r)$ , we obtained in this case a mean value of 0.5 for the C-O bond length of 1.45 Å, confirming again that we are in presence of only one benzyl hydroperoxide molecule in correspondence to that distance and that no bond dissociation is observed.

The absence of O-O and C-O bond dissociations for the benzyl hydroperoxides at 300 K can be reconnected to the high activation and reaction energies that we calculated via DFT in **Chapter 4**, since they prove that higher temperatures are expected for these reactions to occur. On the other hand, what was interesting to observe during this NPT calculation was the propensity of benzyl hydroperoxide molecules to form binary or ternary complexes as the ones represented in **Figure 74**. Also, we can notice that water molecules were also formed during this NPT calculation.



**Figure 74:** Benzyl hydroperoxide molecules forming binary and ternary complexes in the liquid phase at 300 K. Color code: red = oxygen; grey: carbon; white: hydrogen.

This clusterisation between benzyl hydroperoxide molecules appears to open the possibility to the formation of aggregate precursors, which represents one of the phenomenon of major interest for this thesis.

From this dynamic analysis of the liquid “fuel-oxygen” mixture, we can conclude by remarking that no bond dissociations were observed at 300 K in 312.5 ps of calculation time, but instead a clusterisation phenomenon where solute molecules form binary and ternary complexes resembling aggregates precursors was observed.

In the following section, three different heterogeneous systems are discussed: a) the dynamic evolution of the hydroxylated alumina surface when heated up to 500 K, b) the adsorption of liquid droplets of the surrogate “fuel-oxygen” blend interacting with dry and hydroxylated alumina and c) the adsorption of the liquid-phase “fuel-oxygen” blend interacting with dry and hydroxylated alumina.

## 6.2 Heating of hydroxylated alumina up to 500 K

In this paragraph, we examine the dynamic behavior of the hydroxylated  $\alpha$ -Al<sub>2</sub>O<sub>3</sub> when heated from 1 K to 500 K. We compared the obtained MD results with literature works.

### 6.2.1 Computational details

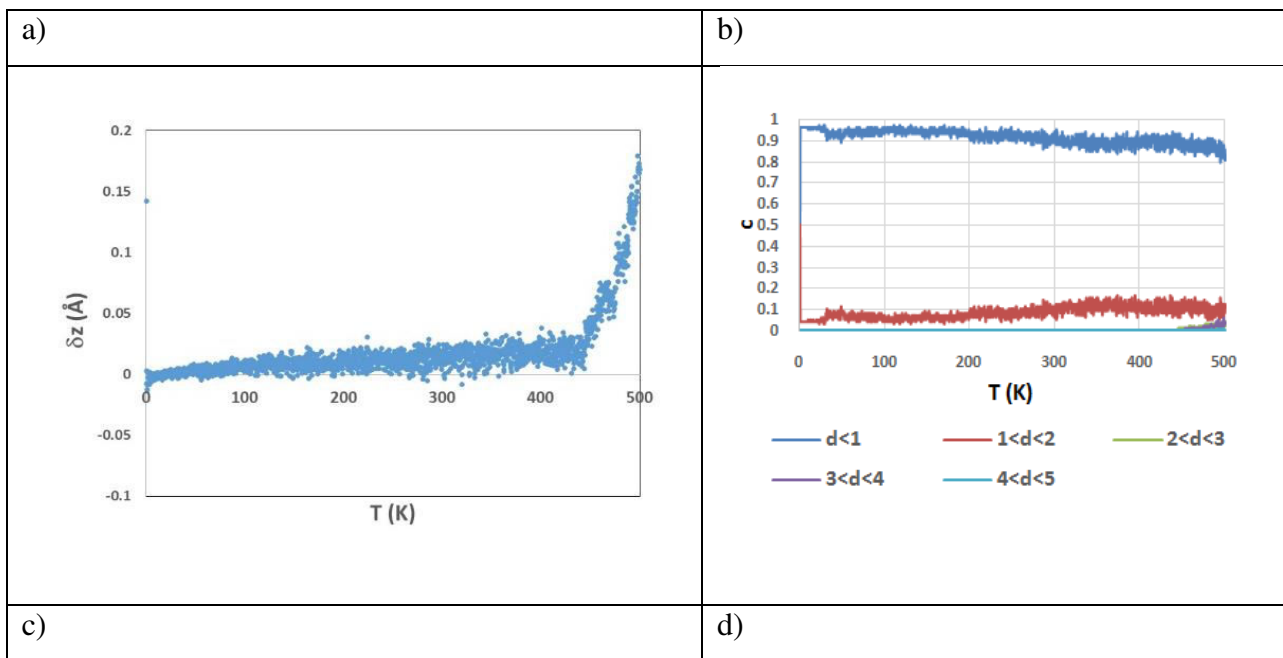
We simulated hydroxylated  $\alpha$ -Al<sub>2</sub>O<sub>3</sub> surface considering an  $\alpha$ -Al<sub>2</sub>O<sub>3</sub>(0001)(4x4) cell with a slab volume of 22670 Å<sup>3</sup> and a surface area of 337.7 Å<sup>2</sup>. A MD simulation was carried out through the implementation of the NVT ensemble, where implementing the NHC thermostat [8] with a damping constant of 100 fs. The torsion 2013-correction was not applied in this simulation. The sample frequency was imposed to be registered every 1000 steps. The total number of steps was set to  $2 \cdot 10^6$  with a time step of 0.25 fs, giving a total simulation time of 500 ps.

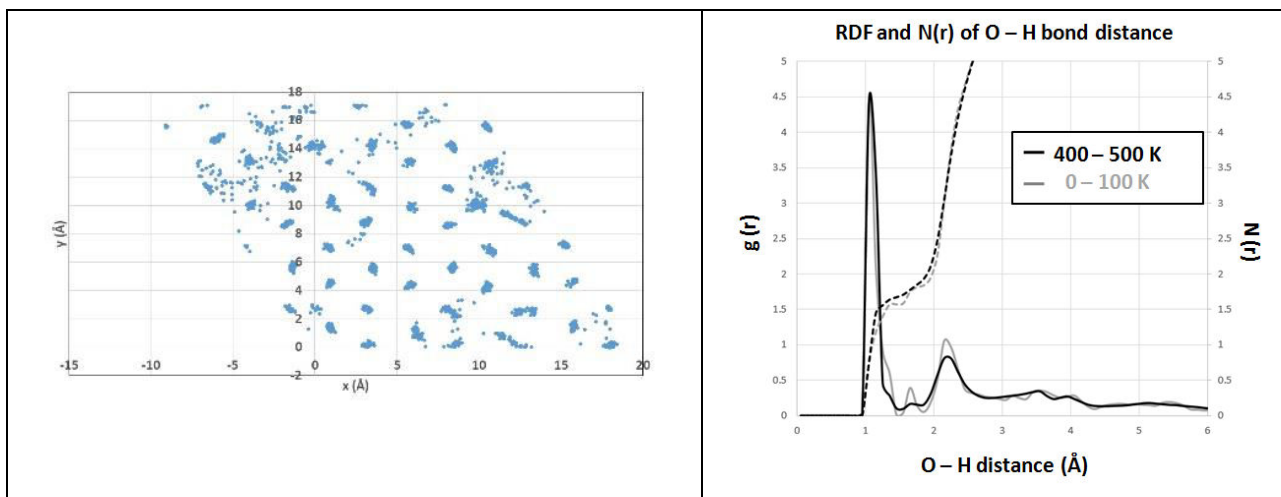
For these NVT simulations, we set the following thermal regime: a linear T function from 1 K to 500 K. In terms of calculation time, the system was heated from 1 K to 500 K during 500 ps with an increasing T rate of 1 K/ps.

A detailed analysis is carried out about the fate of the surface OH groups (hydroxyls and water molecules) on the  $\alpha$ -Al<sub>2</sub>O<sub>3</sub> surface with temperature as well as a brief discussion about the OH-surface distance with temperature and the H bonding network.

### 6.2.2 Results and Discussion

As observed from (**Figure 75a**), the average height deviation  $\delta z$  from the initial OH position is very low, smaller than 0.2 Å. The analysis of the repartition of different  $\delta z$  values with temperature (**Figure 75b**), where  $\delta z$  varies from 1 to 5 Å, shows that OH and H<sub>2</sub>O molecules begin to have larger  $z$  at  $T > 450$  K, and the proportion of those molecules is very low, less than 1%. It is noteworthy that these molecules have a certain lateral mobility at the surface, as illustrated by the **Figure 75c** showing the trace of the O (from the OH groups) along the (X,Y) plane. It is visible in the upper left side that the molecule trace does a continuous patch instead of discrete spots, illustrating surface diffusion.



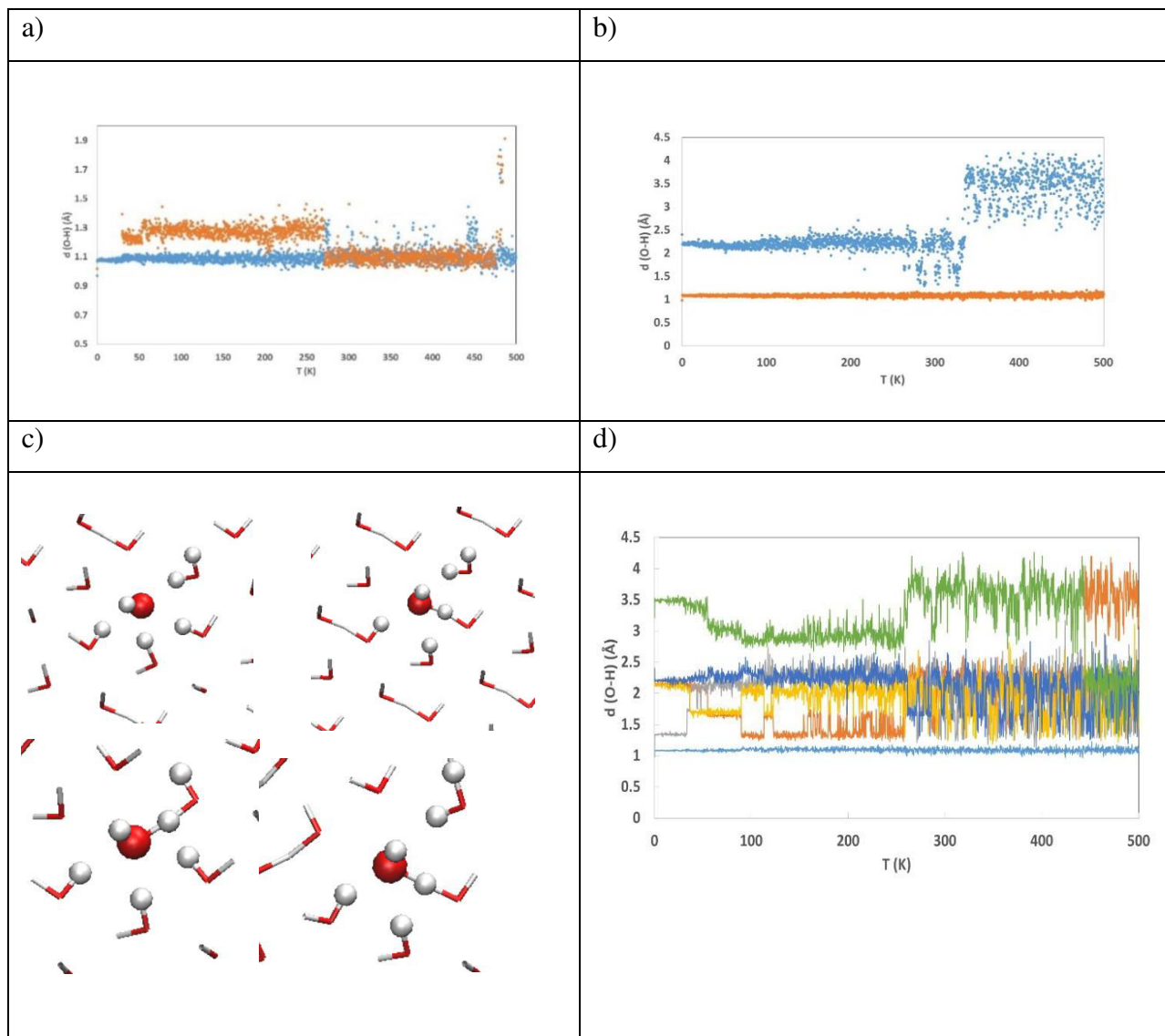


**Figure 75:** Analysis of the OH positions with temperature. a) average  $z(O)$  position (with respect to the initial position), in Å b) proportion of atoms at different distances to the surface during the trajectory c) snapshot for the section 487-500 K, showing OH mobility at the surface d) radial distribution function recorded for the O of the OH groups, and the H atoms. Black: range 400-500 K, grey : range 0-100 K.

The radial distribution function of the O-H distances (**Figure 75d**) shows little changes from the beginning to the end of heating. At low temperature, a small peak at 1.6 Å is observed, due to strong H bonding, and another at 2.2 Å, due to less strong H bonds. The first peak disappears at 500 K, and the second one is smaller than at low temperature. This means that for a certain fraction of OH, there are less H bonds. Plus, the integral  $N(r)$  typical of the covalent bond (1.2 Å) is slightly higher in intensity (1.55 at 500 K versus 1.45 at low temperature) for the first neighbor. The value of 1.5 for the number of H first neighbors is typical of the situation of H sharing, where one surface OH group is stabilized by a vicinal adsorbed water, and the proton is shared between two OH groups. The slightly higher number of covalent bond O-H (~1.1 Å) at higher temperature suggests that some O are turned to a water molecule, a trend in line with the lower amount of H bonds observed. We attribute that to those OH groups that become water molecules and acquire some degree of freedom at the surface.

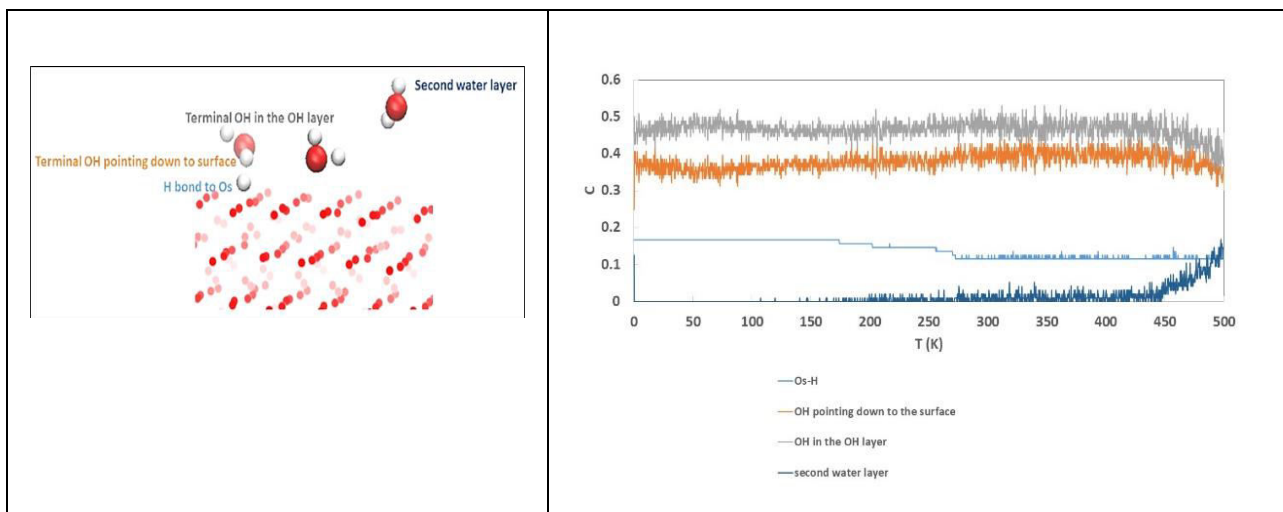
In fact, several typical cases have been identified, and examples are reported here: **Figure 76a** shows the O-H distances of an OH group receiving a strong H bond. It can be observed that at 250 K, this OH group transforms to water. The molecular state of water is maintained at increasing temperature. **Figure 76b** shows another case, where a weak H bond received by a surface OH group is lost at 340 K, illustrating the surface mobility (rotational degree of freedom) acquired by heating. Finally, **Figure 76c** and **Figure 76d** illustrate different configurations of H

bonds received by one OH group at several moments of the trajectory. The O---H distances are reported in **Figure 76d**. The OH group is transformed to a water molecule during 49% of the trajectory. What happens is that the OH group and the vicinal OH<sub>s</sub> change their orientations and that the OH binds to a vicinal H of different OH neighbors (**Figure 76c**). If we closely observe in **Figure 76d** the blue and yellow curves for example, we can deduce that the proton jump frequency increases with the temperature.



**Figure 76:** a) OH distances during the trajectory, for an OH group that transforms to water, b) case of an OH group that loses an H bond with increasing temperature, c-d) case of an OH group that is stabilized by H bonds with several vicinal OH, c) snapshots of several configurations, d) O---H distances showing the increase of frequency of H neighbor change with increasing temperature.

We finally analyze the evolution of location of H atoms during heating (**Figure 77**). A depletion of H bonded to surface oxygen atoms is observed at around 270 K (a result in line with that of Hass et al. [9]). This enrichment in molecular water in the “OH” layer results, with heating, in water “desorption” and mobility at the surface, as already said, above 450 K.



**Figure 77:** repartition of the populations of the H atoms of different OH groups (H adsorbed on surface  $O_s$ , terminal OH pointing down to the surface, H of OH in the OH layer and second water layer) during heating.

To summarize, heating up to 500 K induces an increased degree of freedoms of the surface OH groups, with increased neighboring changes. In addition, some of the dissociated water (terminal OH plus H on surface  $O_s$ ) get molecular at temperature above 270 K, and with temperature, above 450 K, some water molecules (however in very small proportion, less than 1%) tend to lose the bond with the surface (deviation of  $0.2 \text{ \AA}$ ) and get some lateral and rotational degree of freedom.

Noteworthy, the event of some water molecule “desorption” and diffusion at the hydroxylated surface was already observed by Hass et al. [9], at 300 K, who stated: “collective behavior was observed in the vicinity of the  $Al-O_{ads}$  bond that broke during the run; one  $H_2O$  molecule “desorbed” early on from its molecular adsorption site and began to diffuse laterally along the surface in a precursor-like physisorbed state.” The authors also noted that this water molecule was readily trapped into a H bond network of a neighboring molecule.

## 6.3 Droplets of liquid “fuel-oxygen” mixture adsorbed on alumina

In this paragraph, we examine the dynamic behavior of a “drop” of toluene “put” on the dry and hydroxylated  $\text{Al}_2\text{O}_3$  surfaces. The liquid composition was 95% mol toluene and 5% mol benzyl hydroperoxides.

### 6.3.1 Computational details

For the dry alumina case, the simulated box contained 90 toluene molecules and 5 benzyl hydroperoxide molecules, while for the hydroxylated alumina case the MD box contained 93 toluene molecules and 5 benzyl hydroperoxides molecules. Both simulated boxes approximately respected the 95:5 molar composition of the “fuel-oxygen” mixture. We run these MD simulations through the NVT ensemble, implementing the NHC thermostat [8] with a damping constant of 100 fs. The torsion 2013-correction was not applied in this simulation. The sample frequency was imposed to be registered every 500 steps. The total number of steps was set to  $6.25 \times 10^6$  with a time step of 0.25 fs, giving a total simulation time of 1562.5 ps ( $\approx 1.6$  ns), where the first 62.5 ps were of equilibration and the final 1500 ps (= 1.5 ns) of production. In other words, we considered as valid the data taken after the first 250'000 iterations (see **Annex-Figure A6-3**).

For these NVT simulations, we set the following thermal regime: a) an equilibration phase where  $T = 1$  K for 62.5 ps and b) a production phase where we distinguished two thermal sub-regimes: a first, linear  $T$  function from 1 K to 400 K and, second, a constant  $T$  function at 400 K. The final temperature at  $T = 400$  K was chosen since it is significant for autoxidation phenomena (**Chapter 1**). For the anhydrous case, a supplementary “cooling” sub-regime was studied, where the temperature decreased linearly from 400 K to 1 K.

In terms of simulation time, after 62.5 ps at 1 K, the system was heated from 1 K to 400 K during 750 ps with an increasing  $T$  rate of 0.5 K/ps, then a trajectory at 400 K was accumulated during 750 ps, completing the 1.5 ns of total simulation time. For the additional cooling regime for the dry alumina case, the system was cooled from 400 K to 1 K during 750 ps with a decreasing  $T$  rate of 0.5 K/ps.

The dry  $\alpha$ -Al<sub>2</sub>O<sub>3</sub> cell used for this NVT simulation was a (8x8) cell, with a surface area of 1269 Å<sup>2</sup>, while for the hydroxylated case the  $\alpha$ -Al<sub>2</sub>O<sub>3</sub> cell was a (8x8) cell, with a surface area of 1352 Å<sup>2</sup>.

To verify the validity of the NVT results, supplementary simulations were carried out with the “Born Oppenheimer Molecular Dynamics” (BOMD) method. Here, a trajectory was acquired with BOMD at 400 K on the same system, but in a smaller (2x2) cell containing three toluene molecules with a monolayer (ML) density of 3.79 molecule/nm<sup>2</sup>. **Table 16** summarizes the conditions for the MD performed with ReaxFF and with DFT (BOMD) for the system “fuel-oxygen” adsorbed on  $\alpha$ -Al<sub>2</sub>O<sub>3</sub>.

**Table 16: Conditions for the MD performed with ReaxFF and with DFT for “fuel-oxygen”@ Al<sub>2</sub>O<sub>3</sub>.**

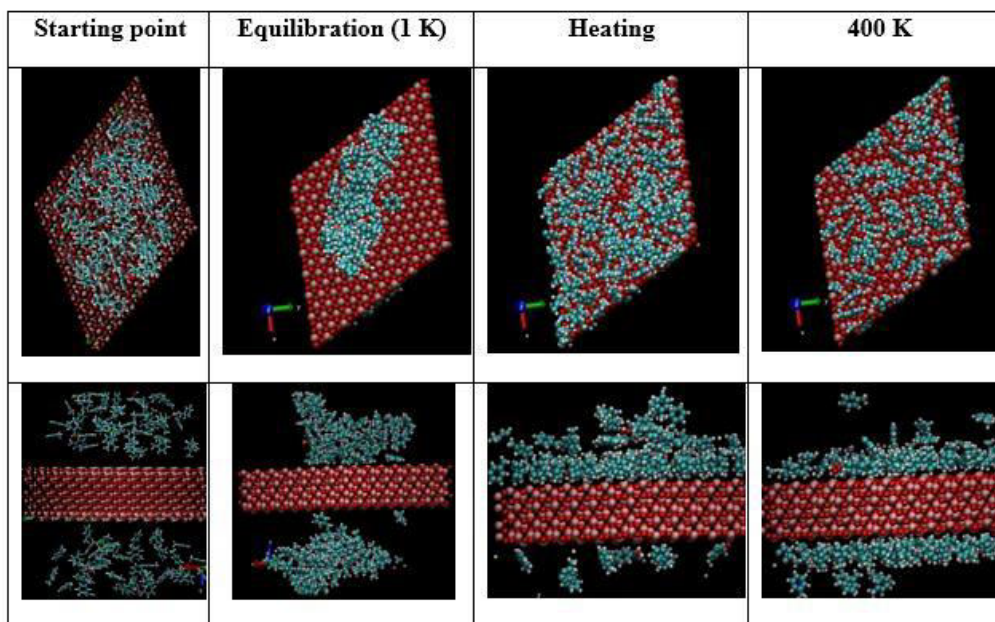
System	Cell Size and Surface Area	Calculation Method	Temperature (K)	Time (ps)
« Fuel-O »@Al <sub>2</sub> O <sub>3</sub>	8x8 ; 1269Å <sup>2</sup>	ReaxFF (MD)	1	62.5
			1 to 400	750
			400	750
			400 to 1	750
« Fuel-O »@Al <sub>2</sub> O <sub>3</sub>	2x2; 79 Å <sup>2</sup>	DFT (BOMD)	400	5.4
« Fuel-O »@Al <sub>2</sub> O <sub>3</sub> -HY	8x8 ; 1352Å <sup>2</sup>	ReaxFF (MD)	1	62.5
			1 to 400	750
			400	750

### 6.3.2 Results and Discussion

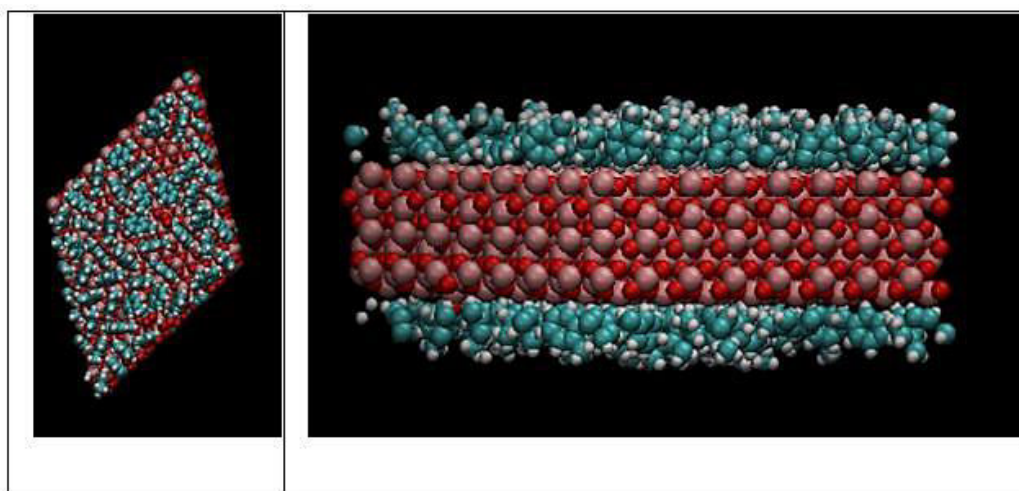
The initial configuration and snapshots of the three domains (equilibration, heating, plateau, cooling) are shown in **Figure 78-Figure 79** for the anhydrous surface. **Figure 79** shows the structure obtained after cooling from 400 K to 1 K.

We observed that at 1 K, the molecules (which were spread homogeneously in the box at the beginning of the calculation, see **Figure 78**), gather together to form a drop. During heating, the molecules acquired velocity and were spread out on the bottom surface in a stochastic orientation, thus no initial preferential orientation was present on this surface. We observed the dispersion of the molecules at the surfaces and the formation of layers, both on the top surface and on the bottom surfaces.

During the plateau at 400 K, those layers are maintained, with some molecules desorbing from the surfaces and readsorbing. During the subsequent cooling down to 1 K (**Figure 79**) no more molecules desorb from the surface, and the two surfaces are covered by a full molecular layer.



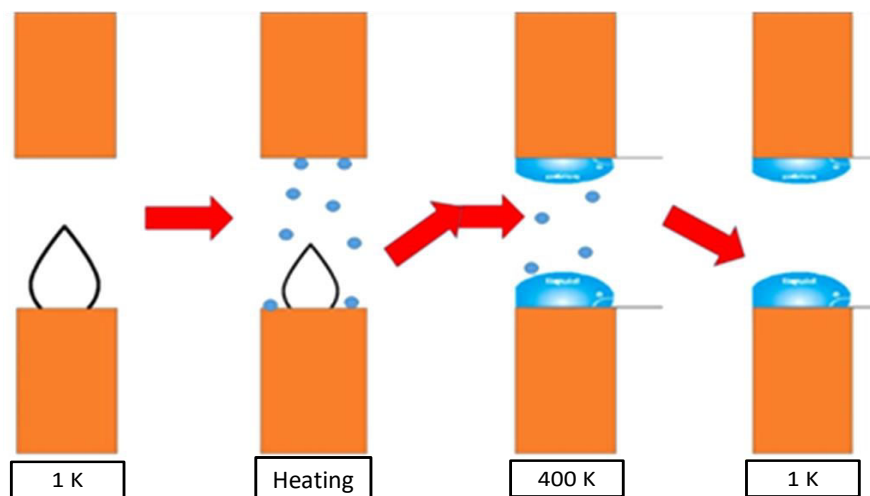
**Figure 78:** Starting point and snapshots of the molecular dynamics of a toluene drop on dry  $\text{Al}_2\text{O}_3$  surface.



**Figure 79:** Toluene monolayer formed on dry  $\text{Al}_2\text{O}_3$  after T decreasing from 400 K to 1 K during 750 ps.

**Figure 80** summarizes the events observed during the heating-plateau-cooling cycle. Now analyzing with more details the behavior of the molecules at the surface and trying to characterize

the layer formed, first we follow the number of molecules adsorbed (in direct interaction with the surface) during heating and at the plateau. We also try to estimate the monolayer density and the tilt angle of the molecules in the formed layer. The molecule-surface interaction is scrutinized. When relevant, we compare the results to those obtained on the hydroxylated surface. The layers formed on  $\alpha\text{-Al}_2\text{O}_3$  after cooling are also analyzed.

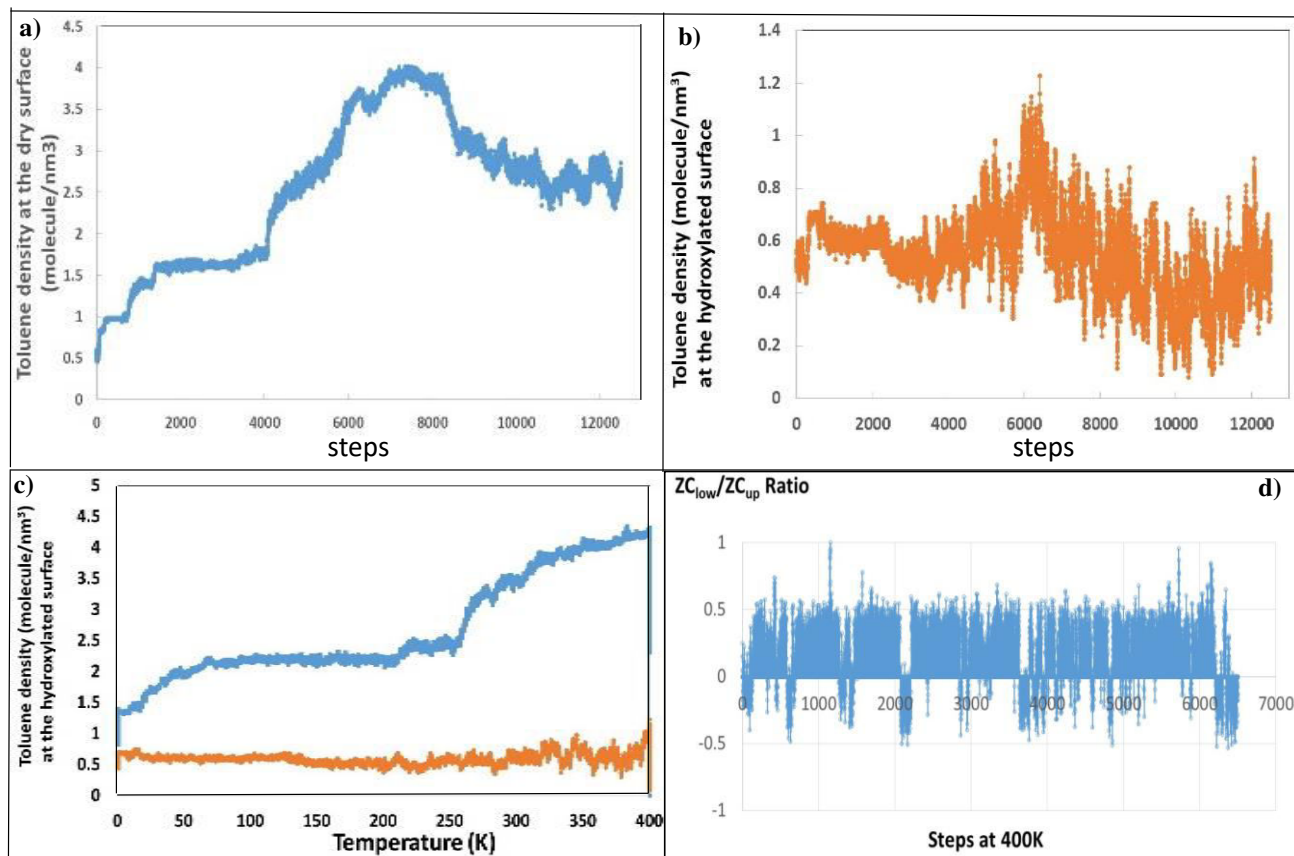


**Figure 80:** Illustration of the “virtual drop evaporation” and adsorption onto the dry  $\text{Al}_2\text{O}_3$  surfaces, and global events observed during the equilibration at 1 K, heating to 400 K, plateau and cooling to 1 K.

**Figure 81** shows the density of toluene molecules at the surface during heating (the toluene molecule length being  $7 \text{ \AA}$ , we integrated the number of C atoms until  $7 \text{ \AA}$  from the surface). We observe that heating (between step 500 and step 6000) induces an increase of the molecules density at the surfaces of both the anhydrous and the hydroxylated surfaces, then a slight decrease at 400 K, until a plateau is reached for both surfaces. We observe that the surface density of molecules (in molecule/ $\text{nm}^2$  units) reached on the anhydrous surface is significantly higher than that on the hydroxylated surface (see **Figure 81c**). For the anhydrous surface, it is interesting to estimate the density of the monolayer adsorbed. It is estimated to  $4 \text{ molecule/nm}^2$ . Such a layer density is typical of self-assembled layers of benzenic ring molecules, such as gallic acid or 2-mercaptobenzothiazole (MBT) or 2-mercaptobenzimidazole (MBI)[10].

The analysis of the molecule-surface tilt angle is not straightforward, as several phenomena occur simultaneously at the surface that can alter the measurements such as surface diffusion and desorption. On some molecules that neither diffuse on the surface nor desorb, we followed the tilt

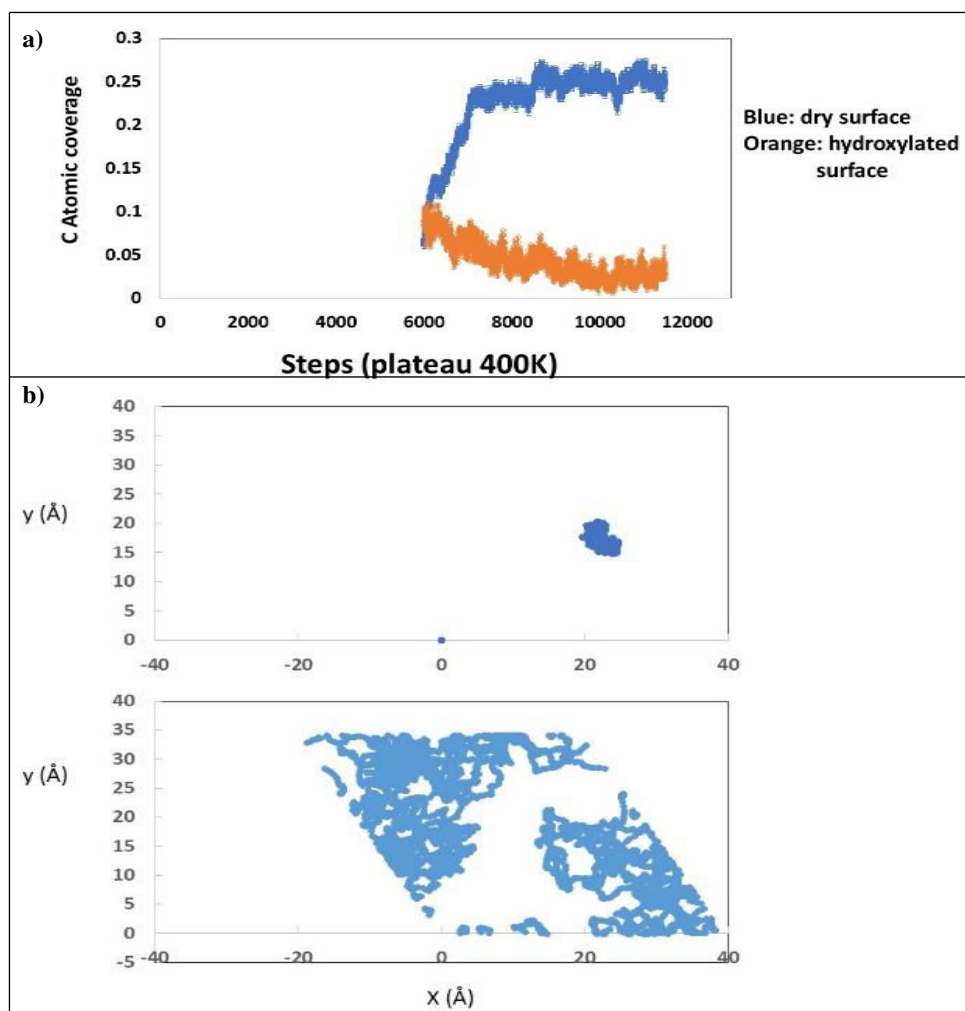
angle of the molecule with the surface. The average angle between molecule and surface normal measured at 400 K was  $15^\circ$ . Notice that this is an average value that does not consider that the molecule cycle flips at the surface. **Figure 81d** shows that the tilt angle is in fact a compromise between  $-60^\circ$  and  $60^\circ$  of the surface normal.



**Figure 81:** Number of toluene in molecules/nm<sup>2</sup> at the dry Al<sub>2</sub>O<sub>3</sub> surface during the whole trajectory (number of steps), a) anhydrous surface (blue), b) hydroxylated surface (orange). c) Snapshot of comparison of the anhydrous and hydroxylated surfaces during heating. d) Ratio of Z coordinates between the upper and lower C in a toluene cycle, indicating the cycle/surface tilt and its variations, on the anhydrous surface.

The behavior of the layers during the plateau at 400 K was thoroughly analyzed. **Figure 82** reports the density of C atoms near the surface (we report as “near the surface” the atoms located at less than 3 Å from the surface). We chose as a descriptor of the layer the percentage of the surface effectively covered by C atoms. Here the scale is taken as an effective surface coverage, i.e., the number of C atoms near the surface multiplied by the projected area of a C atom and divided by the area of  $\alpha$ -Al<sub>2</sub>O<sub>3</sub> surface. Again, a huge difference between the anhydrous and the hydroxylated surface is observed. First, less C atoms approach the surface as near as 3 Å on the

hydroxylated surface. Second, **Figure 82b** shows that whereas these C atoms are rather fixed on the anhydrous surface, they are mobile on the hydroxylated surface.



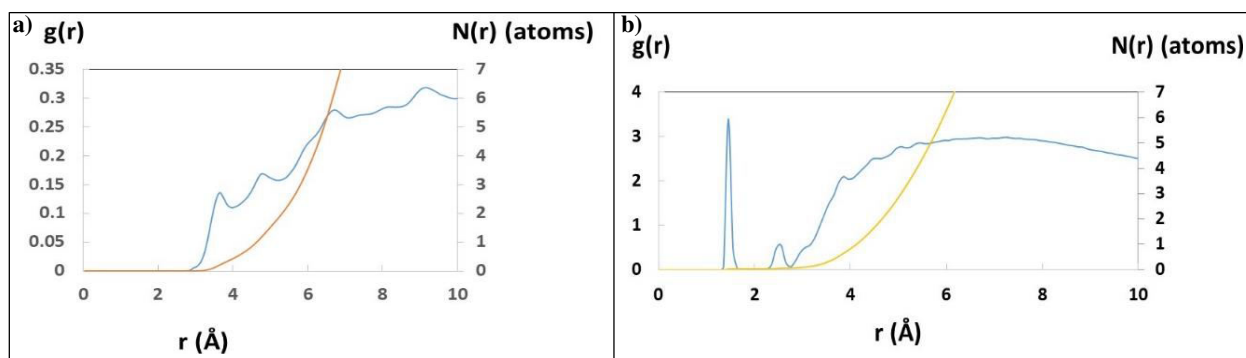
**Figure 82:** Analyses of the toluene layers at 400 K on the anhydrous and hydroxylated alumina surfaces. The “effective atomic coverage” is calculated as  $T(\theta) = N(C) \cdot \pi \cdot \text{Rat}(C)^2 / \text{Surface}$ , where  $N(C)$  is the number of C atoms,  $\text{Rat}(C)$  is the C atomic radius. We considered  $\text{Rat}(C) = 0.65 \text{ \AA}$ . a) Surface “effective atomic coverage” at 400 K; orange: anhydrous, blue: hydroxylated surface; b) Trace of one C atom displacement in the (X,Y) plane during the trajectory at 400K. This shows the lateral degree of freedom of C atoms on the anhydrous (top figure) surface and hydroxylated (bottom figure) surfaces.

We notice that on the anhydrous surface, the effective atomic coverage of 0.25 is equivalent to the surface coverage of Al (i.e. there is one molecule per each surface Al ion); in addition, the molecules are immobile at the surface (**Figure 82b**). This suggests a strong interaction between Al ions and C of toluene and raises the question of a possible Al-C bond formation. To answer this point, we plotted the pair radial distribution function of Al and C, reported in **Figure 83**. We

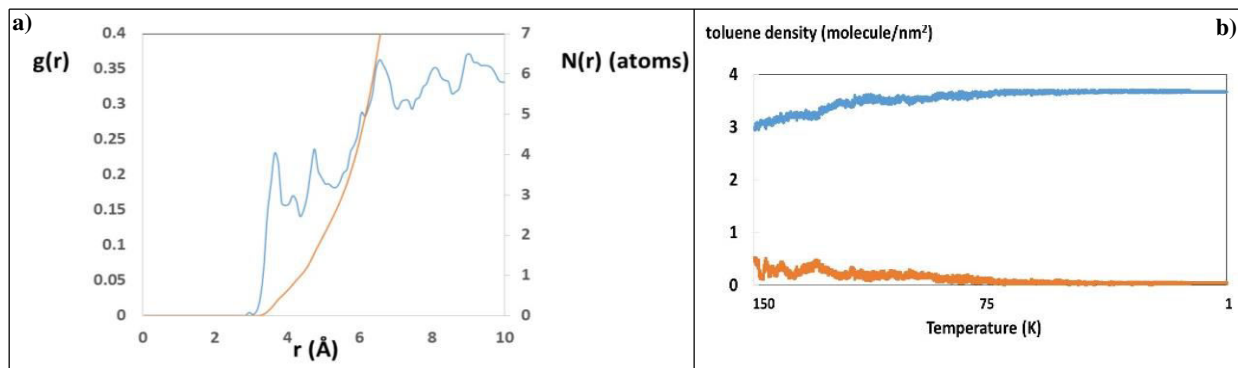
notice a peak at 3.65 Å, with an integrated value corresponding to 0.65 C neighbor. This distance of interaction is typical of van der Waals interactions.

The situation is totally different for the hydroxylated surface, with a low surface coverage and a strong mobility of the molecules at the surface. The radial distribution function OH-C exhibits a pronounced peak at the short distances at 1.45 Å, with however a very weak occurrence (each OH group “sees” 0.03 C atom in average at this distance). An interaction at 2.55 Å is also noted, and again, of weak occurrence. Finally, in average, each surface OH group “sees” one C atom in a radius of 4 Å, again, typical of weak interactions.

**Figure 84a** plots the radial distribution function Al-C during T decreasing, in the 150 K-1 K range. We notice that this radial distribution function is very similar to that recorded at 400 K. At 3.65 Å, Al is “bound” to 0.65 C. This confirms that at 400 K, the toluene ML was equilibrated. **Figure 84b** shows the molecule density in the toluene surface layer (distance to surface  $\leq 7$  Å) and above this layer. From 150 K and below, one can consider that all molecules belong to the surface layer. The (8x8) surface cell contains 47 molecules, corresponding to a layer density of 3.70 molecule/nm<sup>2</sup>. Among these 47 molecules, only five molecules (10%) have tilt angle greater than 15° towards the surface normal. It might be possible that a somewhat denser layer can be formed where all molecules adopt an orientation perpendicular to the surface.

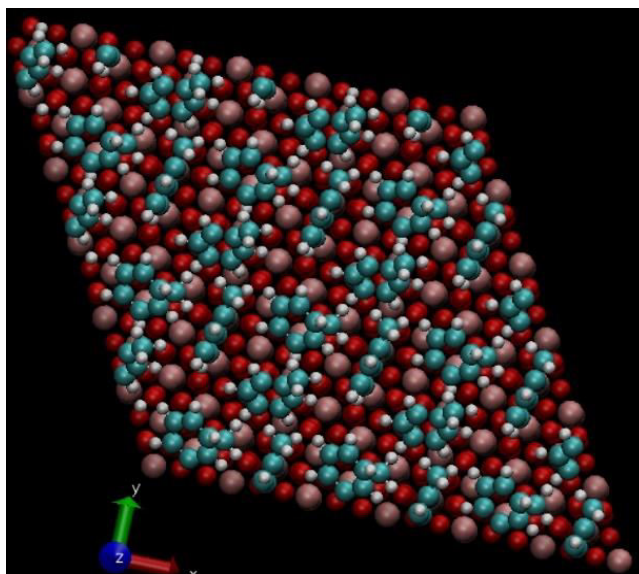


**Figure 83: Radial distribution function (blue) and integrated value (orange), of a) Al and C atoms, at 400 K, on Al<sub>2</sub>O<sub>3</sub>. We notice the formation of an Al-C interaction at 3.65 Å. In average, each Al binds 0.5 C atoms; b) Oxygen from OH groups and C atoms at 400 K on the hydroxylated surface. We notice a pronounced peak at short distances at 1.45 Å which however displays a very weak occurrence (0.03 atom). An interaction at 2.55 Å is also noted, and again, of weak occurrence. In average, each surface OH group “sees” one C atom in a radius of 4 Å.**



**Figure 84:** a) radial distribution function Al-C during T decreasing from 150 to 1 K, with ReaxFF. B) Toluene coverage (in unit of molecules/nm<sup>2</sup>) in the first layer (blue) and above the first layer (orange). We notice that under 150 K, this number is very small.

To confirm the monolayer stability at the surface, a trajectory was acquired with BOMD at 400 K as shown in **Figure 85**.

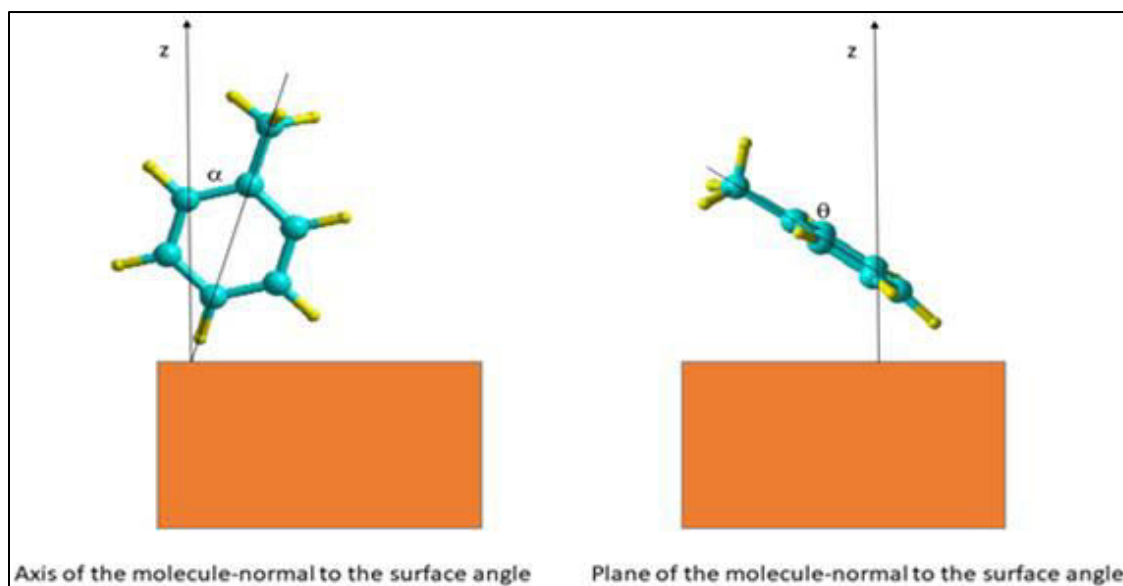


**Figure 85:** Snapshot of the monolayer of toluene on  $\text{Al}_2\text{O}_3$ , trajectory at 400 K with BOMD. The simulation was performed with a (2x2) surface supercell of  $\alpha$ - $\text{Al}_2\text{O}_3$  (0001).

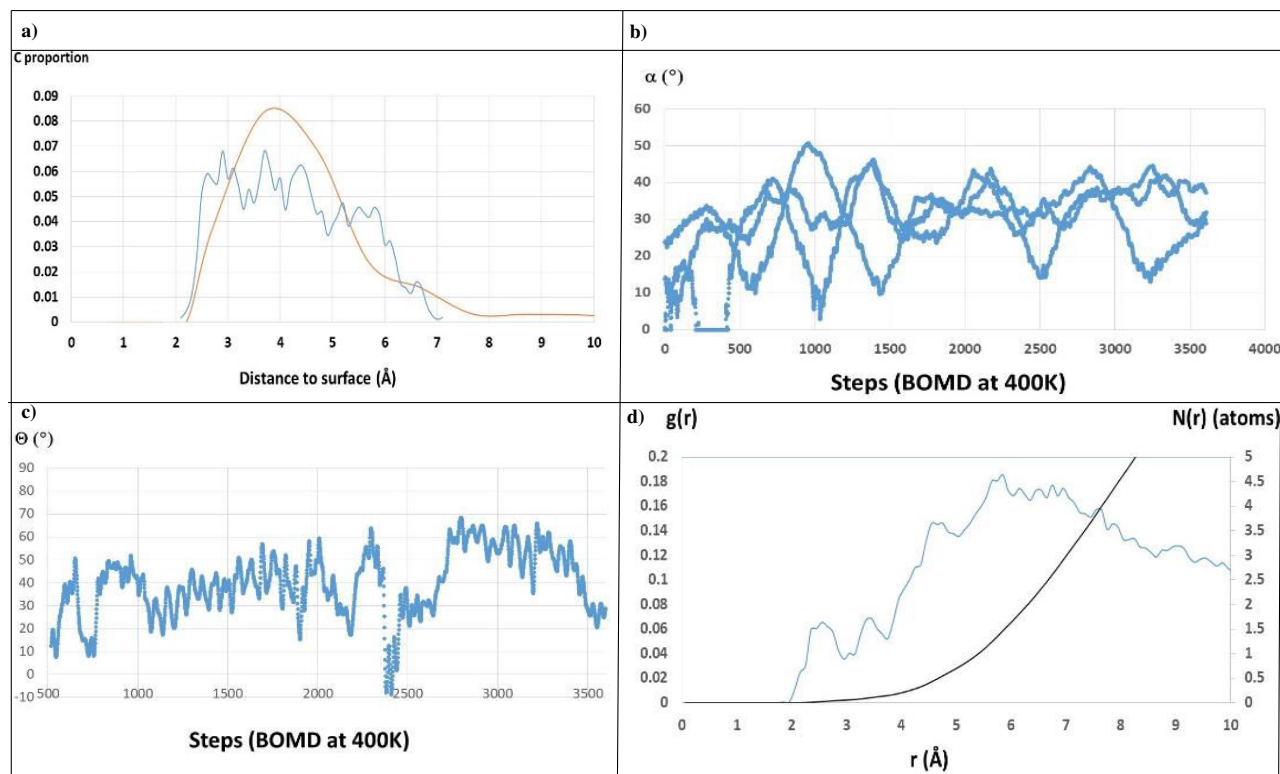
During the BOMD trajectory, no molecule desorption is observed. We have a full toluene layer, where we can analyze the molecule surface orientation. The angles chosen are shown in **Figure 86**.

The **Figure 87** gathers all data acquired during the BOMD trajectory. **Figure 87a** compares the C density collected with respect to the distance to the surface with DFT (blue) and with ReaxFF (purple). We notice that the C-surface distances found with ReaxFF and with DFT exhibit similar profiles, albeit the maximum at 3.7 Å is marked with ReaxFF and not with BOMD. To this respect, the ReaxFF trajectory and the DFT trajectory are compatible. **Figure 87b** shows the angle of the toluene molecules C-C axis with the Z axis (DFT trajectory). The molecules C-C axis are tilted by 20-30°. The analysis of the molecule plane-Z axis angle (**Figure 87c**, DFT trajectory) reveals that the molecule plane can be also tilted and found oscillating between 10 and 40°.

The radial distribution function Al-C collected during the BOMD run is shown in **Figure 87d**. A peak at 2.65 Å corresponds to 0.15 C neighbor. DFT calculations reveal that the Al-C distances are shorter than the values of 3.65 Å found with ReaxFF. A closer examination of the Al-C distances during the ReaxFF run reveals that the shortest Al-C distances are around 3.1 Å, but no distances smaller than 3 Å are reported. This discrepancy between ReaxFF and DFT is the price to pay for the fit of the average properties.



**Figure 86: Illustration of the molecule surface tilt angles: angle between the axis of the molecule and the axis Z, and angle between the plane of the molecule and Z axis.**

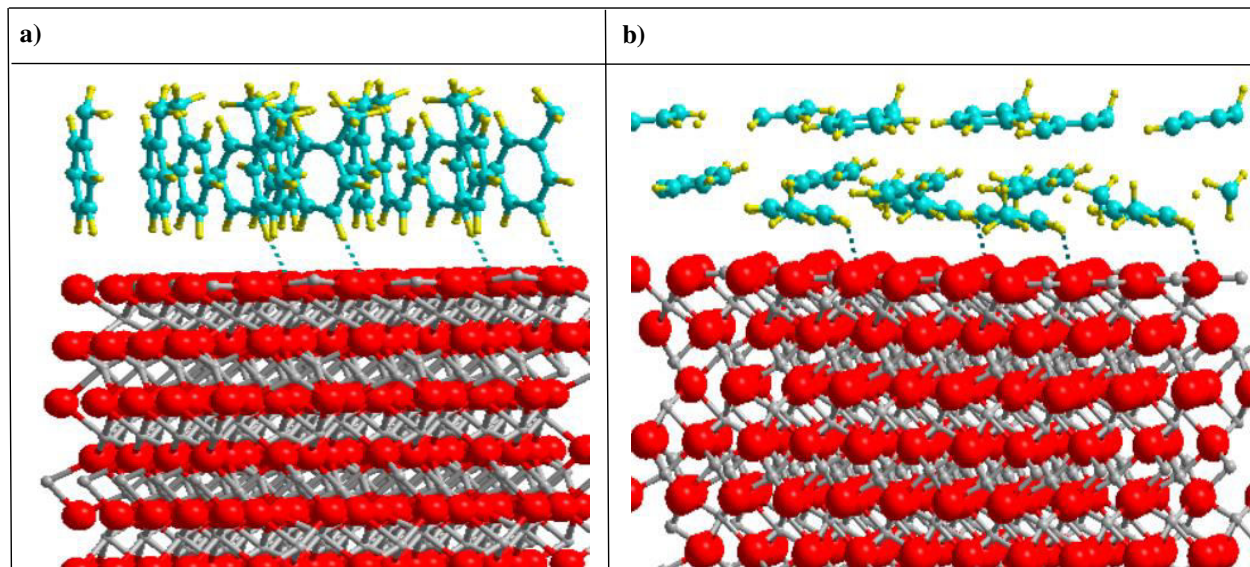


**Figure 87:** a) C proportion of the total C amount versus distance to the surface (blue, DFT, purple, ReaxFF) ; b) Variation of the angle  $\alpha$  of the axis of the toluene molecule with the Z axis, acquired during the DFT trajectory; c) dihedral angle  $\theta$  between the molecular plane and the surface normal (DFT trajectory); d) pair correlation function Al-C for the BOMD of toluene on  $\text{Al}_2\text{O}_3$  at 400 K (blue:  $g(r)$ , black,  $N(r)$ ).

In the preceding sections, we have investigated the organization and thermal behavior of a toluene ML at the  $\alpha\text{-Al}_2\text{O}_3$  surface, with an organization in a dense layer where the molecules are perpendicular or slightly tilted towards the surface. It is worth comparing this structure derived from the ReaxFF study with the formation of toluene multilayers that are parallel to the surface. **Figure 88** shows the result of the DFT geometry optimization of such a multilayer. We found that it was nearly isoenergetic (difference 0.1 eV/molecule  $\approx 9.6 \text{ kJmol}^{-1}$ ) to the perpendicular ML.

To summarize, we find that starting from a toluene droplet deposited at the  $\text{Al}_2\text{O}_3$  surface, and heating up to 400 K, a dense monolayer of toluene is formed on the anhydrous surface, with a molecular density of  $3.7 \text{ molecule/nm}^2$ . The molecules are adsorbed in a slightly tilted orientation to the surface. This layer is stable during 750 ps at 400 K on the anhydrous surface. The ML found was confirmed to be stable at the anhydrous surface through a comparative DFT BOMD

study at 400K. The Al-C interaction is 2.65 Å with DFT and 3.65 Å with ReaxFF, pointing to a discrepancy.



**Figure 88:** DFT geometry optimization of a) dense monolayer ( $E_{\text{ads}} = -49.2$  kJ/mol), b) two layers of toluene, ( $E_{\text{ads}} = -58.9$  kJ/mol) on  $\text{Al}_2\text{O}_3$

Complementary DFT calculations also show that this dense ML is however nearly iso-energetic to a bilayer of molecules adsorbed parallel to the surface. It is possible that for a longer accumulation period, transitions between monolayer and multilayers could occur at the surface.

In contrast, no toluene layer forms when heating or during the plateau at 400 K on the hydroxylated surface. In average, at 400 K, 0.2 ML is still present on the hydroxylated surface, with significant surface diffusion of the molecules.

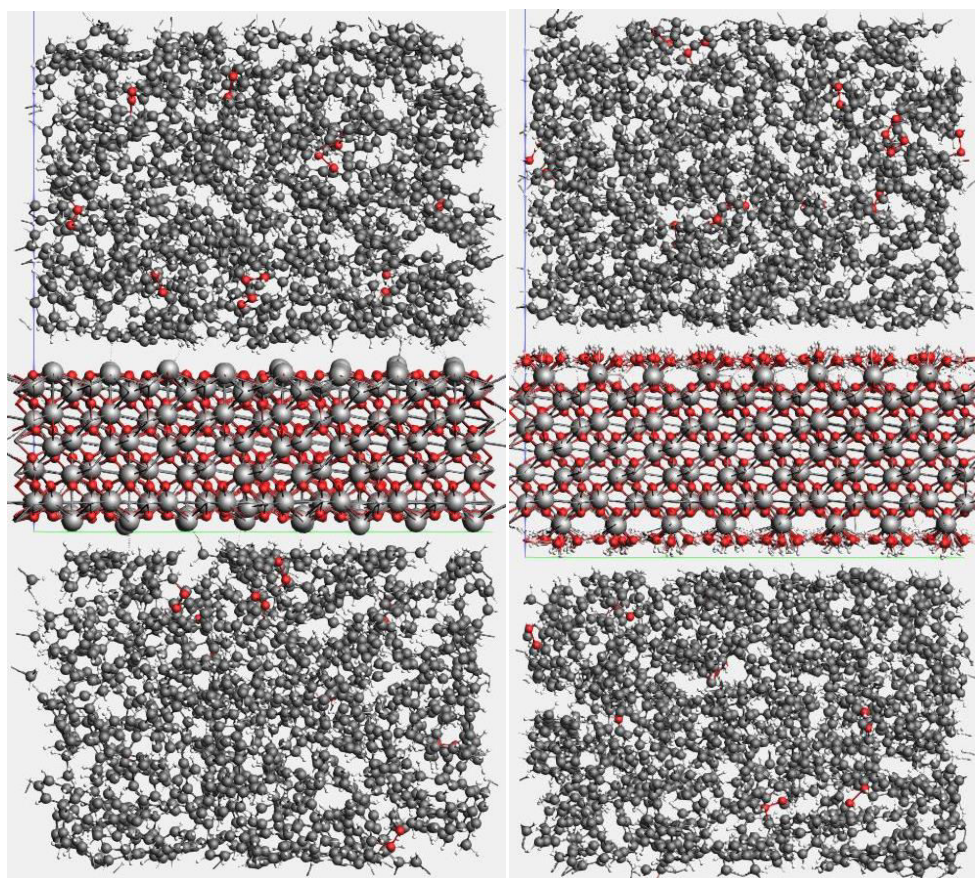
The reason of this different behavior lies in the differences in adsorption energies of toluene on dry and hydroxylated  $\alpha\text{-Al}_2\text{O}_3$ .

ReaxFF has allowed us to propose a valuable structure for the drop of toluene adsorbed on  $\alpha\text{-Al}_2\text{O}_3$  surface and evidenced that hydroxylation strongly changes the toluene-surface interaction, which is much weaker.

Finally, the present results confirm the general view that a strong adsorption leads to the immobilization of the molecules at the surface, whereas weak adsorption leads to surface diffusion and desorption when the temperature rises up.

## 6.4 Liquid-phase “fuel-oxygen” mixture adsorbed on alumina

We do now a step further towards a realistic system. To investigate the behavior of the liquid “fuel-oxygen” surrogate mixture when adsorbed on the alumina substrate, we created two different systems represented in **Figure 89**, the one on the left identifying the adsorption of the organic liquid phase on top of the dry  $\text{Al}_2\text{O}_3$  surface, while the one on the right identifying the same organic liquid phase on top of the hydroxylated overlayer of the alumina surface.



**Figure 89:** Simulated box containing the “fuel-oxygen” mixture of 95% mol toluene and 5% mol benzyl hydroperoxide adsorbed on a) dry  $\text{Al}_2\text{O}_3$  (on the left) and b) fully-hydroxylated  $\text{Al}_2\text{O}_3$ . Color code: grey: Al; red: O; dark grey: C; white: H.

For the organic liquid phase, we considered the same mixture as in the previous **section 6.1**, with a 95:5 ratio of solvent (i.e. toluene) and of solute (i.e. benzyl hydroperoxide).

To analyze the trajectories obtained putting in contact the liquid phase and the surfaces, we report in the following paragraphs the following analyses:

- ❖ Behavior of the solvent (toluene) when put in contact with the surface : density and organization (if any) at the surface.
- ❖ Density and organization (if any) of the peroxide molecules at the surface.
- ❖ Chemical reactions (if any).

### 6.4.1 Computational details

For the dry alumina case, the simulated box contained 400 toluene molecules and 20 benzyl hydroperoxide molecules, while for the hydroxylated alumina case the MD box contained 470 toluene molecules and 25 benzyl hydroperoxides molecules. Both simulated boxes respected the 95:5 molar composition of the “fuel-oxygen” mixture.

We carried out a NPT simulation where we selected the MTK [7] as barostat and the NHC [8] as thermostat, with a damping constant of 500 fs and of 100 fs for the barostat and thermostat, respectively. The torsion 2013-correction was not applied in this simulation. The sample frequency was imposed to be registered every 500 steps. The total number of steps was set to  $4.5 \cdot 10^6$  with a time step of 0.25 fs, giving a total simulation time of 1125 ps ( $\approx 1.1$  ns), where the first 125 ps were of equilibration and the final 1000 ps (= 1 ns) of production. In other words, we considered as valid the data results taken after the first 250'000 iterations (see **Annex-Figure A6-4**).

For these NPT simulations, we set the following thermal regime: a) an equilibration phase where  $T = 300$  K for 125 ps and b) a production phase of 1000 ps where we distinguished four sequential thermal sub-regimes:

- A linear T function from 300 K to 400 K .
- A constant T function at 400 K..

- A linear T function from 400 K to 500 K.
- A constant T function at 500 K.

The thermal range  $T = 400\text{-}500$  K was chosen since it is significant for the occurring of autoxidation phenomena (**Chapter 1**).

In terms of calculation time, after 125 ps at 300 K, the system was heated from 300 K to 400 K during 250 ps with an increasing T rate of 0.4 K/ps, then it was stabilized at 400 K for 250 ps, then reheated 400 K to 500 K during 250 ps with an increasing T rate of 0.4 K/ps and finally stabilized at 500 K for the last 250 ps, completing 1 ns of total production data.

Our first objective was to observe how the liquid mixture would behave when interacting with dry and hydroxylated alumina surface at ambient conditions and later see if changes in behavior would be detected by gradually increasing the temperature, first at 400 K ( $\approx 130^\circ\text{C}$ ) and secondly at 500 K ( $\approx 230^\circ\text{C}$ ).

The dry  $\alpha\text{-Al}_2\text{O}_3$  cell used for this NPT simulation was a (8x8) cell with a surface area of  $1260 \text{ \AA}^2$ , while for the hydroxylated case the  $\alpha\text{-Al}_2\text{O}_3$  cell was a (8x8) cell with a surface area of  $1351 \text{ \AA}^2$ .

## 6.4.2 Results and discussion: toluene-surface interaction

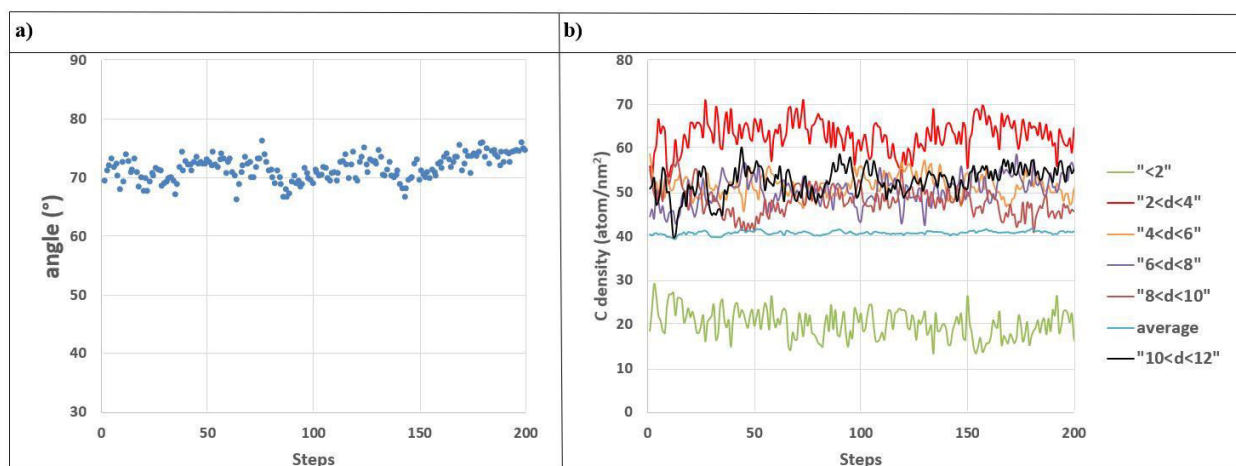
We first analyze the equilibration runs. From the energy plot (see **Figures A6-4-A6-5** in the **Annex**), we notice that a plateau is quickly reached, after 1000 time frames (equal to 125 ps). It came out that a structuration of the liquid phase occurred during the equilibration, so we will also analyze this part.

In the starting configurations, the toluene molecules were located near the surface were in a highly tilted orientation with  $70^\circ$  angle against the surface normal.

On the hydroxylated surface, during the equilibration, we observe no change of the average angle of the surface layer to the surface normal (see **Figure 90a**). In the right panel (**Figure 90b**), the C densities (in  $\text{at}/\text{nm}^3$ ) are reported for different distances to the surface. At very short distance ( $<$

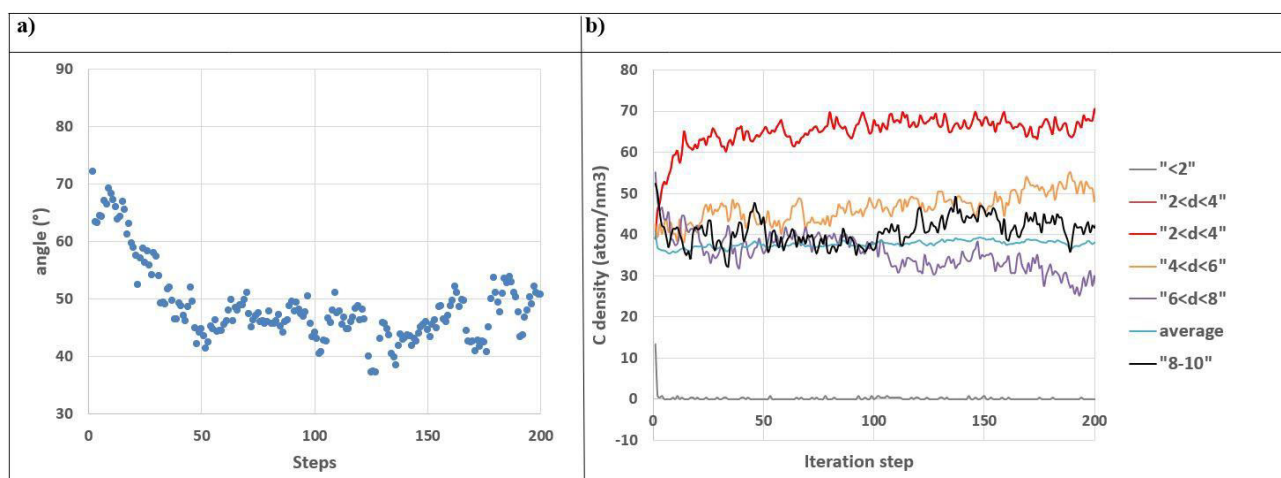
2Å), the C density is depleted with respect to the bulk value, and between 2 and 4 Å from the surface, we observe a C enrichment. It is maintained (but to a lesser extent) in the subsequent layers. We verify that the average C density (blue curve) is 39.8 C/nm<sup>3</sup>, which corresponds to the C density in toluene at room temperature. All in all, during the equilibration at the hydroxylated surface, no drastic modification of the liquid phase is observed, neither in density nor in molecule/surface angle.

In strong contrast, during the very first moments of the equilibration of the trajectory on the dry surface (**Figure 91**), we notice an evolution of the average molecule/surface angle. Starting with most of the molecules nearly parallel to the surface (molecule/normal to the surface angle near 70°), since the first iterations, the tilt angle with the normal to the surface falls to 45°, thus the molecules do not have any more a parallel orientation to the surface, but rather a tilted one. The analysis of the C density during the equilibration shows that at short distance (2 to 4 Å from the surface) a C enrichment occurs, whereas above (6 to 8 Å from the surface) C depletion is observed. Thus, already during the equilibration step, the toluene organization at the two surfaces is different.



**Figure 90: Analysis of the equilibration of toluene on the hydroxylated Al<sub>2</sub>O<sub>3</sub> surface, a) Average molecule/normal to the surface angle (°), b) C density (atom/nm<sup>3</sup>), during the equilibration, at different distances from the surface, in Å.**

We check now if this difference is maintained during the production run at 300 K. **Figure 92** compares the C proportion (of the total C amount) as a function of the distance to the surface, on the dry and hydroxylated surfaces at 300 K. For both surfaces, we identify three zones: the near-surface region (distance to 4 Å, first adsorbed layer), an intermediate region (second adsorbed layer, distance to surface 8 Å), and the bulk liquid (above 8 Å).



**Figure 91: Analysis of the equilibration of toluene on dry  $\text{Al}_2\text{O}_3$  surface at 300 K: a) Average molecule/normal to the surface angle ( $^\circ$ ) ; b) C density ( $\text{atom}/\text{nm}^3$ ), during the equilibration, at various distances from the surface (in  $\text{\AA}$ ).**

However, the layer profiles are different, confirming that the toluene structuration at the two surfaces is different. On both surfaces, the C density is larger than in the bulk, indicating attraction by the surface and/or structuration of a layer at the surface, with a depletion at 4  $\text{\AA}$ , indicating the formation of a toluene monolayer, especially in the case of the hydroxylated surface. In contrast, on the dry surface, the C profile suggests more a bilayer formation than a monolayer, thus a more important accumulation of molecules at the surface, with a more important depletion, now at 8  $\text{\AA}$  from the surface.

The analysis layer by layer during the plateau at 300 K shows that the C density in the layers does not vary significantly, suggesting that a stationary state was reached (see **Annex- Figure A6-6**).

We now analyze the effect of temperature increase on the toluene-surface interactions.

We found no significant change in the C profile on the dry surface, we observe that the bilayer structuration at the surface is maintained at 400 K and 500 K (**Figure 93**). The persistence of this bilayer structure at high temperatures suggests that this layer is strongly adsorbed at the surface.

A very different profile is obtained for the hydroxylated surface (**Figure 94**), where the profile at 400 K is similar as at 300 K but at 500 K, the toluene-surface interaction is less marked, certainly because the molecules are more mobile at this temperature. This indicates that the toluene-hydroxylated surface interaction is less intense than the toluene-dry surface.

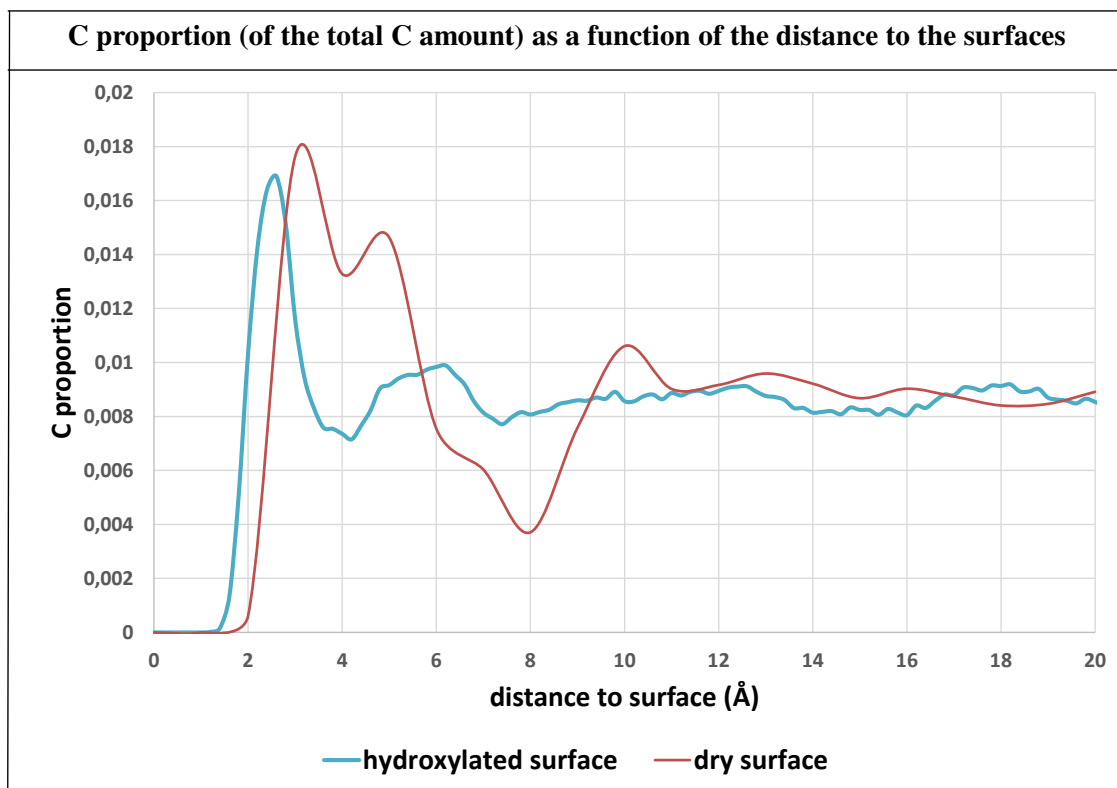


Figure 92: C amount (proportion of the total amount) at 300 K for toluene on  $\text{Al}_2\text{O}_3$  surfaces.

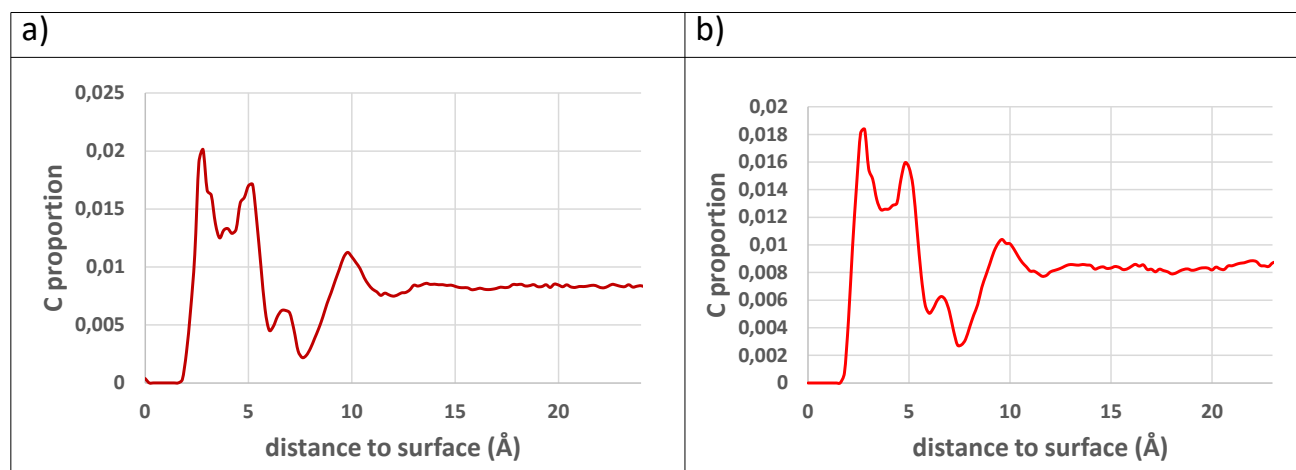
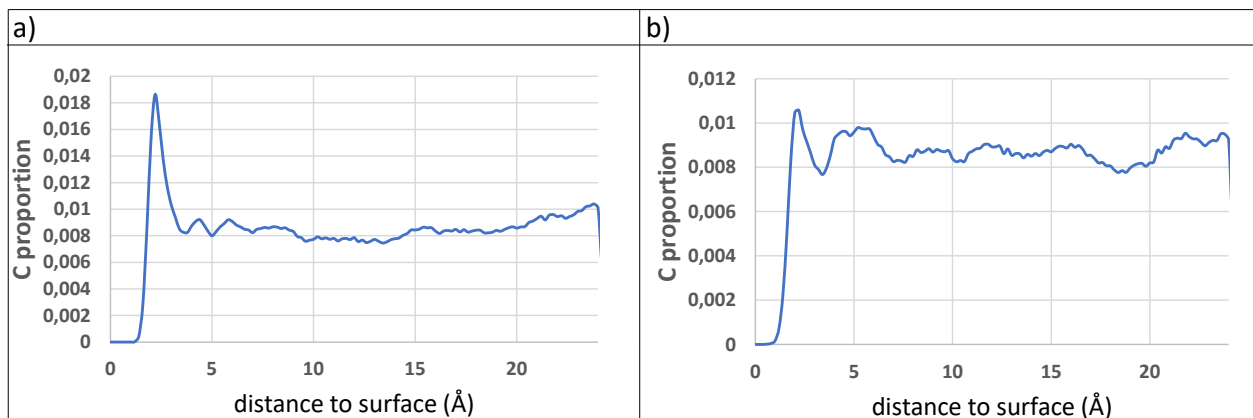


Figure 93: C proportion for toluene on dry  $\text{Al}_2\text{O}_3$  surface, recorded at a) 400 K b) 500 K.

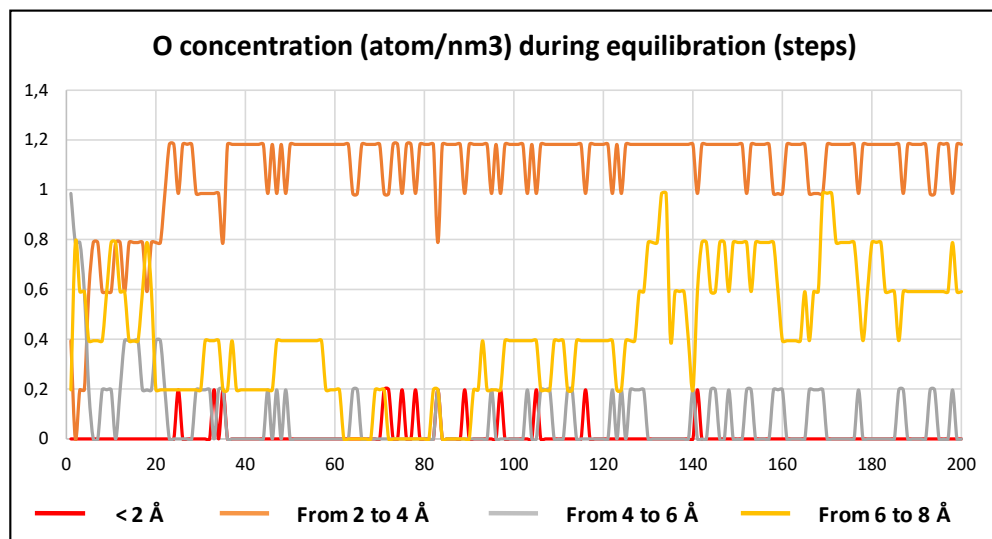


**Figure 94:** C proportion for toluene on hydroxylated  $\text{Al}_2\text{O}_3$  surface, recorded at a) 400 K b) 500 K.

### 6.4.3 Results and Discussion: benzyl hydroperoxides-surface interaction

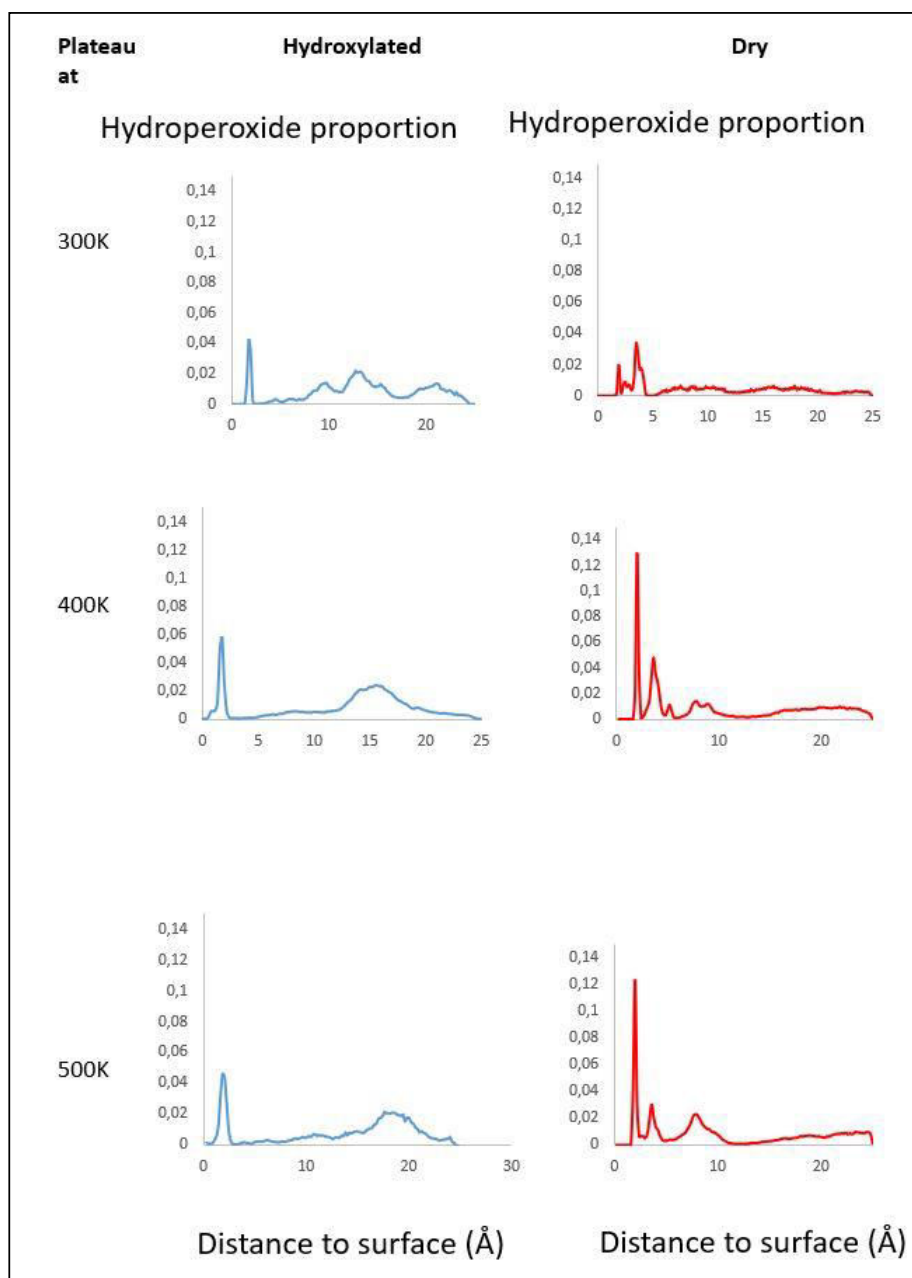
Let us now focus on the behavior of the hydroperoxide molecules at the surface.

**Figure 95** reports in the case of the anhydrous surface, the O densities at distances up to 8 Å to the surface.



**Figure 95:** variation of the peroxide oxygen concentration during the equilibration steps, case of the anhydrous surface.

We notice that the O density nearest the surface ( $< 2 \text{ \AA}$ , red curve) do not increase during the equilibration time. A similar behavior was observed for the hydroxylated surface (not shown).



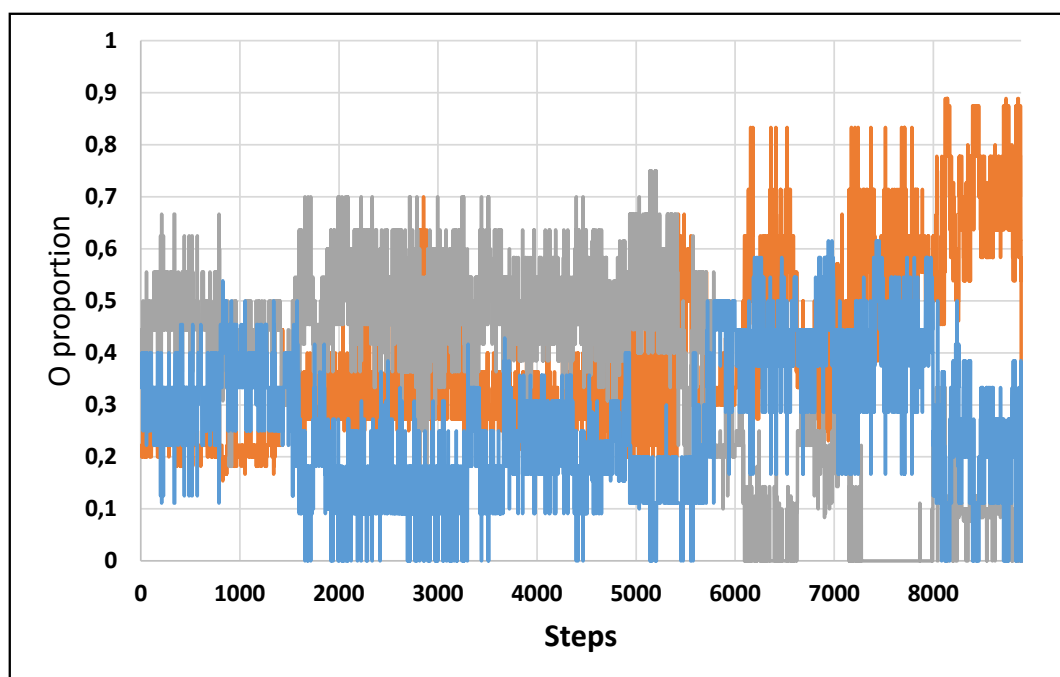
**Figure 96: Hydroperoxide O proportion with respect to the distance to the surface, X axis: distance to surface ( $\text{\AA}$ ), Y axis: proportion.**

During the trajectory at 300 K (**Figure 96**, top panels), similarly as for the C atoms, we notice for the hydroperoxide oxygens a “single surface layer” regime on the hydroxylated surface, and a

“bi-layer regime” at the dry surface. Indeed, on the anhydrous surface, two peaks are visible at the near surface, one at 2 and one at 3.4 Å, whereas one peak is noticeable on the hydroxylated surface, at 1.8 Å.

On both surfaces, a first zone corresponds to the near surface region, from zero to 3 Å. Above this zone, the hydroxylated surface exhibits a region without O species, and then hydroperoxide accumulation seems to occur between 7 and 15 Å from the surface at 300 K. In contrast, the hydroperoxide distribution above the bilayer seems to be more homogeneous above the dry surface.

On the hydroxylated surface, it seems that at 400 and 500 K, the peroxide molecules are confined in a cluster/layer in the bulk liquid. The hydroperoxide concentration seems to be depleted at the surface at 500 K. On the anhydrous surface, the bilayer structure evolves towards a single layer, where the molecules from the second layer could have diffused to the surface, and this will be analyzed in the next section. The bulk liquid is depleted in peroxides.



**Figure 97: Proportion of peroxide at the interface toluene/ $\text{Al}_2\text{O}_3$ . Orange: surface; grey: second layer; blue: liquid; temperature ranges: steps 0-2222: from 300 to 400 K; steps 2222-4444: 400 K; steps 4444-6666: from 400 to 500 K; above: 500 K.**

This analysis is completed by the analysis of the proportion of O at different distances from the anhydrous surface (**Figure 97**), recorded during the whole sequence (heating up to 400 K, plateau at 400 K, heating to 500 K, plateau at 500 K). We observe that at the beginning, the hydroperoxides are distributed equally in the three zones (near surface, second layer and “liquid” phase). Then, the liquid zone is depleted and the second layer enriched. When the temperature 500 K is reached, the bulk and second layer zones are depleted and the molecules accumulate at the surface.

To summarize, peroxides adopt at 300 K the bilayer structure of toluene, but at higher temperature, a single surface layer is obtained. Very interestingly, the behavior with temperature is dramatically different when comparing the hydroxylated and dry surfaces: whereas the molecules tend to cluster in the liquid phase near hydroxylated surfaces, a liquid phase depletion and accumulation of peroxides at the surface is observed on the dry surface.

#### 6.4.4 Results and discussion: chemical reactivity

To have an idea of the reactivity of the benzyl hydroperoxides at the alumina surfaces, we tried to comprehend their behavior in two different instances: a) when they interact above the alumina surfaces and b) when they interact in the liquid medium above the alumina surfaces.

We start by discussing the mechanisms that we observed when the benzyl hydroperoxides come in contact with the alumina surfaces.

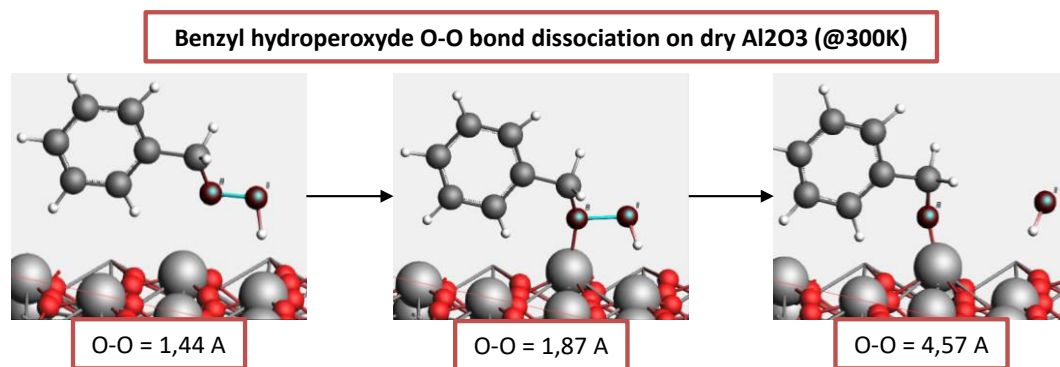
Starting from the dry  $\text{Al}_2\text{O}_3$  system, we registered two different types of solute-surface interactions during the thermal range of 300 – 500 K: the O-O bond dissociation of a single benzyl hydroperoxide molecule interacting with the outermost  $\text{Al}_s$  atom and the O-O bond dissociation of this molecule on top of the surface while firstly interacting with other solute molecules through H bonds.

The first solute-surface type of case is shown in **Figure 98**, where we traced the steps that led towards the O-O bond breaking: we start from an original O-O bond distance of 1.44 Å that start to stretch after the establishing of the covalent  $\text{O}_{\text{mol}}\text{-Al}_s$  covalent bond, to finally break with a bond distance of almost 5 Å. What we were able to observe from these MD steps was that the

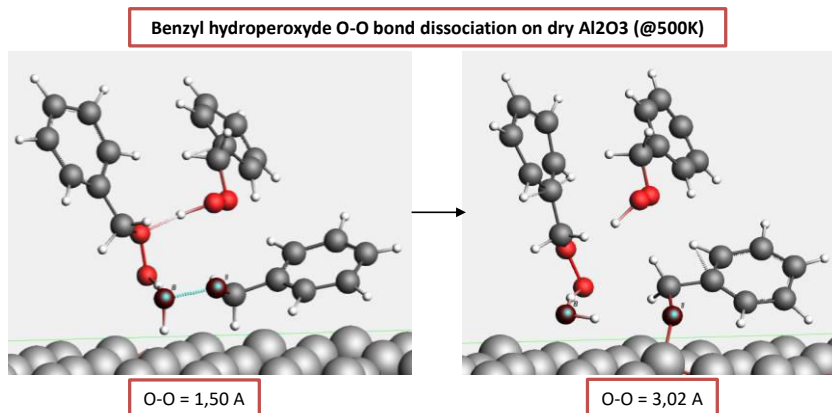
surface appears to facilitate the O-O pair breaking once the solute molecule strongly interacts with its metallic Al layer.

DFT calculations where the bond dissociation  $\text{-CO---OH}$  for a benzyl hydroperoxide occurs when it adsorbs on dry alumina showed that this process is very favored (giving a  $\Delta E_{\text{tot}} = -232.5$  kJ/mol).

The second solute-surface type of interaction is pictured instead in **Figure 99**, where this time we observed a different behavior compared to the previous case: here solute molecules are firstly interacting between them through H bonds established by their polar  $\text{-OOH}$  terminations, while at a certain point one of the polar head of a benzyl hydroperoxides bonds with a  $\text{Al}_s$  atom causing an instantaneous O-O bond breaking.



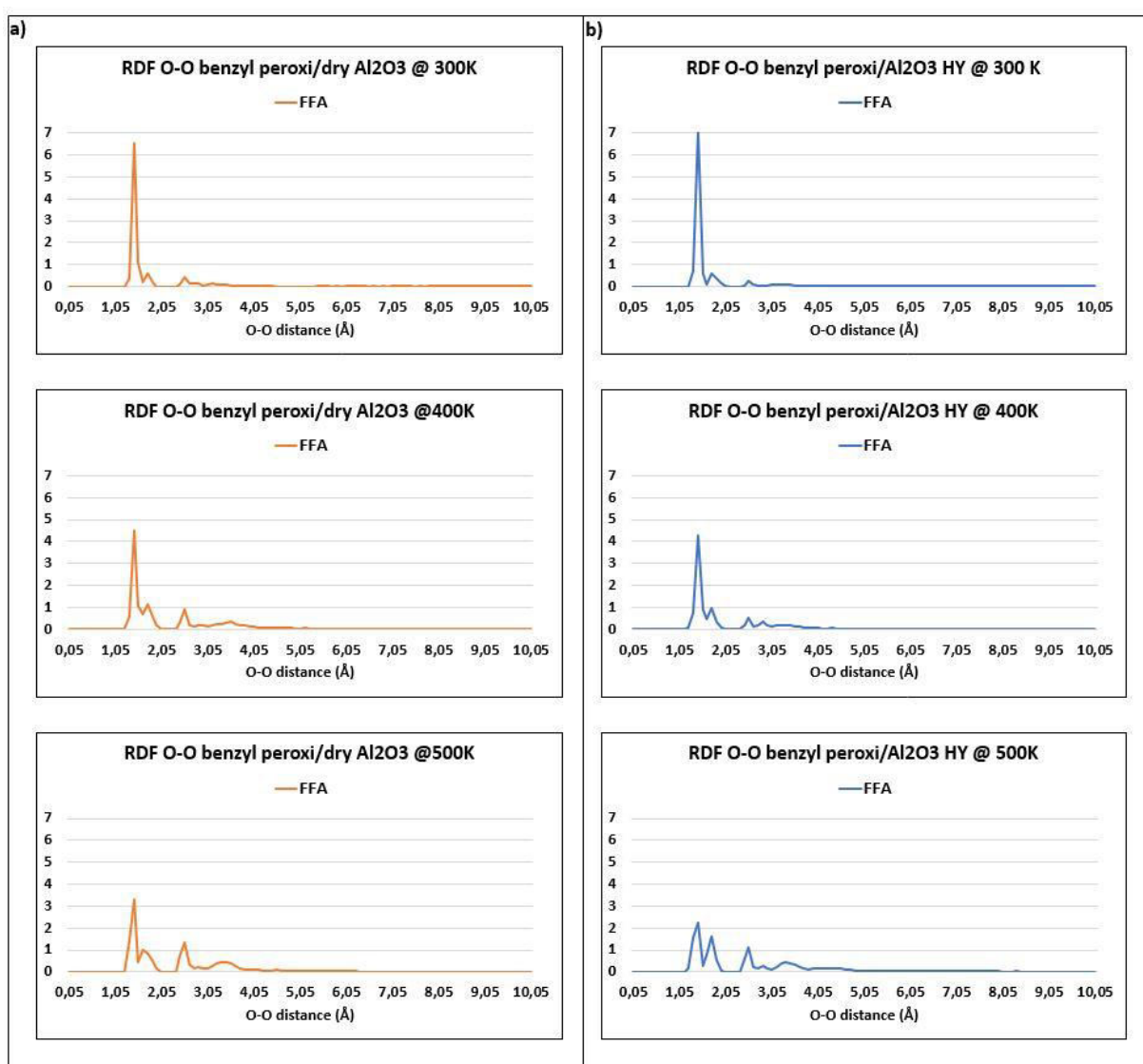
**Figure 98:** O-O bond dissociation for a benzyl hydroperoxide molecule on top of Al terminated surface layer of dry  $\text{Al}_2\text{O}_3$  (at 300 K).



**Figure 99:** O-O bond dissociation for a benzyl hydroperoxide molecule on top of Al terminated surface layer of dry  $\text{Al}_2\text{O}_3$  (at 500 K).

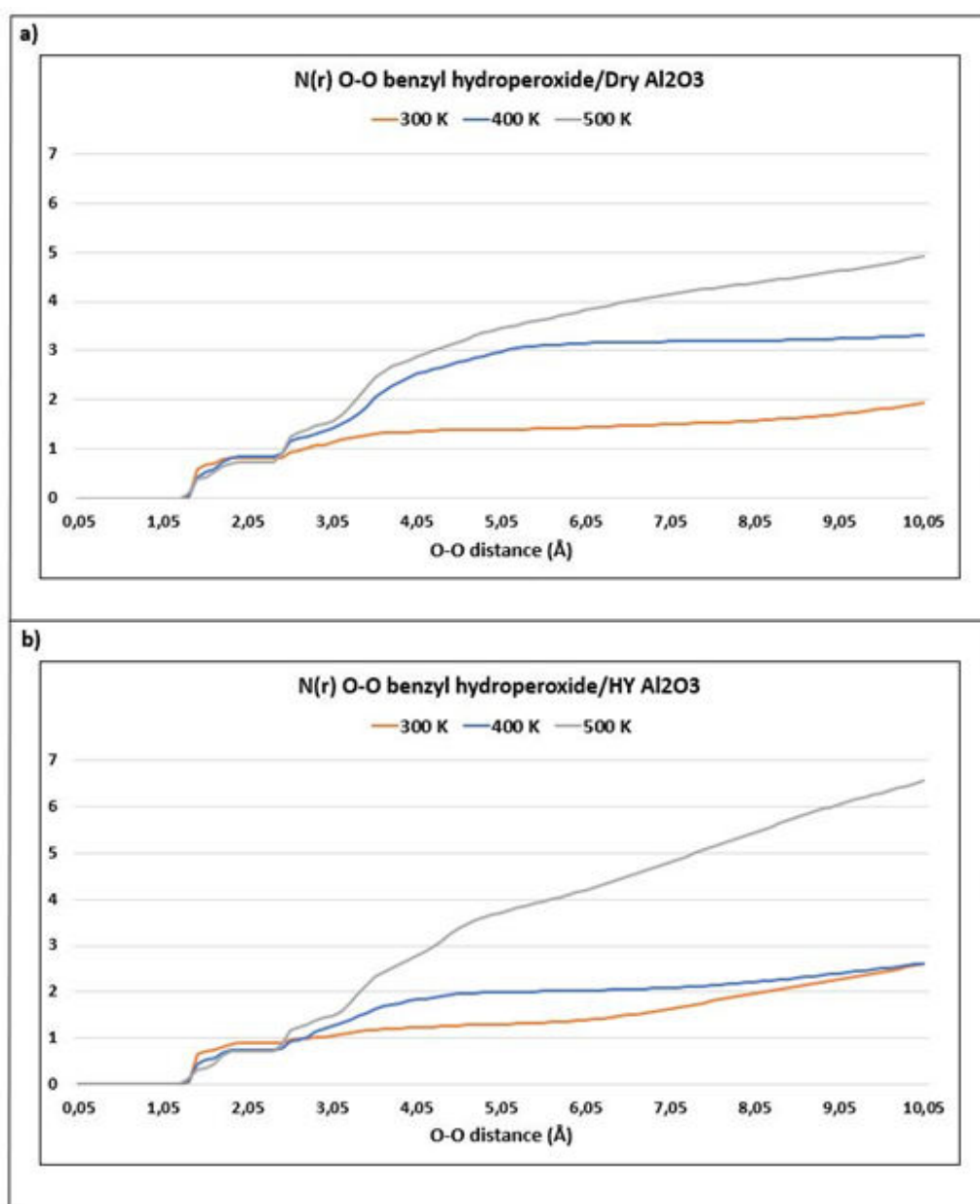
The major difference of this second case with the first one is that here the solute molecule that undergoes the O-O pair breaking comes from an already occurring solute-solute interaction (thus in the liquid phase), which could have “weakened” the O-O bond, causing an easier bond rupture for the benzyl hydroperoxide.

On the other hand, the discourse is different for the hydroxylated  $\text{Al}_2\text{O}_3$  system. In fact in this case, no bond dissociation was registered neither in the liquid phase nor above the surface. The -OH groups that are found above the surface come from the hydroxylated layer of the surface that start desorbing towards the reaching of 400 K.



**Figure 100: RDF plots for the O-O bond of benzyl hydroperoxides present in the liquid phase in a) the anhydrous case and b) the hydroxylated case for the three different T: 300 K; 400 K and 500 K.**

In **Figure 100** (top side) we observed that the behavior of the oxygenated solute molecules in the liquid medium is exactly the same as the one reported in **Figure 73a** for the liquid phase: we observe again the highest peak at the O-O distance of 1.5 Å. In this case, we can conclude that the benzyl hydroperoxides found in the liquid medium at distances  $> 10$  Å from the surface behave as in the bulk liquid.



**Figure 101:**  $N(r)$  plots for the O-O bond of benzyl hydroperoxides present in the liquid phase in a) the anhydrous case and b) the hydroxylated case for the three different  $T$ : 300 K; 400 K and 500 K.

This result is confirmed by plotting the integral of the  $g(r)$  (**Figure 101**), where at 300 K we found again an average of one benzyl hydroperoxide molecule in correspondence of 1.7-1.8 Å either in presence of the dry or hydroxylated alumina surface. It is also confirmed, integrating at higher distances, that the amount of benzyl hydroperoxide in the liquid phase is temperature dependent for each surface and is also surface-dependent, due to the accumulation of the benzyl hydroperoxide at the surfaces.

To discover what happens when benzyl hydroperoxides interact in the liquid medium, we plotted in **Figure 100** the RDF for the O-O pair of the benzyl hydroperoxides that are found in the liquid phase in both heterogeneous cases (in this case, the “liquid phase” is defined as the liquid at distance to the surfaces  $> 10\text{Å}$ ). For the cases taken at 300 K, we wanted to obtain a direct connection with the studied case of section **6.1.3**(bulk liquid).

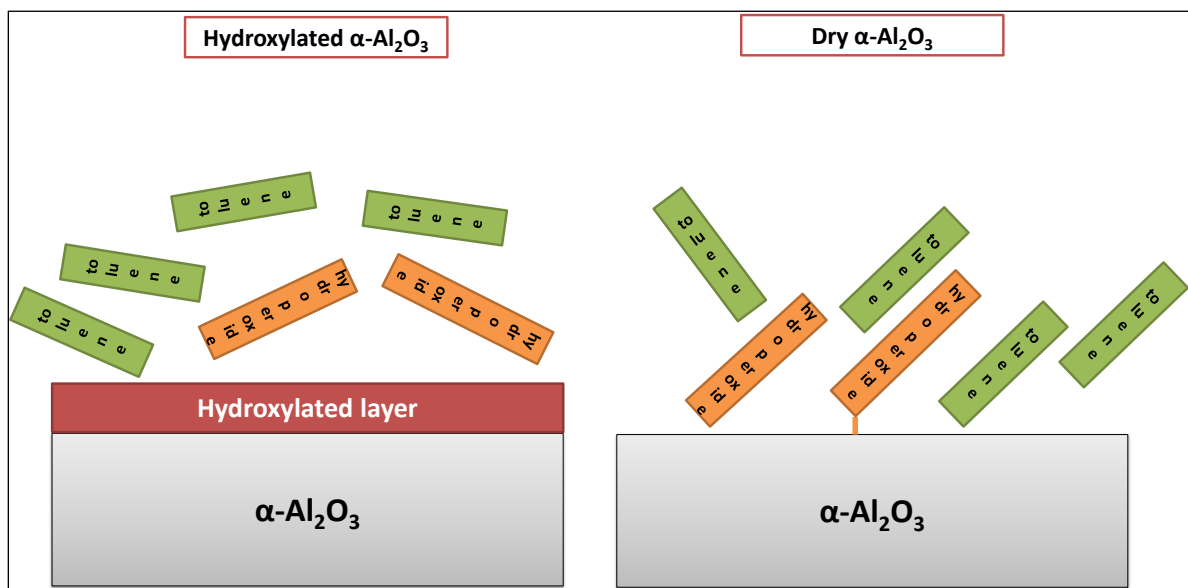
Another important aspect to highlight is that the formation of binary and ternary complexes due to the benzyl hydroperoxides interactions in the liquid phase were observed for both heterogeneous cases too (not reported), as was the case in the bulk liquid.

#### 6.4.5 Conclusion of ReaxFF study of liquid-phase “fuel-oxygen” mixture- $\text{Al}_2\text{O}_3$ system

In this section **6.4**, we presented the results of our MD study where we investigated the dynamic evolution of a liquid organic solution adsorbed above the alumina, either in its anhydrous or hydroxylated state. We summarize the main conclusions of these structural analyses as follows:

1. The toluene is structured at the surface in a monolayer (hydroxylated surface) and a bilayer (dry surface); the tilt angle of the molecules towards the surface differs, the toluene molecules on the anhydrous surface being tilted by  $45^\circ$  in average, whereas the tilt is  $30^\circ$  on the hydroxylated surface.
2. The consequence of this tilt angle is that for the dry surface, a second toluene layer is strongly adsorbed, as schematized in **Figure 102**.

3. The reason behind this difference lies in the difference in adsorption energy of toluene at the surface. We have already observed (**Chapter 5**) that the toluene-dry surface interaction induces the formation of a dense layer at the surface, and this is not the case on the hydroxylated surface. This trend is observed also at the liquid-solid interface, the toluene structuration being even reinforced with the formation of a dense bilayer at the dry surface. This is a nice example of the complexity of the balance of the difference of interaction at the atomic scale that induce different structuration patterns. This study also allows us to make a bridge from the gas-surface interaction to the liquid-surface interaction, and how the properties observed in the first system are maintained and adapted in the second one.
4. The hydroperoxides tend to aggregate at the surfaces, again this effect being more marked for the anhydrous surface, where it seems that the toluene bilayer structure also induces the presence of peroxide in a bilayer structure. We also notice the tendency of peroxides to form aggregates. It seems that there are less aggregates in the liquid phase on the dry surface, due to the highest tendency to adsorb at the surface. This preliminary results must however be confirmed/informed on larger systems.
5. The hydroperoxide molecules react with the alumina dry surface and not with the hydroxylated surface.
6. The behavior of the benzyl hydroperoxides in the liquid medium is the same as the one observed for the homogeneous case in section **6.1.3**, meaning that no bond dissociations occur when the solute molecules interact between each other.
7. The benzyl hydroperoxide clusterisation in the liquid medium provokes the formation of binary and ternary complexes that resemble aggregate precursors and this is observed even in case of the surface presence.



**Figure 102:** Simplified scheme of the toluene molecule layers and tilt angles on the hydroxylated alumina surface (on the left) and on dry alumina surface (on the right).

## 6.5 Conclusions

In this chapter, we reported the analyses and results of our ReaxFF study where the dynamic behavior of a model liquid “fuel-oxygen” solution was investigated in two main instances: a) when this liquid organic solution is isolated (e.g. homogeneous phase) and b) when this liquid organic solution is put in contact with the alumina surface either in anhydrous or hydroxylated conditions. The composition of this organic solution is the following: 95% mol toluene (e.g. solvent) and 5% mol benzyl hydroperoxide (e.g. solute).

Our main objective was to verify if our validated force field FFA was able to “capture” and describe accordingly the possible phenomena occurring in a slightly oxidized liquid fuel blend either when treated as a solution at ambient conditions (section 6.1) or when interacting with a metallic substrate such as aluminium covered with an oxide layer (sections 6.3-6.4). In addition, the adsorption/desorption behavior of the water layer characterizing the alumina in its hydroxylated state up to 500 K was also examined via FFA (section 6.2).

In section 6.1, we investigated via ReaxFF the behavior of the liquid oxidized fuel at ambient condition through the implementation of the NPT ensemble. We created a simulated box that

would correspond to a liquid density of  $0.87 \text{ g/cm}^3$  (i.e. the experimental toluene density at ambient T and P). We found that FFA reproduced quite accordingly the liquid density of the organic solution, giving a liquid density of  $0.96 \text{ g/cm}^3$ . We calculated a  $\Delta\rho_l\% = 9\%$  between the experimental and simulated liquid densities, which we considered as a good estimation. We also provided a study of the benzyl hydroperoxides reactivity in the organic medium, where we found that no bond dissociation is register at 300 K (either for O-O or C-O intramolecular bonds). However, formation of aggregates precursors starting from benzyl hydroperoxides clusterisation was observed already at ambient conditions in 312.5 ps of time calculation.

From the homogeneous conditions, we proceeded towards the study of the heterogeneous cases, starting from the MD study of the alumina hydroxylated surface when heated from 1 K to 500 K (section 6.2). From this analysis, we found that heating the hydroxylated  $\text{Al}_2\text{O}_3$  surface up to 500 K induces an increased degree of freedoms of the surface OH groups and, in addition, some of the dissociated water (terminal OH plus H on surface  $\text{O}_s$ ) get molecular at temperature above 270 K. Our results are in good agreement with the work of Hass et al. [9], where they remarked “premature” event of some water molecule “desorption” and diffusion at the hydroxylated surface was observed already by at 300 K.

In section 6.3, we investigated via NVT simulations the behavior of small droplets of liquid oxidized fuel adsorbed on  $\text{Al}_2\text{O}_3$  surface in two thermal regimes: a first regime of heating from 1 K to 400 K and a second constant T regime at 400 K. For the dry  $\text{Al}_2\text{O}_3$  surface, we found that a dense monolayer of toluene is formed during the heating stage and it remained stable at constant  $T = 400 \text{ K}$ . Complementary DFT BOMD simulations confirmed this result. For the hydroxylated  $\text{Al}_2\text{O}_3$  surface, no toluene layer formed when heating or during the plateau at 400 K, showing an average toluene coverage of 0.2 ML at 400 K with significant surface diffusion of the molecules. We attributed this different behavior to the differences in adsorption energies of toluene on dry and hydroxylated  $\alpha\text{-Al}_2\text{O}_3$ .

Finally in section 6.4, we investigated via NPT simulations the behavior of the liquid oxidized fuel adsorbed on  $\text{Al}_2\text{O}_3$  surface in four sequential T regimes: a) a first heating phase from 300 to 400 K, b) constant T regime at 400 K, c) a second heating phase from 400 to 500 K and d) a final constant T regime at 500 K. To better comprehend the reactivity of the solute molecules in this

section, we decided to distinguish two instances: a) solute/surface interactions and b) solute/solute interactions in the liquid medium.

For the first instance, the NPT simulations showed a toluene structuration as a monolayer for the hydroxylated  $\text{Al}_2\text{O}_3$  surface and as bilayer for the dry  $\text{Al}_2\text{O}_3$  surface. Similar to conclusion from the previous section **6.3**, we again attributed the reason behind this discrepancy to different adsorption energies of toluene on the two surfaces. For the solute molecules, we found an aggregation tendency for the benzyl hydroperoxides at the anhydrous alumina surface, where they were found to react with the terminal surface  $\text{Al}_s$  atoms. However, such aggregation and reactivity tendencies were not observed for the hydroxylated case. This preliminary study suggests that the degree of hydroxylation of the aluminium surface plays a key role in the aggregation at the surface of compounds of oxidation.

For the second instance, we studied the behavior of the benzyl hydroperoxides in their liquid medium in order to find a connection with the case reported in section **6.1.3**. What we found was that, even in the presence of the alumina surface, the benzyl hydroperoxides interacting in the organic medium at 300 K behave exactly in the same manner as when we only have the liquid phase as in section **6.1.3**: no bond dissociation is registered at 300 K and the formation of aggregate precursors was again observed also for the heterogeneous cases. This behavior of the benzyl hydroperoxides in the organic medium is conserved also for the 400 – 500 K thermal range.

## References

- 1 Mielczarek D.C., Matrat M., Amara A.B., Bouyou Y., Wund P., Starck L. Toward the Accurate Prediction of Liquid Phase Oxidation of Aromatics: A Detailed Kinetic Mechanism for Toluene Autoxidation, *Energy Fuels***31**, 11 (2017), 12893–12913. DOI: 10.1021/acs.energyfuels.7b00416.
- 2 J.A.A. Hoorn, P.L. Alsters, G.F. Versteeg A Kinetic Model for Toluene Oxidation Comprising Benzylperoxy Benzoate Ester as Reactive Intermediate in the Formation of Benzaldehyde, *International Journal of Chemical Reactor Engineering***3** (2005).
- 3 Hermans I., Peeters J., Vereecken L., Jacobs P.A. Mechanism of thermal toluene autoxidation, *Chemphyschem : a European journal of chemical physics and physical chemistry***8**, 18 (2007), 2678–2688. DOI: 10.1002/cphc.200700563.
- 4 da Silva G., Hamdan M.R., Bozzelli J.W. Oxidation of the Benzyl Radical: Mechanism, Thermochemistry, and Kinetics for the Reactions of Benzyl Hydroperoxide, *Journal of chemical theory and computation***5**, 12 (2009), 3185–3194. DOI: 10.1021/ct900352f.
- 5 da Silva G., Bozzelli J.W. Kinetic modeling of the benzyl+HO<sub>2</sub> reaction, *Proceedings of the Combustion Institute***32**, 1 (2009), 287–294. DOI: 10.1016/j.proci.2008.05.040.
- 6 W.M. Haynes *CRC handbook of chemistry and physics: A ready-reference book of chemical and physical data*, CRC Press, Boca Raton, Fla. (2013).
- 7 Martyna G.J., Tuckerman M.E., Tobias D.J., Klein M.L. Explicit reversible integrators for extended systems dynamics, *Molecular Physics***87**, 5 (1996), 1117–1157. DOI: 10.1080/00268979600100761.
- 8 W. G. Hoover, B. L. Holian Kinetic moments method for the canonical ensemble distribution, *Phys. Rev. A (Physical Review A)***211** (1996), 253–257. DOI: 10.1016/0375-9601(95)00973-6.
- 9 Hass, Schneider, Curioni, Andreoni The chemistry of water on alumina surfaces: reaction dynamics from first principles, *Science (New York, N.Y.)***282**, 5387 (1998), 265–268. DOI: 10.1126/science.282.5387.265.
- 10 Tao J., Wang X., Han Z., Feng B., Xue L. Selection of solvent for the mechanical activation process: A molecular dynamics simulation and experiment study, *Surf Interface Anal***49**, 11 (2017), 1147–1152. DOI: 10.1002/sia.6294.

## General conclusions and Perspectives

The objective of this thesis was to better understand the phenomenology related to the formation of deposits produced by the autoxidation process that occurs for fossil and renewable fuels and the impact of the material in contact with the fuel.

To achieve this goal, a methodology combining two different numerical approaches was adopted: an ab initio study conducted via Density Functional Theory (DFT) and a successive empirical Molecular Dynamics (MD) approach carried out via the implementation of a reactive force field (ReaxFF). The preliminary theoretical DFT study was carried out to acquire useful energetic data (i.e. reaction and adsorption energies) from the geometry optimization of gas-phase and gas/solid systems of interest, with the intention to use them as input data to train the empirical reactive force field. The objective was to optimize and validate the reactive force field so that it would be able to correctly predict the behavior of the chemical species involved, in both homogeneous and heterogeneous phases. Once validated, MD simulations implementing the validated ReaxFF were carried out, with the objective to obtain useful insights into the adsorption and deposition processes while considering the degradation/oxidation phenomena occurring in the fuel liquid phase.

From our DFT study (**Chapter 4**), we acquired important notions in regards of the deposits reactivity either in their gas-phase or when they are adsorbed above aluminum and stainless steel surfaces. From the homogeneous gas-phase study, we obtained the reaction energies of a set of representative reactions describing the toluene autoxidation, while from the heterogeneous gas/solid study, we obtained the adsorption energies of small representative organic molecules (i.e. models of deposit precursors) on  $\alpha$ -Al<sub>2</sub>O<sub>3</sub> and  $\alpha$ -Cr<sub>2</sub>O<sub>3</sub> surfaces (i.e. representatives of aluminum and stainless steel surfaces). Both anhydrous and hydrated surface states were considered in our study. From this study, the scrutinized trend of the adsorption strength on dry surfaces is the following: oxygenated molecules > aromatics > linear alkanes. The alumina surface was found more reactive than the chromia surface. The adsorption on the two hydroxylated surfaces were of similar characteristics, but for alumina a net difference in reactivity between the dry and hydroxylated surface was considerably more pronounced, pointing to the influence of the surface state on the adhesion properties.

In our ReaxFF study (**Chapter 5**) we carried out a ReaxFF study centered on the reparametrization and validation of two different force fields, one describing alumina-based systems (FFA) and the other chromia-based systems (FFB).

The two force field optimizations were evaluated through the reproduction of the data in the training set used to reparametrize the force fields. Next, the quality of the FF was evaluated through the reproduction of data from a validation set (data that are not included in the training set), including the reproduction of the cell parameters of the bulk oxides, adsorption energies of organic molecules, representative reactions of the autoxidation of toluene, and the dynamic structuration of pure organic liquids (mass/volume density, radial distribution functions). At the end of this study, FFA (for alumina-based systems) was validated, but not FFB for chromia-based systems. For this reason, we decided to retain for our production study only the FFA force field.

In our ReaxFF production study (**Chapter 6**), we conducted MD studies where the dynamic behavior of a model liquid “fuel-oxygen” solution, composed of 95% mol toluene and 5% mol benzyl hydroperoxide, was investigated in two main instances: a) when this liquid organic solution is isolated (e.g. homogeneous phase) and b) when this liquid organic solution is put in contact with the alumina surface either in anhydrous or hydroxylated conditions. Our main objective was to verify if FFA was able to “capture” and describe accordingly the possible phenomena occurring when examining the model blend as a solution at ambient conditions (section **6.1**), when put on the alumina surface at the solid-gas interface (section **6.3**), or when interacting with a metallic substrate such as aluminium covered with an oxide layer at the solid-liquid interface (section **6.4**). In addition, the adsorption/desorption behavior of the water layer characterizing the alumina in its hydroxylated state up to 500 K was also examined via FFA (section **6.2**).

In section **6.1**, we found that FFA reproduced quite well the liquid density of the organic solution (that we approximated with the toluene density at ambient conditions), giving a  $\Delta\rho_l\% = 9\%$  between the experimental and calculated value. We considered this difference between experimental and simulated densities as a good estimation. We also found that no bond

dissociation is registered from the benzyl hydroperoxides (section 4.3.1) at 300 K, neither for O-O nor C-O intramolecular bonds. However, formation of aggregates precursors starting from benzyl hydroperoxides clusterisation was observed already at ambient conditions.

Regarding the solid-gas interfaces, in section 6.2, we found that heating the hydroxylated  $\text{Al}_2\text{O}_3$  surface up to 500 K induces an increased degree of freedom of the surface OH groups and, in addition, some of the dissociated water (terminal OH plus H on surface  $\text{O}_s$ ) get molecular at temperature above 270 K. Our results are in good agreement with the work of Hass et al. [9], where they remarked “premature” event of some water molecule “desorption” and diffusion at the hydroxylated surface was already observed by at 300 K.

In section 6.3, we found that starting from a toluene “drop” at the surface, a dense monolayer of toluene is formed during the heating stage and it remained stable at constant  $T = 400$  K. Complementary DFT BOMD simulations confirmed this result. For the hydroxylated  $\text{Al}_2\text{O}_3$  surface, no toluene layer formed when heating or during the plateau at 400 K, showing an average toluene coverage of 20% at 400 K with significant surface diffusion of the molecules. We attributed this different behavior to the differences in adsorption energies of toluene on dry and hydroxylated  $\alpha\text{-Al}_2\text{O}_3$ .

In section 6.4, the solid-liquid interactions were captured with the MD conducted with FFA, thus considering the biofuel-alumina interface. To better comprehend the reactivity of the solute molecules in this section, we decided to distinguish two instances: a) solute/surface interactions and b) solute/solute interactions in the liquid medium (more than 10 Å from the surface). In the first instance, we observed a toluene structuration as a monolayer for the hydroxylated  $\text{Al}_2\text{O}_3$  surface and as bilayer for the dry  $\text{Al}_2\text{O}_3$  surface. As concluded from the previous section 6.3, we again attributed the reason behind this difference to different adsorption energies of toluene on the two surfaces. For the solute molecules, we found an aggregation tendency for the benzyl hydroperoxides on both surfaces. At the anhydrous alumina surface, they were found to react with the terminal surface  $\text{Al}_s$  atoms. However, these reactivity tendencies were not observed on the hydroxylated surface. This preliminary study suggests that the degree of hydroxylation of the aluminium surface plays a key role in the molecule-surface reactivity. In the second instance, we found that, even in the presence of the alumina surface, the benzyl hydroperoxides interacting in the organic medium at 300 K behave exactly in the same manner as when we only have the liquid

phase as in section **6.1.3**:no bond dissociation is registered at 300 K and the formation of aggregate precursors was again observed also for the heterogeneous cases. This behavior of the benzyl hydroperoxides in the organic medium is conserved also for the 400 – 500 K thermal range.

From this study, we have recognized that the combination of DFT and ReaxFF methods could be a valuable asset for further investigations of the aggregation/deposition phenomena occurring in the fuel liquid phase. We observed that the metallic aluminum surface does not influence per se the aggregation phenomena of the liquid phase, however it can cause the formation of an oxidized organic layer in case of anhydrous conditions.

However, our validated FFA force field need to be further tested and applied to bigger systems in terms of both atomic-size and simulation time. In this way, possible new reactions could be seen and a new prospective of the system reactivity could be envisaged. This statement is even more emphasized on the FFB force field, which need to be further reoptimized with new suitable data in order to achieve a validated form.

## Annexes

### Chapter 4

#### Bulk oxides

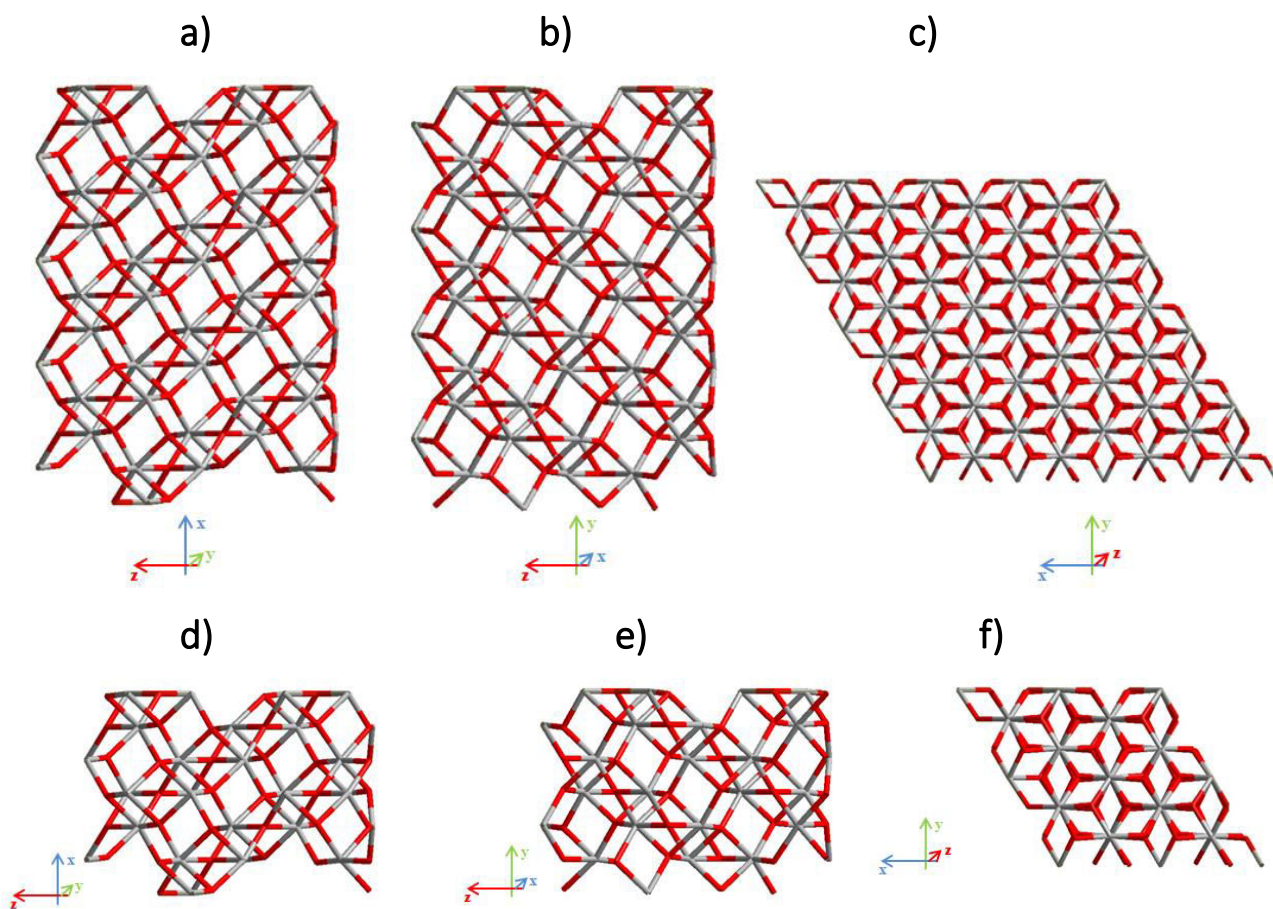
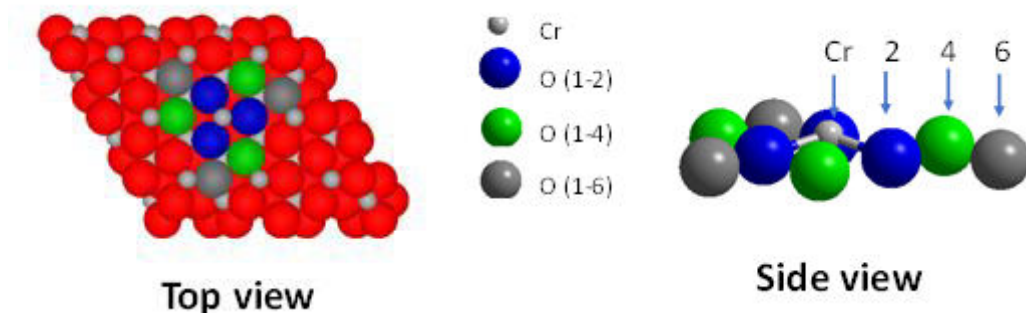


Figure A4-1: Slabs used to represent for the (0001) corundum surfaces: a-c) 4x4 cell; d-f): 2x2 cell. Grey: Al, Cr; red: O.



**Figure A4-2:** Nomenclature for adsorption and dissociation of protic molecules at corundum  $\text{Al}_2\text{O}_3$  and  $\text{Cr}_2\text{O}_3$  (0001) surfaces. Top-view of  $\text{Al}_2\text{O}_3$  or  $\text{Cr}_2\text{O}_3$  with a metal cation (grey) in the center of 3 oxygen atoms (blue). If the metal (Cr/Al) ion is considered at position 1, the blue (oxygen) atoms are at position 2, and the green (oxygen) at position 4.

**Table A4-1:** Calculated (VASP) versus experimental bulk structural parameters of  $\alpha\text{-Al}_2\text{O}_3$ .

	Bulk $\alpha\text{-Al}_2\text{O}_3$	
	d) Experimental <sup>[19]</sup>	e) Calc. Bulk DFT (this work)
<b>a = b (Å)</b>	4.76	4.79
<b>c (Å)</b>	12.99	13.07
<b>c/a (Å)</b>	2.73	2.73
<b>V (Å<sup>3</sup>)</b>	254.93	259.11
<b>Al-O<sub>1</sub> (Å)</b>	1.85 <sup>[20]</sup>	1.87
<b>Al-O<sub>2</sub> (Å)</b>	1.97 <sup>[20]</sup>	1.98

**Table A4-2:** Calculated (VASP) versus experimental bulk structural parameters of  $\alpha\text{-Cr}_2\text{O}_3$ .

	Bulk $\alpha\text{-Cr}_2\text{O}_3$	
	d) Experimental <sup>[21]</sup>	e) Calc. Bulk DFT (this work)
<b>a = b (Å)</b>	4.95	5.07
<b>c (Å)</b>	13.57	13.85
<b>c/a (Å)</b>	2.74	2.73
<b>V (Å<sup>3</sup>)</b>	-	308.75
<b>Cr-O<sub>1</sub> (Å)</b>	-	2.05
<b>Cr-O<sub>2</sub> (Å)</b>	-	2.01

## Comparison between Gaussian and VASP results for the reaction energies

In section 4.3.2, the values of the reaction energies calculated with the M06-2X functional have been reported. Below, we report these aforementioned reaction energies results with the corresponding values calculated in this case through the implementation of the PBE-GGA functional (VASP).

**Table A4-3: Comparison of the reaction energies  $\Delta E_r$ (kJ/mol) between the adopted M06-2X functional (Gaussian 16) and the PBE-GGA functional (VASP).**

Reaction label	Reactions	$\Delta E_r$ Gaussian (M06-2X) (kJ/mol)	$\Delta E_r$ VASP (PBE-GGA) (kJ/mol)
R1	$(C_6H_5)CH_2O_2H + (C_6H_5)CH_2^\circ \rightarrow (C_6H_5)CH_3 + (C_6H_5)CH_2O_2^\circ$	-31	-33.4
R2	$(C_6H_5)CH_2O_2H \rightarrow (C_6H_5)CH_2O^\circ + HO^\circ$	232.4	194.7
R3	$(C_6H_5)CH_2O_2H \rightarrow (C_6H_5)CH_2O_2^\circ + H^\circ$	353	374.4
R4	$(C_6H_5)CH_2O_2H \rightarrow (C_6H_5)CH_2^\circ + HO_2^\circ$	230.3	264.0
R5	$(C_6H_5)CH_2O_2H \rightarrow (C_6H_5)CH_2^\circ + H^\circ + O_2$	561.5	638.3
R6	$(C_6H_5)CH_2O_2H + HO_2^\circ \rightarrow (C_6H_5)CH_2O_2^\circ + H_2O_2$	-6.7	-2.7
R7	$(C_6H_5)CH_2O_2H + HO_2^\circ \rightarrow (C_6H_5)CH_2^\circ + H_2O_2 + O_2$	201.8	261.2
R8	$(C_6H_5)CH_2O_2^\circ \rightarrow (C_6H_5)CH_2^\circ + O_2$	206.4	263.9
R9	$HO_2^\circ \rightarrow O_2 + H^\circ$	331.2	374.4

From **Table A4-3** above, we can observe that the majority of the reaction energies are very similar when comparing the use of the two different functionals, at the exception of the R2 and R5, where a huge energetic gap can be seen between these two reactions.

## Water/OH substitution on corundum surfaces

**Table A4-4: Energy decomposition for water/OH substitution by methyl propionate/acetate on hydroxylated  $Al_2O_3$  and  $Cr_2O_3$  (kJ/mol)**

System	Water desorption (kJ/mol) Equation 84	Binding energy molecule/surface (kJ/mol) Equation 85	Erelax (kJ/mol) Equation 86	Substitution energy (kJ/mol) Equation 83	$\Delta E(Al_2O_3-Cr_2O_3)$ (kJ/mol)
Methyl propionate@ $Al_2O_3$ -HY	54.6	-46.6	9.0	17	51.7
Methyl propionate@ $Cr_2O_3$ -HY	22.6	-62.6	5.4	-34.7	

Acetic acid@ Al <sub>2</sub> O <sub>3</sub> -HY	54.6	-285.1	213	-17.5	26.3
Acetic acid@ Cr <sub>2</sub> O <sub>3</sub> -HY	22.6	-307.18	240.8	-43.8	

We observe that the substitutive adsorption of methyl propionate and acetic acid are favored on Cr<sub>2</sub>O<sub>3</sub> over Al<sub>2</sub>O<sub>3</sub>. This can be explained by the decomposition of the energy: firstly, water desorption is less endothermic for Cr<sub>2</sub>O<sub>3</sub> than Al<sub>2</sub>O<sub>3</sub>; secondly, the binding energy of MP is slightly stronger for Cr<sub>2</sub>O<sub>3</sub>; thirdly, the relaxation energies are practically equivalent for both surfaces.

We note in the case of acetate adsorption, both a strong molecule-surface interaction and a strong component of the relaxation energy to accommodate the adsorbed anion.

## Thermodynamic data

**Table A4-5: Energy, ZPE contribution, Free energy and Entropy contributions of the free molecules**

Molecule	E <sub>EZPE</sub>	G-(E <sub>SCF</sub> +E <sub>ZPE</sub> )	S <sub>tot</sub>	S <sub>trans</sub>	S <sub>rot</sub>	S <sub>vib</sub>	S <sub>elec</sub>
	(Hartree)	(Hartree)	(cal/K.mol)	(cal/K.mol)	(cal/K.mol)	(cal/K.mol)	(cal/K.mol)
acetaldehyde	0.055205	-0.024933	62.655	37.273	21.639	3.744	0
propane	0.102984	-0.025003	64.139	37.275	21.311	5.552	0
oxirane	0.150382	-0.033482	90.23	39.306	26.871	22.676	1.377
ethanol	0.079745	-0.025375	64.412	37.406	22.313	4.692	0
toluene	0.127346	-0.030587	79.441	39.471	26.976	12.993	0
acetic acid	0.061692	-0.0271	68.594	38.196	23.846	6.551	0
benzene	0.100151	-0.027459	69.026	38.979	25.65	4.397	0
methyl-3-trans-hexanoate	0.178943	-0.037844	104.663	40.456	29.879	34.328	0
methylacrylate	0.094708	-0.030746	80.689	39.27	26.595	14.824	0
acetone	0.083122	-0.029398	75.383	38.096	24.147	13.139	0
methylpropionate	0.117702	-0.031456	83.6	39.339	26.78	17.481	0
water			74.247	42.55	7.21	0.05	0

## Desorption temperature calculations

To further confirm the trends observed in the previous paragraphs for the molecules interactions on alumina and chromia surfaces, we decided to calculate the desorption temperatures ( $T_{\text{des}}$ ) for all the molecules on the two substrates either in their anhydrous and hydrated states, respectively.

### Computational details

The thermochemical calculations for the obtention of the  $T_{\text{des}}$  values were performed with Gaussian 16 [1]. The desorption temperatures  $T_{\text{des}}$  were calculated using the thermodynamic corrections of the molecules in the gas phase, while for the heterogeneous systems “slab+molecule” only the electronic energies were used.

Finally, using atomistic thermodynamics allows us to evaluate the free energy of adsorption at temperatures above 0 K, and we introduce the thermodynamics data for the molecule in the gas phase, as explained in ref. [24]. The  $\Delta G$  value of the system is given by:

$$\Delta G = \Delta E + \Delta \mu$$

Equation 88

Where  $\Delta \mu$  is the chemical potential of gaseous molecule. The thermodynamic data ( $H(T)$  and  $S(T)$ ) are calculated with the Gaussian 16 code [1] for the free molecule.

Upon considering the general desorption reaction:



Equation 89

At thermal equilibrium between the gas phase and the adsorbed molecule, we can write that

$$\Delta G_{\text{desorp}} = \Delta H_{\text{desorp}} - T \Delta S_{\text{desorp}} = 0$$

Equation 90

We now make three key assumptions:

- 1)  $\Delta H_{\text{desorp}} \approx \Delta E_{\text{desorp}}$ . In other words, the corrections (zero-point energy, translational, rotational and vibration internal energies and PV corrections) are equal for reactant and product.
- 2) Upon adsorption of the organic molecule, the entropic contributions for translation and rotation become zero. Thus:

$$\Delta S_{\text{desorption}}^{\text{transl.}} = S_{\text{molecule gazphase}}^{\text{transl.}} - S_{\text{molecule adsorbed}}^{\text{transl.}} = S_{\text{molecule gazphase}}^{\text{transl.}} - 0$$

**Equation 91**

and

$$\Delta S_{\text{desorption}}^{\text{rot.}} = S_{\text{molecule gazphase}}^{\text{rot.}} - S_{\text{molecule adsorbed}}^{\text{rot.}} = S_{\text{molecule gazphase}}^{\text{rot.}} - 0$$

**Equation 92**

- 3) Entropic contributions from the vibrations modes of the organic molecules remain constant upon adsorption so  $\Delta S_{\text{desorp}}^{\text{vib}} = 0$

These three assumptions allow us to write:

$$\Delta G_{\text{des}} = \Delta H_{\text{des}} - T_{\text{des}} \Delta S_{\text{des}} = 0$$

**Equation 93**

$$\Delta H_{\text{des}} = T_{\text{des}} \Delta S_{\text{des}} = \Delta E_{\text{des}}^{\text{electronic}} = T_{\text{des}} (\Delta S_{\text{des}}^{\text{transl.}} + \Delta S_{\text{des}}^{\text{rot.}} + \Delta S_{\text{des}}^{\text{vib.}})$$

**Equation 94**

Solving for  $T_{\text{des}}$ :

$$T_{\text{des}} = \frac{\Delta E_{\text{des}}^{\text{electronic}}}{\Delta S_{\text{des}}^{\text{transl.}} + \Delta S_{\text{des}}^{\text{rot.}} + \Delta S_{\text{des}}^{\text{vib.}}} = \frac{\Delta E_{\text{des}}^{\text{electronic}}}{S_{\text{mol. gas phase}}^{\text{transl.}} + S_{\text{mol. gas phase}}^{\text{rot.}} + 0}$$

**Equation 95**

Consequently, we avoid the time-consuming vibrational frequencies calculations for the systems in which the organic molecule is adsorbed on the slab.

Ideally, the entropic contributions should be calculated at the desorption temperature, but here we used the values at 298 K and 1 atm.

## Results and discussion

We also considered the free energies of the molecules in the gas phase and deduced the desorption temperature from the surface which results are reported in **Table A4-6**. The gas phase molecular thermochemical data are reported in **Table A4-5**.

**Figure A4-3** reports the desorption temperature from the hydroxylated surface with respect to the anhydrous one. The left-upper zone corresponds to molecules that have more affinity for the hydroxylated than the anhydrous surface. The right lower zone corresponds to molecules that have more affinity with the anhydrous surface than with the hydroxylated one, and the zone near  $y = x$  to molecules that have equivalent affinity with the dry and hydroxylated surfaces. On  $\text{Al}_2\text{O}_3$  molecules (especially oxygenated molecules) stick predominantly on the anhydrous  $\text{Al}_2\text{O}_3$  surface until elevated temperatures (500-600 K), whereas most molecules are expected to detach from the  $\text{Cr}_2\text{O}_3$  surface at temperature above RT, independantly on the surface state (hydroxylated versus anhydrous).

The present results suggest that at temperatures of the injection system, around 500 K, the stainless steel surface should be free of residual molecules, but the aluminium surface could be contaminated with water and some oxygenated molecules. Obviously in the operating conditions, the chemical potentials of the diverse species have also to be considered in the thermochemistry evaluations and some species could be further stabilized at the surface.

It is interesting to compare the adsorption of the different molecules with that of water. We calculate water desorption temperatures around 750 K for  $\text{Al}_2\text{O}_3$  and 450 K for  $\text{Cr}_2\text{O}_3$ . This allows us to identify the molecules susceptible to substitute water at the surface. The results suggest that only acetic acid, which desorption temperature is as high as water, is susceptible to compete with water adsorption on chromia.

Molecule	Tdesorb Al <sub>2</sub> O <sub>3</sub> (K)	Tdesorb Al <sub>2</sub> O <sub>3</sub> -HY (K)	Tdesorb Cr <sub>2</sub> O <sub>3</sub> (K)	Tdesorb Cr <sub>2</sub> O <sub>3</sub> -HY (K)	
propane	181.3	129.9	165.4	158.7	
benzene	249.9	185.8	178.4	244.1	
toluene	309.3	219.3	204.9	193.2	
water	759.6	192.3	452.4	192.3	
acetaldehyde	458.5	172.6	258.7	147.3	
acetone	485.8	181.8	274.4	268.7	
methylacrylate	550.3	185.6	266.2	260.8	
hexenoate	554.8	236.4	315.0	247.5	
methylpropionate	586.5	228.3	317.7	291.3	
ethanol	599.3	162.2	220.3	187.9	
oxirane	620.7	202.4	289.6	161.7	
acetic-acid	751.5	197.0	464.3	228.3	

Table A4-6: Desorption temperature (K) calculated for the different molecules adsorbed on the M<sub>2</sub>O<sub>3</sub>, dry and hydroxylated.

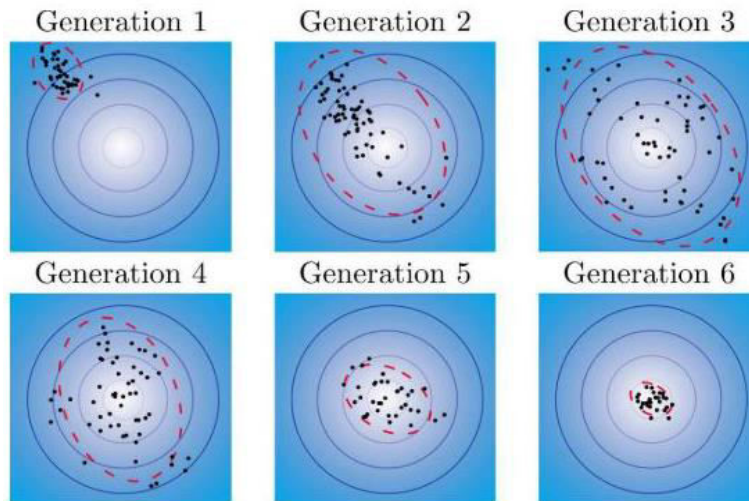
Figure A4-3: Desorption temperature on hydroxylated surfaces with respect to the anhydrous surfaces. The y = x line is plotted for a guide to the eye. Black : Cr<sub>2</sub>O<sub>3</sub>, grey : Al<sub>2</sub>O<sub>3</sub>.

## Chapter 5

### CMA-ES algorithm

In section 2.11.3 we have described the major features of the adopted FF optimizer used in this thesis, namely the CMA-ES algorithm. However, more specific details regarding this algorithm will be described in this following paragraph.

The CMA-ES algorithm is part of what are known as the “evolution strategies” approaches, which are stochastic methods adopted for the optimization of non-linear or non-continuous problems.



**Figure A5-1:** Illustration of CMA-ES algorithm. Small values of the cost function are represented in light colors. Image taken from ref. <sup>1</sup>.

**Figure A5-1** resumes the principles according to which the CMA-ES algorithm is based on:

- i. At the start, a random population is generated from the normal distribution (see the ellipses in **Figure A5-1**).
- ii. The error function  $f(x)$  is computed for all the points of the random population.

---

<sup>1</sup>Tan U., Rabaste O., Adnet C., Ovarlez J.-P. On the Eclipsing Phenomenon with Phase Codes 1–5, 2019 International Radar Conference (RADAR); DOI: [10.1109/RADAR41533.2019.171349](https://doi.org/10.1109/RADAR41533.2019.171349)

- iii. **Selection step:** the best random population candidates (i.e. with lower  $f(x)$ ) are selected and this step is followed by an “update” of the normal distribution parameters.
- iv. **Generation step:** from this distribution, a new population is generated.
- v. This process is repeated until the convergence of the algorithm.

In the merits of the FF optimization, the “population” to which we are referring to in the above description are the ReaxFF training-set parameters.

Among the main advantages of the CMA-ES algorithm we can recognize a good reliability for the local minima and global optimizations. Instead, as main disadvantage we have that the CMA-ES can be rather imprecise in the case of a single optimization run since this occurrence can present a higher risk of obtaining parameters with high errors.

## Binding energy calculations: dissociation curves

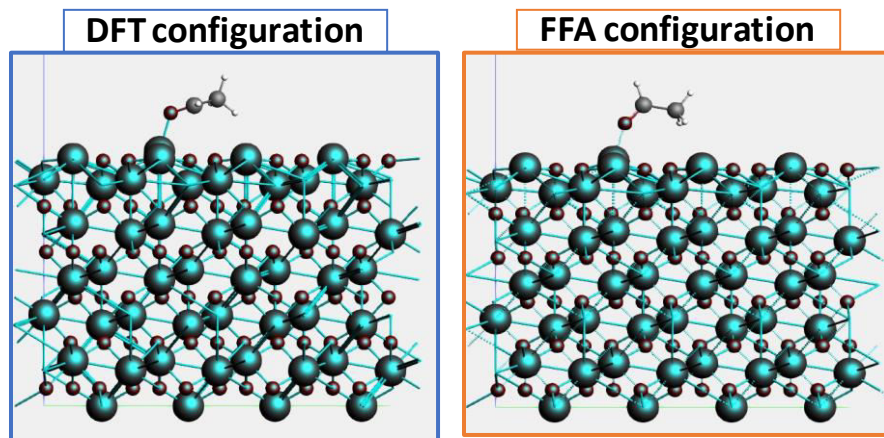
In section , we reported the calculated binding energies between the model molecules and the dry alumina surface. Here in this section, we describe in further detail each one of the energetic terms.

To calculate the binding energy  $E_{binding}$  we have considered the three following terms:

- $E_{ads_{mol}^*}$ : energy of the optimized fixed surface when considering the rigid z coordinate with the relaxed molecule.
- $E_{surface^*}$ : energy of the optimized fixed structure of the dry alumina surface.
- $E_{mol}$ : energy of the optimized molecule in the gas phase.

We chose to calculate the binding energies in this manner because our objective was to observe the molecular distortion when the molecule/surface bond has been fixed with the surface.

Below we report a clear example of this behavior, where we compared the optimized configurations of the acetaldehyde adsorbed on the dry alumina surface obtained with VASP and with FFA, respectively.



**Figure A5-2:** Optimized configurations of the acetaldehyde adsorption on dry  $\alpha$ -alumina calculated via DFT (blue square) and via FFA (orange square).

In **Figure A5-2** we can see that the major difference between the two cases is given by the rotation of the molecule obtained when simulating with FFA force field (on the right) from its original configuration (i.e. DFT result on the left), which did not translate into a huge gap in terms of binding energies values calculated with the two different approaches (see **Figure 63**).

## Preliminary ReaxFF study

### 5.1 First “static” test: adsorption energies

The first step was to verify if FF0 was able to describe our DFT optimized configurations (Chapter 4), so carried out geometry optimizations with AMS2019 [7] through the implementation of FF0 and consequently compare them with our DFT results. However, in this first stage we decided to consider only configurations related to the hydroxylated  $\alpha$ -Cr<sub>2</sub>O<sub>3</sub>, since this surface was not considered in the ReaxFF parametrization in the work [6].

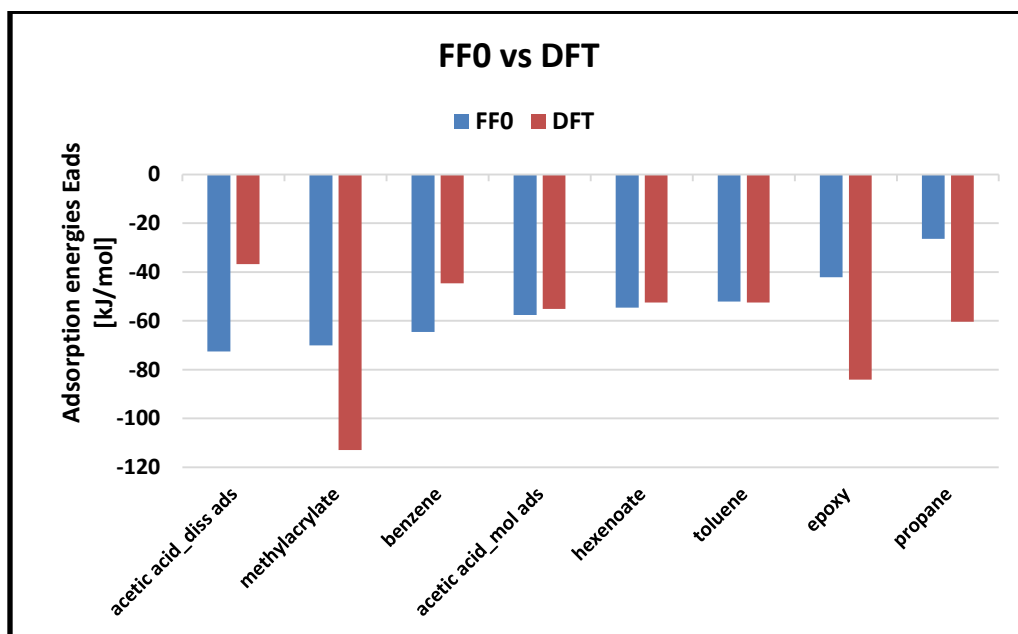
#### 5.1.1 Computational details

The FF0 geometry optimization were carried out with AMS2019 [7] using the implementation of the “Fast Inertial Relaxation Engine” (FIRE) algorithm [8]. The cartesian coordinates were optimized and the following convergence criteria were selected: a gradient and energy

convergence criterion of  $2.625 \text{ kJmol}^{-1}/\text{\AA}$  and of  $0.02625 \text{ kJmol}^{-1}$  respectively (both coinciding with the AMS2019 default values). The maximum number of steps was set to 5000 for the adsorption configurations and 1000 steps for the single molecules.

### 5.1.2 Results and discussion of the 1<sup>st</sup> static test

**Figure A5-3** below shows the comparison between the optimized configurations obtained with FF0 and some of the DFT results shown in **Chapter 4**. We can notice that certain molecules are well described by FF0 (e.g. the acetic acid in its molecular adsorption, the methyl-3-trans-hexenoate and the toluene), i.e. the difference between DFT and FF0 result is less than 20%, while others are either overestimated by FF0 (e.g. the acetic acid in its dissociated configuration and the benzene) or either underestimated by FF0 (e.g. methylacrylate, 2-ethyl-3-methyloxirane and n-propane).



**Figure A5-3:** Comparison between the  $E_{\text{ads}}$  calculated from FF0 and the  $E_{\text{ads}}$  obtained from the previous DFT study.

From this first attempt of “static” analysis, we concluded that FF0 was able to decently describe some of our model molecules. Thus, we decided to proceed to a first “dynamic” test in liquid phase.

## 5.2 First “dynamic” test: acetic acid desorption from $\alpha$ -Cr<sub>2</sub>O<sub>3</sub>

In this first “dynamic” attempt, we chose to study the molecule/surface interaction behavior between an acetic acid molecule and the hydroxylated  $\alpha$ -Cr<sub>2</sub>O<sub>3</sub> surface.

We simulated both the dissociative and molecular adsorptions of the acetic acid molecule by setting a linear thermal regime, starting from  $T^{\circ} = 0$  K till  $T^{\text{fin}} = 1000$  K.

### 5.2.1 Computational details

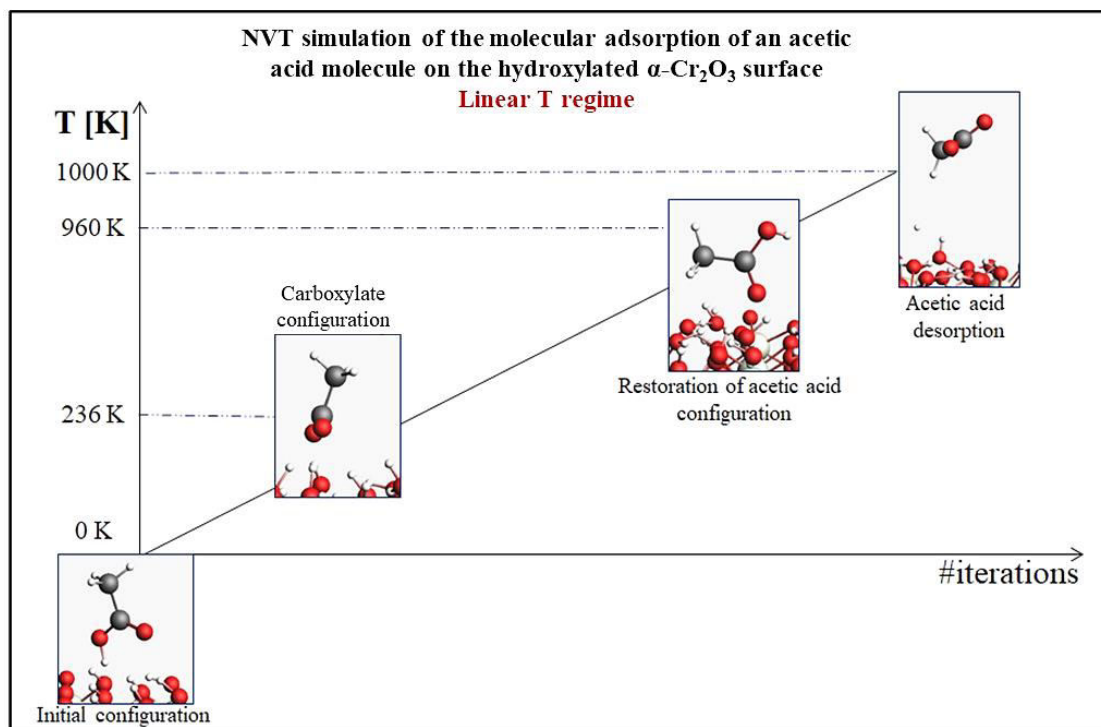
These MD simulations were run with the NVT ensemble with the implementation of the Berendsen thermostat [9]. We started with a first 1000 non-reactive steps and the time step was set to 0.25 fs and the temperature damping constant was set equal to 100 fs.

For the dissociative case of the acetic acid, the total number of iterations was set to 600'000, while for the molecular case it was set to 500'000 iterations.

### 5.2.2 Results and discussion of dynamic test for acetic acid desorption from $\alpha$ -Cr<sub>2</sub>O<sub>3</sub>

This first MD study implemented for both molecular and dissociative adsorption of the acetic acid on top of the hydroxylated  $\alpha$ -Cr<sub>2</sub>O<sub>3</sub> surface had the aim to observe the dynamic behavior of this adsorbed organic molecule when the system temperature increases with a linear trend; the choice of this thermal regime was to ascertain eventual strange behavior from the surface structure when the temperature would hit a very high value, such as the happening of a disruption of the outer layers or a rupture of the crystalline structure. None of these phenomena were registered from these simulations, further ensuring the accuracy of FF0.

In **Figure A5-4** below, we reported the dynamic evolution of the molecular adsorption of the acetic acid molecule when an increasing linear T regime is set in this system.

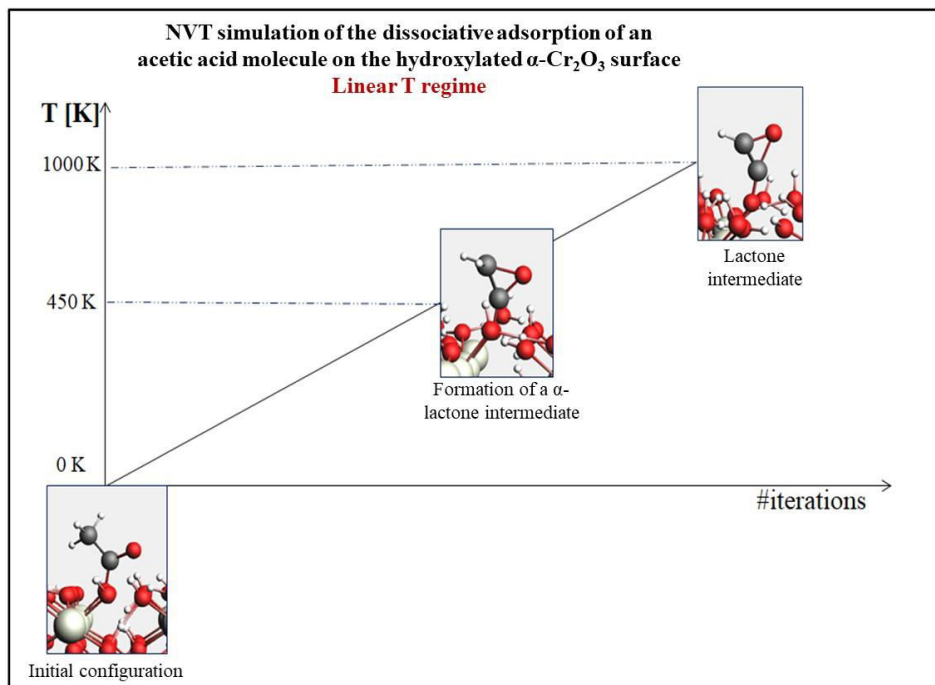


**Figure A5-4: Dynamic behavior of the molecular adsorption of the acetic acid molecule on hydroxylated  $\text{Cr}_2\text{O}_3$  when an increasing linear T regime is established.**

The initial configuration at  $T^\circ = 0 \text{ K}$  corresponds to the optimized DFT configuration and the first change of this configuration was registered at  $T = 236 \text{ K}$  ( $\sim -37^\circ \text{C}$ ), when a proton transfers from the acetic acid molecule to the nearby OHs group, resulting in an adsorbed carboxylate configuration. From this point on, this carboxylate configuration is maintained till reaching  $T = 960 \text{ K}$  ( $\sim 687^\circ \text{C}$ ), where the original carboxylic acid configuration is restored.

In contrast, in the MD study of the dissociative adsorption of the acetic acid a different behavior were detected. By starting again with the DFT optimized structure, we can observe from **Figure A5-5** that a new intermediate is formed, resembling an  $\alpha$ -lactone molecule.

This event is very peculiar since the adsorbate changes somewhat its chemical nature, from a carboxylate to a sort of lactone (e.g. cyclic carboxylic esters) [10]. What seems to have occurred at this step is that one of the H atoms of the methyl group of the former carboxylate was abstracted by an  $\text{OH}_s$  that in turn becomes a water molecule and provokes the “closure” of the molecule by forming an  $\alpha$ -lactone molecule. This lactone intermediate seems to be stable with the raising of temperature till  $T = 1000 \text{ K}$  ( $\sim 730^\circ \text{C}$ ), where another H atom is abstracted from the adsorbate molecule.



**Figure A5-5: Dynamic behavior of the dissociative adsorption of the acetic acid on hydroxylated  $\text{Cr}_2\text{O}_3$  when a linear T regime is established.**

In previous experimental studies conducted at IFPEN [11], among the oxygenated products from the biofuel degradation, molecules resembling lactones have been detected; thus, the identification of an  $\alpha$ -lactone molecule through MD simulations may be seen as a further validation of these results.

Thus, we conclude this first “dynamic” analysis with the objective to “isolate” the formation of this lactone intermediate to study it through DFT.

### 5.3 DFT study of the lactone intermediate

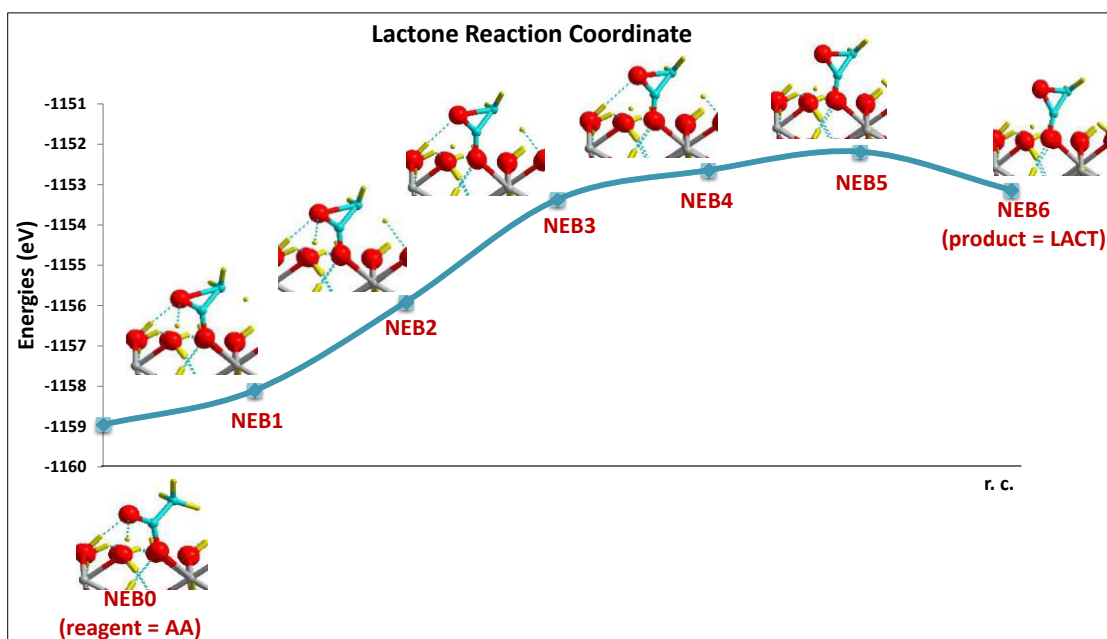
To calculate the energetic landscape of this lactone intermediate found in the previous MD study, we implemented the Nudged Elastic Band (NEB) method (cf. §2.4.7). We report below the settings and results obtained from this calculation.

### 5.3.1 Computational details

To obtain the energetic landscape of the lactone intermediate through the NEB method, we selected the two molecules that in this case represent the reagent and the product of this reaction, respectively: the acetic acid molecule (labeled as “AA”) and the lactone molecule (labeled as “LACT”). We run the NEB calculation with VASP package [12], imposing to create 5 different images of the transition state between the reactant (AA) and the product (LACT).

### 5.3.2 Results and discussion for lactone formation

**Figure A5-6** below reports the minimum energy path profile of the lactone formation starting from the dissociative adsorption of the acetic acid on the hydroxylated  $\alpha$ -Cr<sub>2</sub>O<sub>3</sub> surface. What occurs in this reaction is the proton transfer from the -CH<sub>3</sub> group belonging to the acetic acid molecule to an -OH<sub>s</sub> group that gradually leads towards the formation of the lactone molecule through the constitution of the O-ring.



**Figure A5-6:** Reaction coordinate diagram for the lactone formation starting from the proton transfer from the -CH<sub>3</sub> group of the acetic acid to an -OH<sub>s</sub> group.

**Figure A5-6** shows that the activation energy  $E_a$  of this reaction is very high ( $E_{\text{NEB5}} - E_{\text{NEB0}} = 653,1$  kJ/mol) and that the reaction is very endothermic ( $\Delta E_r = E_{\text{NEB6}} - E_{\text{NEB0}} = 561,5$  kJ/mol).

This so high activation energy dramatically contradicts the reaction observed at 450 K with ReaxFF and shows that the latter one is all but realistic. From this NEB analysis, we concluded that the chemistry of this reaction was wrongfully reproduced by FF0, leaving us with no other possibility than reparametrizing FF0 through the integration of this energetic curve.

## 5.4 First ReaxFF parametrization test

To achieve a good description of the chemistry related to the dissociative adsorption of the acetic acid molecule on the hydroxylated  $\alpha$ -Cr<sub>2</sub>O<sub>3</sub> surface at increasing temperature, we chose to reparametrize FF0 through the insertion of the DFT calculated energy path describing the lactone formation (**Figure A5-6**) in the ReaxFF training-set. All the obtained DFT optimized adsorption configurations related to the hydroxylated  $\alpha$ -Cr<sub>2</sub>O<sub>3</sub> surface (**Chapter 4**) were added in the training-set to increase the possibility of an improved reproducibility of the energetic data from the reparametrized force field.

### 5.4.1 Computational details

To ensure a good parametrization of FF0 through the inserted DFT data, we selected the parameters describing the properties of the following atomic bonds: C-H, H-O, Cr-O. In **Table A5-1** below the reported parameters are listed and they are: the sigma bond dissociation energy  $E(\sigma)$ , the sigma bond orders *pbo1* and *pbo2* (**Chapter 2**), the overcoordination penalty *povun1* and the bond energies *pbe1* and *pbe2* (**Chapter 2**). For H-O and Cr-O bonds, we optimized the terms linked to the van der Waals dispersion forces: the vdW energy  $E(vdW)$ , the vdW radius  $R(vdW)$ , the vdW coefficient  $\alpha(vdW)$  and the sigma bond length  $R(\sigma)$ . The formalism linked to these parameters is taken from reference [13].

The choice to optimize the bond orders and energy terms for C-H bond was to achieve an improved description of the C-H properties since the lactone formation from the adsorbed acetic acid on the hydroxylated  $\alpha$ -Cr<sub>2</sub>O<sub>3</sub> surface showed a failed description in regards of the C-H bond.

About the O-H bond, the selection of all the aforementioned ReaxFF parameters was due to the fact that this bond describes both the feature of intramolecular interactions (e.g. OH group belonging to the acetic acid molecule or OH surface layer) and intermolecular interactions (e.g. H-bonds established between molecules and OH surface layer), thus we believed that optimizing these parameters could help us achieving a better descriptions of both kind of interactions.

Finally, for the Cr-O bond, we did not consider the bond order and energy terms in this first round because we did not want to “touch” the parameters linked in the surface structure (at least beforehand). On the other hand, we selected the vdW parameters because they contribute to the establishing of the interface interactions between molecules and the hydroxylated chromia surface.

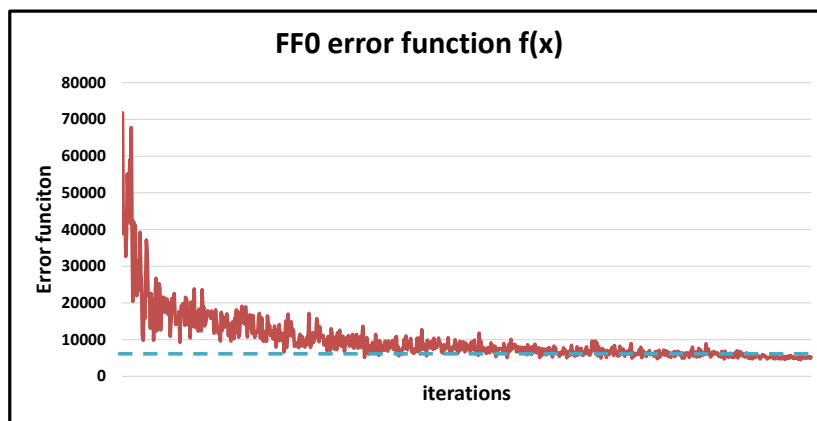
**Table A5-1: Training-set parameters selected for ReaxFF reparametrization.**

Parameters	C-H	H-O	Cr-O
E(sigma) [kcal/mol]	✓	✓	-
pbe1	✓	✓	-
povun1	✓	✓	-
pbe2	✓	✓	-
pbo1	✓	✓	-
pbo2	✓	✓	-
E(vdW) [kcal/mol]	-	✓	✓
R(vdW)	-	✓	✓
Alpha(vdW)	-	✓	✓
R(sigma)	-	✓	✓

We imposed 1000 fit iterations for the CMA-ES FF optimizer. For the geometries setup, the Conjugate Gradient (CG) algorithm was implemented and the DFT data of the training-set were calculated as “geometry optimizations”, with their maximum number of iterations set to 50 iterations. Instead, the energetic steps composing the lactone formation (e.g. NEB0-6 in **Figure A5-6**) were calculated as single points.

### 5.4.2 Results and discussion

The new optimized FF0 (labeled hereinafter as “FF1”) was obtained at the end of the CMA-ES run, which gave the error function value (**Chapter 2**) displayed in **Figure A5-7** below.



**Figure A5-7:** Error function  $f(x)$  obtained from FF0 optimization.

From **Figure A5-7** we can see that the error function reached a plateau at around 5000 iterations starting from an original error value  $f(x)^o \approx 70000$ , so it was reduced by one order of magnitude.

The ReaxFF results against the training-set DFT data is reported in **Table A5-2**.

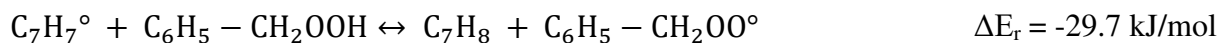
**Table A5-2:** Comparison between the FF1 calculated energies and the DFT corresponding values.

Input data	FF1 [kJ/mol]	DFT [kJ/mol]
NEB1 - NEB0	50.0	82.0
NEB2 - NEB0	289.2	293.3
NEB3 - NEB0	496.0	538.4
NEB4 - NEB0	559.4	608.8
NEB5 - NEB0	435.9	653.2
NEB6 - NEB0	452.3	561.6
Acetaldehyde	-48.6	-33.7
Acetic acid	-60.1	-82.8
Acetone	-178.9	-68.5
Benzene	-24.6	-64.6
Ethanol	-56.8	-48.2
Methylacrylate	-221.5	-70.0
2Ethyl-3methyloxirane	-199.7	-42.1
Toluene	-75.0	-52.0

From **Table A5-2** we can see that the FF1 single point predictions are relatively decent with respect to the DFT data, although they could be further improved. Regarding the geometry optimizations, the majority of the reported FF1 predictions did not reach a convergence with the imposed criterion of 50 maximum iteration for the CG. Taking this result in consideration, we decided to augment the number of maximal iterations in the CG settings and to verify if this solution could aid us obtaining converged configurations.

## 5.5 First ReaxFF MD test of a surrogate “fuel-oxygen” blend: Production set

To verify if the optimized FF1 was capable to simulate the dynamic behavior of molecular systems representing surrogates of deposit precursors, we identified a preliminary “fuel-oxygen” blend with the following composition: 95% mol toluene ( $C_7H_8$ ), 3% mol benzyl hydroperoxide ( $C_7H_8O_2$ ) and 2% mol benzyl radical ( $C_7H_7^\circ$ ). To describe the chemistry of this system, we selected the following reaction as reference:



**Equation 96**

Where the H atom is abstracted from  $-COOH$  of the benzyl hydroperoxide from the reactive benzyl radical resulting in the formation of toluene and the benzyl peroxy radical ( $C_6H_5 - CH_2OO^\circ$ ). The  $\Delta E_r$  of this reaction was calculated via DFT and its value is close to the one reported in reference [14].

### 5.5.1 Computational details

To simulate the dynamics of our chosen preliminary “fuel-oxygen” blend, we implemented the NVT ensemble with the Nosé-Hoover Chain (NHC) thermostat [15] and divided the MD study into two different parts:

- i. An equilibration phase, where the energy, temperature and pressure of the system must reach a plateau (e.g. equilibrium of the system).
- ii. A production phase, which follows the equilibration phase and coincides with the simulation data that will be taken as final result.

For the equilibration phase, we selected a constant thermal regime at  $T = 1$  K in order to equilibrate the system and a maximum number of step equal to 500'000. The time step was set at 0.25 fs, thus obtaining a total of 125 ps of simulation time.

For the production phase we set two consecutive thermal regimes:

- i. a linear T regime starting from  $T^{\circ} = 1$  K to  $T_{\text{fin}} = 500$  K for the duration of  $2 \cdot 10^6$  iterations. The time step is set to 0.25 fs, giving a total simulation time of 500 ps.
- ii. A constant T regime at  $T = 500$  K for the duration of  $2 \cdot 10^6$  iterations. The time step is set at 0.25 fs, giving a total simulation time of 500 ps.

The molecular box was composed of a total of 95 molecules, where 90 are toluene molecules, 3 are benzyl hydroperoxydes and 2 are of benzyl radical with a cell volume of  $15813.3 \text{ \AA}^3$ . This molecular composition was chosen to simulate the liquid density of this blend at ambient conditions (e.g.  $P = 1$  atm and  $T = 20^{\circ}\text{C}$ ) taking the toluene density as reference since it represents the solvent of the examined solution (e.g.  $0.87 \text{ g/cm}^3$ [16]).

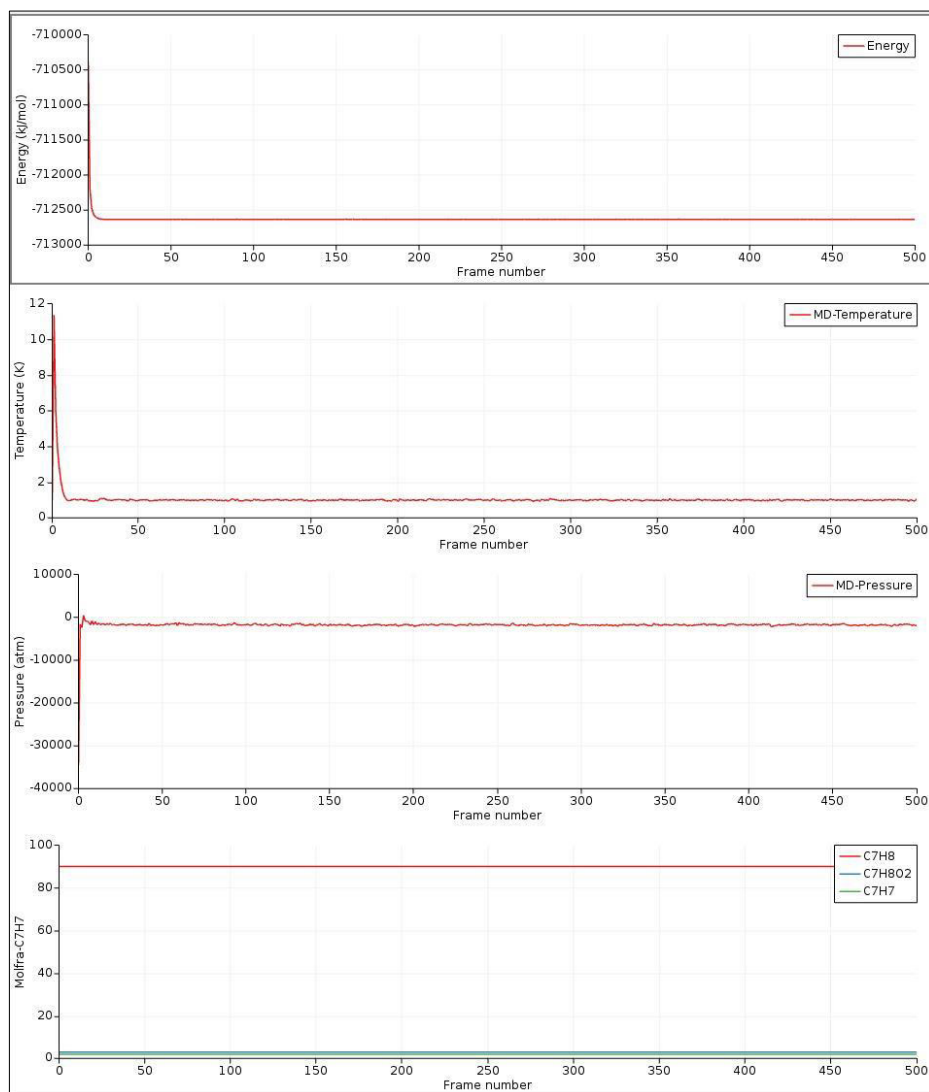
### 5.5.2 Results and discussion of ReaxFF MD test: “fuel-oxygen” blend

In **Figure A5-8** we report the plateau obtained respectively from: the total energy, the temperature, the pressure, and the number of molecules contained in this molecular box during the equilibration phase. From **Figure A5-8** we can deduce that 125 ps were enough to reach the system equilibrium. Also, we can observe that no abnormal reactions took place in this time fragment, since the number of molecules registered in this phase did not change. Thus, we farther proceeded with the production phase.

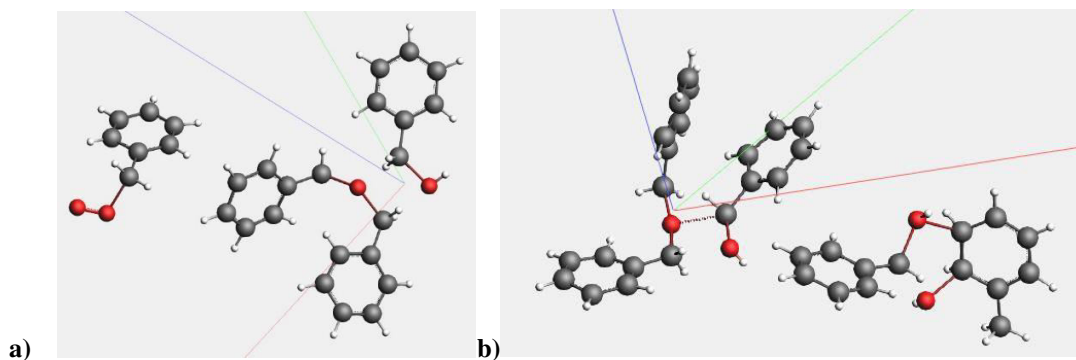
During the first 250 ps of the linear T regime no reactions were detected, but at  $T \approx 250$  K ( $\approx -23^{\circ}\text{C}$ ) we started to see the production of unexpected intermediates (**Figure A5-9a**).

The formation of these intermediates was not expected to occur at  $T \approx 250$  K since the temperature are definitely too low to encourage the reactivity of this system towards this direction. According to other works [11, 17], hydroperoxydes tend to react readily in the fuel autoxidation process, but reactions take place for temperatures equal or slightly above the ambient conditions.

During the constant thermal regime at  $T = 500$  K, the previously observed intermediates continue to interact, creating binary and ternary molecular complexes (**Figure A5-9b**). Since these complexes are formed as a consequence of the interaction of unusual intermediates, we concluded that the chemical reactivity of the whole system was not correctly described.



**Figure A5-8: NVT equilibration phase plots of energy, temperature, pressure and number of molecules of the homogeneous system defined by the liquid “fuel-oxygen” mixture.**



**Figure A5-9: Intermediates registered in the production phase during a) the linear T regime (around  $T = 250$  K) and b) the constant T regime at  $T = 500$  K.**

## 5.6 Second “static” test: adsorption energies

In this second cycle of ReaxFF parametrization we decided to add to the training-set also the DFT adsorption configurations of dry  $\alpha\text{-Cr}_2\text{O}_3$  and dry and hydroxylated  $\alpha\text{-Al}_2\text{O}_3$  (**Chapter 4**). The strategy of this additional data contribution was to realize a new training-set as complete as possible in order to achieve a higher accuracy for the new optimized ReaxFF.

### 5.6.1 Computational details

As to obtain a better dynamic description of our molecular systems, for the second cycle of ReaxFF optimization we decided to test two different versions of FF1: the first coinciding with the “original” FF1 optimized version and the second coinciding with a “changed” FF1, where more precisely we chose to substitute the ReaxFF parameters of H and O atoms by inserting the values coming from the “CHON-2017\_weak.ff” force field developed by Zhang and van Duin [18]; we called this second version as “FF2”.

For both force fields, the same DFT data and parameters were selected for the reparametrization; the parameters are reported in **Table A5-3** below.

In addition to the C-H bond, this time we also selected the C-C and the C-O bonds. In particular, for the C-O bond, similarly to what was done for the O-H bond, the selection of all the aforementioned ReaxFF parameters was due to the fact that the C-O bond also describes both the

feature of intramolecular interactions (e.g. C=O group belonging to the carbonylic compounds) and intermolecular interactions (e.g. C-O vdW forces established between the molecular carbon chain and the OH groups at the chromia surface). The choice to optimize again the bond orders and energy terms for the C-H bond was to further increase the improvement of the description of the C-H properties for the lactone configurations.

About the O-H bond, we reconducted to the selection of the *E(sigma)* value for O-H bond to direct change the behavior of the OH groups on the hydroxylated chromia surface. For this reason, in this new ReaxFF optimization, we decided to not select the bond order and energy terms linked to the O-H bond, to verify if we could obtain an improvement of the description of the interface interactions without altering these parameters.

For the C-Cr and C-Al bonds, only the vdW parameters were selected since these bonds represent the interactions between the molecular carbon chain and the metallic atoms (e.g. Cr/Al) terminating the dry chromia and alumina surfaces.

**Table A5-3: Parameters selected for ReaxFF parametrization of both FF1 and FF2.**

Optimized parameters	C-C	C-H	C-O	H-O	C-Cr	C-Al	Al-O	Cr-O
E(sigma)	✓	✓	✓	-	-	-	-	-
pbe1	✓	✓	✓	-	-	-	-	-
povun1	✓	✓	✓	-	-	-	-	-
pbe2	✓	✓	✓	-	-	-	-	-
pbo1	✓	✓	✓	-	-	-	-	-
pbo2	✓	✓	✓	-	-	-	-	-
E(vdW)	-	-	✓	✓	✓	✓	✓	✓
R(vdW)	-	-	✓	✓	✓	✓	✓	✓
Alpha(vdW)	-	-	✓	✓	✓	✓	✓	✓
R(sigma)	-	-	✓	✓	✓	✓	✓	✓

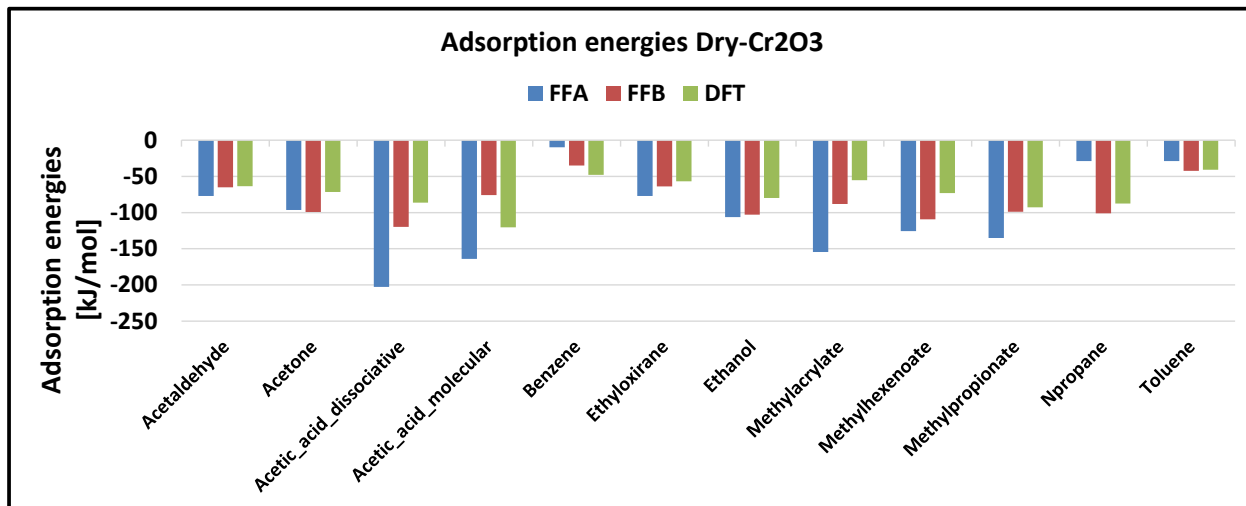
Finally, for the Cr-O and Al-O bonds, again we did not consider the bond order and energy terms because we still did not want to alter the parameters linked in the surface structure (even though these bonds can also describe the intermolecular interactions between the oxygenated molecules

and the Cr/Al-terminated dry chromia and alumina surfaces). Again, we only selected the vdW parameters because they contribute to the establishing of the interface interactions between molecules and the metal-oxide surfaces.

We imposed again 1000 fit iterations for the CMA-ES FF optimizer. For the geometry optimization setup, we implemented again the CG algorithm and this time we augmented the number of maximum iterations up to 100 iterations following what was mentioned in section 5.4.2.

### 5.6.2 Results and discussion of 2<sup>nd</sup> static test

We report below respectively in **Figure A5-10** and **Figure A5-11** the adsorption energies calculated with both new optimized force fields compared with the DFT  $\text{Cr}_2\text{O}_3$  data. The optimized version of FF1 is labeled as FFA and the one for FF2 is labeled as FFB.

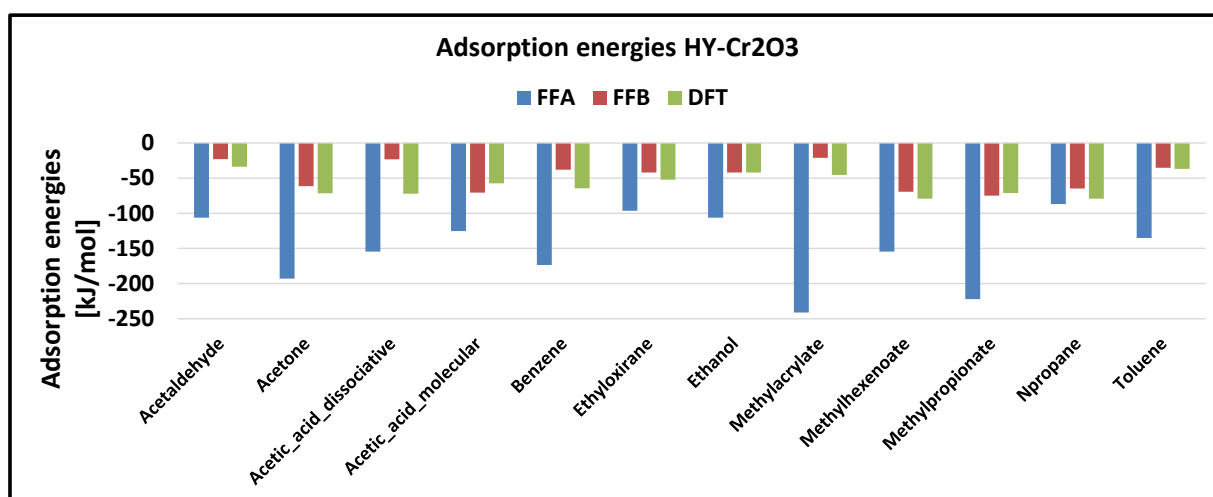


**Figure A5-10:** Comparison of the adsorption energies for dry  $\alpha\text{-Cr}_2\text{O}_3$  calculated for both FFA and FFB against the DFT values.

**Figure A5-10** shows the results for the adsorption energies related to the dry  $\alpha\text{-Cr}_2\text{O}_3$  configurations. We can see easily here that the optimized FF1 (namely FFA) does not reproduce satisfactorily certain configurations, in certain cases with a very high discrepancy compared to DFT values (e.g. the dissociative and molecular adsorption of the acetic acid, the methylacrylate

and the methylpropionate adsorptions). On the other hand, the optimized FF2 (namely FFB) is able to decently describe the majority of the adsorption configurations when compared to the DFT results.

**Figure A5-11** shows the results for the adsorption energies related to the hydroxylated  $\alpha$ -Cr<sub>2</sub>O<sub>3</sub> configurations. Here it appears even more clearly that the optimized FF1 (FFA) is not capable to reproduce almost all the configurations, while on the other hand, the optimized FF2 (FFB) is able to describe accordingly the majority of the adsorption configurations when compared to the DFT results.



**Figure A5-11:** Comparison of the adsorption energies for hydroxylated  $\alpha$ -Cr<sub>2</sub>O<sub>3</sub> calculated for both FFA and FFB against the DFT values.

Even though the description of  $\alpha$ -Cr<sub>2</sub>O<sub>3</sub> configurations worsened for the FFA force field, we found on the other hand that it was capable to decently reproduce the DFT data of dry  $\alpha$ -Al<sub>2</sub>O<sub>3</sub> configurations (**Figure A5-12**). A similar trend was found also for the hydroxylated  $\alpha$ -Al<sub>2</sub>O<sub>3</sub> configurations (not reported).

From these results, we acknowledged the newfound difficulty for FFA to reproduce accordingly the  $\alpha$ -Cr<sub>2</sub>O<sub>3</sub> configurations, especially the ones related to the hydroxylated state and at the same time to reproduce accurately enough the dry  $\alpha$ -Al<sub>2</sub>O<sub>3</sub> systems.

For this reason, we decided that a good course of action could be to divide the ReaxFF reproduction of  $\alpha$ -Cr<sub>2</sub>O<sub>3</sub> and  $\alpha$ -Al<sub>2</sub>O<sub>3</sub> towards two different reactive force fields: the FFA for the description of alumina systems and FFB for the chromia systems.

In addition, the augmentation of the number of maximum iterations from 50 (section 5.4.2) to 100 was still not sufficient to reach a convergence for the majority of the analyzed configurations. Therefore, we opted again to increase the number of maximal iterations in the CG settings and to verify if this solution could aid in obtaining converged configurations.

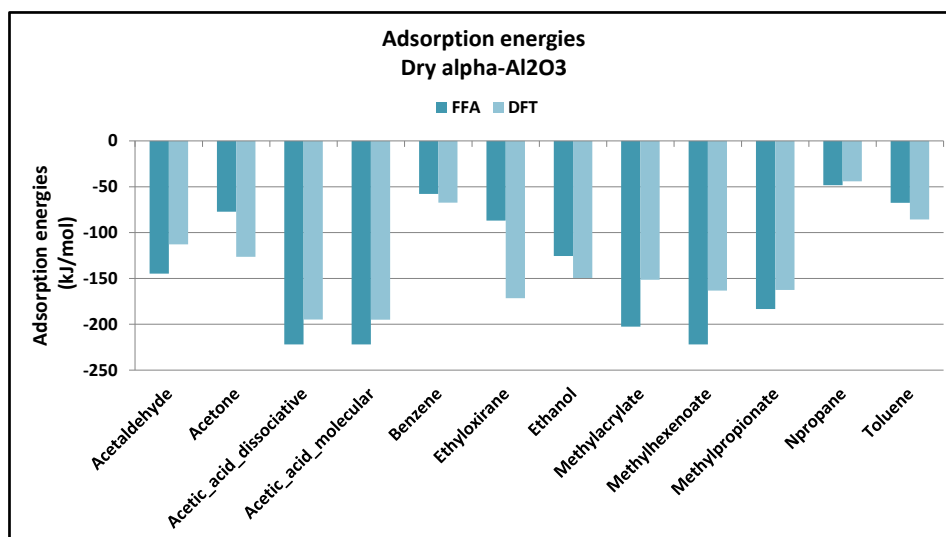


Figure A5-12: Comparison of the adsorption energies for dry  $\alpha$ -Al<sub>2</sub>O<sub>3</sub> calculated for FFA against the DFT values.

## 5.7 Conclusion of the preliminary ReaxFF study

From the ReaxFF analysis conducted so far, we made the following conclusions:

- i. To improve the ReaxFF reproducibility of DFT data, it is necessary to have a training-set as conspicuous as possible. In our case, the systematic addition of adsorption configurations (first only chromia-based, then with the addition of dry/hydroxylated alumina configurations) confirmed this statement.
- ii. To obtain a further confirmation for the good fitting of the reactive force fields, the addition of supplementary tests for the ReaxFF validation-set (i.e. FF tests for the bulk

and surface geometries and gas phase reactions for the static study, liquid-phase density analysis for the dynamic study) is necessary.

- iii. From the results reported in paragraph 5.6.2, we decided to optimize two separate force fields for  $\alpha$ -Cr<sub>2</sub>O<sub>3</sub> and  $\alpha$ -Al<sub>2</sub>O<sub>3</sub> systems respectively to ensure a higher possibility for a good description of each systems.

## 5.8 Heterogeneous systems: Desorption temperature analysis

The next step consisted in studying the behavior of adsorbed molecules with temperature. One of the advantage of the force field is that we can perform simulated heating and accumulate a trajectory long enough to describe the system degrees of freedom as adsorption/desorption and molecule diffusion at the surface.

To do this, we choose molecules of different chemical families, i.e. molecule adsorbing with dissociation at the surface (acetic acid), molecules with a specific interaction with the surface (ethanol, benzyl ethanol), and molecule with a weak, non-specific interaction with the surface (benzene). Also, in **Chapter 4**, we have evidenced the difference in reactivity of the hydroxylated versus anhydrous  $\alpha$ -Al<sub>2</sub>O<sub>3</sub> surfaces, and thus, the adsorption of the molecules on the hydroxylated surface is also investigated. Thus, we compare different molecules on a given surface and different surfaces for a given molecule.

### 5.8.1 Computational details

For this MD study on the desorption temperatures, we implemented the NVT ensemble, where we selected the Nosé-Hoover Chain (NHC) thermostat [10]. We selected an initial  $T^0 = 0$  K at the start of these simulations, with a damping constant of 100 fs for the thermostat and setting the NHC length at 10. The total number of steps was set to  $6.5 \cdot 10^6$  for the acetic acid, ethanol and benzyl alcohol and to  $4.5 \cdot 10^6$  for the benzene. For all the cases, the time step was 0.25 fs, corresponding to a total calculation time of 1625 ps ( $\approx 1.6$  ns). For each case, we divided the simulations into two stages: a first equilibration stage and a production stage. For the first stage,

we fixed  $T = 1$  K thermal regime with a duration of 125 ps ( $= 5 \cdot 10^5$  steps). Once the system was equilibrated by the end of the equilibration phase, we proceed to the production phase.

For the production phase, we divided the thermal regime into two different sub-regimes: a) a first linear  $T$  increase from 1 K to  $T_{des}^{DFT}$  and b) a second constant  $T$  regime where  $T = T_{des}^{DFT}$ . The increasing  $T$  rate was equal to 0.8 K/ps for the ethanol, the acetic acid and the benzyl alcohol, while it was set to 0.5 K/ps for the benzene.

In **Table A4-4** we reported the gas phase entropy of the molecules, and in **Chapter 4**, we applied these values together with the calculated adsorption energies to estimate the temperature of molecule desorption,  $T_{des}^{DFT}$ , from the surface.

The  $\text{Al}_2\text{O}_3(0001)$  surface was described by a (4x4) cell and the number of adsorbate molecules was equal to 4 on the alumina surface, two on each surface (top and bottom). This allowed a weak surface coverage, with no molecule-molecule interaction, and to acquire more statistic data, studying four molecules instead of one. In addition to these MD simulations, Born Oppenheimer Molecular Dynamics was performed to compare both approaches.

## 5.8.2 Results and discussion

**Table A5-4** summarizes the molecules studied, surface state and temperature applied at the plateau.

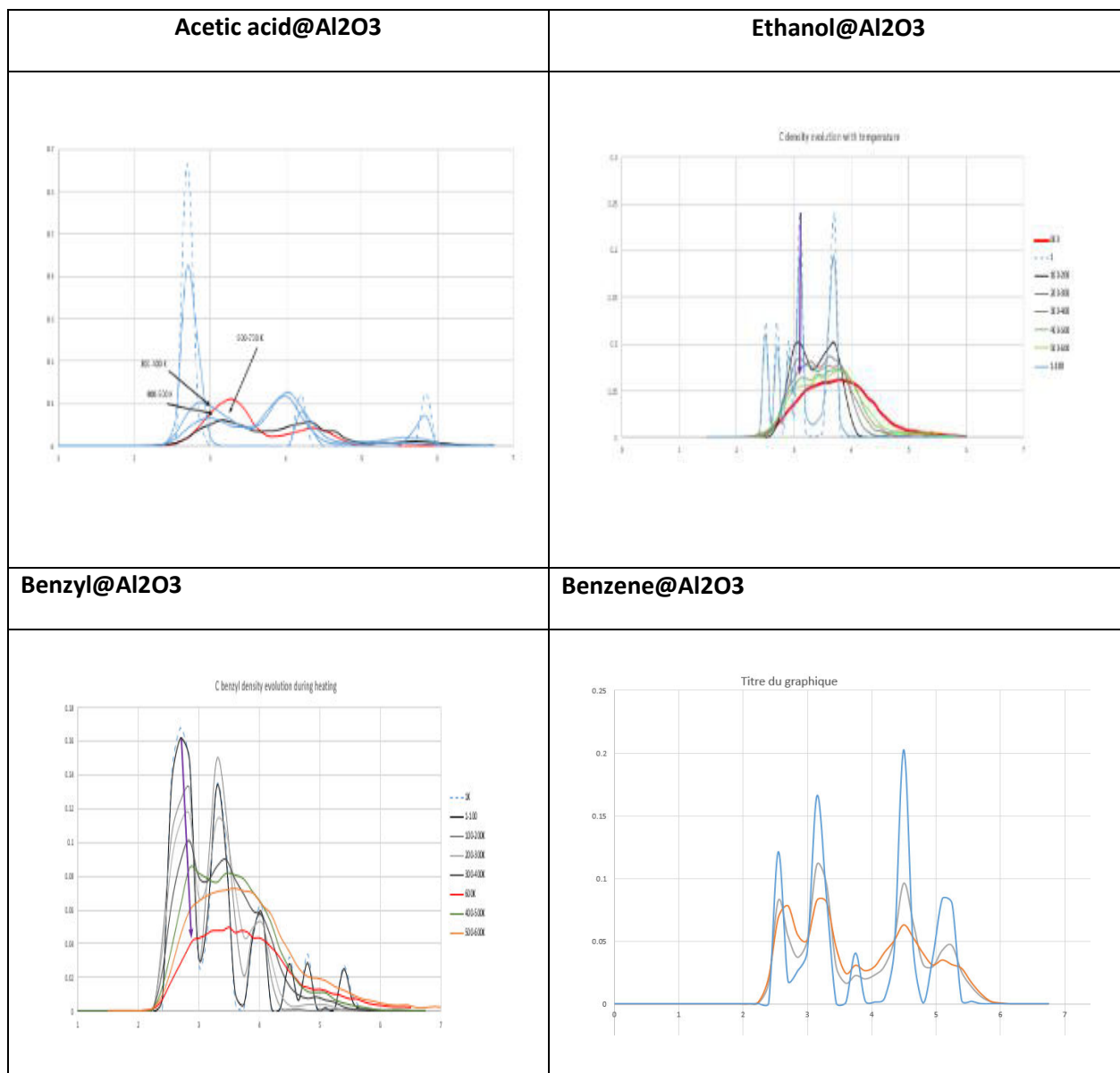
**Table A5-4: the molecules studied, surface state and temperature applied.**

Surface Molecule	$\text{Al}_2\text{O}_3$ $T_{des}^{DFT}$ (K)	$\text{Al}_2\text{O}_3\text{-HY}$ $T_{des}^{DFT}$ (K)
Acetic acid	750	196
Ethanol	600	160
Benzyl alcohol	600	250
Benzene	250	186

Rising the temperature enhances, as expected, the molecules mobility. As a general trend, we did not observe “desorption” when rising up the temperature, rather, we observed more diffusion of the molecules on the surface, molecules rotation, and desorption/readsorption phenomena. All these phenomena are not easy to describe. The first, intuitive descriptor, e.g. the molecule/surface distance, turned to render a partial information. Thus, for the present study, we used several descriptors and their combination:

- i. The first descriptor is that of a “specific” molecule-surface interaction, if any. This implies that we searched for the reactive moiety in the molecule–surface interaction, at low temperature, and then followed its evolution with temperature increase.
- ii. The second descriptor is that of the molecule mobility on the surface. Here, the accumulated trajectories were not sufficient to calculate a diffusion coefficient of the molecule at the surface, thus, we report a qualitative analysis of surface mobility.
- iii. A third descriptor is the variation of the molecule/surface orientation, which is related to molecule rotation at the surface. Again, the accumulated trajectories do not allow to calculate a true “flip frequency” of the molecule at the surface, and when necessary we report a semi-quantitative analysis.

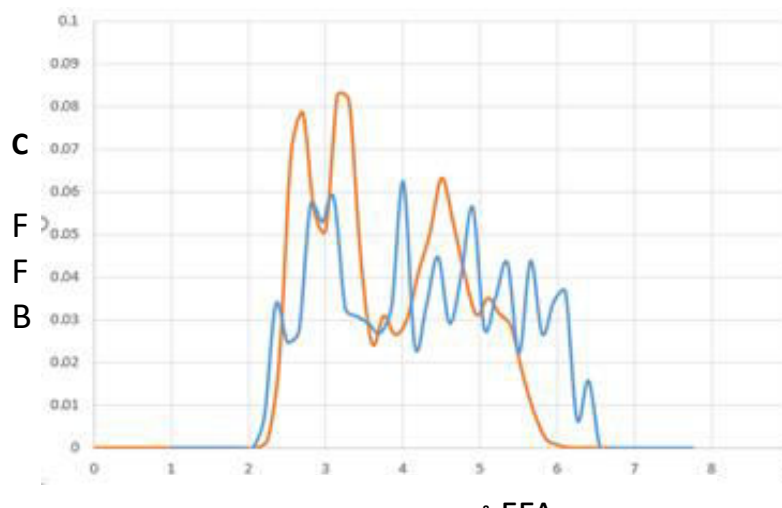
For the anhydrous surface, **Figure A5-13** shows the molecular signature, the C density versus the distance to the surface, at different temperatures. For acetic acid, increasing temperature, the peak at Al-C = 2.8 Å, attributed to the formation of an Al-O bond with the carboxylate O atom, disappears and a peak at 3.3 Å appears. For ethanol, as soon as  $T > 100$  K, the short range interaction (C-Al =  $2.6 \pm 0.1$  Å, due to the formation of the Al-alcohol O bond) is broken. A peak at Al-C = 3.1 Å is maintained until 600 K. This peak at 3.1 Å disappears at 600 K, with a maximum at 3.7 Å, and a broad distribution of C localization. For benzyl alcohol, the peak Al-C at 2.6 Å assigned to the Al-benzyl alcohol interaction decreases with increasing temperature and vanishes at  $T_{des}^{DFT}$ . Only in the case of benzene, the Al-C distance typical for the molecule-surface interaction does not vanish at increasing temperature.



**Figure A5-13: Evolution of the carbon amount (proportion of the total number of C atoms) of the adsorbed molecule with respect to the distance to the surface (Å) with increasing temperature.**

In order to further understand the case of benzene adsorbed on Al<sub>2</sub>O<sub>3</sub>, we performed a Born Oppenheimer Molecular Dynamics (BOMD) trajectory of benzene/Al<sub>2</sub>O<sub>3</sub> system at 150, 250, 350 and 450 K. The cell chosen for the BOMD was (2x2), with one molecule in the cell. The dynamics was a NVT, with a time step of 1.5 fs. To save computational time, a cutoff of 300 eV (PREC = LOW) was used instead of 520 eV (PREC = HIGH) in the geometry optimizations. The simulation time was 7.5 ps.

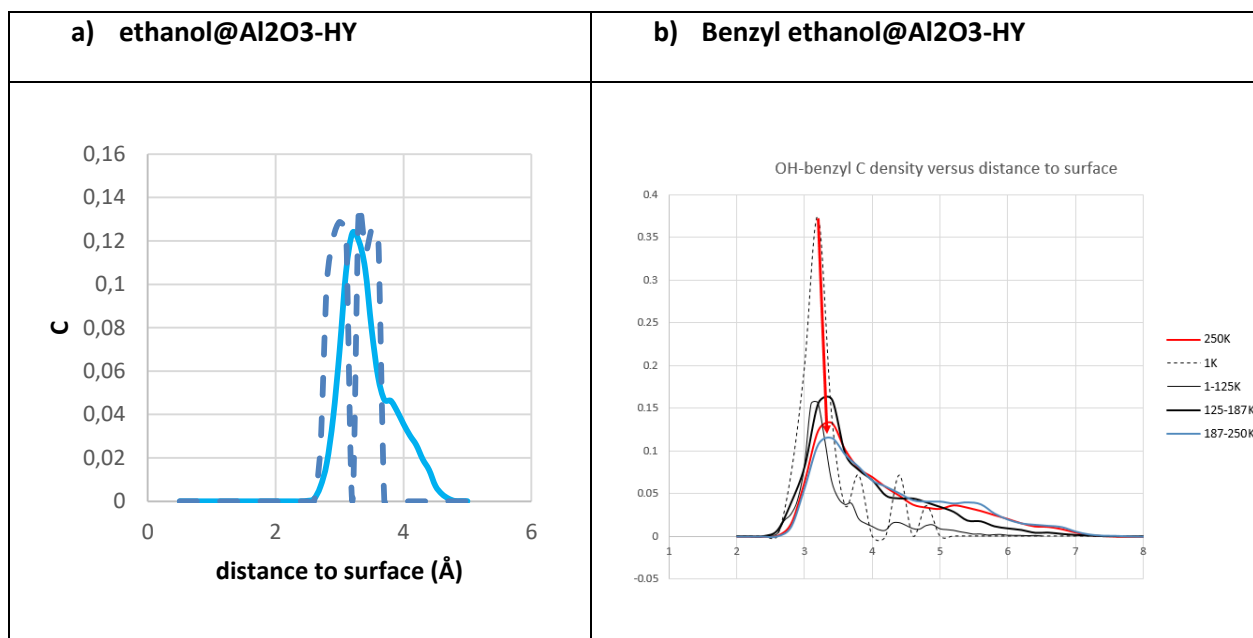
We report in **Figure A5-14** the C amount versus the distance to surface, at 250 K, for FFA (orange) and DFT (blue).



**Figure A5-14:** C amount of benzene at the  $\text{Al}_2\text{O}_3$  surface ( $\text{\AA}$ ) during the plateau at 250 K (orange: FFA; blue: DFT).

We notice that the two curves exhibit the same profile, albeit the DFT curve has sharper peaks, due to a much smaller accumulation time. We conclude to a good correspondence between FFA and the DFT trajectory. In particular, the peak at 2.8  $\text{\AA}$ , typical of the Al-C interactions, is present both in FFA and DFT profiles. The present result thus suggests that benzene is not desorbed from the  $\text{Al}_2\text{O}_3$  surface at 250 K, at least for short acquisition times accumulated here.

For the hydroxylated surface, we report in **Figure A5-15** the C amount with respect to the surface distance for ethanol and benzyl alcohol at the hydroxylated surface, two molecules able to form a H-bond with the hydroxylated surface. For ethanol, because  $T_{des}^{DFT}$  is low (160 K), we just compare the C amounts at 1 K and at  $T_{des}^{DFT}$ , whereas for benzyl alcohol, we could follow the progression with temperature increasing. Again, we find that at  $T_{des}^{DFT}$ , the signature of the molecule-surface interaction has vanished: for ethanol, the C from the molecule is located at a precise distance from the surface at 1 K, and the two C atoms of the molecule are distinguished. In contrast, at 160 K, the molecule is slightly farther from the surface and the signal is broad, indicating that the molecule has acquired some degrees of freedom. For the benzyl alcohol, the disappearance of the C surface interaction appears clearly with the increasing temperature.

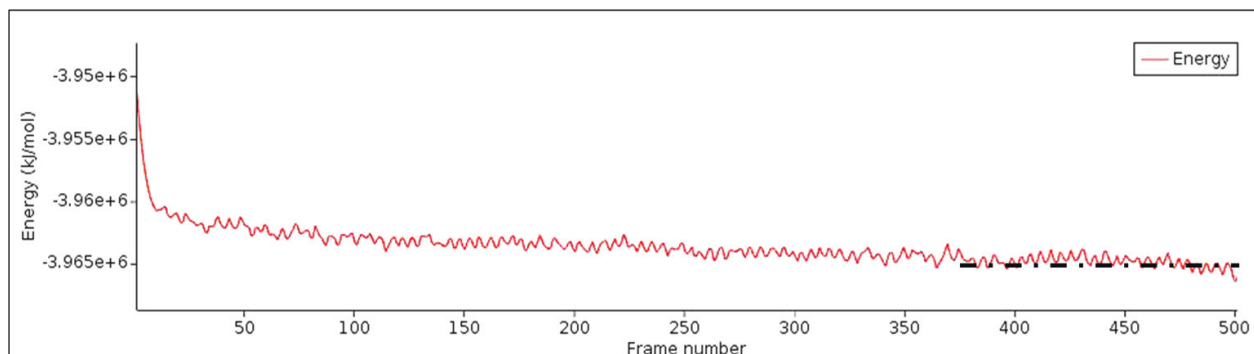


**Figure A5-15:** C amount with respect to the hydroxylated Al<sub>2</sub>O<sub>3</sub> surface distance (Å) for a) ethanol: dashed line: 1K; plain line: 160K, and b) benzyl ethanol at different temperature ranges

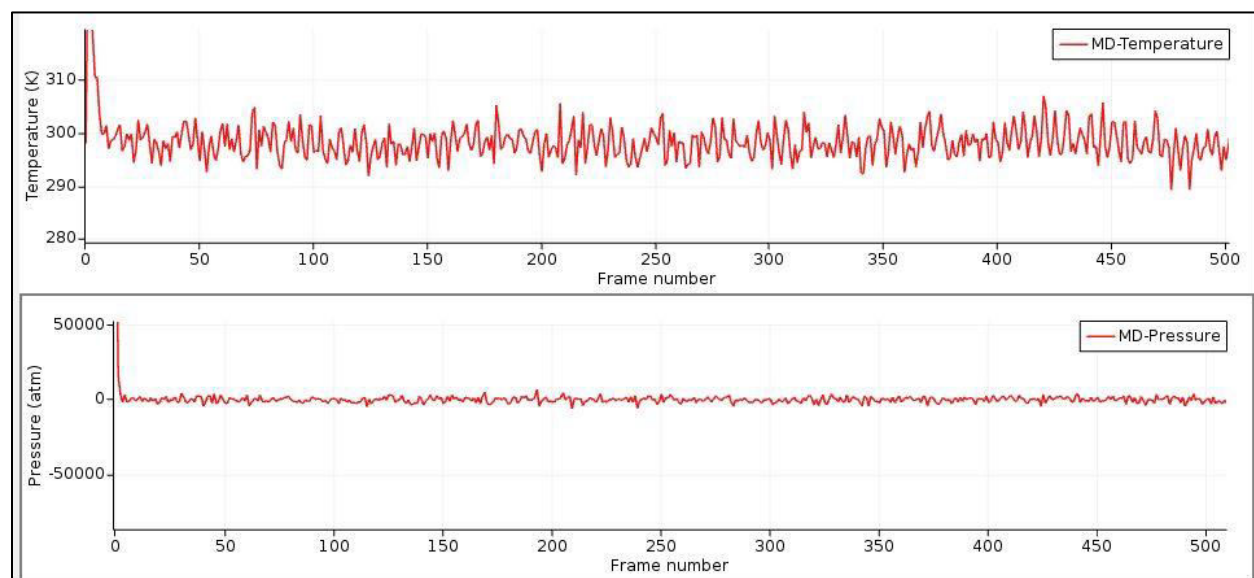
In this second MD stage, only the FFA was implemented; this choice was due to the FFB inaccuracy shown on the description of realistic dynamic behaviors. Thus, the only analyzed substrate in this analysis was the alumina. From these MD simulations, we did not observe “desorption” when rising up the temperature, but rather phenomena like molecular diffusion on the surface, molecular rotation and desorption/readsorption combinations. For the anhydrous alumina surface, the results of the molecular signature (either C or O) density versus the distance to the surface, at different temperatures, for ethanol, acetic acid and benzyl alcohol showed a good correspondence between ReaxFF and BOMD approaches, while for the benzene/Al<sub>2</sub>O<sub>3</sub> supplementary calculations at higher temperatures revealed that the reason of the reminiscence of the peak at short distances is due to a molecular flip frequency augmentation with temperature. For the hydroxylated alumina surface, the C amount with respect to the surface distance for ethanol and benzyl ethanol was reported. This analysis revealed that at  $T_{des}^{DFT} = 160$  K, the ethanol molecule is slightly farther from the surface and the signal is broad, indicating that the molecule has degrees of freedom, while for the benzyl alcohol, the disappearance of the C surface interaction appears clearly with the increasing temperature.

## Chapter 6

### Liquid-phase “fuel-oxygen” mixture

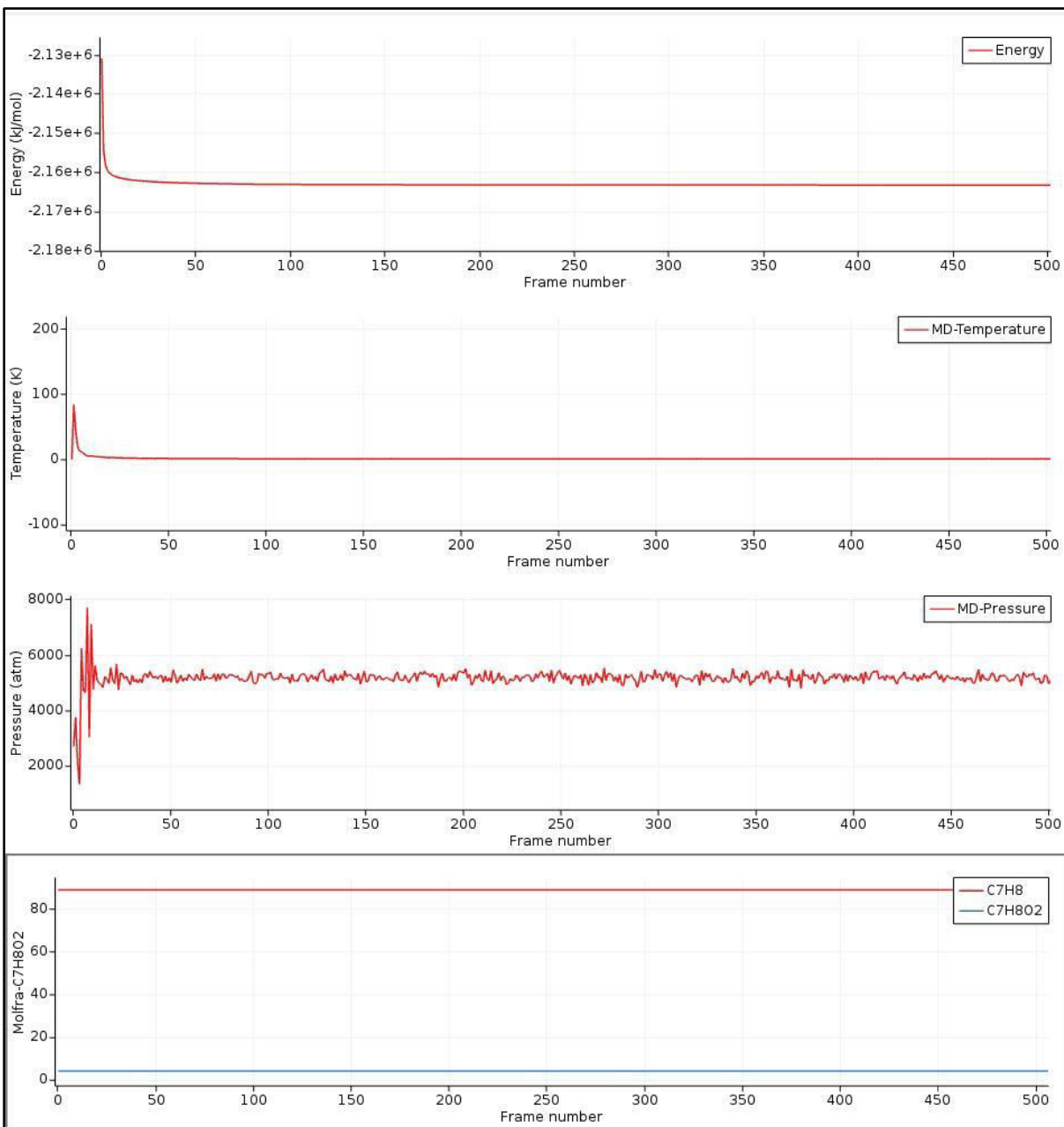


**Figure A6-1:** Reached plateau for the system total energy by the end of the equilibration phase of the NPT simulations (homogeneous phase of the “fuel-oxygen” mixture).



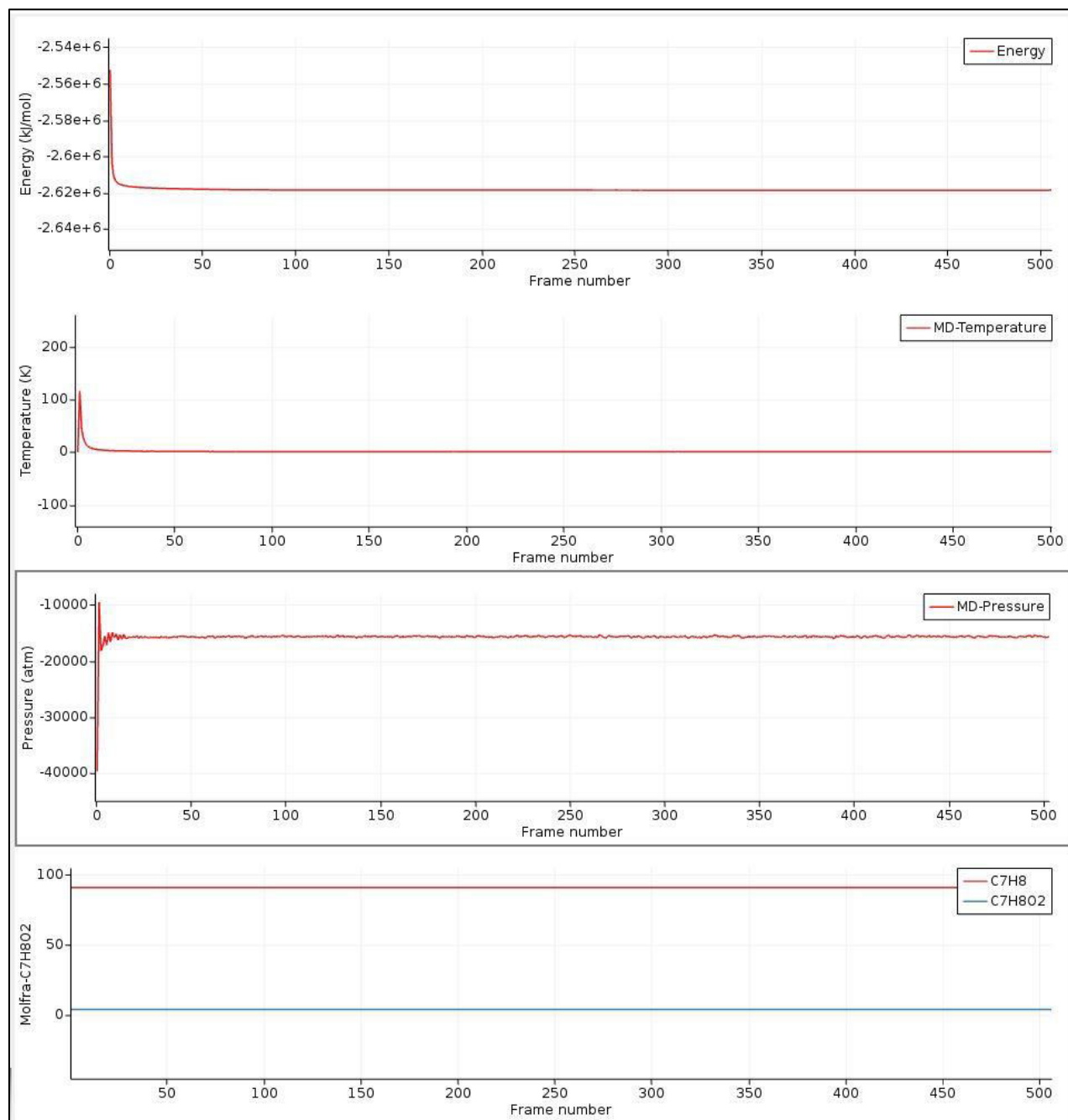
**Figure A6-2:** Reached plateau for the system temperature and pressure by the end of the equilibration phase of the NPT simulations (homogeneous phase of the “fuel-oxygen” mixture).

## Droplets of liquid “fuel-oxygen” mixture adsorbed on alumina

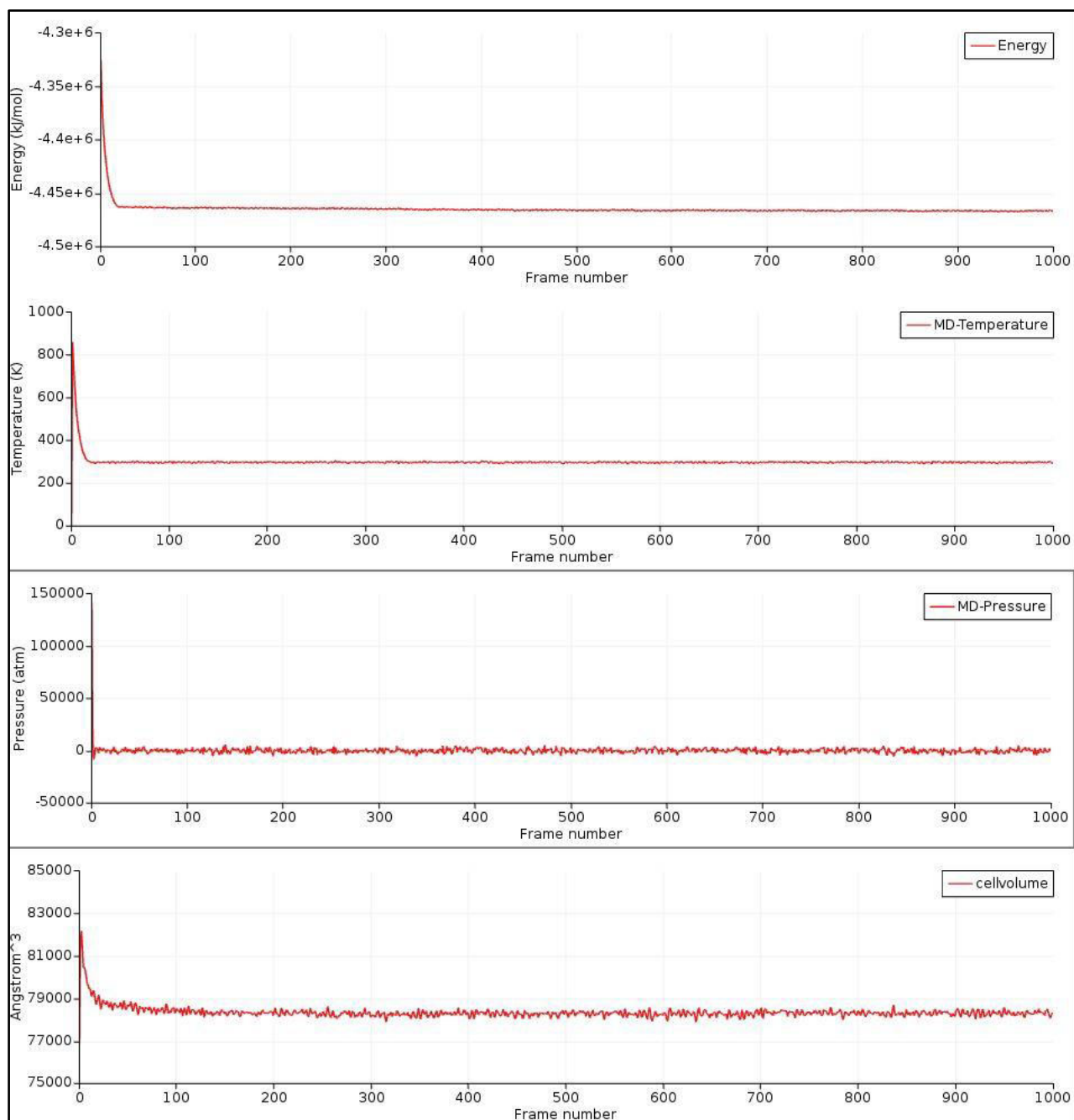


**Figure A6-3: NVT equilibration phase plots of energy, temperature, pressure and number of molecules (heterogeneous case of the adsorption of the liquid droplet of “fuel-oxygen” mixture on dry  $\text{Al}_2\text{O}_3$  surface.**

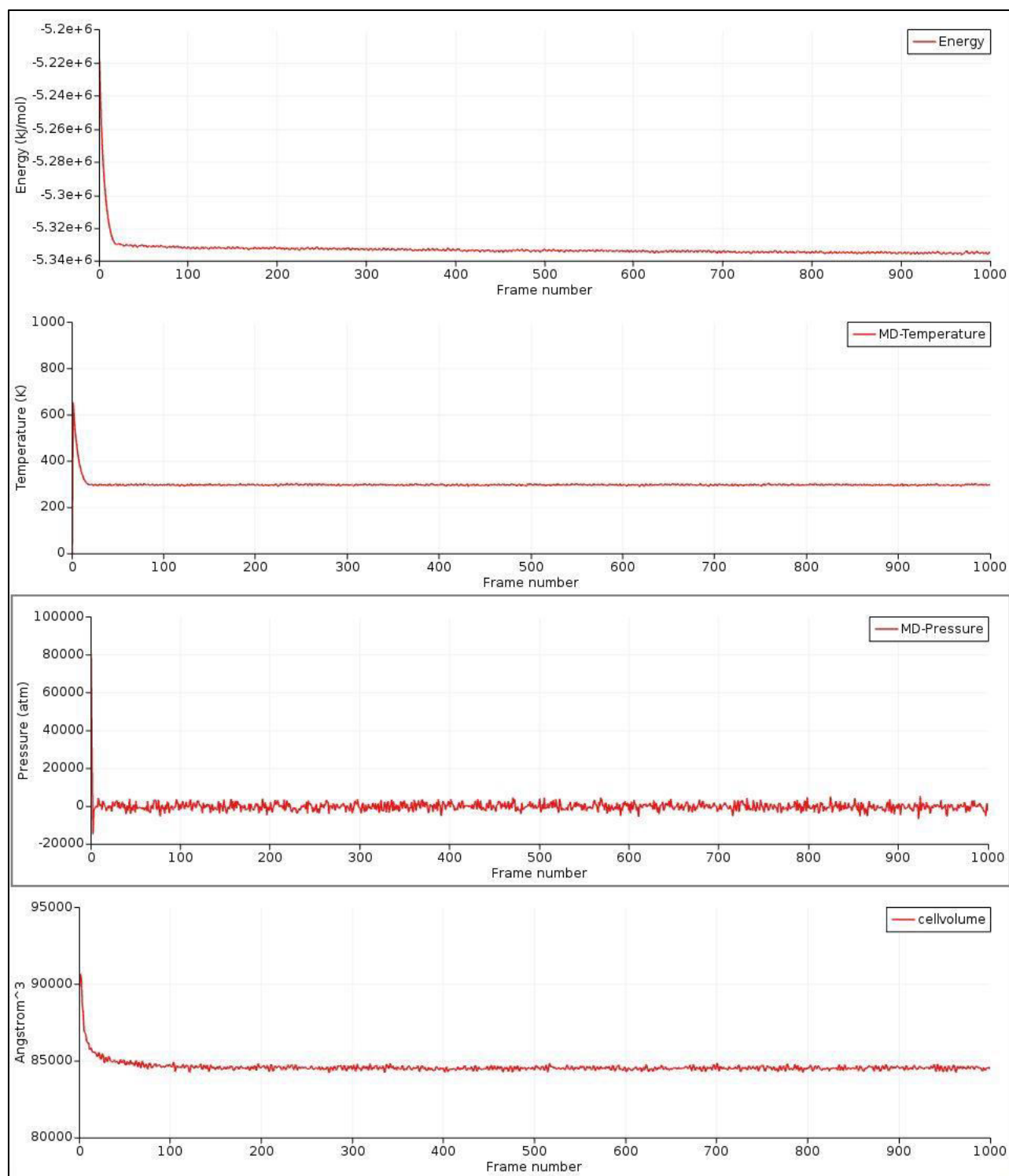
## Liquid-phase “fuel-oxygen” mixture adsorbed on alumina



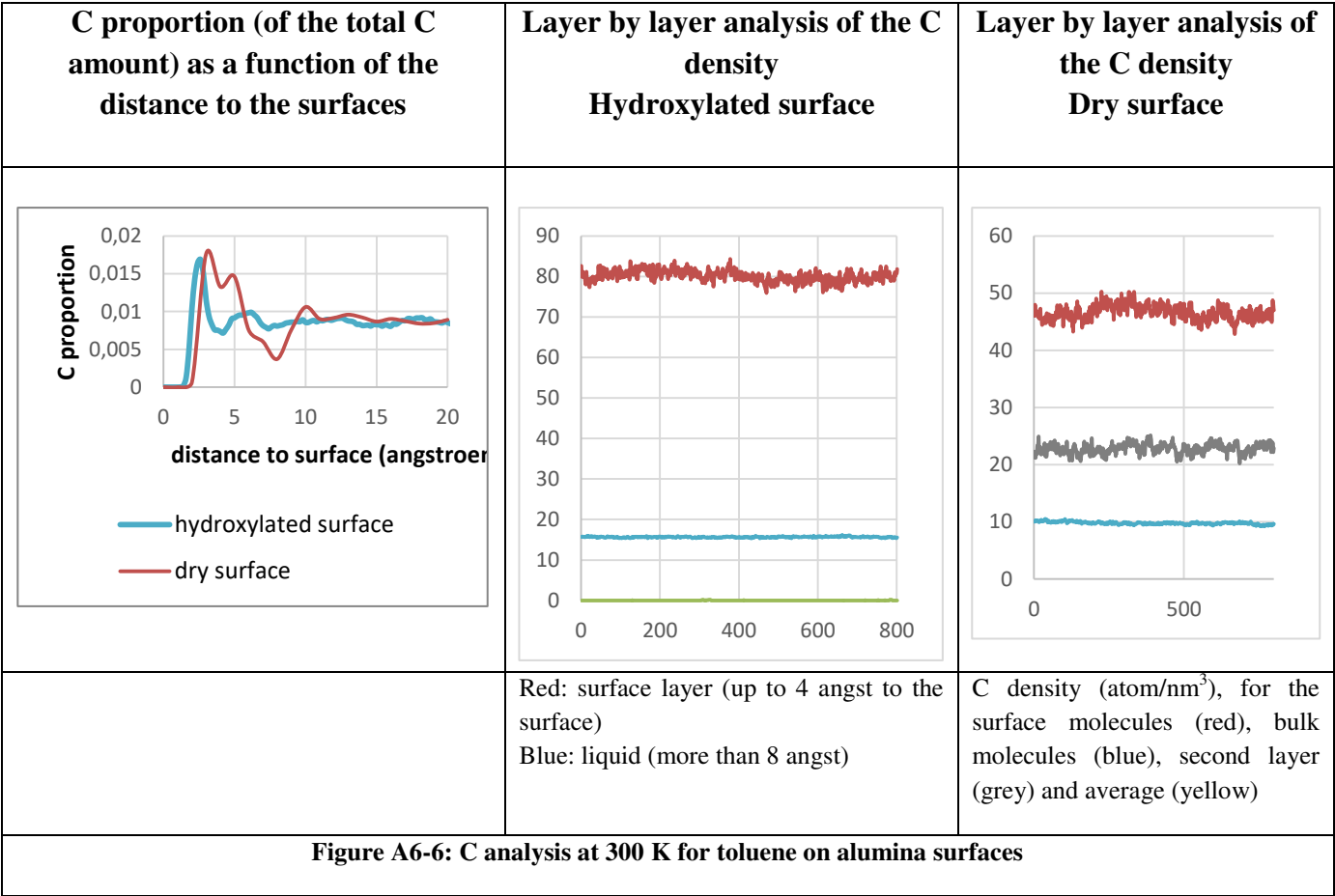
**Figure A6-4:** NVT equilibration phase plots of energy, temperature, pressure and number of molecules (heterogeneous case of the adsorption of the liquid droplets of “fuel-oxygen” mixture on hydroxylated  $\text{Al}_2\text{O}_3$  surface.



**Figure A6-4: NPT equilibration phase plots of energy, temperature, pressure and cell volume (heterogeneous case of the adsorption of the liquid-phase of “fuel-oxygen” mixture on dry  $\text{Al}_2\text{O}_3$  surface).**



**Figure A6-5: NPT equilibration phase plots of energy, temperature, pressure and cell volume (heterogeneous case of the adsorption of the liquid-phase of “fuel-oxygen” mixture on hydroxylated  $\text{Al}_2\text{O}_3$  surface).**



*This page is intentionally left blank*

## RÉSUMÉ

---

L'utilisation de biocarburants est l'un des principaux leviers permettant au secteur des transports d'atteindre les objectifs environnementaux ambitieux. Cependant, l'un de leurs inconvénients majeurs est leur stabilité thermique et chimique vis-à-vis de l'oxydation. En effet, l'oxydation provoque la dégradation des hydrocarbures, ce qui entraîne la formation d'agrégats et de dépôts insolubles dans le système d'alimentation en carburant des automobiles et des avions, conduisant ainsi à des défaillances mécaniques du moteur, telles que le blocage des injecteurs ou le colmatage des filtres.

L'objectif de cette thèse est de mieux comprendre la phénoménologie liée à la formation de dépôts produits par le processus d'autoxydation qui se produit pour les carburants fossiles et renouvelables et l'impact de la surface métallique en contact avec le carburant. Pour atteindre cet objectif, la méthodologie adoptée pour cette thèse est basée sur la combinaison de deux approches numériques différentes: la théorie de la fonctionnelle de la densité *ab initio* (DFT) et une simulation empirique atomistique par champ de force réactif (ReaxFF).

## MOTS CLÉS

---

DFT, Biocarburant, Adsorption, Dépôt, ReaxFF

## ABSTRACT

---

The use of biofuels is one of the main levers for the transport industry to meet the ambitious environmental targets. However, one of their major drawbacks is their thermal and chemical stability towards oxidation. Indeed oxidation causes hydrocarbon degradation, which results in the formation of insoluble aggregates and deposits in the fuel system of automobiles and aircraft that consequently leads to mechanical engine failures, such as injector blockage or filter plugging.

The objective of this thesis is to better understand the phenomenology related to the formation of deposits produced by the autoxidation process that occurs for fossil and renewable fuels and the impact of the metal surface in contact with the fuel. To achieve this goal, the methodology adopted for this thesis is based on the combination of two different numerical approaches: *ab initio* Density Functional Theory (DFT) and an empirical atomistic Reactive Force Field (ReaxFF) simulations.

## KEYWORDS

---

DFT, Biofuel, Adsorption, Deposit, ReaxFF